Modeling, performance evaluation, and post-process planning for directed energy deposition

by

Deniz Sera Ertay

A thesis
presented to the University of Waterloo
in fulfillment of the
thesis requirement for the degree of
Doctor of Philosophy
in
Mechanical and Mechatronics Engineering

Waterloo, Ontario, Canada, 2021

Examining Committee Membership

The following served on the Examining Committee for this thesis. The decision of the Examining Committee is by majority vote.

External Examiner:	Jill Urbanic Professor, Dept. of Mechanical, Automotive & Materials Engineering, University of Windsor
Supervisor(s):	Mihaela Vlasea Professor, Dept. of Mechanical and Mechatronics Engineering, University of Waterloo Kaan Erkorkmaz Professor, Dept. of Mechanical and Mechatronics Engineering, University of Waterloo
Internal Member:	Ehsan Toyserkani Professor, Dept. of Mechanical and Mechatronics Engineering, University of Waterloo
Internal Member:	Kyle Daun Professor, Dept. of Mechanical and Mechatronics Engineering, University of Waterloo
Internal-External Member:	John McPhee Professor, Dept. of System Design Engineering, University of Waterloo

Author's Declaration

This thesis consists of material all of which I authored or co-authored: see Statement of Contributions included in the thesis. This is a true copy of the thesis, including any required final revisions, as accepted by my examiners.

I understand that my thesis may be made electronically available to the public.

Statement of Contributions

In this dissertation, Chapter 3 consists of an article that was co-authored by myself, my supervisor prof. Mihaela Vlasea and my co-supervisor prof. Kaan Erkorkmaz. I developed and implemented the physics-based modeling, conducted experiments, collected and processed data, analyzed the results, interetated the results, and wrote the article. Prof. Vlasea and peof. Erkorkmaz guided the conceptualization of the research and helped with reviewing and editing the article.

Chapter 4 consists of an article that was co-authored by myself, Dr. Mohamed Naiel, Professor Mihaela Vlasea and Professor Paul Fieguth. Dr. Naiel and I contributed towards developing and evaluating the vision-based feature detection algorithm, performed experiments and analyzed the results. My direct contribution was towards experimental design, data collection, data processing, modeling, conceptualization of the feature extraction algorithm, data annotation, data processing, interpretation of results, and in-depth discussion, and major contributions to writing the article. Prof. Vlasea and prof. Figueth guided the conceptualization of the research and helped with reviewing and editing the article.

Chapter 5 consists of an article that was co-authored by myself, Dr. Mohamed Naiel, prof. Mihaela Vlasea and prof. Paul Fieguth. I generated process maps, performed experiments, analyzed the results, interpreted the results, and contributed to the majority of writing of the article. Dr. Naiel performed detection algorithm for the new experimental dataset and expanded the previous study in Chapter 4 to detect material ejecta. Prof. Vlasea and prof. Fieguth guided the conceptualization of the research and helped with reviewing and editing the article.

Chapter 6 consists of an article in preparation that is currently co-authored by myself, Andrew Katz, prof. Mihaela Vlasea and prof. Kaan Erkorkmaz. I extended the study in Chapter 3 to simulate 3D objects, performed the experiments and pyrometry data acquisition, developed the statistical algorithms, collaborated in performing machining tests, analyzed and interpreted the results. Andrew Katz developed the cutting force model, collaborated in performing machining experiments and analyzed results. Prof. Vlasea and prof. Erkorkmaz guided the conceptualization of the research and helped with reviewing and editing the article.

Abstract

This dissertation focuses on improving part quality and process reliability by proposing methods for predicting process outcomes, detecting defects and process anomalies in DED. These methods include physics-based process modeling, in-situ process monitoring, statistical and machine learning algorithms. Furthermore, these methods are utilized to assist the post-process or layer-intermittent machining as a corrective action in response to defects or process anomalies.

The physics-based model predicts the melt pool temperature, keeps track of the thermal history, and simulates the deposition geometry using a voxel-based approach by discretizing the scan path. This approach provides the capability of simulating 3D objects, where the layer-based scan path includes not only 1D deposition tracks, but also 2D features such as curvatures.

In-situ vision data acquisition, feature extraction, and analysis are performed to propose a method for detecting target regions in the laser-material interaction zone based on a low-cost high-dynamic-range (HDR) vision sensor. Adaptive image thresholding, connected component analysis, and iterative energy minimization are used to identify target regions in the field of view. The method is designed to be adaptive, in terms of obtaining parameters based on simple training data, and robust, in terms of feature detection performance subject to under-melt, conduction and keyhole melting mode phenomena. The performance of the proposed region detection scheme is quantitatively and qualitatively evaluated against annotated data. It was found that the True Positive Rate in detection was above 90%, while the False Detection Rate was less than 10%.

The proposed feature extraction algorithm from melt pool images and the physics-based modeling are then leveraged to define, identify and classify regions of process stability in DED. The research efforts are focused on generating process maps to identify unstable process zones, with a reference to process physics, process signatures, and process outcomes using analytical modeling, in-situ melt pool monitoring, and ex-situ characterization, respectively. The goal is to classify the process signatures in pre-defined process zones (under-melt, conduction, keyhole, balling) to avoid instabilities, defects and anomalies using a low-cost high-dynamic range camera and a kNN (k-nearest neighbor) classifier, which has achieved 13% error rate. With this approach, decisions may be made to perform corrective actions (e.g. machining, re-manufacturing), or to scrap the manufactured part.

A dual wavelength pyrometer was also deployed to monitor the laser-material interaction zone coaxially with the laser beam to validate the proposed physics-based thermomechanical model in a multi-layer, multi-track 3D part manufactured via DED process. The pyrometry data was further analyzed to find a correlation between the melt pool signatures and the process outcomes and to detect geometric defects. Such defects can be addressed with post-process machining via two correction strategies. In the first approach, machining is used as a post-processing operation, where geometric fidelity of the overall part is not met and/or surface quality requires improvement. The second strategy is a layer-intermittent approach, where the deposition quality of each layer is assessed and layers are flagged for machining based on the melt pool signatures.

This dissertation contributes towards accelerating the industrial adoption of DED and advancing the competitive advantages of metal additive manufacturing compared to conventional manufacturing processes. This is achieved by improving the part quality, process performance and reliability by advancing the DED process modeling, process monitoring and data analysis, and by proposing an intelligent decision-making schema for a hybrid machining approach.

Acknowledgements

I would like to acknowledge and express my deep gratitude to my research supervisors Prof. Mihaela Vlasea and Prof. Kaan Erkorkmaz, who provided me invaluable mentorship, unlimited support, and encouragement throughout my PhD. I very much appreciate the tremendous opportunities they were able to provide. It has been a great pleasure to work with them and learn from them.

I hereby acknowledge my thesis examining committee members, Prof. Jill Urbanic from University of Windsor, Prof. Ehsan Toyserkani, Prof. Kyle Daun, and Prof. John McPhee from the University of Waterloo for taking time to review my thesis and provide their valuable and constructive insights.

I would like to thank Professor Paul Fieguth, Dr. Mohamed Naiel and Andrew Katz for their contributions in this dissertation and their guidance and support. I would also like to thank the members of the Multi-Scale Additive Manufacturing Laboratory for their willingness to share knowledge and experience with me. I would particularly thank Sagar and Gitanjali for their support and friendship, who were more than labmates. I am very grateful to have my friend Damla's support, love and kindness throughout this journey.

I would like to acknowledge the sponsors of this dissertation: Natural Sciences ans Engineering Research Council of Canada (NSERC) - CANRIMT2 network (grant number NETGP 479639-15) and Federal Economic Development Agency for Southern Ontario (FedDev Ontario - grant number 814654). In addition, I would like to acknowledge the financial and in-kind support from the team at Xiris Automation Inc. (Burlington, ON) and Optomec Inc. (Albuquerque, NM) for giving me the opportunity to pursue an internship at their facilities.

Finally and most importantly, I would like to thank my parents, Semra and Bahadir, and my brother Levent for their unconditional love, support, and encouragement.

Dedication

To my beloved parents Semra and Bahadir

Table of Contents

List of Tables

List of Figures

Chapter 1

Introduction

1.1 Motivation

Additive manufacturing (AM) is a fairly new class of technology compared to conventional manufacturing processes, where units of materials are fused to build a part from a 3D model data in a layer-by-layer manner. The concept of metal AM appears first in 1920s, where electric arc and metal electrode were used to form decorative objects [302]. The industrial applications of AM were limited to rapid prototyping technology for many years; however, the transition from rapid prototyping applications to industrial adoption has accelerated since the early 2000s, specifically in metal AM. This notable momentum stems from the exciting opportunities that the AM processes can offer, ranging from flexibility in part design complexity, improvements in manufacturing sustainability and efficiency, and enhanced manufacturability of materials [116]. As such, AM has become one of the significantly critical pillars of Industry 4.0 [150]. Metal AM processes and specifically laser-based techniques such as directed energy deposition (DED), also known as laser directed energy deposition (LDED), laser material deposition (LMD), laser engineered net shaping (LENS), have been demonstrated to have a high potential for high-value, low-volume parts, or technology-disruptive designs. Nowadays, directed energy deposition techniques are based on similar ideas as laser cladding, but integrate layered manufacturing concepts to create parts directly from computer-aided design (CAD) data [97]. The first commercial effort in DED started with the formation of Aeromet Corporation in 1997, which focused on a laser-based directed energy deposition technology for large aerospace components made of Titanium alloys. In 1998, the LENS process initially developed at Sandia National Laboratories was licensed by Optomec Inc. and University of Michigan, resulting in the commercial launch of the DMD process by the POM Group (now known as DM3D Technology); this development brought further advancements and technology acceptance for metal additive manufacturing. Due to part costs and long manufacturing time scale, early efforts on metal AM were focused on low volume and high value components, with aerospace and medical sectors being a natural fit for initial industry up-take [98]. The current impact of such technologies is however still limited and the industrialization has not reached maturity yet. In DED, the prohibitive gaps include and are not limited to the complex physics of the laser-material interaction process, poor surface quality, and challenges in predicting and controlling mechanical properties. This is because there are many process parameters in metal AM interacting with each other and affecting the quality of the final part. Furthermore, there are random events as well, which occur during the manufacturing process and can result in defects.

The applications of metal AM range from automotive, aerospace, medical, and energy industries. The driver behind metal AM technology adoption is the flexibility in part design complexity, where increasing the complexity of 3D designs does not raise the manufacturing tooling costs [373, 31]. One example of a competitive advantage in metal AM is that sub-components in assemblies can be consolidated to reduce the final part count, often improving the functionality of the assembly and reducing the time loss during assembly and testing. The components fabricated via metal AM using current technologies are commonly followed by a post-process, which could be a machining operation or a heat treatment [205, 300, 290]. These can be performed to meet the required dimensional tolerances of the final part [324], improve surface quality [205], relieve residual stresses [249], and improve the overall mechanical properties [300]. A hybrid additive and subtractive manufacturing system is an effective way to adopt metal AM in industrial applications, while meeting the needs for post-processing of complex part designs. The integration of the two manufacturing processes requires further refinement to fully leverage the advantages of AM and machining in tandem. This synergy requires research into custom (i) process modeling, (ii) advanced sensor data analysis, (iii) process mapping in correlation to part qualities, (iv) process control, and (v) process planning schema to address random defects and sites which cannot be machined. This dissertation focuses specifically on (i), (ii), (iii), and (v).

The main motivation of this dissertation is to contribute towards accelerating the industrialization of metal AM processes to raise the competitive advantages of metal AM processes, in line with existing advances in conventional manufacturing processes. To accelerate the industrialization of AM, the proposed research will focus on the key transformative technology advancements that would enable improved part quality, process reliability and repeatability, with a direct application in DED. The DED technology of focus for this dissertation deploys a metal powder stream delivered and deposited through a nozzle, while a laser beam melts and fuses part of the metal powder stream. In this dissertation, to address items (i), (ii), (iii), and (v) as listed above, the research efforts have focused on modeling of the DED process and thermal history of the product, observing and extracting features of interest from sensor data (NIR vision, dual wavelength pyrometry), identifying process instabilities, detecting and predicting defects using different methods to enhance part quality, and enhancing process reliability and repeatability by proposing a schema intended for hybrid machining. Machining strategies are herein intended to correct the defective regions of the additively manufactured parts using intelligent algorithms based on process physics, process signatures, and part quality outcomes.

1.2 Objectives

The main goal of this dissertation is to enhance part quality by detecting process defects, anomalies and instabilities using process modeling, in-situ monitoring, and data science. Furthermore, planning schema is developed to provide intelligent decision-making in terms of machining corrective action, as needed, based on the process physics, signatures and outcomes. In this regard, the objectives of this dissertation are:

1. To develop a fast physics-based thermal and geometry model to predict melt pool temperature, morphology and cooling of the deposited part in DED, which is not only applicable to single track geometries, but also to 3D objects. Fast modeling approaches can be used either as process simulation tools for process mapping and planning, or as surrogate models running in parallel with the process, with modeling outcomes influenced by sensor data.

2. To integrate in-situ vision monitoring sensors into the DED manufacturing system to observe the melt pool morphology and detect process signatures, and furthermore to develop an algorithm to extract features of interest from the melt pool. The melt pool features are then analyzed further to detect process instabilities, and to assign quality metrics to the deposited parts via data science and machine learning techniques, where the labels are predefined based on process physics and modeling.

3. To generate statistical algorithms using multiple data sources such as process signatures (sensor data), process physics (modeling), and part quality outcomes (part geometry, hardness, etc.) that establish correlations between the deposition process parameters and the part quality outcomes. The main intention is to use multiple

data sources to increase the robustness of the DED process and machining towards a hybrid approach.

4. To propose machining schema for additively manufactured parts using a hybrid approach, combining process modeling, monitoring and data science. The machinability of the additively manufactured parts are investigated.

1.3 Outline

This dissertation consists of seven chapters, including the introduction chapter. Chapter 2 presents a literature review, where the gaps in literature in metal AM and hybrid manufacturing are highlighted. The contributions of the dissertation are listed at the end of Chapter 2. This chapter provides a literature overview of the big picture of this dissertation, where more detailed literature review is provided at the introduction sections of Chapters 3, 4, 5, and 6. Chapter 2 is an article in preparation as a brief review paper.

In Chapter 3, an interlinked physics-based thermal and geometry model for DED using a voxel-based approach is proposed. The model predicts the melt pool temperature, thermal cooling throughout the deposited part, and the final geometry of the deposition. This model aims to not only predict the geometric features for simple depositions, but also it is also able to simulate 3D objects with complex single-plane multi-tracks and subsequent layers. This study is published in Journal of Additive Manufacturing [106].

In Chapter 4, an adaptive vision-based detection algorithm is developed to extract predefined regions from the laser-material interaction zone in a DED process. The algorithm shows a robust detection performance in different processing conditions such that the effects from illumination variations in the environment and saturation in the field of view as a function of variable exposure time settings have a minimal impact on the detection performance. This study is published in Journal of Additive Manufacturing [264].

In Chapter 5, the work focuses on the development of process performance maps using process modeling (physics of laser-material interaction), process signatures (in-situ vision sensor), and part quality outcomes (deposition geometric profile); such maps can help in identifying process parameter thresholds. A classifier algorithm is proposed to predict the pre-defined labels based on the features defined from process physics and signatures. This study has been accepted for publication in the CIRP Journal of Manufacturing Science and Technology.

In Chapter 6, DED experiments are performed, while collecting thermal signatures (dual wavelength pyrometry) from the laser-material interaction zone coaxially with the laser beam. The sensor data is used to validate the physics-based model for a 3D object with multi-tracks and layers. Clustering and classification algorithms are proposed to detect regions with defects using the sensor data; furthermore machining strategies are proposed to address these defects. The machinability of the additively manufactured parts is investigated by measuring the cutting forces and observing the tool wear. Chapter 6 is an article in preparation for submission to a peer review journal. Chapter 7 presents the conclusions and future work.

Furthermore, as additional work beyond the scope of the dissertation, but in-line with the idea of correlative analytics between process physics and product quality outcomes [104], it describes two machine learning algorithms developed to predict sub-surface level pores in laser powder bed fusion (LPBF). This study is published in ASME Journal of Manufacturing Science and Technology [104].

Chapter 2

Literature review

2.1 Preface

Hybrid manufacturing is a rapidly-evolving manufacturing technology class, with one classification combining metal additive manufacturing (AM) and machining processes in one manufacturing system. Conventional machining is a well-developed and well-studied manufacturing process, when compared to AM, and it is commonly required as a post-process step after the AM part is produced to enhance the dimensional accuracy and the surface quality of the final part. Additionally, machining can be used intermittently during the AM process to re-work defective depositions or to finish internal cavities, which may not be accessible by the cutting tool after the AM of the complete part. Hybrid manufacturing systems are more advantageous if the machining step is used layer-intermittently, rather than as a post-processing option. Hybrid manufacturing requires full integration of the two processes and often leverages advanced process and toolpath planning strategies, as well as process quality monitoring to assess and prioritize machining strategies. This review looks at the state of art of process integration and planning for hybrid manufacturing and proposes a research approach to improve the reliability of the joint processes.

2.2 Introduction

In this chapter, a literature review is provided on metal additive manufacturing (AM), machining and hybrid manufacturing technologies. The chapter mainly focuses on process integration of metal AM and machining in a hybrid system, as well as machinability of additively manufactured parts. The gaps in the literature are highlighted and discussed to maximize the benefits of having two manufacturing technologies in one system. Detailed literature review for DED process modeling, in-situ monitoring sensors and data processing, anomaly detection, and quality assessment are provided at the beginning of Chapters 3, 4 and 5, respectively, to frame the literature context and motivation behind research contributions towards achieving hybrid machining approaches. Chapter 6 provides an insights into strategies for combining these approached towards hybrid manufacturing process planning.

2.2.1 Introduction to metal additive manufacturing processes, with a focus on directed energy deposition

Metal AM is a class of manufacturing processes, where 3D parts are constructed by fusing units of material layer-upon layer, at select locations in space. Metal AM presents numerous advantages over conventional manufacturing processes by virtue of drastically-increased design potentials, reduced tooling needs, and the overall ability to customize the parts at the micro-, meso-, and macro-scale. The industrialization of AM continues to be accelerated by research and industry-sector efforts [89]. Research efforts are focused on optimizing the metal AM processes to achieve better dimensional accuracy, surface roughness, material and mechanical properties of the final part [47, 345]. However, the repeatability, reliability and accuracy of the AM processes still needs improvement, compared to conventional manufacturing processes. As a result, post-processing after the metal AM step is needed for most of the components poised for industrial end-use applications [101].

Metal AM involves more than one technology class; laser powder bed fusion, directed energy deposition, electron beam melting, and powder bed binder jetting [135, 54] are part of the original metal AM categories, with emerging technologies such as metal infused filament [395], material jetting [323], metal-infused slurries for stereolithography [27], to name a few. The original metal AM technologies have advantages and limitations when compared and contrasted, whereby depending on the application type, part design and desired mechanical properties, the most appropriate metal AM technology can be chosen [261]. This chapter focuses on directed energy deposition (DED), as it is one of the most common metal AM technologies preferred in a hybrid manufacturing approach. In this process, the metal is delivered through a nozzle assembly and it is melted by virtue of an energy source onto a substrate under the influence of a shielding gas [402]. The metal delivered via the nozzle assembly can be in powder, wire, or filament form, while the energy source is typically a laser or an electron beam. The layer deposition toolpath is executed by the relative motion between the DED processing head (comprised of the powder delivery nozzle assembly and the energy source) and the substrate (typically on the x-y plane). The process continues in a layer-by-layer manner until the final geometry is achieved. The focus of the present work is on DED deploying metal powders as the material feedstock and a laser as an energy source. For this type of powder-fed laser DED process, there are many process parameters driving performance outcomes such as laser power, laser focus, scan speed, powder deposition rate etc., which affect the physics of the melting, solidification and cooling of the deposited material system, and results in different mechanical properties and deposition geometric profile characteristics [372]. Figure 2.1 visualizes how the process parameters and signatures affect the process outcomes, where process parameters are at the core influencing both process signatures and outcomes. Table 2.1 provides a further overview of the process parameters, process observable signatures, and process outcomes relevant for powder-fed laser DED processes [240].

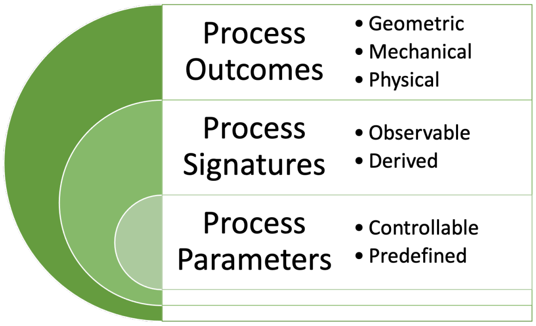

Figure 2.1: The correlations between process parameters, signatures and outcomes, where process parameters being in center affecting both process signatures and outcomes and process signatures only affecting process outcomes.

DED is one of the commonly-used AM processes in industry known by its capability of manufacturing high-density parts and controllable microstructure. The most important application areas of DED are repair, also referred as remanufacturing, and featurization, which addresses the addition of complex-shaped features onto a part [280, 223, 410]. In part re-manufacturing and repair, the defective portion of a high-value component can be removed via a cutting operation and re-manufactured on the spot by selectively adding material via a DED process [427, 21]; post processing such as machining and heat treatments are common. This approach would prevent scrapping the high-value part owing to a localized minor defect, resulting in saving cost, time, and energy [182]. In featurization, material can be deposited onto an existing part at selected locations. This allows for the bulk of a part to be produced using inexpensive methods such as casting, forging etc., while

Table 2.1: Overview of process parameters, signatures and outcomes. Here, the process parameters were lumped together, with the typical controllable parameters highlighted (*)

Process parameters	**Process signatures**	**Process outcomes**
Laser power (*)	Melt pool height	Deposition geometry
Scan speed (*)	Melt pool width	Strength
Laser beam diameter (*)	Melt pool length	Hardness
Powder feedrate (*)	Melt pool temperature	Thoughness
Gas flow rates (*)	Plume characteristics	Fatigue life
Scan path (*)	Unmelted particles	Residual Stress
Powder size	Particle spatter	Surface roughness
Powder shape	Defects	Porosity
Build plate temperature (*)	Temperature gradient	Defects
Laser wavelength		
Nozzle design		

the complex features can be added using DED processes [30]; similarly, post processing steps such as machining and heat treatments are common during the featurization process. Hybrid manufacturing approaches integrating both machining and DED metal AM have gained interest towards simplifying the manufacturing workflow and present advantages in manufacturing of customized parts in small batches [15].

2.2.2 Introduction to machining

Machining is a manufacturing process, where a bulk material is shaped into its final geometry via material removal; as such, material is cut in form of chips by a machining end-effector tool to impart the final shape of the part. There have been a wealth of research efforts in this domain to solve the mechanics and dynamics of the machining process and to increase its accuracy, repeatability and reliability[14]. Research efforts have been dedicated to estimate the cutting forces, which are solved typically for orthogonal cutting and transformed into oblique cutting based on the process geometry [51]. The cutting forces are highly dependent on material properties, process parameters (e.g. spindle speed, feedrate, depth of cut etc.) and chip geometry [383]. Due to cyclic loading in the cutting process, the spindle column is prone to vibrations. Unstable vibrations, also called chatter vibrations, result in a poor surface finish [50, 12]. This can be avoided by modeling the machine structure and obtaining the stability lobes for that process [13].

Advanced control systems are applied to have a better positioning precision and accuracy of the CNC (Computer Numerical Control) system [275, 341]. These control systems are mainly for avoiding excessive positioning errors (in the servo system) or vibrations, in order to decrease the contour error and surface finish marks. Toolpath smoothing is proposed to decrease the fluctuations in the trajectory profiles [14, 102]. Optimization algorithms are proposed to decrease the cycle time of machining and minimize the contour error without violating the drive limits [340].

2.2.3 Introduction to hybrid manufacturing

The hybrid process combines two or more manufacturing processes in one machine [358]. This could be a combination of different manufacturing processes such as subtractive, additive, joining, forming and heat treatment etc. [231, 29, 359, 244]. This chapter focuses on hybrid systems that combine metal AM (DED) and subtractive (milling) manufacturing processes together, with an example shown in Figure 2.2. As the part is built layer-by-layer via AM, the sequence of the processes is commonly to deploy the additive and then subtractive steps in sequence [124]. For part remanufactuirng and part featurization, this sequence may be preempted by a machining step to remove a defect or to prepare a surface, respectively. The main idea behind the hybrid DED manufacturing systems is to simplify the workflow and to compensate for the disadvantages of the AM and machining standalone process by complementing their capabilities. As such, hybrid additive manufacturing processes are poised to decrease the tooling cost and the downtime required in alternating between two processes when the part is transferred between the AM and the machining system for finishing [433, 231, 241]. Furthermore, hybrid manufacturing can be used as a layer-intermittent process, between the deposition of consecutive layers or at select stages in the DED process.

Hybrid manufacturing systems, although advantageous, do introduce additional challenges in terms of process planning [68]; such challenges can be grouped in three categories. Firstly, the machinability of additively manufactured parts is different than cutting metals manufactured by conventional processes (e.g. metal forming, casting), as the hardness is usually higher in additively manufactured parts [315]. Secondly, it is typical to have anisotropy in mechanical properties for additively manufactured DED parts due to different local cyclic thermal loading [10]. A similar anisotropy can be observed in cast metal due to different solidification and cooling rates at thin geometric features [350]. Lastly, the DED process can create parts with complex geometries and uncertain layer-by-layer dimensional fidelity [131, 308]. As such, the mechanical properties, as well as the machinability, can vary within the part [253], with the added challenge of part geometric complexity. This can result in excessive wear of the cutting tool, excessive loading and vibrations on the

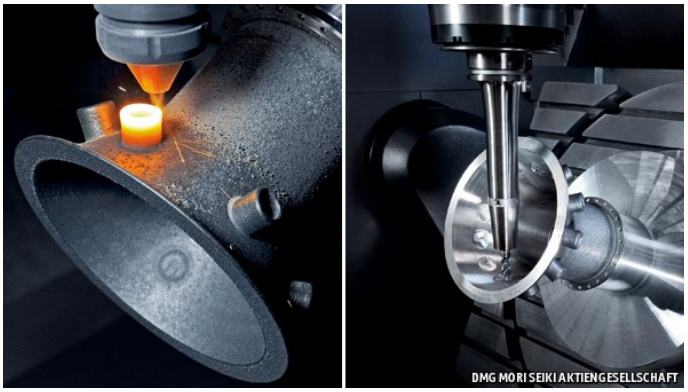

Figure 2.2: Hybrid manufacturing system, where DED and machining processes are combined in one manufacturing system [1]

cutting tool assembly, as well as uncertainty in geometric shape of the underlying material. These challenges call for advanced process planning strategies, where predictive models, in-situ monitoring and characterization methods can be used to plan the hybrid process [413]. Figure 2.3 shows different in-situ monitoring sensors detecting variety of features from the laser-material interaction zone by observing different process signatures.

In literature, there are models for process planning for machining as an AM post-process, where part orientation, fixture and machinability are modeled based on the geometry of the part [181]. Another approach has been presented by Kerbrat et al., where the manufacturability of the part for both of the processes is modeled from the 3D CAD model of the part [183]. In-situ measurement systems have been recently introduced in hybrid manufacturing systems to detect process signatures from both of the processes [393], with a detailed overview of in-situ monitoring for DED captured in Chapter 4 and 6. For machining processes, acoustic emission sensors can be used to detect the depth of cut during milling process [130]. Due to the uneven surface finish resulting from the AM step, the depth of cut can vary, as the milling tool moves along the toolpath, which presents a current technological challenge [22].

2.3 Review of opportunities and limitations

In this section, a review of hybrid AM and machining approaches is presented with a focus on the opportunities and limitations of the two processes performed independently and performed together in a hybrid system. Although machining is a well-studied and

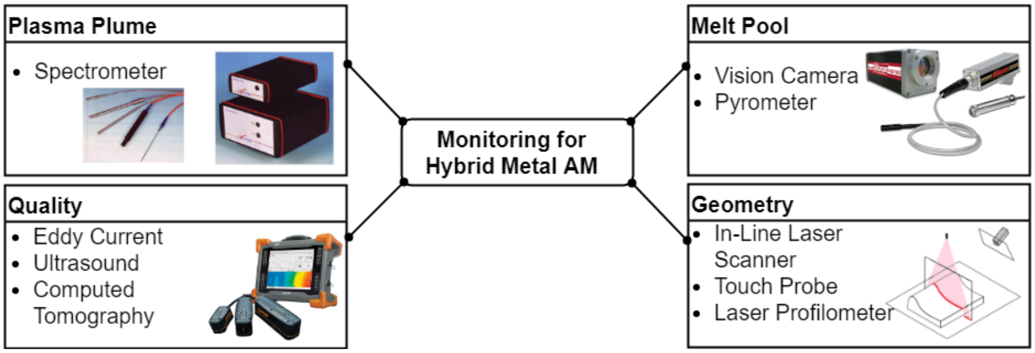

Figure 2.3: Monitoring sensors detecting different process in hybrid additive/subtractive manufacturing systems

well-established manufacturing process, machining of additively manufactured parts and hybrid manufacturing give rise to novel research questions. The industrial applications are discussed, where hybrid systems play an important role and become more advantageous production strategies. Furthermore, the state of art in process integration and machining of additively manufactured parts are reviewed. Finally, a reflection is made based on the current status of how hybrid systems are used and how it could be improved for a more efficient process, as a motivation to research contributions in this dissertation work.

2.3.1 Opportunities and limitations of metal AM and machining

The philosophy behind the machining process and the DED process is the exact opposite; material is removed from a bulk piece in machining, while the material is added to a substrate in DED to build the final part [291]. Similarly, the process physics of these two manufacturing processes is completely different [18]. The relative motion between the rotary cutting tool and the workpiece shears metal chips from the workpiece to shape the final part, which creates mechanical forces acting on the workpiece and the cutting tool [14]. In DED, the metal powder is fused by an energy source and the process physics involves melting, vaporisation, solidification, and cooling dynamics, as well as cyclic thermal loading as a result of the layer-by-layer deposition process. Thus, it can be stated that DED is a thermal-based process, while milling is a mechanics-based process [173]. Due to different process philosophy and physics, the fabrication opportunities they can offer are different, which are shown in Figure 2.4. Thus, combining these two processes in one manufacturing system could be advantageous [68]. The opportunities and limitations, that these two processes can offer and introduce, will be reviewed and discussed in this section.

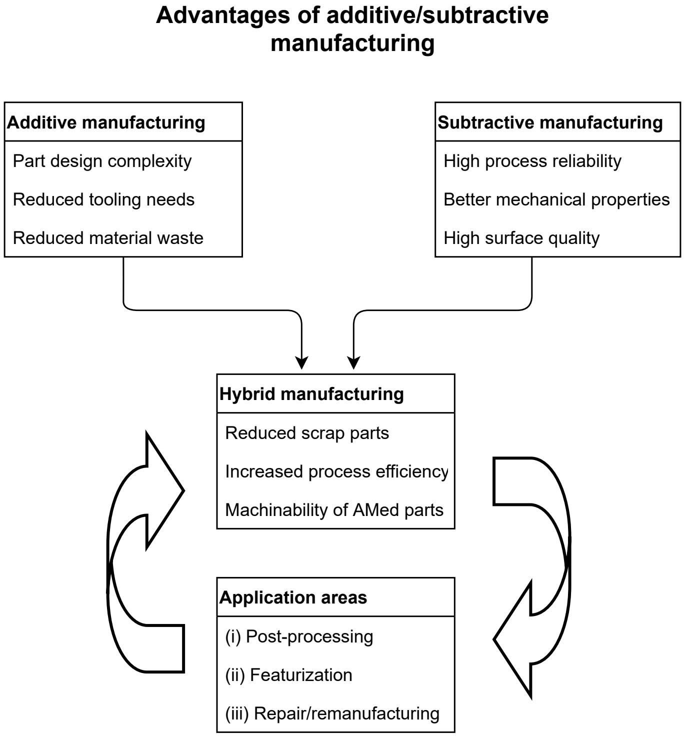

Figure 2.4: Opportunities that additive and subtractive manufacturing systems can offer separately and the complementary advantages of having these two manufacturing systems in a hybrid system.

Design potentials

The most important opportunity that DED, and in general metal AM processes can offer, is the ability to address part design complexity without the need for specialized tooling [71]. Due to the layer-by-layer manufacturing, design for manufacturing in metal AM presents less limitations compared to any other conventional manufacturing process including milling, opening up new design potentials, where the design complexity can be introduced without sacrificing the overall manufacturing cost [128]. Deploying AM strategies can lead to design optimizations to maximize the performance of the component(s) [222], reduce their weight [19], and consolidate assemblies [330, 272], which directly increases the productivity and efficiency of the manufacturing process, as well as customization of the micro- and meso-scale material properties [221], which can lead to unique component performance. There are also notable limitations in design for AM, which are process-specific. For DED processes; since the material is deposited in a layer-by-layer fashion, the deposition sequence must consider mitigation of overhang regions, minimum-feature constraints such as thin walls and small cavities, as well as regions in space where the deposition process results in thermal accumulation such as large cross-sectional areas and sharp angles. Thus, in DED, consideration of these factors, as well as accessibility for post-processing machining need to be considered as design constraints [40]. In milling, complex geometries with enclosed cavities or freeform surfaces are difficult or impossible to manufacture, as the process and toolpath planning can become rather complex, or tool accessibility may be prohibitive [84]. Furthermore, as a contrast between capabilities of DED and machining strategies, some geometries may be impossible to manufacture using milling such as lattice structures due to design complexity and tool reachability; moreover, structural topology optimization opportunities are very limited or impossible to achieve with machining processes.

Specialized tooling

Tooling is another aspect where AM becomes more advantageous over machining processes [113]. The only tool needed for the AM processes to be deployed is a build plate and fixturing for it, where in machining the cutting tool needs to be changed due to wear and different types of cutting tools might be needed for different cutting operations [115, 382]. Furthermore, the fixturing of the workpiece may need to be changed to avoid tool collision in a single cutting operation [298]. This results in disruption in the manufacturing process and causes downtime [224].

Environmental impact and sustainability

The material waste in machining is one of the reasons why metal AM is considered to be more environmentally-friendly by comparison [403, 303]. In machining, a bulk workpiece is shaped to a final geometry by removing metal chips from the surface by a cutting tool, whereas metal AM processes are considered to be near-net-shape manufacturing, with the final part being manufactured by adding material only where it is needed [245]. Furthermore, coolant is used in most of the machining operations to decrease the friction between the tool and the workpiece and hence the cutting forces and tool wear [225, 148]; using coolant makes the process less environment friendly. Furthermore, the digitization of the product data into designs and build files to be produced by an AM process, on-demand, provides an opportunity for geographically-distributed manufacturing close to the end-consumer, which contributes towards sustainability in manufacturing and lower environmental impact in transportation and warehousing costs [39]. Ford and Despeisse [116] summarize the potential sustainability benefits of AM processes in three main categories, which are improved resource efficiency, extended product life (via repair, remanufacture and refurbishment) and reconfigured value chains (localised production, shorter and simpler supply chains, etc.). Such benefits are presented in contrast to conventional manufacturing processes, such as machining.

Repeatability, accuracy and reliability

Repeatability, accuracy and reliability of the process persist as challenges of metal AM, when compared to advances in machining processes [95]. In DED, the mechanical properties are highly affected by the printing process parameters and by the laser scan strategy [156]. The process parameters and the scan strategy can be optimized to achieve required mechanical properties [278] with a high repeatability; however, defects and poor mechanical properties can be observed due to thermal cyclic loading, different thermal boundary conditions, temperature build up, and random events [416, 60]. These random events could be caused by deviations in laser power, perturbations in scan speed and powder feed rate, material ejections and spatter, which can result in a transition to different process physics and defects. Examples of defects from DED processes are represented in Figure 2.5. The defects shown in images (I)-(IV) in Figure 2.5 are pores caused by different process physics such as insufficient energy input (lack of fusion phenomena), excessive energy input (keyhole phenomena), or deposition overlap (track/clad spacing issues). Furthermore, there is lack of dilution on the right side of the depositions in the same images from (I) to (IV) resulting in poor bonding with the substrate and raised edges. This can be due to improper selection of energy input, as well as an excessive track overlap (distance between two adjacent deposition tracks), which resulted in subsequent tracks being deposited on top of each other towards the right, instead of onto the substrate.

Full-density parts may be difficult to achieve in DED due to the nature of the process, where powder particles are fused by an energy source. Even with optimized process parameters, stochastic pore defects may occur such as entrapped gas porosity and spatter [96].

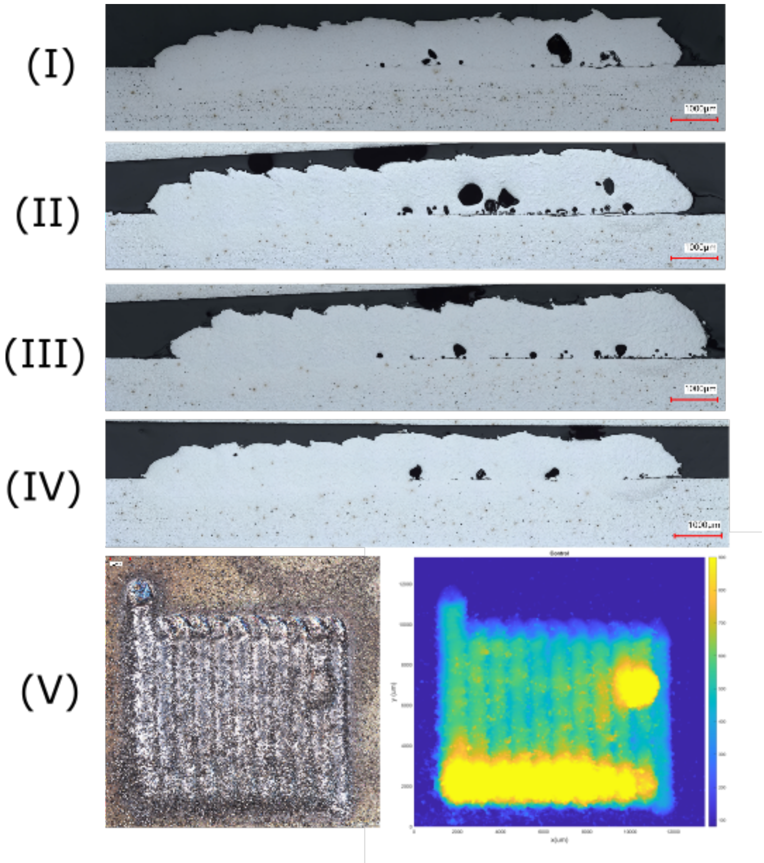

Figure 2.5: Examples of geometric and porous defects occurring in the DED process. The samples were cut perpendicular to the deposition weld tracks, with a base plate as a substrate. (I)-(IV) showing pores as well as raised edges on the right side of depositions, as well as surface asperities due to the overlapped depositions; (V) showing uneven top surface at the beginning of depositions track due to changes in scan speed, as well as a large metal bead on the right had of the deposition due to a random material spatter event.

Using optimized process parameters and sensible scan strategies can enhance the overall part quality; however, the acceleration and deceleration zones in the DED trajectory profile can cause instability in the process due to entering into different melting modes [246]. High surface quality is more challenging to achieve in metal AM compared to machining due to layer-by-layer manufacturing approach [426]. A better surface finish can be obtained by optimizing the process parameters, scan strategy especially at the border and layer thickness to enhance the staircase profile [399]. However, due to high temperature processing, there could be adhered metal powder particles or material ejecta present on the manufactured part, which affects the surface roughness negatively and may propagate to future layers [121].

Machining is commonly used as a post-processing step after DED to enhance the overall quality of the final part and to introduce high-precision features which cannot be addressed in the AM stage such as threads, high-precision surfaces, etc. [426, 279]. Having the AM and machining processes in one manufacturing system can enhance the productivity and efficiency [180]; however, it introduces new challenges. The opportunities and limitations that hybrid manufacturing offers are discussed more into detail in the next subsection.

2.3.2 Applications, opportunities, and limitations of hybrid manufacturing

Hybrid manufacturing offers the opportunity to combine two manufacturing processes in one system [115]. Metal AM has competitive advantages against machining when it comes to part design complexity [437]; however, due to challenges inherent to the metal AM process (porous defects, limitations in minimal feature size, deviations in geometric fidelity due to distortion, material under-or-over accumulation and spatter, rough surface topography, etc.), the AM processes are usually followed by a post-processing step [30, 338]. Thus, hybrid manufacturing provides the opportunity for the two processes to complement each other, where part complexity and performance can be improved significantly [15]. For instance, layer-intermittent machining can be performed for two purposes [243]. Firstly, it can machine the regions that could become inaccessible by the cutting tool when the part is completed by AM [239]. Secondly, deposition error correction per layer could be performed based on sensor data or visual inspection during the process [232]. For example, if a defect is detected, that layer can be machined and redeposited. This approach can prevent scrap parts and thus increase production efficiency [410]. Similarly, hybrid systems become more advantageous in repair applications because removing the defective region and remanufacturing can occur seamlessly [298].

Hybrid systems introduce new challenges such as increased complexity in sequential process planning [62, 305], new paradigms for process parameter optimization and toolpath planning [101, 317], and design-driven and material-driven challenges due to dynamically changing part geometry and traditionally low machinability of AM parts [424, 258] . The AM and machining sequence of operations should be optimized such that the disturbances in the manufacturing process are minimized [318, 37]. Hybrid manufacturing can be preplanned or machining can occur based on a corrective action decision in-process [46, 17]. Layer-based corrective actions can be taken due to process anomalies based on either visual observation of the process or process signatures captured by in-situ monitoring data [355].

2.4 Hybrid manufacturing

2.4.1 Application areas

Hybrid additive/subtractive systems have a high potential in manufacturing highly customized, small batch and large volume parts applicable to the aerospace, aviation, energy, and medical device sectors. Accelerated research efforts corroborate the idea that there is a growing interest in this field [296], with the main relevant production being categorized in three groups: (i) complex-geometry post-processing, (ii) featurization via adding/subtracting geometric details, and (iii) repair and remanufacturing.

Complex-geometry post-processing

Post-processing is one of the most common application areas of hybrid manufacturing. DED is known as a near-net shape manufacturing technology, where post-processing could be needed to meet the dimensional tolerances and surface finishing requirements of the part. The research efforts focus on automating the post-processing to improve productivity and overall efficiency of the process. Seidel et al. proposed a novel method to semi-automate the post-process machining of additively manufactured parts based on geometry acquisition in the as-clamped position using laser profile sensors and an automated milling path planning strategy [338]. An iterative milling path is followed to minimize the cutting forces. Post-processing can be also used as a final step for part featurization or repair/remanufacturing [115]. There are gaps in literature to identify the regions to machine as post-processing operation. Some of these regions may be predefined due to part quality requirements such as tight dimensional tolerances and high surface quality. However, other regions that need post-process machining can be caused by process instabilities and random events during DED process, which can result in geometric deviations. These critical regions need to be identified to address by post-process machining.

Featurization via adding/subtracting geometric details

As part of featurization, geometric features can be added or subtracted via hybrid manufacturing systems. For instance, a part could be manufactured by additive technology and holes and pockets can be subtracted by using milling or drilling tools for better precision and dimensional accuracy [251]. On the other hand, geometric features can be added to parts, where the bulk material is manufactured by a conventional manufacturing process (e.g. forging, casting), followed by post-processing [126]. These geometric features can be small and complex, which could drastically increase the manufacturing cost if they are manufactured by conventional processes [437, 271, 183].

Repair and remanufacturing

Repair and remanufacturing are commonly used when there is a local defect in an expensive part, to address the need to salvage the part and avoid scrap. The defective portion can be machined and re-deposited in a hybrid manufacturing system, which can increase the life time of the part and saves time, cost and energy. It is important that the mechanical properties of the redeposited region match with the rest of the part. Remanufacturing and repair have four main steps: defining the damaged feature, generating machine toolpaths for removing the damaged part, generating the deposition toolpath for remanufacturing the damaged feature, and post-processing [115]. Xu et al. repaired cracked parts by removing the defective region and redepositing while achieving 87% of the micro-hardness and 89% of the tensile strength of the original part [410]. Moreover, it is important to keep track of the part geometry, while adding and subtracting material in order to avoid tool collision and keep the nozzle standoff distance consistent. Zhang et al. proposed a method to predict the geometry during hybrid manufacturing in a voxel-based geometry reconstruction model [428], where the process interruptions are optimized. Addressing the appropriate integration of the two processes, time-efficiency and productivity are substantially improved.

2.4.2 Commercial hybrid manufacturing machines

There are a few commercial machines, which combine DED and machining in one manufacturing system. These manufacturers are DMG-Mori, Optomec, Mazak and DMS, where these offer a CNC-based system with two columns of one being the nozzle head for DED process and the other one being the spindle for the milling operation. Another alternative for this type of hybrid manufacturing system is offered by Hybrid Manufacturing Technologies, where the nozzle head is integrated into a CNC system with a tool holder mechanism.

DMG Mori is one of the leaders in the machine tool industry, which introduced the LASERTEC 65 3D Hybrid system which leverages the Siemens NX CAD/CAM module for additive and subtractive toolpath and process programming. The DMG Mori system uses a laser head handled by a fully automatic shuttle without manual intervention, for 5-axis material deposition by a coaxial nozzle, resulting in homogeneous powder distribution, independent from direction of laser deposition welding. This is combined with a full 5-axis milling machine and run through process monitoring and adaptive process control. DMG Mori's control software also enables continuous measuring and monitoring of the laser buildup process as well as automatic regulation of the laser power in real-time for homogeneous part qualities. This machine can build metal parts on cylindrical base with a diameter of 650 mm, weighing up to 600 kg.

Mazak's INTEGREX i-400 AM is one of the largest hybrid manufacturing systems available on the market, which fuses AM technology and advanced multi-tasking capabilities in a 615 x 260 x 2563 mm work envelope. The machine was developed specifically for small lot production of very difficult-to-cut materials and uses its additive capability to easily generate near-net-shape component features and then completes them via high-precision finish machining operations. It can also join different types of metals together, which allows for the efficient repair of existing worn or damaged components such as aerospace turbine blades. In terms of its Multi-Tasking capabilities, the INTEGREX i-400 AM provides full 5-axis machining to process prismatic parts from solid billets or castings (chuck or bar fed), round parts, highly contoured parts and now those with features built using additive technology.

As one of the very first manufacturers of additive DED systems, using its own proprietary LENS technology, Optomec has now broken new ground by recently beginning to offer a series of hybrid systems priced below $250,000. The company has made the top ten hybrid manufacturing companies list by introducing the new Optomec LENS 860 Hybrid CA system.

This hybrid, LENS-based metal 3D printer has an 860 x 600 x 610mm work envelope. It is equipped with a hermetically-sealed build chamber for processing reactive metals, such as Titanium. The system can be configured with closed-loop controls and a high-power 3kW fiber laser, making it ideal for building, repairing or coating mid to large size parts with superior metal quality. In addition to the LENS 860 Hybrid CA model, three more configurations are available. One key advantage of the LENS Hybrid configuration is the ability to use the milling capability to perform finish machining on a printed part without re-fixturing or aligning the component on a second machine.

Hybrid Hero CNC, designed by DMS, is to be an entry-level machine for customers who are interested in hybrid manufacturing processes. The machine has been designed to fit through a standard 74"x 81" double door, and does not require as much floor space to operate as our larger machines. It is equally suited for process development and research or production runs of small parts. The optional tilt rotate table adds 5-axis deposition and machining capabilities.

There are a growing number of DED systems in the commercial space, targeting production parts at different scales. Across these technologies, one key advantage of the DED hybrid configuration is the ability to use the milling capability to perform machining as a finishing step on a printed part without re-fixturing or aligning the component on a second machine or as a secondary operation. In addition, there is a trend towards integrating intelligent toolpath planning for the deposition and machining process, as well as process monitoring options and process control modules in an effort to continuously improve the performance of the DED and machining processes independently or in tandem.

2.4.3 State of art in machining of additively manufactured parts

The machinability of a material varies depending on how it is manufactured. Machining of additively manufactured parts presents challenges because such materials are different than wrought, casted and forged materials in terms of microstructure and mechanical properties. The DED process parameters affect the machinability of deposited materials systems by virtue of localized laser-material interaction effects (melting, vaporisation, material ejection, solidification, oxidation), as well as due to inter-layer and intra-layer cyclic thermal loading of the bulk material system. In addition, varying process parameters can also result in different mechanical properties and microstructure. Moreover, machining performance of a workpiece is highly dependent on the selected tool and coating material, tool design, and cutting parameters such as spindle speed, feedrate, and cutting depth. Considering there are many factors affecting the machinability of an additively manufactured workpiece, there are limited studies in literature focusing on this matter. The current studies evaluate the machining performance mainly by examining the cutting forces, cutting tool wear and surface finish quality, which are measureable process outcomes of the machining process.

Cutting tool wear is usually attributed to cutting forces, since the friction between the tool, the workpiece and the chip contributes in both cutting forces and tool wear. As the tool wear progresses, the cutting forces increase because the cutting edge gets blunter and causing more force acting on the workpiece [425]. However, the tool life can be further improved by coatings. Although cutting additively manufactured material may cause higher cutting forces compared to wrought material, the tool wear could be similar in both cases [10]. Careri et al. studied the tool wear on additively manufactured Inconel 718 alloy in conditions of "as-deposited" and "heat-treated" and observed both adhesive and abrasive tool wear mechanisms [59]. It is observed that flank wear progresses rapidly at higher cutting speeds while cutting additively manufactured Ti-6Al-4V [348]. Thus, the machining parameters need to be optimized based on tool wear and cutting forces. Fei et al. studied machining of additively manufactured Inconel 625 and experienced edge chipping and coat peeling on the cutting tool, where fan-shaped and saw tooth chips are generated [113].

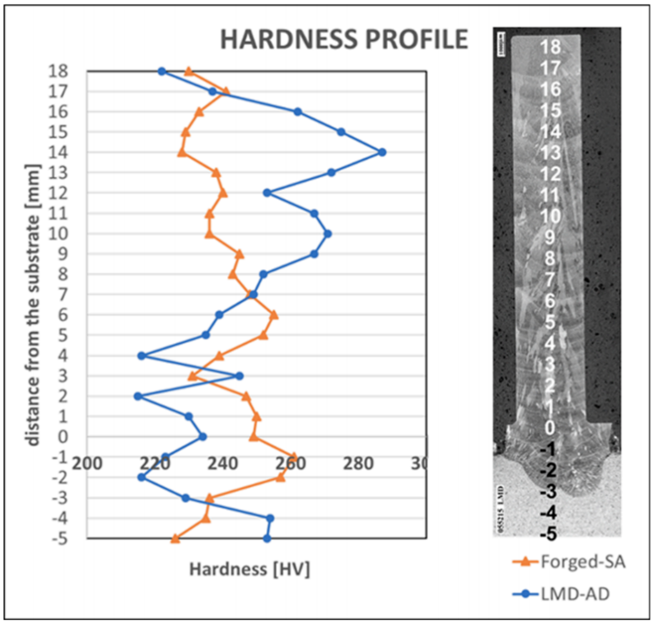

Figure 2.6: The hardness analysis of Inconel 718 thin wall manufactured by DED and forging from Ostra et al.'s study [276]

Cutting forces are generally higher in cutting AM materials compared to conventionally manufactured materials. The hardness has a direct correlation with the cutting forces and additively manufactured materials tend to have a higher hardness compared to conventionally manufactured ones, due to high solidification and cooling rates present during the AM process [227]. Furthermore, the hardness can vary throughout the additively manufactured material due to anisotropy caused by cyclic thermal loading and varying thermal boundary conditions [60]. Thus, the cutting forces are generally higher while cutting AM materials.

Ostra et al. studied the hardness profile and machinability of an additively manufactured and forged Inconel 718 thin walls [276]. They found that the average hardness profile is similar in these samples, but the variation of hardness throughout the additively manufactured wall was a lot more when compared to the forged material, as shown in Figure 6.29. The chips are shorter and straighter in the AM wall, whereas the forged wall generated longer chips in a spiral form due to higher elongation at fracture [276]. Post-processing heat treatment can improve the machinability [279]; however, this would increase the overall manufacturing cost and time. To address this, studies have shown that laser preheating can help in reducing the cutting forces and increasing the tool life, significantly [170, 149, 161]. Li et al. studied machining of deposited Ti-6Al-4V at different initial temperature values varying from 200^o C to 380^o C, which is achieved 120 s and 20 s right after deposition, respectively [220]. It is observed that forces in x and y direction are reduced by 19% at 300^o C. Pre-heating the material lower than 300^o C does not cause a significant reduction in cutting forces because the thermal softening is not enough at this temperature to overcome the work hardening of the material [220]. Thus, it causes acceleration of tool flank wear, which also contributes in increasing cutting forces. Tapoglou and Clulow concluded that the skin of the additively manufactured part is easier to machine compared to the core of the part due to higher cooling rates and slightly different microstructure [372]. In addition, down milling performs better compared to up milling on additively manufactured parts by enhancing the tool life and surface quality. These studies offer insights into the opportunity to improve the machinability of the additively manufactured material, specifically in a hybrid system. Given the challenges of additively manufactured materials such as high hardness, anisotropy in mechanical properties, and uneven surface finish, the integration between additive and subtractive processes needs to be improved such that it can overcome these challenges.

Surface quality after the machining step depends on the initial surface roughness of the additively manufactured part and the machining process parameters [315, 38]. The existing literature shows experimental approaches to optimize the machining process parameters to achieve better surface finish from the additively manufactured part [253, 22]. The empirical approach may be not comprehensive, as it depends on the dynamics of the process. The process parameters need to be optimized based on process statics, dynamics and machine capabilities to achieve a high surface quality and avoid unstable and inefficient processing conditions. Furthermore, the relative orientation of the machining direction to the build direction of DED process affects the surface integrity of the final part [415, 416].

2.5 Research gaps and research contributions

Hybrid manufacturing can leverage a material deposition process (AM) and post-processing (machining) in the same system. Such an approach can be significantly advantageous compared to alternating between AM and post-processing as separate systems, when considering three areas of application. The first application where hybrid manufactuirng can have a substantial benefit is manufacturing of customized, small batch, high dimensional volume parts due to the simplification in the manufacturing workflow, ability to finish complex internal cavities, and ability to address in-situ deviations in geometric fidelity typical to DED processes, which may lead to part fabrication failures if not addressed periodically via machining [219]. Secondly, hybrid approaches can be highly beneficial in the repair and remanufacturing of high-value components due to the simplified workflow of addressing the removing of the defective site, deposition of replacement materials at select locations to complete the defect infill with good geometric fidelity, and final post-process finishing, all in a single manufacturing system. Thirdly, hybrid manufacturing approaches can be beneficial for the layer-intermittent machining applications, where correcting defective depositions by machining is possible during AM.

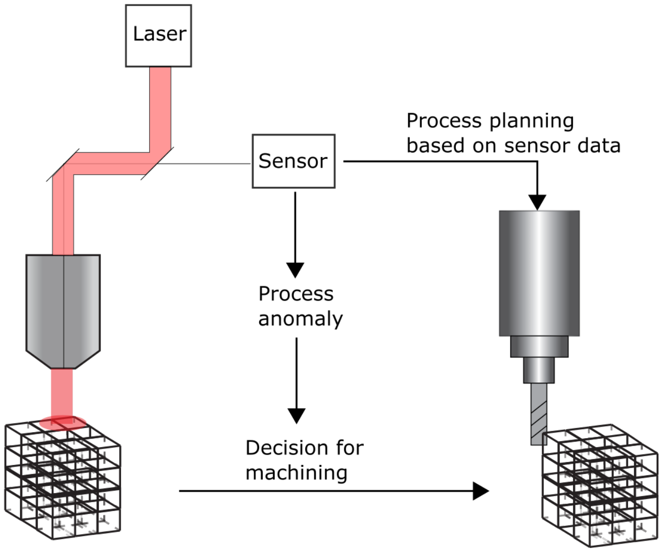

Figure 2.7: In-situ sensor systems can help in integrating additive and subtractive manufacturing system such that the machining decision can be given and the machining process can be planned based on process signatures, in conjunction with process modeling.

Significant research efforts should focus on improving the integration of two processes in terms of process modeling, process monitoring and process control for DED and machining processes respectively, and for hybrid process planning in terms of strategies for detection and classification of DED defects, prioritization of defects for machining, and economic machining strategy for defect mitigation. Although research has accelerated in the domain of machinability of additively manufactured materials, there is still a gap to optimize the machining process for AM parts. The microstructure of the AM parts should be modeled and experimentaly validated to correlate with the machinability, as there are many variables which can affect the outcome of hybrid manufacturing such as additive/subtractive process parameters, part geometry design, material system, tool design and manufacturing conditions (coolant, atmosphere etc.).

In this dissertation, the research efforts have focused on process modeling of DED, in-situ monitoring, feature detection and error detection as a contribution towards solving the problem of understanding the thermal history of the parts, modeling the geometry of the deposited layer, modeling the melt pool temperature, identifying in-process signatures and finding correlations between process signatures and outcomes that are indicative of defects, pores and instable processing conditions.

The process modeling in Chapter 3 proposes a voxel-based approach to keep track of the thermal history and predict the melt pool temperature. This work adds contributions to the scientific body of knowledge and application space towards performing the simulation not only in single deposition tracks but also in 3D objects with curvatures, sharp corners, and multi-layers.

In-situ vision monitoring is integrated in a DED system in Chapter 4, where a feature detection algorithm is developed, which is robust against disruptive conditions such as variations in background illumination, particle ejecta from melt pool.

The methodologies in Chapter 3 and 4 are combined in Chapter 5 to generate process maps, identify thresholds for unstable process conditions and train a classifier to predict out-of-bound behavior of the process detected by the in-situ sensor.

A dual-wavelength pyrometer is used to experimentally validate the model in Chapter 3 and correlate the process signatures with the geometric deviations in the final deposition in Chapter 6. In addition, in this dissertation, two decision-making schema are proposed to enhance the machinability of additively manufactured parts. One schema is for post-process machining and the other one is for layer-intermittent machining following a similar logic. In-situ process monitoring is utilized to detect process anomalies and intelligent decision making algorithms can be used to correct the defective depositions as shown in Figure 2.7. Furthermore, correlations can be made between process signatures detected by in-situ sensors and mechanical properties of the material, which could help in planning the machining process parameters. For instance, if the process signatures are indicative of higher hardness, then the depth of cut can be decreased to enhance the overall machinability of the material including tool life, surface finish and cutting forces.

In Chapter 7, conclusions and future work are proposed towards growing the research methodologies described herein, as well addressing present limitations in experimental implementation and testing.

Chapter 3

Thermal and geometry model for directed energy deposition with 2D/3D toolpaths

3.1 Preface

Directed energy deposition (DED) is a metal additive manufacturing (AM) process, where dimensional accuracy and repeatability are traditionally challenging to achieve. Strategies for computationally inexpensive process modelling and fast-response process controls of the laser deposition process are necessary to keep the geometric features close to the required dimensional tolerances. The deposition geometry depends highly on the complex local laser-material interaction and global thermal history of the substrate. In order to control the deposition geometry, an accurate and computationally inexpensive discretized state space thermal history model coupled with an analytical deposition geometry model is developed. The model accounts for the local laser-material interaction using the mass and energy governing equations coupled in a lumped parameter solution, and also accounts for the global thermal history of the product using a state space thermal discretization. In literature, studies have only focused on 1D toolpaths with constant process parameters such as speed, powder feedrate, and laser power. It is important to implement models compatible with 2D/3D complex toolpaths, to accommodate for the highly complex geometric shapes achievable via AM. In this study, an analytical thermomechanical model and a deposition geometry model for a DED process are presented and experimentally validated. The thermal history of the deposited part is predicted throughout the process and the geometric features are predicted for complex 2D toolpaths.

3.2 Introduction

Directed energy deposition (DED) is an additive manufacturing (AM) process, where the powder is guided using a gas flow onto a substrate and melted by exposure with an energy source, typically a laser, to manufacture a part in a layer-by-layer manner. DED is one of the most common and most powerful metal AM processes, known for its capability of manufacturing high density parts [331, 342]. Another advantage of DED is that the microstructure of the deposited material is more feasible to control, when compared to other metal AM processes [171, 168, 301, 320], by carefully choosing the process parameters to adjust the cooling and solidification rates of the deposited material. One of the important drawbacks of DED is that high design complexity is more challenging to achieve than in other metal AM processes due to the larger beam spot diameter [356] and the inherent limitations in travel and reach of the mechanism used for generating toolpaths [408]. In addition, support structures are difficult to print with DED [134]; this is why having overhang structures is almost impossible to implement, unless the nozzle head or the built table can move in more than 3 axes [432].

The most common application areas of DED are repair, also referred to as re-manufacturing [295, 401], and adding features on a part, also referred to as featurization [133]. The ability to address repair and featurization are unique to DED processes, when compared to the other metal AM techniques. For part re-manufacturing, the region with a failure or defect can be removed via subtractive manufacturing processes, followed by the selective deposition of new material to re-create the original geometry as closely as possible [134]. Further machining is typically required to address geometric fidelity. Using this method, a localized defect in a high-value component can be addressed as to prevent part scrap, while saving cost, time, and energy. For part featurization, material can be deposited onto an existing part at select locations [401]; the existing part could be produced via other manufacturing processes to reduce overall production costs.

In metal AM in general, and in DED specifically, there are numerous process parameters involved in driving the phenomena behind melting, solidification, and cooling of the material, which increase the complexity of the process and implicitly the complexity of developing high-fidelity models [252, 184]. The main parameters in laser-based DED are the laser power, scan speed, focal distance, laser beam diameter, and powder flow rate. These parameters determine the energy input to the metal powder and substrate, and affect the resulting melt pool morphology (length, width and height) [212, 344, 267, 76]. The melt pool morphology ultimately affects the geometry of the deposition, which is defined by the deposition width (i.e. feature resolution) and the height (i.e. layer thickness).

In order to take these complex process phenomena into account, multidimensional models are proposed, where the physics of the laser-material interaction is solved numerically [411] to achieve the most accurate prediction results [292]. One challenge is that high fidelity numerical models require high computation time and it is prohibitive to use such models in applications such as process optimization and process control. High fidelity numerical models, however, can simulate the material transformations (solid to liquid, liquid to solid) and are used to also predict the microstructure [33] and residual stress [262, 263]. Despite the complexity of the laser-material process dynamics, there are many studies focused on predicting the geometry and the thermal behavior of the manufactured features analytically [411, 163, 293, 270, 207, 218, 389, 94, 326, 294, 387, 364, 177]. Although the main aim of these models are in simulating the process, there are some models used in optimization problems [177] and also in process control schemes [112, 58, 327].

The focus of this work is to develop a two-tiered model by coupling a discrete state-space model for predicting the thermal history of the deposition substrate, with a physics-based analytical model predicting the geometry of the metal deposition. The goal of this coupled model is two-fold: (i) to obtain fast predictions without sacrificing accuracy, (ii) to build the capability to simulate depositions in complex 2D/3D toolpaths, with curvatures and sharp corners, and variable process parameter inputs. In order to achieve this, the state-space model considers a toolpath discretization into voxels, where the thermal propagation to neighbouring voxels and the deposition geometry equations are solved for each voxel. With this approach, the proposed model differentiates itself from the existing models in literature [326, 387, 217, 242, 288] by enabling the simulation of 2D/3D scan paths and variable process parameters. This work describes the development of the coupled physics-based model, as well as simulation and experimental validation results. This work uncovers the potential of adopting recursive closed form models for tracking and predicting the thermal history and deposition geometry for complex 2D/3D toolpaths in DED.

3.3 Modeling of thermal history and deposition geometry

3.3.1 Background on analytical model development

The DED process has been established for some time; however, the demand on robust industrialization of this class of technologies has accelerated the efforts on process modeling [331]. There are a few examples of processes which follow the same principles as DED such as laser cladding, gas metal arc welding, and laser welding. In early studies of such processes, the modeling approaches were limited to empirical models, where the relationship between the input process parameters and the output mechanical properties was investigated [167, 191].

To gain a better understanding of the complex laser-material interaction phenomena, physics-based models were developed [24, 123]. In DED, there are a range of physics-based process phenomena to consider, such as powder material transport, powder catchment, energy transfer, laser-material interactions, and thermal behavior of the part [252]. Furthermore, optical, mechanical, and thermal properties of metal powder are a function of temperature, which adds another dimension to the degree of complexity required for the development of process predictive models [397]. Depending on the application area, the models can be lumped parameter [218], or highly complex numerical models [404]. There are ongoing efforts towards advancing both classes of models to achieve lower computational cost, and better accuracy in predicting process signatures [164].

an example of analytical modeling efforts is the work by Doumanidis and Kwak, who developed a lumped parameter analytical model for predicting the welding profile in gas metal arc welding [94]. The mass, momentum, and energy balance equations of the melt pool were solved decoupled for melt pool cross section, melt pool height and width, and melt pool temperature, respectively. Furthermore, Sammons et al. [326] adopted the Doumanidis and Kwak [94] model and applied it for laser metal deposition process. They accounted for material solidification in the mass and momentum balance equations, which has been shown to affect the melt pool cross section prediction. Another example, which follows Doumanidis and Kwak's model, was proposed by Wang et al. [387, 386]. The novelty of their method is in the parametrization of the material transfer rate as a function of process parameters instead of calculating the powder catchment efficiency, which makes the melt pool height prediction more dependent on laser power.

In order to predict the geometry of multi-layer structures with complex geometries, the temperature history needs to be known throughout the process, as the temperature of the substrate influences the melt pool characteristics and ultimately the geometric properties of the deposited features. Li et al. proposed a method of placing a virtual heat source at the end of each layer to keep track of the temperature history of each layer [218, 217]. The virtual source is designed to move along the same direction as the last deposition in the layer and predicts the temperature decay by using Rosenthal's moving point heat source equation. Similarly to Sammons et al. [327], this model assumes that the deposition is in a simple straight line and cannot accommodate for complex deposition geometries.

Rosenthal's equation is commonly used for laser welding and cladding applications to predict the temperature in a substrate by taking the laser beam as the reference coordinate [313]. In addition to predicting melt pool temperatures, melt pool shape is also predicted at the boundary of the melting temperature of the material [353]. The main assumptions in using Rosenthal's equation are that the convection and radiation heat losses are neglected, the workpiece is semi-infinite, the thermal properties of the material are constant, and that the scan speed and laser power are constant. Rosenthal's moving point heat source equation is given below:

$$T - T_0 = \frac{\beta q}{4\pi k} \frac{e^{-\frac{v(\xi + R)}{2\alpha}}}{R} \tag{3.1}$$

In the equation above, R is the distance between the point of interest and the laser beam, considering a spherical surface around the heat source with radius $R = \sqrt{\xi^2 + y^2 + z^2}$, α is the diffusivity of the material, and k represents the material thermal conductivity. The equation assumes that the heat is supplied by a point heat source q moving with a constant speed v along the x-axis and that β is the absorption coefficient. The moving coordinate system is located on the x-axis and, as such, x is replaced by $\xi = x - vt$, where ξ is the distance of a point considered away from the point source with the scan speed v. Rosenthal's moving point heat source equation is traditionally used for predicting the temperature of the deposited material while the heat source moves in a single (1D) direction with a constant scanning speed.

Overall, most of the background literature provide results in good agreement with the experimental data; however, they are only applicable for 1D toolpaths. In this study, the ultimate goal is to predict the geometry of a multi-layer structure, which has a complex 2D toolpath at each layer. The novelty of this study, compared to the models in existing literature [94, 48, 100, 260, 57], relies on the need to address 2D/3D depositions by means of discretizing the scan path. Moreover, the process parameters can be allowed to vary along the scan path and can be used to simulate the temperature history and deposition geometry by solving the governing equations at each discrete voxel. In order to achieve this in a multi-layer part, the temperature history at each point (x, y) within a layer at height z of the 2D layer-by-layer deposition tracks should be computed. This temperature will be used as an input in predicting the deposition geometry, when the laser comes back at the same point (x, y) on the next layer, or close to a neighboring voxel previously deposited in the same layer. The proposed model is intended to be adopted for more complex 3D toolpaths.

3.3.2 Discretized state space thermal history model

A simplified thermodynamic model is used to predict the temperature during the laser exposure and to predict the transient cooling after the laser exposure. This model is used to keep track of the thermal history and to predict an approximate temperature value of the previously deposited material. This substrate temperature is then used as an input to the geometry model for predicting the geometry at the same x-y coordinates on the current deposition layer. The energy input to the system comes from the laser heat source, and after the deposition, the cooling of the laser track is assumed to happen through convection to ambient and through conduction to the substrate. In addition, the heat input from the laser to a point of interest further away from the melt zone should be considered as a heat input contribution when updating the thermal history of each point within the deposited material space. To achieve this, the deposition toolpath is discretized into discrete voxels, and the thermal history is updated recursively.

In this voxel-based model, the part is first virtually divided into discrete voxels along the desired toolpath. The order of the voxels is intended to match with the toolpath deposition sequence, to keep track of the order in which the voxels are subjected to the laser heat input. In Figure 3.1, an example of a discretized 2D toolpath is shown, where the toolpath is divided into voxels and each voxel is indexed with a number sequence. In this model, the minimum size of the blocks is assumed to be equal to or larger than the diameter of the laser beam in order to keep the effective instantaneous heat input limited to one block. The actual size of the voxel is determined by simulating the melt pool geometry using Rosenthal's equation by taking the melt pool boundary as the approximations of the x, y, and z voxel dimensions, where the voxel is assumed to be the bounding box of the melt pool. The energy balance equations are written for each voxel as the laser moves on, depending on the sides neighbouring to adjacent voxels, substrate, and/or exposed to ambient. The laser energy input is assumed to be applied on the voxel being deposited at that time step. The set of energy balance equations are solved for temperature in a state space model for each time step recursively.

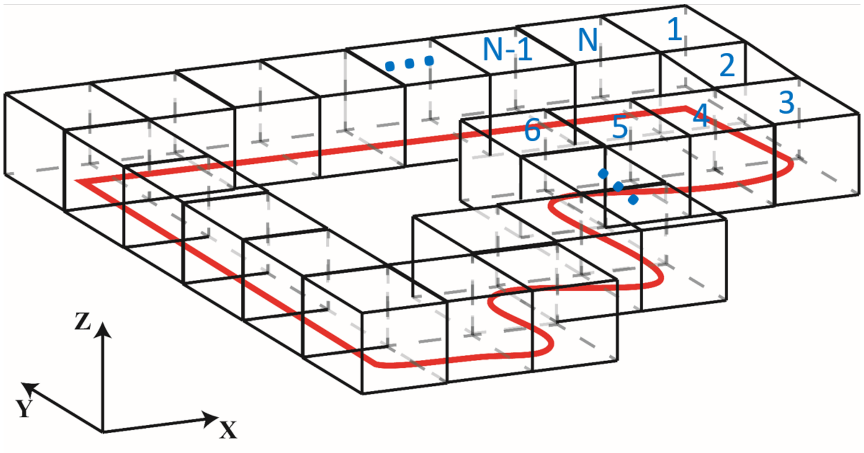

Figure 3.1: Visualization of a discretized 2D toolpath

The control volume of the thermal model is shown in Figure 3.1(a). The energy input q_{in} is provided by the laser, therefore the energy input is a function of the laser power. T_k is the instantaneous temperature once the laser hits the material; the material is assumed to exist already in the discretized block. The energy loss q_{out} is lost through the remaining five surfaces of the block. The energy loss is in the form of conduction or convection, depending on the neighboring environment. The radiation heat losses are neglected [184] and a constant substrate temperature is assumed [218] for each voxel independently. The heat transfer model assumes that the material already exists in the voxel currently being deposited and the model is used to keep track of the thermal history of the deposited voxels.

The thermal history model is sequential and recursive. In the first time step, the first voxel is deposited; at that location, the energy input comes from the laser and the energy loss is assumed to happen through convection. The change in temperature of the first voxel is approximated as:

$$\dot{T}_1 = \frac{dT}{dt} = \frac{1}{C}(q_{in}^{(1)} - q_{out}^{(1)}) \tag{3.2}$$

In the equation above, C is the heat capacitance, representing the energy storage capacity of the material, $q_{in}^{(1)}$ is the energy input, expressed below, and $q_{out}^{(1)}$ is the energy loss.

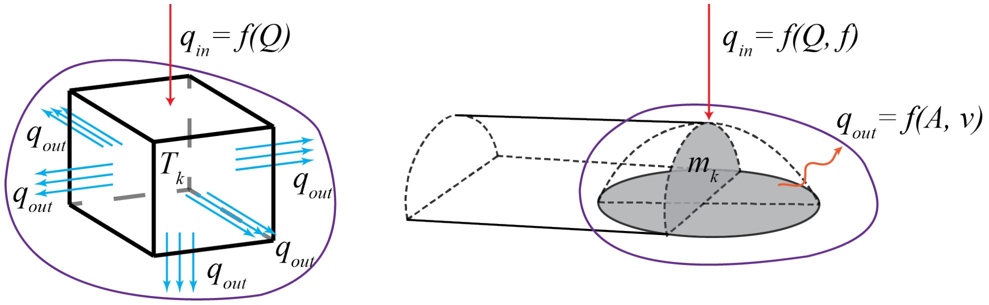

(a) (b)

Figure 3.2: Control Volumes of the (a) thermomechanical model energy input qin from the laser and energy loss qout through the five sides of the voxel as an approximation of the physics (b) meltpool geometry model illustrating a closer representation of the physics at the deposition point.

$$q_{in}^{(1)} = \frac{1}{R_p}(T_1 - T_s) \tag{3.3}$$

In this model, T_1 is the peak temperature of the voxel when the laser is exposed to the material at that location and T_s is the initial substrate temperature. The instantaneous peak temperature is predicted by Rosenthal's moving point heat source equation:

$$q_{in}^{(1)} = \frac{1}{R_p}(T_1 - T_s) = \frac{1}{R_p}\left[\frac{\beta q}{2\pi k R} e^{\frac{-v(\xi + R)}{2\alpha}}\right] \tag{3.4}$$

In the equation above, T_1 is the temperature of the first voxel, and T_s is the initial substrate temperature. T_s is constant (assumed to be ambient) for the first layer of deposition and it is updated at the upper layers based on the temperature value below the current deposition point. R_p is the thermal resistance, k is the thermal conductivity and α is the thermal diffusivity of the metal powder, q is the laser power, v is the scan speed, and R represents the distance between the point heat source and the point of interest, which is set equal to the length of the block. The thermal resistance is defined as:

$$R_p = \frac{\Delta x}{A \times k} \tag{3.5}$$

In the equation above, Δx is the thickness and A is the cross section area that the heat goes through and k is the thermal conductivity.

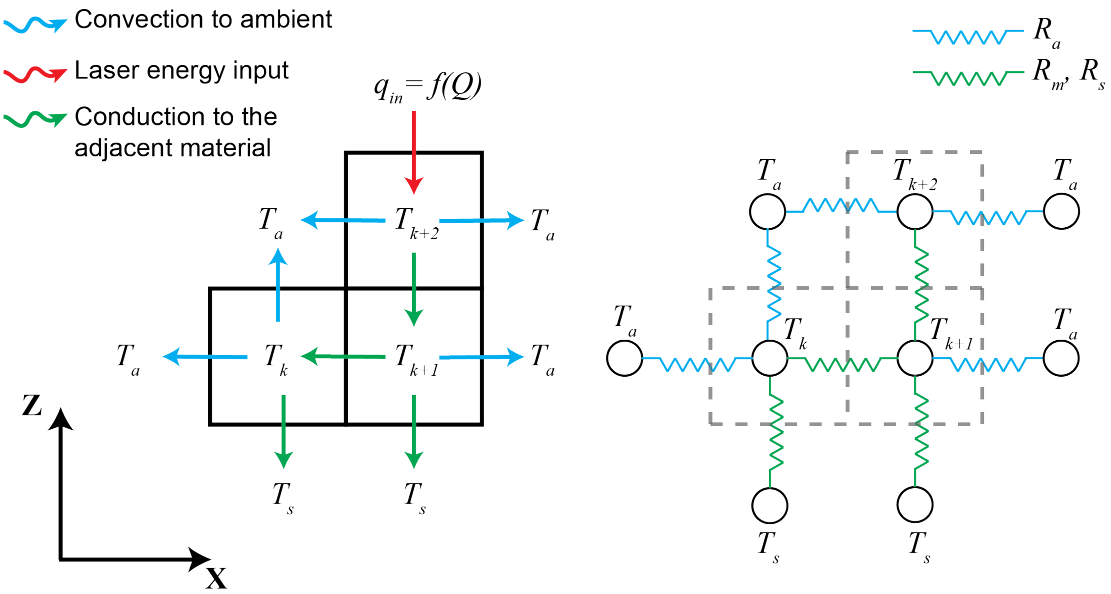

Figure 3.3: Heat transfer (conduction and convection) schematic between three blocks, ambient and substrate in steady state

For visualization purposes, the heat transfer between the discretized voxels is shown in Figure 3.3 in 2D. In this illustration, T_k, T_{k+1}, T_{k+2} show the temperature of each block in the order of toolpath deposition sequence, where $k \epsilon \{1, 2, \ldots, N\}$ and N is the total number of blocks. The blue resistance elements R_a show the convection resistance to ambient and the green resistance elements R_m, R_s show the conduction resistance to adjacent material and substrate, respectively. The heat input is shown with the red arrow and is governed by T_{k+2}, as predicted by using Rosenthal's moving point heat source equation.

The energy loss through convection to the ambient is represented as shown in Figure 3.3 and in the equation below.

$$q_{in}^{(1)} = \frac{4}{R_a}(T_1 - T_a) \tag{3.6}$$

In the equation above, R_a is the thermal resistance to ambient. For the first voxel, as four faces of the block are exposed to the ambient, the energy loss through convection is multiplied by a factor of 4; in general, this number factor changes depending on the spatial configuration of adjacent voxels and is accounted for as such based on the voxel sequence in the toolpath.

The rate of change in temperature in the first voxel can be represented with the combination of Equation 3.3 and Equation 3.6:

$$\dot{T}_1 = \frac{1}{C}(q_{in}^{(1)} - q_{out}^{(1)}) = \frac{-4}{R_a C}T_1 + \frac{4}{R_a C}T_a + \frac{1}{R_p C}\left[\frac{\beta q}{2\pi k R}e^{\frac{-v(\xi+R)}{2\alpha}}\right] \tag{3.7}$$

In the equation above, C is the heat capacitance of the material. T_a and q are system inputs and they represent ambient temperature and laser power, respectively. The thermal resistance terms represent the resistance of the material to heat flow because of a temperature difference. Once the second voxel of material is deposited (second time step), the energy balance equation is rewritten for the first voxel. At this time step, the energy input to the first voxel comes through conduction from the second block ($T_2 > T_1$), which is being deposited and is shown in Equation 3.8 below.

$$q_{in}^{(1)} = \frac{1}{R_m}(T_2 - T_1) \tag{3.8}$$

For the first voxel, the energy loss is the same except there is one less face exposed to the ambient, which is now adjacent to the second block.

$$q_{out}^{(1)} = \frac{4}{R_a}(T_1 - T_a) + \frac{1}{R_s}(T_1 - T_s) \tag{3.9}$$

Second voxel's energy balance equation is very similar to the first voxels' equation at the first time step.

$$\begin{aligned} q_{in}^{(2)} &= \frac{1}{R_p}(T_2 - T_0) = \frac{1}{R_p}\left[\frac{Q}{2\pi k R}e^{\frac{-v(\xi+R)}{2\alpha}}\right] \\ q_{out}^{(2)} &= \frac{3}{R_a}(T_2 - T_a) + \frac{1}{R_m}(T_2 - T_1) \end{aligned} \tag{3.10}$$

The visual representation of the thermal heat transfer relationship between the deposited adjacent voxels is represented in Figure 3.4.

Therefore $q_{in}^{(1)}$, $q_{out}^{(1)}$ and $q_{in}^{(2)}$, $q_{out}^{(2)}$ are then accounted for using a similar equation to Eqn. 3.7.

$$\begin{aligned} \dot{T}_1 &= \frac{1}{C}(q_{in}^{(1)} - q_{out}^{(1)}) \\ \dot{T}_2 &= \frac{1}{C}(q_{in}^{(2)} - q_{out}^{(2)}) \end{aligned} \tag{3.11}$$

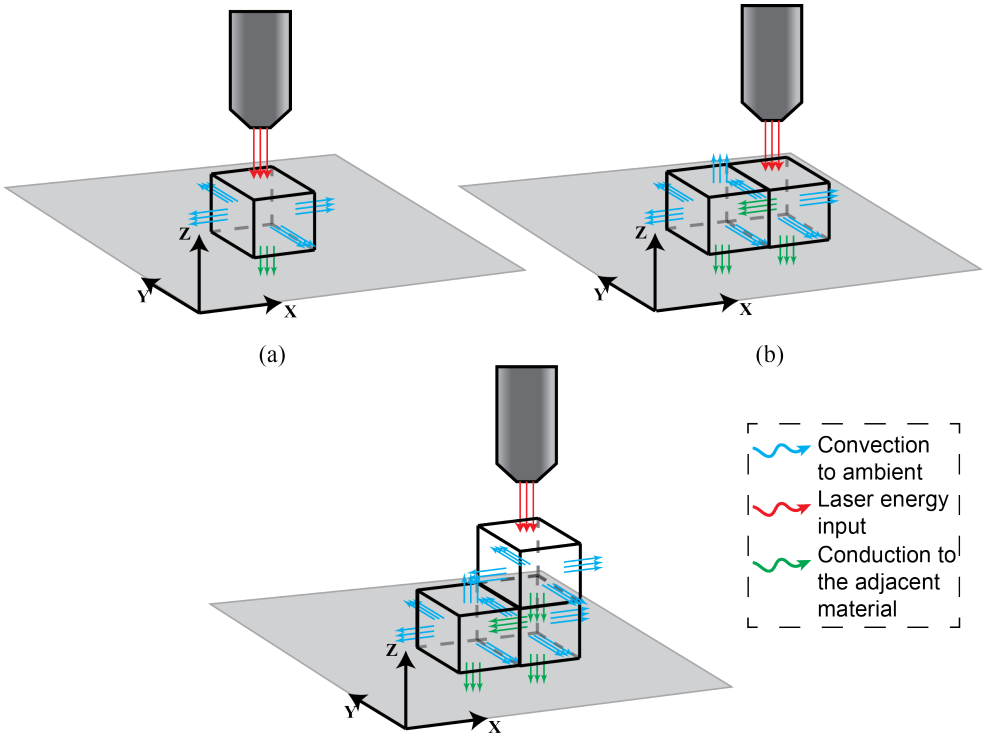

(a)

(b)

(c)

Figure 3.4: Examples of energy input and losses shown on the discretized toolpath voxels, where (a) is a visual representation of the heat transfer for the first material voxel being deposited, (b) is the visual representation of the second voxel being deposited adjacent to the initial voxel, while (c) illustrates a third voxel being deposited stacked vertically on top of the second voxel

For each time step, a set of differential equations are solved in a state space form in discrete time as per Equation 3.12.

$$\frac{d}{dt}[T] = (A)_{n\times n}[T]_{n\times 1} + (B)_{n\times p}[u]_{p\times 1} \tag{3.12}$$

In Equation 3.12, T is the state vector, u is the input vector, n is the number of blocks and p is the number of inputs. A and B are the state transition and input matrices respectively and are updated at each iteration. The total iteration time of the simulation is determined by the time required to move the laser from one voxel to the next one, which depends on the scan speed of the process. The temperature is simulated at each iteration for a discrete sampling time step, while the laser is travelling along one block. The last temperature value for each block is used as the initial temperature for each block in the next iteration. Once the last block is deposited, the cooling of the blocks can be observed before starting the second layer above. Using this approach, the temperature of the substrate (previous layer) is now known and can be used as a temperature input to predict the geometry of the laser track on the second layer. Similarly, the temperature gradient history propagating through multiple layers is also retained and updated when simulating the newest layer being deposited.

3.3.3 Analytical geometry model

The thermal history behaviour of the deposited voxels is coupled with an analytical deposition geometry model used to predict the melt pool area, the melt pool width, and the height of the deposition for each voxel position. For single layer parts, the surface temperature is approximated to be equal to the substrate temperature, which is typically assumed to be equal to the ambient temperature [162]. However, while depositing subsequent layers of a multiple-layer part, the temperature of the substrate will increase due to heat accumulation from previous depositions [217]. The output of the thermal history model, as previously derived, which predicts the current temperature of the deposition surface and the temperature of the neighbouring voxels, is used as an input to the geometry model.

The melt pool geometry is predicted by deploying two decoupled equations, the mass and the momentum balance of the deposition. Both equations assume that the melt pool has an elliptical shape [207, 177], which is a common approach in the literature to predict melt pool geometries for laser-based manufacturing processes such as metal DED, welding, and cladding processes [404, 377]. The control volume for both mass and momentum balance equations is the melt pool boundary, which is shown in Figure 3.2 (b). The mass

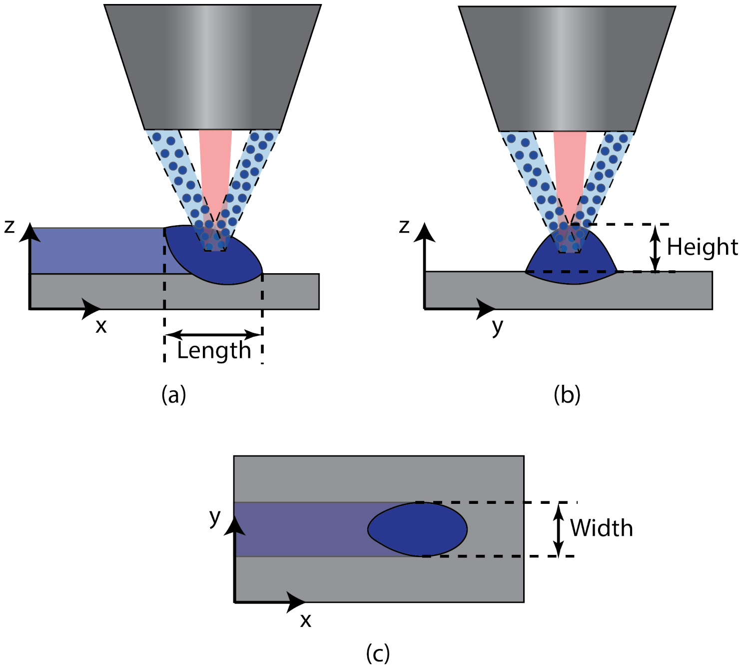

Figure 3.5: Melt pool geometry layout from different views (a) Side view, (b) Front view, (c) Top view

balance equation is used for predicting the area of the deposition, where the height and width of the melt pool are coupled. The momentum balance equation decouples the width and the height of the area prediction, which can be seen in Figure 3.5 from the mass balance equation [94]. The momentum balance equation defines how the material is captured into the substrate, which affects the width and thus deposition height.

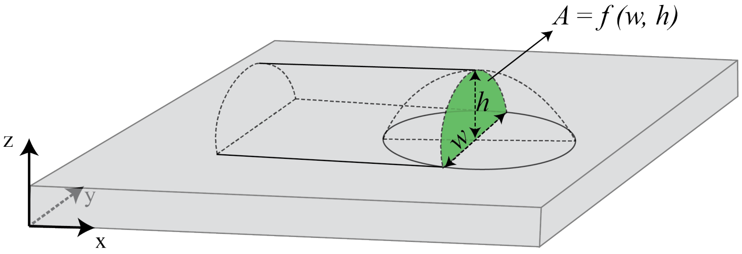

Figure 3.6: Vertical deposition area as a function of width and height of the deposition

The mass change rate at the melt pool boundary relates the material transfer rate due to the deposition, and the material loss due to the solidification shown as in Equation 3.13 [94]. The density ρ of the material is assumed to be constant throughout the melting and solidification phases.

$$\underbrace{\frac{d(\rho V(t))}{dt}}_{\text{Mass change rate}} = \underbrace{-\rho A(t)v(t)}_{\text{Material loss due to solidification}} + \underbrace{\mu f}_{\text{Material transfer rate by deposition}} \tag{3.13}$$

In the equation above, ρ, V, A and v are density, deposition volume, area, and scan speed, respectively. The material transfer parameters are μ representing the powder catchment efficiency and f representing the deposition rate. The deposition volume represents the whole volume of the melt pool and it is calculated based on the width, height, and length of the melt pool. The area represents the cross-section of the melt pool and it is calculated using the melt pool width and height, which are shown in Figure 3.6. In volume and area calculations below, the wetting angle (contact) of the melt pool is assumed to be 90^o.

$$\begin{aligned} V(t) &= \frac{\pi}{6} w(t)h(t)l(t) \\ A(t) &= \frac{\pi}{4} w(t)h(t) \end{aligned} \tag{3.14}$$

In the equation above, w, h and l are the width, height and length of the deposited material, respectively.

In this work, the material transfer rate μf is parametrized as a function of the laser power and critical laser power, instead of estimating the powder catchment efficiency [387]. The reason for the estimation approach is that the laser power is the dominant parameter, which defines the capacity how much powder is transferred to the melt pool. Eagar and Tsai [99] modeled the weld pool size and shape in a dimensionless manner with respect to process parameters and material properties. The dimensionless operating parameter n is modeled starting from the dimensionless form of a Gaussian heat distribution in order to model the dimensionless form of the shape of the melt pool. This dimensionless operating parameter is modeled by Christensen et al. to get a dimensionless form of the Rosenthal's equation for a moving point heat source [70]. In a later study Eagar and Tsai used it for formulating the weld shape assuming the Gaussian heat distribution for the laser beam input [99], with the expression below:

$$n = \frac{qv}{4\pi\alpha^2\rho c_l(T_m - T_0)} = \frac{v\lambda}{4\pi\alpha} \cdot \underbrace{\frac{Q}{k(T_m - T_0)\lambda}}_{\text{Dimensionless net heat input}} \tag{3.15}$$

In the equation above, Q, α, c_l, T_m, k, ρ are the laser power, thermal diffusivity, melt specific heat, melting temperature, thermal conductivity, and density, respectively. T_0 is the surface temperature, where deposition occurs on, and λ is the characteristic length, which stands for the thickness of the substrate. The thermal diffusivity is $\alpha = k/(\rho c_l)$. The parameter n expresses the laser-material interaction in a dimensionless fashion, as a function of the dimensionless net heat input, the diffusivity and the scan speed. Starting from this dimensionless operating parameter, Wang et al. proposed a model for the steady-state dimensionless cross-sectional area of the melt pool ($\overline{A} = Av^2/4\alpha^2$), which is parametrized with a dimensionless operating parameter $\overline{n}$ [387]

$$\overline{A} = \Gamma(\overline{n}) \tag{3.16}$$

The function will be determined later, while $\overline{n}$ represents a modified version of the dimensionless process parameter (n) from Equation 3.15.

$$\overline{n} = \frac{\eta(Q - Q^c)v}{4\pi\alpha^2\rho c_l(T_m - T_0)} \tag{3.17}$$

In the above equation, η represents the laser absorption efficiency, Q is the laser power and Q^c is the critical value for the laser power. If the laser power is lower than the critical value, then melting does not occur; in another words, it can be said that the powder catchment will be zero if the laser power is under a certain threshold (i.e. critical value of the laser power Q^c). This modified dimensionless operating parameter calculates the net heat input into the metal powder used for melting the powder [70, 99]. With this energy input, the cross-section area of the melt pool at the steady-state can be calculated using the function $\Gamma(\cdot)$.

$$\frac{Av^2}{4\alpha^2} = \Gamma\left(\frac{\eta(Q - Q^c)}{4\pi\alpha^2\rho c_l(T_m - T_0)}\right) \tag{3.18}$$

From Equation 3.13, the mass balance equation at the steady-state becomes $\mu f = \rho A v$. The $\Gamma(\cdot)$ function is assumed to be a linear function with a coefficient β. Then, the steady-state cross-section area of the melt pool can be written as follows:

$$A = \beta\frac{\eta(Q - Q^c)}{\pi\rho c_l(T_m - T_0)v} \tag{3.19}$$

The approximation for the steady-state cross-section area of the melt pool matches with the relation between process parameters and melt pool area. As such, from Equation 3.19, it can be observed that the area of the melt pool increases with increasing laser power and with decreasing scan speed. The material transfer rate can be then approximated as:

$$\mu f(t) \approx \beta\frac{\eta(Q - Q^c)}{\pi c_l(T_m - T_0)} \tag{3.20}$$

In Equation 3.20 the material transfer will be zero in case the input laser power is less than the critical value for the laser power. This equation calculates the material transfer rate by considering that the powder catchment efficiency is at steady state. This approximation for the material transfer rate can be substituted into the mass balance equation (Equation 3.13):

$$\frac{d(\rho V(t))}{dt} = -\rho A(t)v(t) + \beta\frac{\eta(Q - Q^c)}{\pi c_l(T_m - T_0)} \tag{3.21}$$

In Equation 3.13, it is assumed that the density remains the same from liquid to solid phase, and that the melt pool length is approximately constant through the process in steady state. The melt pool volume can thus be represented as a function of the cross-section area.

$$\frac{2}{3}\rho l\frac{dA(t)}{dt} + \rho A(t)v(t) = \beta\frac{\eta(Q - Q^c)}{\pi c_l(T_m - T_0)} \tag{3.22}$$

The laser power can be represented as $Q(t) = Q - Q^c$ and the scan speed $v(t)$ is assumed to be constant at steady state. The transfer function between laser power and melt pool cross-section area can be represented in frequency domain after taking the Laplace transformation (with 's' denoting the Laplace operator).

$$\frac{A(s)}{Q(s)} = \frac{\beta\eta}{\pi c_l(T_m - T_0)[2/3\rho ls + \rho v]} \tag{3.23}$$

The cross-section area shown in Figure 3.5(b) is assumed to be half ellipsoid, which has a width and a height. The width and height can vary, while keeping the same cross-section area depending on the process parameters, such as laser power and scan speed. Both of the inputs can vary in this model, as the area is solved for each deposition voxel.

The width and height are determined according to the melt pool momentum Equation 3.24, which describes the material-surface interactions. This surface could be either the substrate or the deposited material on the previous layer. This can be quantified by writing the momentum balance equation as follows:

$$\underbrace{\frac{d(\rho V(t)v(t))}{dt}}_{Meltpoolmomentum} = \underbrace{\rho A(t)v^2}_{Momentumlosstosolidification} + \underbrace{\sum F_v}_{Momentumlosstosurfacetensionforces} \tag{3.24}$$

The total surface tension forces in the direction of scan speed can be represented as follows:

$$\sum F_v = (1 - \cos\theta)\cdot(\gamma_{GL} - \gamma_{SL})w \tag{3.25}$$

The mass balance equation (Equation 3.13) and the total surface tension forces (Equation 3.25) can be substituted into the momentum balance equation (Equation 3.24) as follows:

$$[\mu f - \rho A(t)v]v + \left[\rho\frac{\pi}{6}(wh)l\right]\dot{v} = \rho A(t)v^2 + (1-\cos\theta)\cdot(\gamma_{GL} - \gamma_{SL})w \tag{3.26}$$

where γ_{GL} and γ_{SL} represent gas-to-liquid and solid-to-liquid surface tension coefficient, θ is the contact angle of the deposition head with respect to the substrate, and assumed to be equal to 90^o because the material deposition and the laser beam re coaxial and perpendicular to the substrate. At steady state deposition with a constant scan speed, the acceleration term can be eliminated for further simplification.

$$\mu f v - 2\rho A(t)v^2 = (1-\cos\theta)\cdot(\gamma_{GL} - \gamma_{SL})w \tag{3.27}$$

Some of the parameters in Equation 3.23 and 3.27 need to be calibrated with experimental data such as laser absorption efficiency (η), coefficient (β) and the surface tension coefficients (γ_{GL}, γ_{SL}). The experimental calibration and validation are represented in the next section. The width is calculated from Equation 3.27. The height is found based on the assumption that the deposition area is half of an ellipse and calculated from the area prediction in Equation 3.23 and the width prediction in Equation 3.27.

3.4 Materials and methods

3.4.1 Theoretical performance validation of the thermal history model

To illustrate the behaviour of the state space thermal history model, the thermal behaviour of a 40 mm long single track deposition (Figure 3.7) is simulated and the temperature response is compared against the simulation results of Li et al. [218]. The performance comparison is illustrated in Figure 9, after depositing the first and third layer. The process parameters and thermal coefficients for simulating the deposition of a Ti64 material are kept the same with the reference work for comparison purposes and can be found in the work by Li et al. [218].

In this simulation, the first step was to establish the voxel size. The voxel width, length and depth were determined based on the melt pool dimensions in steady state, as approximated by using Rosenthal's equation (Equation 3.1), with a reference to ambient temperature. The equation is resolved in 3D to simulate the temperature field, with the coordinate system located at the surface and instantaneous beam location. The melt pool

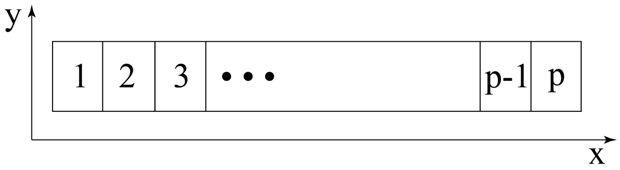

Figure 3.7: Simulated voxel sequence for model validation based on literature for a straight line deposition [218]

dimensions are approximated based on the boundary where the temperature reaches the melting temperature of the material; the melting boundary contour is therefore assumed to be the boundary of the melt pool. The voxel xyz dimensions are approximated by using the melt pool dimensions (width, length and depth), which can be seen in Figure 3.8 for a Ti64 material system under laser power 410 W and scan speed 8.5 mm/s. Based on these parameters, the voxel size is set to 1.6 mm in length, 1.3 mm in width and 0.8 mm in depth. The voxel size was kept constant through the simulation for each combination of process parameters. In future work, it can be made to change dynamically based on the dynamic changes in process parameters and substrate temperature.

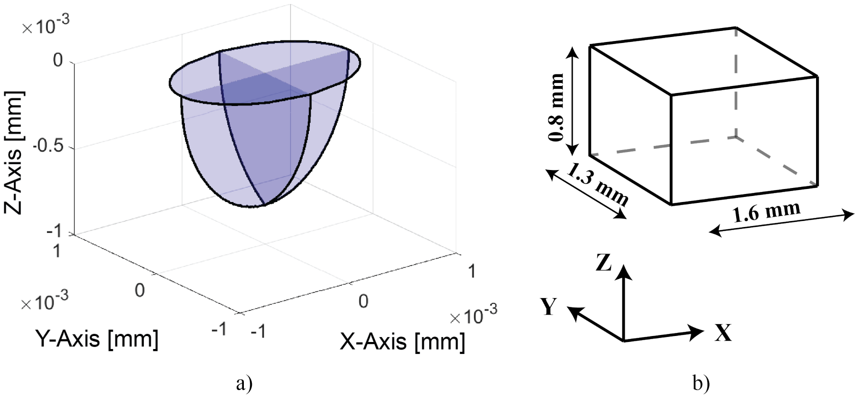

Figure 3.8: Determination of the voxel size based on Rosenthal's equation a) Simulated melt pool shape by using Rosenthal's equation, b)Voxel size created based on the melt pool dimensions (width, length, depth)

The limitation in the model proposed by Li et al. [218] is that it can be applicable to keeping track of the thermal history only for straight lines (1D toolpath). Furthermore, in multiple layered structures, the model by Li et al. [218] ignores the heat loss through conduction to the depositions on the previous layers and neglects the heat loss through convection. These facts are taken into account in the proposed model. Thus, the initial temperature prediction on the third layer reported in literature shown in Figure 3.9b is slightly higher than the simulation result from the model proposed in this study, in steady state. The results show the temperature along the deposited material when the laser is off at the end of the track. The significant research contribution presented herein is the development of the state space thermal history model which can, for the first time, analytically keep track of the thermal history of the laser powder fed deposition process. The thermal behaviour of the substrate has a significant impact on the geometric features being deposited, which will be the focus of the experimental validation work.

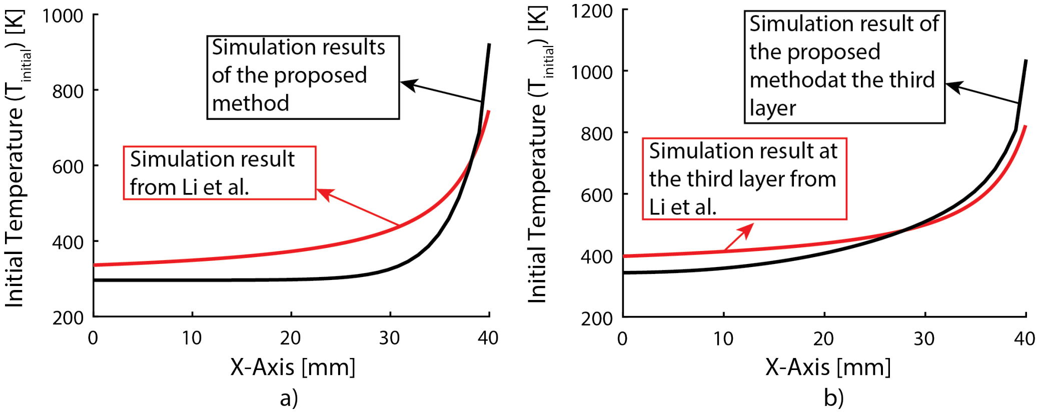

Figure 3.9: Simulation results for the proposed model compared to simulation results from the model of Li et al. [218]. The cooling curves show the temperature values of voxels (a) after depositing the first layer b) after depositing the third layer

The same process parameters were simulated in a circular scan path, where the voxel size is kept the same for constant process inputs, where the scan speed and laser power are assumed to be constant. The periphery of the circle is 32 mm and there are 20 voxels. The distortion of the voxels due to the curvature is neglected. The discretized scan path can be seen in Figure 3.10. The simulation results are shown in Figure 3.11. In Figure 3.11, the black solid line illustrates the temperature predictions after depositing the first layer of a circular scan path as a function of the distance. Figure 3.11 shows the temperature predictions after depositing the third layer in black dashed line. The temperature predictions show a similar trend as in the simulation results for the straight line. The temperature increase can be seen at the beginning of the deposition (voxel 1) because it is a neighbor voxel to the last voxel in the simulation (voxel 20). Deposition of the last voxel increases the temperature in voxel 1 due to conduction heat transfer.

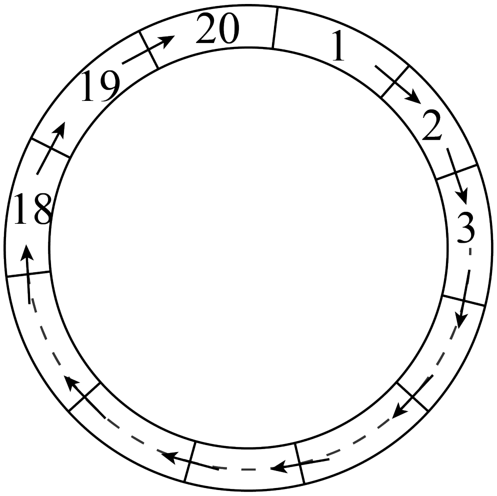

Figure 3.10: Circular toolpath discretized with 20 voxels

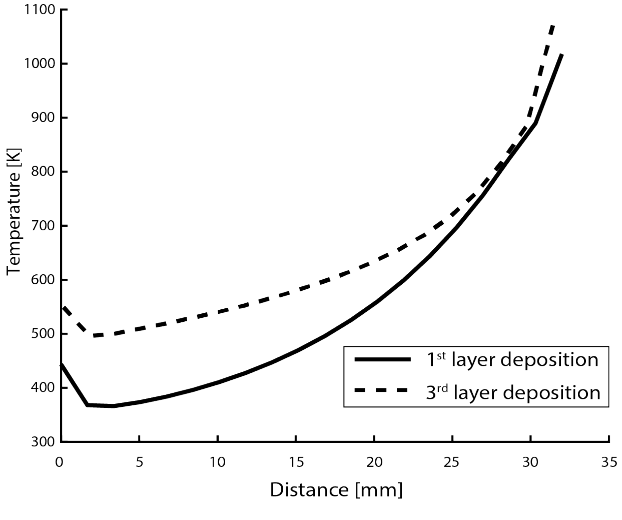

Figure 3.11: Temperature predictions after depositing the first layer and the third layer on a circular scan path along the deposited track as a function of traveling distance

A planar surface with five adjacent deposition lines are discretized shown in Figure 3.12(a) to simulate the resulting thermal history. The voxel size is kept the same as in previous simulations, the total length of each deposition track is 32 mm. The step over between adjacent deposition lines is assumed to be 0.6 mm. The simulation results for each voxel after depositing the 100th voxel are represented in Figure 3.12(b). Fluctuations in the predicted temperature values can be seen because of the zig-zag motion of the scan path. A peak in the simulated temperature values can be seen at voxel number 61. As the last voxel deposited (100th voxel) is a neighboring with voxel 61, the effect of heat transfer from this neighbouring voxel can be observed at voxel 61.

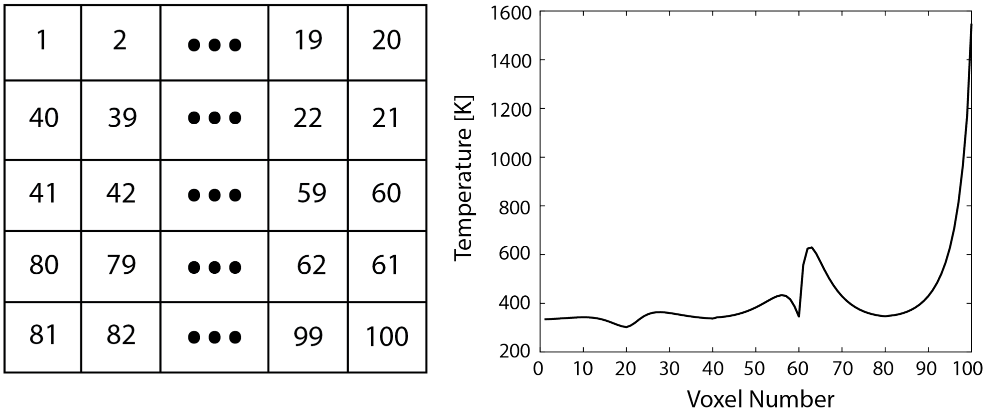

(a) (b)

Figure 3.12: Simulated planar scan path with 5 adjacent lines (a) Discretized scan path sequence, from voxel 1 to voxel 100, (b) Temperature predictions for each voxel after depositing 100th voxel

An extra layer was added to the same scan path as in Figure 3.12(a) to simulate the temperature values at each voxel (200 voxels in total). The second layer starts from the same location and follows the same scan path. The simulated temperature values at each voxel immediately after deposition the 200th voxel can be seen in Figure 3.13(a). The heat input effect from the upper layer can be seen on the first layers' voxels. For example, the peak at voxel 100 is a result of heat input coming from voxel 200. Moreover, the temperature raise in voxel 100 causes temperature increase in the neighboring voxels such as voxel 99 and 61 (Figure 3.12(a)). In Figure 3.13(b), the cooling of voxel 1 is simulated throughout the 200 voxel deposition simulation, at each time step. The results are shown as a function of unit time step, where one voxel is deposited at each time step. The effect of the heat input coming from the neighboring voxels on voxel 1 can be seen as being highest at time step 40, where voxel 40 is deposited, the nearest to voxel 1. Another high peak is at time step 101, when the deposition occurs on top of voxel 101.

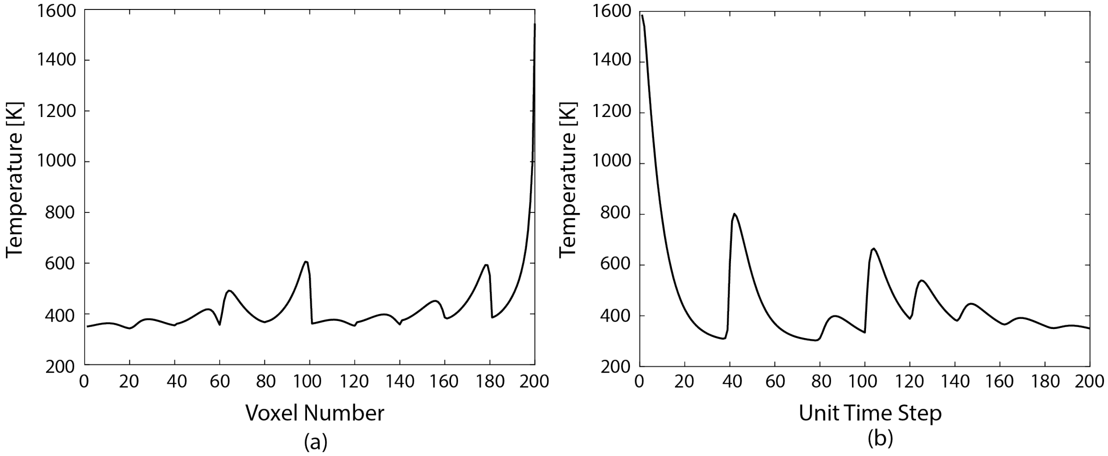

Figure 3.13: (a) Simulated temperature values for each voxel at the end of the 2nd layer, (b) Temperature of voxel 1 simulated until the end of the deposition process shown as a function of unit time step

Experimental validation and analysis of the temperature predictions is performed in Chapter 6 with a dual-wavelength pyrometer coaxial with the laser beam as a part of a comprehensive study and scholarly work. As cooling of the deposition is challenging to validate experimentally, the melt pool temperature detected by the pyrometer will help calibrate the temperature predictions in this future work.

3.4.2 Experimental performance validation of the geometry model

3.4.2.1 Directed energy deposition system

The experiments were performed in a robotic laser powder fed system DMD IC106, which can be seen in Figure 3.14. The robotic system, ABB IRB140, has 6 axes; however, the toolpaths created for the experiments herein are 3D toolpaths, with sequential layer-by-layer depositions in the xy plane stacked along the z direction. The end effector, directs the 2 kW disk laser beam (TRUMPF TruDisk 2000) and coaxially the metal powder flow through a nozzle assembly. The laser beam diameter is 1.2 mm at focus and the wavelength is 1030 nm. The material delivery system has two hoppers, which can be used at the same time. The process chamber is fully gas sealed and isolated when the laser is in operation.

Figure 3.14: DED experimental setup used for model validation

3.4.2.2 Powder material system

Single line depositions were performed using stainless steel powder. SS316L was chosen, with the chemical content detailed in Table 3.1. Stainless steel is known for its high corrosion resistance and is used in a wide variety of industrial applications. In these experiments, fully inert atmosphere in the environmentally controlled process chamber is not used because processing SS316L is not as prone to oxidation. The shape of the powder particles are spherical, with the powder size distribution described in Table 3.2. The particle size distribution of the powder was found using a Retsch Camsizer X2 Optical Particle Size Analyzer with the X-Jet dispersion module. Minimum chord length of the powder particles is measured and averaged.

Table 3.1: Chemical content of SS316L

	Elements						
	Fe	Cr	Ni	Mo	Mn	Si	C
Wt.%	Balance	16.5	12.6	2.5	1.5	0.7	0.009

Table 3.2: Powder size distribution of SS316L (Camsizer analysis)

	D10	D50	D90
Average size of min. x_c (μm)	73.06	106.26	141.25

Table 3.3: Material Properties of SS316L

Parameter	Value
Density ρ $[kg/m^3]$	7990
Melting temperature T_m $[K]$	1648
Thermal conductivity k W/mK	16.3
Thermal diffusivity α $[m^2/s]$	4.08×10^{-6}
Melt specific heat c_l $[J/kgK]$	500

3.4.2.3 Experimental plan for model performance validation

In the Experimental Plan (EP, described in Table 3.4), only the laser power was varied, while all the other process parameters were kept constant. The range of laser power is selected such that the welding mode spans the conduction mode, which is considered to be a stable process state [152]. The minimum laser power level to achieve melting is selected as 400 W based on experience. The upper limit of the power level is selected to transition to keyhole welding mode and is calculated by using an analytical model, which predicts this transition based on the normalized enthalpy level [152]. The normalized enthalpy is calculated as follows [152]:

$$h^* = \frac{\Delta H}{h_s} \tag{3.28}$$

h^* is the normalized enthalpy calculated by dividing the specific enthalpy ΔH by the enthalpy at melting h_s.

$$h^* = \frac{A \cdot P}{h_s \sqrt{\pi \alpha v \sigma^3}} \tag{3.29}$$

In this equation, the material properties are A and α, which represent the absorptivity and the thermal diffusivity, respectively. The process parameters are captured, where P is the laser power, v is the scan speed and σ is the laser beam diameter. The enthalpy at melting h_s is expressed below, where k is the thermal conductivity and T_m is the melting temperature. The normalized enthalpy can be calculated by substituting h_s in Equation 3.28.

$$h_s = \frac{k \cdot T_m}{\alpha} \tag{3.30}$$

The keyhole welding mode transition can be predicted by calculating the normalized enthalpy. If the normalized enthalpy exceeds a certain threshold, this indicates the transition to keyhole welding mode. Based on existing literature for SS316L, this threshold is approximately equal to 6 [195]. For the highest laser power selected, 1000W, the dimensionless enthalpy is 6.13, indicating that keyhole transition has been theoretically reached. The Experimental Plan (EP) is given in Table 3.4. The laser power is varied from 400W to 1000W with an increment of 150W. The laser power and scan speed are chosen such that the experiments span from low power to keyhole. Each experiment is replicated three times to establish a statistical range. The powder flow rate is kept constant at approximately 8 gr/min. as Additionally, gas flow parameters, laser beam diameter and nozzle standoff distance remained the same.

Table 3.4: Process parameters selected for the Experimental Plan (EP)

Scan speed $[mm/s]$	Laser power $[W]$				
5	400	550	700	850	1000

3.4.2.4 Deposition geometry characterization

The depositions were scanned by a laser profilometer (VK-X250K, Keyence) to measure the geometric features of the depositions such as width and height. 2.5X magnification lens was used. The resolution in x and y direction is 17.05 μm and the resolution in z direction is 0.1 μm.

3.5 Results and discussion

The point cloud data is shown in Figure 3.15 at different laser power levels; the experiments were done in triplicate, with a representative profile shown. It can be seen that there are some peaks in the data. These peaks are mainly caused by the metal powder particles adhered onto the deposited profiles. These particles are not completely molten, but they stick on the profile because of the high temperatures on the surface or due to the high temperature of ejected particles from the process zone. The laser profilometer measurements are taken through the whole length of the depositions at discrete locations along the x-axis, where the x-axis is along the deposition path. The output is the height map of the deposition with given resolution in x, y and z direction. In order to measure the width and height at each deposition cross-section, an algorithm is developed.

Each deposition cross-section, at discrete locations along the x-axis, is filtered first with a moving average filter (window size of 10) to remove noise caused by adhered particles. In Figure 3.16, the raw data is shown in black solid line and the filtered data is shown in green dashed line. Subsequently, the discrete-domain first derivative of the profile is obtained and shown in orange line in Figure 3.16. The global maxima and minima in the deposition profile derivative indicate the sharp slope at the beginning and the end of the deposition. Once the location of the global minima and maxima are found, then linear interpolation is used at these points with the local derivative (slope) values. Finally, the intersection with the substrate points are calculated. These points are defined as the edges of the deposition profile, which gives the boundaries of the added material. The height at the middle point between the deposition edges is taken as the height of the deposition. Based on these measurements, the average width, height, and the standard deviation are found, which are used to validate the proposed model (Figure 3.17). A parabola (Figure 3.16(b)) is fitted to the computed edges and height of deposition profile. The geometric deviations are mostly caused by the metal powder ejections during the deposition. The fluctuation in the height profile throughout the whole deposition can be seen Figure 3.18.

The multiplication of η and β in the mass balance equation (Equation 3.23) is calibrated using MATLAB's System Identification Toolbox. ARX function is used and a first order transfer function is fitted to the first order differential equation of the mass balance. The calibrated value for the multiplication of $\eta\beta$ is 0.073.

The melt pool length was assumed to be approximately equal to 1.2 times of the laser beam diameter, as indicated by the steady state melt pool prediction given by Rosenthal's equation. Least squares minimization is used to calibrate the unknown difference of the γ_{GL} and γ_{SL} in Equation 3.27. The difference of $(\gamma_{GL} - \gamma_{SL})$ is found 4460 x 10^3 N/m.

The simulation and experimental results can be seen in Figure 3.17. The deposition area is solved by using the mass balance equation and the deposition width is solved by using the momentum balance equation (Equation 3.24). The deposition height is solved by assuming that the deposition cross-section area is half of an ellipse (Equation 3.14).

The simulation results show a good agreement with the experimental results, especially in predicting the average deposition area shown in Figure 3.17(a). The experimental area

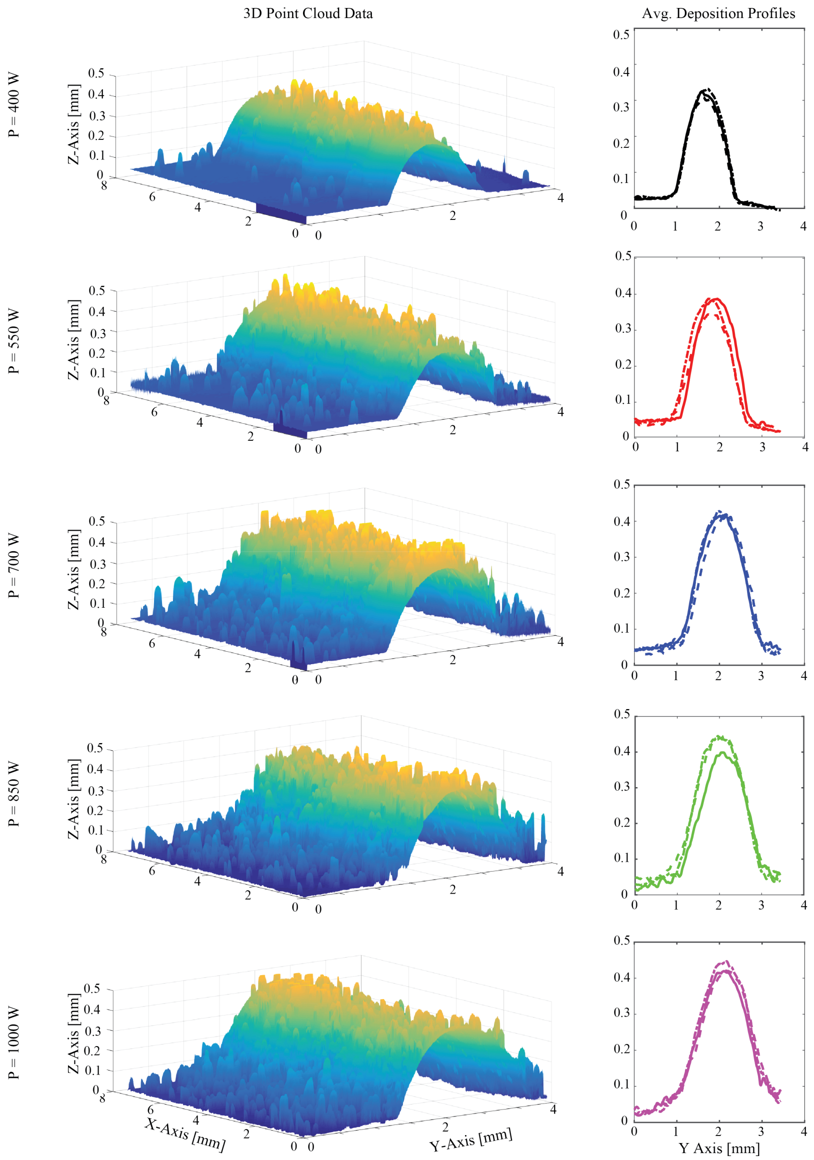

Figure 3.15: Point cloud data from the laser profilometer at different power levels. Column (A) rows (i)-(v) show the raw point cloud data of the deposited lines at different power levels. Column (B) rows (i)-(v) show the averaged deposition profiles through the sections shown in column (A) and rows (i)-(v) for each of the three replicate depositions in different line types showing the repeatability of the process.

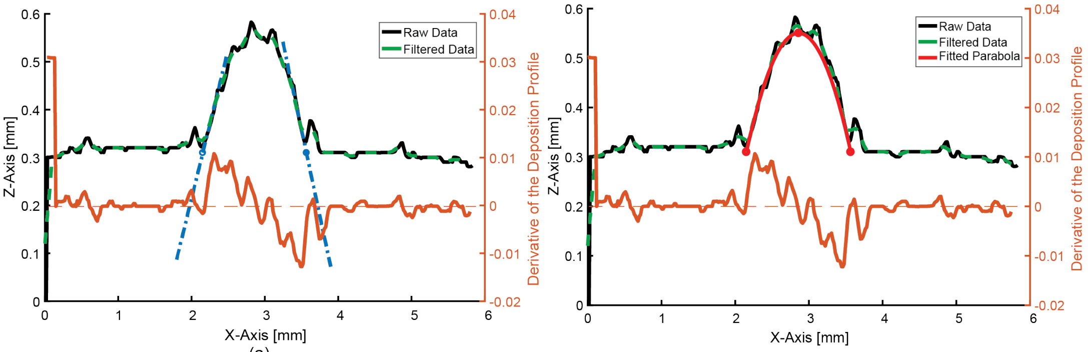

(a)

(b)

Figure 3.16: Geometric Feature Extraction from Laser Profilometer Data

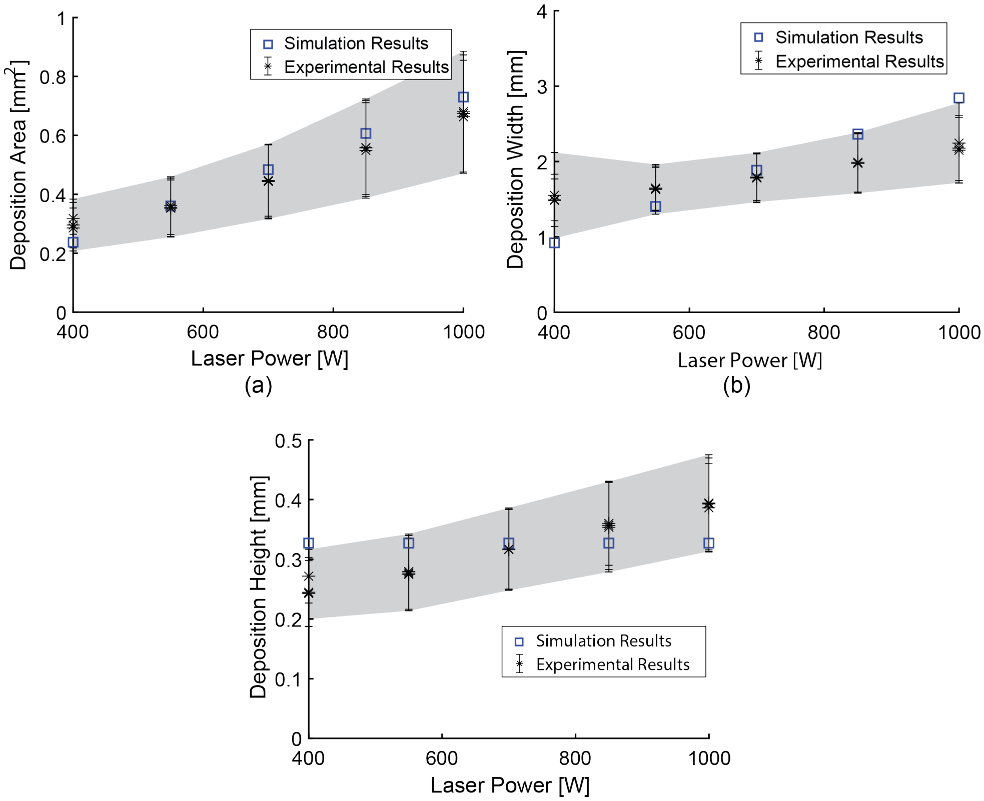

(a)

(b)

(c)

Figure 3.17: Comparison of simulation and experimental results (a) Deposition area, (b) Deposition width and (c) Deposition height

ranged from $0.290mm^2 \pm 0.044mm^2$ at 400W, to $0.67mm^2 \pm 0.105mm^2$ at 1000W. Similarly, the simulated deposition cross-sectional area ranged from $0.242mm^2$ at 400W to $0.730mm^2$ at 1000W, following a similar trend. The minimum standard deviation occurred at 400W and it increases with the laser power. The increase can be caused by increased instability of the process while approaching the keyhole welding mode with higher laser power levels [184]. The deposition area prediction was consistent with the simulation within the experimental process parameter span, which spanned the conduction, transition and keyhole ranges. As the deposition area is calculated with the mass balance equation (Equation 3.13), it may be less sensitive to transitions between welding modes compared to the momentum balance equation (Equation 3.24).

The simulation results for predicted deposition width is given in Figure 3.17(b) in comparison with the experimental results. The deposition width in experimental measurements ranged from $1.464mm \pm 0.204mm$ at 400W, to $2.152mm \pm 0.256mm$ at 1000W. The minimum experimental standard deviation occurred in the range of 550-700W. This may be caused by the conduction mode in this range, where 400 W is slightly under-melt creating deposition discontinuities. This results in high variability in the width profile. The high variability above 700W laser power is caused by entering the keyhole welding mode. The simulated deposition widths range between 0.952 mm at 400W, to 2.843 mm at 1000W. Compared to the simulation data, the deposition width predictor appears to deviate from experimental averages outside of the 550-700W. This is likely because the material parameters and process conditions were assumed to be in conduction, where material vaporization effects were not accounted for [195, 86]. In addition, the melt pool typically becomes significantly deeper in keyhole, while the melt pool width does not increase significantly [195, 390]. These findings in terms of trends of deposition width as a function of laser power across the different conduction and keyhole melting modes are in accordance with experimental datasets in literature [174].

In Figure 3.17(c), the comparison in deposition height between experimental and simulation results is presented. The experimentally obtained deposition height ranged from $0.271mm \pm 0.023mm$at 400W, to $0.388mm \pm 0.043mm$ at 1000W. The minimum experimental standard deviation occurred at 400W and it increases with increasing laser power. This can be a result of increased instability of the process with increasing laser power as the welding mode switches from under-melt to conduction and from conduction to keyhole mode [123]. The deposition height has an increasing trend in experimental results shown in Figure 3.17(c), which could be due to increased powder catchment efficiency with higher laser power. In addition, the 400W was the first deposition in the sequence, where each subsequent deposition line may have had a contribution from material ejections escaping the process zone and adhering to neighboring lines and substrate plate, which may have created a different surface initial condition. In terms of simulation datasets, it can be seen that the deposition height prediction is least sensitive to increasing laser power as seen in Figure 3.17(c). When looking at the measurements of height and width, taken along each deposition at all power levels, a periodic fluctuation in experimental values can be observed as seen in Figure 3.18. The cause of this periodic fluctuation is currently being investigated, with the possibility of having a contribution from parasitic effects caused by, and not limited to, the gas flow circuit, the powder circulation system, and the pull from the mounted cables and hoses on the robotic system. Such effects are not captured by the model and may contribute to further deviations in the simulated versus experimental results obtained.

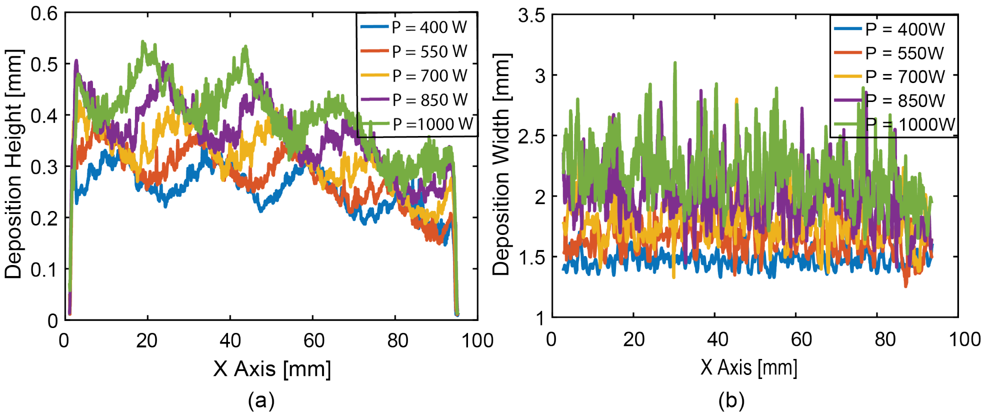

Figure 3.18: (a)The deposition height and (b) Deposition width along the whole deposition line

In this work, the proposed model was simulated at different laser power levels , while the scan speed was kept constant. Simulations were performed to compare the performance of the temperature history model against modeling results in literature, whereas experiments were performed to validate the physics-based analytical geometry model. In Figure 3.17, it can be seen that the experimental and simulation results are in a good agreement especially at the range of laser power of 550-700W, where extreme power levels are avoided and conduction welding mode is achieved [195]. The limitation to this modelling approach is the weaker performance in keyhole welding mode as the model does not account for complex physics of keyhole mechanism including changes in material properties across the different melting modes, as well as the effects of material evaporation, Marangoni convection etc. [99]. Including more complex process physics phenomena increases the model complexity and computational time.

A 2D planar deposition is simulated using the same scan path sequence as illustrated in Figure 3.12(a) to predict the width and height using the second set of parameters given in Table 3.4 (laser power: 550 W). It is aimed to observe the thermal effect of the recently deposited material on the adjacent deposition profile. The prediction results in terms of deposition geometry for each voxel can be seen in Figure 3.19, where the labeled rows and columns correspond to the voxel index in the deposition sequence from Figure 3.12(a). The color scale in Figure 3.19 is given on the right side of the deposition width (Figure 3.19(a)) and height (Figure 3.19(b)) maps. As the temperature of the substrate is assumed to be constant on the first deposition line, the deposition profile does not deviate; however, fluctuations can be observed in the deposition profile of the following deposition lines. The red voxels show an increase in deposition width and height caused by previously deposited voxels' residual temperature. Overall, the deposition width and height increase progressively with the scan path sequence, as the steady state temperature of the deposition increases based on the thermal history. It can also be observed that the deviations in the width predictions are higher compared to the height predictions, showing a higher sensitivity in response to neighboring voxels' temperature. This phenomenon is in agreement with literature [387].

The main goal of this work was to develop a physics-based thermal and geometry model, which is compatible with 2D/3D toolpaths. The proposed model gives adequate predictions within the conduction welding mode, with a low computational time. Thus, this approach can be used in process control schemes. Future work will focus on validation approaches for the thermal history model using dual wavelength pyrometry. Experimental validation will be also performed on deposition geometry of planar surfaces (Figure 3.19) as well as multi-layer structures. In addition, the coupled thermal history and geometry model will deployed for multi-layer and complex toolpath depositions.

3.6 Summary and conclusions

In this study, coupled analytical thermal and geometry models for the DED process were presented, which are compatible with 2D/3D toolpaths. With a voxel-based approach, the initial voxel dimensions and temperature are predicted using Rosenthal's moving heat source equation. At each time step, a single voxel is assumed to be deposited. The time-dependent heat transfer between the voxels is solved with a state space model in discrete time, recursively. The heat transfer equations are updated at each time step based on the deposition toolpath. The substrate temperature predicted in the thermal model is used as an input to the analytical geometry model. The experimental plan was performed, where

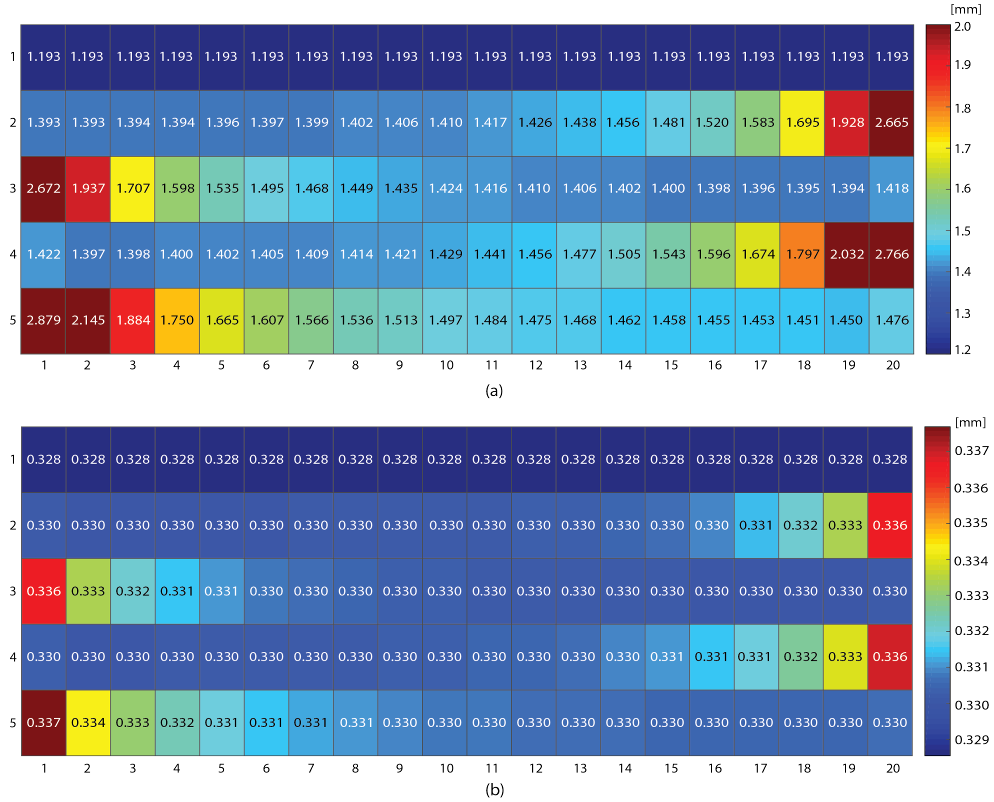

	1	2	3	4	5	6	7	8	9	10	11	12	13	14	15	16	17	18	19	20
1	1.193	1.193	1.193	1.193	1.193	1.193	1.193	1.193	1.193	1.193	1.193	1.193	1.193	1.193	1.193	1.193	1.193	1.193	1.193	1.193
2	1.393	1.393	1.394	1.394	1.396	1.397	1.399	1.402	1.406	1.410	1.417	1.426	1.438	1.456	1.481	1.520	1.583	1.695	1.928	2.665
3	2.672	1.937	1.707	1.598	1.535	1.495	1.468	1.449	1.435	1.424	1.416	1.410	1.406	1.402	1.400	1.398	1.396	1.395	1.394	1.418
4	1.422	1.397	1.398	1.400	1.402	1.405	1.409	1.414	1.421	1.429	1.441	1.456	1.477	1.505	1.543	1.596	1.674	1.797	2.032	2.766
5	2.879	2.145	1.884	1.750	1.665	1.607	1.566	1.536	1.513	1.497	1.484	1.475	1.468	1.462	1.458	1.455	1.453	1.451	1.450	1.476

(a)

	1	2	3	4	5	6	7	8	9	10	11	12	13	14	15	16	17	18	19	20
1	0.328	0.328	0.328	0.328	0.328	0.328	0.328	0.328	0.328	0.328	0.328	0.328	0.328	0.328	0.328	0.328	0.328	0.328	0.328	0.328
2	0.330	0.330	0.330	0.330	0.330	0.330	0.330	0.330	0.330	0.330	0.330	0.330	0.330	0.330	0.330	0.330	0.331	0.332	0.333	0.336
3	0.336	0.333	0.332	0.331	0.331	0.330	0.330	0.330	0.330	0.330	0.330	0.330	0.330	0.330	0.330	0.330	0.330	0.330	0.330	0.330
4	0.330	0.330	0.330	0.330	0.330	0.330	0.330	0.330	0.330	0.330	0.330	0.330	0.330	0.330	0.331	0.331	0.331	0.332	0.333	0.336
5	0.337	0.334	0.333	0.332	0.331	0.331	0.331	0.331	0.330	0.330	0.330	0.330	0.330	0.330	0.330	0.330	0.330	0.330	0.330	0.330

(b)

Figure 3.19: Deposition geometry predictions for a deposition of 5 adjacent lines and total of 100 voxels (a) deposition width results in mm (b) deposition height results in mm

the laser power was varied such that the experiments span from under-melting welding mode to keyhole welding mode. The deposition geometry was characterized using a laser profilometer, with the geometric features extracted from the point cloud data. To sum up the main results, in this work:

1. The thermal history model was compared against an existing model performance in literature; the existing model having the limitation of only simulating thermal history for single direction deposition. The model shows a good agreement compared to the predictions in [218], and the maximum prediction error is less than 15% depending on the layer of deposition.

2. The average value and standard deviation of the deposition height and width were calculated to compare them with the predicted values from the proposed coupled thermal history and deposition geometry models. Overall, across the entire experimental range, the maximum prediction error was ±16.6% (0.290 mm actual measurement, 0.242 mm predicted), ±33.6% (1.464 mm actual measurement, 0.972 mm predicted) and ±17.1% (0.271 mm actual measurement, 0.327 mm predicted) in deposition area, width and height, respectively.

3. The simulation results show a good agreement with the measured values from the laser profilometer data within the conduction melting mode. Within the conduction mode range (at power levels from 550 to 700W), the maximum prediction error compared to experimental datasets was 7%, 13% and 17% in deposition area, width and height, respectively.

4. The model is structured to be able to predict the thermal history and deposition geometry for complex toolpaths, including for multi-layers, as well as complex toolpath depositions in 2D/3D. The model performance is expected to be optimal in conduction mode.

The thermal model is aimed to be improved by calibrating the parameters based on experimental thermal data as a future research direction. Using in-situ thermal sensors such as IR camera or dual wavelength pyrometer would increase the reliability of the predicted temperature values. Hence, it will have a positive effect on the predictions for deposition geometry. More complex scan paths with curvatures and sharp corners can be simulated to see the effect of variation in scan speed on geometric features of the deposition.

Chapter 4

Adaptive vision-based detection of laser-material interaction for directed energy deposition

4.1 Preface

In-situ vision data acquisition, feature extraction, and analysis are ongoing challenges for quality assessment in directed energy deposition (DED). This work proposes a method for detecting target regions in the laser-material interaction zone based on a low-cost high-dynamic-range (HDR) vision sensor. Adaptive image thresholding, connected component analysis, and iterative energy minimization are used to identify target regions. The method is designed to be adaptive, in terms of obtaining parameters based on simple training data, and robust, in terms of feature detection performance subject to under-melt, conduction and keyhole melting mode phenomena. The performance of the proposed region detection scheme is quantitatively and qualitatively evaluated against annotated data. It was found that the True Positive Rate in detection was above 90%, while the False Detection Rate was less than 10%. Extensive experimental results show that the proposed scheme is able to detect and follow target regions under a variety of power levels and process conditions.

4.2 Introduction

In-situ process monitoring is one of the key strategies to improve AM performance. Researchers have observed melting and solidification phenomena using various sensing techniques to develop a better understanding of the physics behind laser-material interaction, to identify process instabilities, and to control the process [127]. In-situ radiometric sensors are commonly used in metal AM systems to detect temperature-related signatures [108], such as melt pool temperature and geometry, and plasma plume characteristics [268]. Radiometric sensors can detect process signatures from different spectral bands such as visible, near infrared and infrared [178, 146]. Similarly, vision detectors, such as CCD or CMOS cameras, are commonly used to monitor the laser-material interaction and to draw conclusions about possible process instabilities resulting in defects within a part. Finally, photodiode, pyrometer and infrared detectors are commonly-used devices which can detect infrared and near infrared wavelengths [65, 256], either point-based (thermometry) or image-based (thermography) [77].

In metal AM, monitoring sensors can be placed co-axially or off-axis with respect to the energy source. In a co-axial configuration, the field of view is focused on the melt pool specifically, where the process zone is monitored. Off-axis sensors observe the process from the side, and have a wider process landscape in their field of view. Off-axis detectors can be static, capturing the build environment either at the beginning and end of printing one deposition layer, or mounted on the deposition actuator, thus following the deposition of the whole layer [354, 233].

The detectable process signatures, captured by radiometric sensors at different spectral ranges, are the melt pool geometry, the plasma plume, the deposition geometry, as well as defects such as pores and cracks. Using such detectors, the melt pool geometry can be observed during the process and geometric features extracted, depending on the field of view [283, 79, 208]. The brightest region is typically labeled as the melt pool area, regardless of the temperature gradient within the melt pool image [42]; however, the bright region may include recently-solidified incandescent material. Kriczky *et al.* use a dual wavelength pyrometer to detect the melt pool temperature and geometry by using the solidus-to-liquidus temperature as the boundary of the melt pool [204]. Although thermal sensors are generally more expensive, they can capture richer details in the melt pool region compared to visual ones. Examples of such imaging include the work by Demir *et al.* [87], who used a low cost CMOS camera and extracted melt pool geometric features to compare the effects of pulsed and continuous wave laser regimes on the melt pool characteristics. Other efforts focused on monitoring the part geometry in macro-scale for dimensional accuracy, quality [200], part distortion [201] and porosity [235, 73].

Sensor data collected from the laser-material interaction zone has been used to gain a deeper understanding of the physics behind DED [356, 238] and how the process parameters affect the melt pool morphology [155]. For instance, Heigel and Lane used high-speed thermographic measurements and observed that increasing the scan speed shortens the melt pool length. However, the linear relationship between scan speed and melt pool length cannot be seen at high power levels [155]. These observations and investigations lead to the development of control algorithms [299, 248], and/or the development of quality criteria for deposition based on either on-line or off-line analysis of datasets [409, 357]. Emerging approaches for deposition quality evaluation focus on machine learning algorithms trained based on melt pool, plasma plume, and spatter images generated using high-speed vision detectors [127, 430, 114, 334, 145, 429, 337, 418, 268]. Other examples look at the evolution and growth of the deposition geometry or of the melt pool morphology to flag the zones where a performance threshold was reached during the process, which may be an indication of unstable processing conditions [198]. Process control schemes can be established based on this idea; for instance, Bardin *et al.* uses a CMOS sensor to predict the melt pool temperature and the resulting penetration depth of the melt pool in order to keep a conduction melting mode throughout the process [26].

The DED process operates typically at velocities ranging between 1 and 30 mm/s [356, 238, 325], with laser beam spot sizes ranging between 0.5 and 3 mm [356, 238] and powers from 200 to 1500 W [394], depending on the material being processed and the beam spot size. The resulting melt pool regions for such processes are therefore on the order of a few mm [79]. As a result, when deploying thermography detectors focused on the laser-material interaction zone, there needs to be sufficiently high spatial resolution, thermal resolution (dynamic range), and response time to capture spatial thermal gradients at a high temporal resolution [208, 198]. Detector costs for high resolution, high dynamic range, high frequency performance are often prohibitive, limiting their adoption as industrial solutions to process monitoring, performance analytics, quality control, and process control [328].

This study focuses on an adaptive method for extracting regions in the laser-material interaction zone based on a low-cost high dynamic range (HDR) vision detector. The method is designed to be adaptive in terms of defining regions of interest, optimizing feature extraction parameters, and robust feature detection performance under test cases spanning lack-of-fusion, conduction, and keyhole melting mode phenomena. In the context of this work, three laser-material process zone regions were defined, namely the Core, Melt pool, and Incandescent regions. The importance of this work resides in the flexibility of the algorithms in defining regions of interest, in the optimization of region detection parameters, as well as in the robustness of detecting the regions of interest under all melting mode regimes studied.

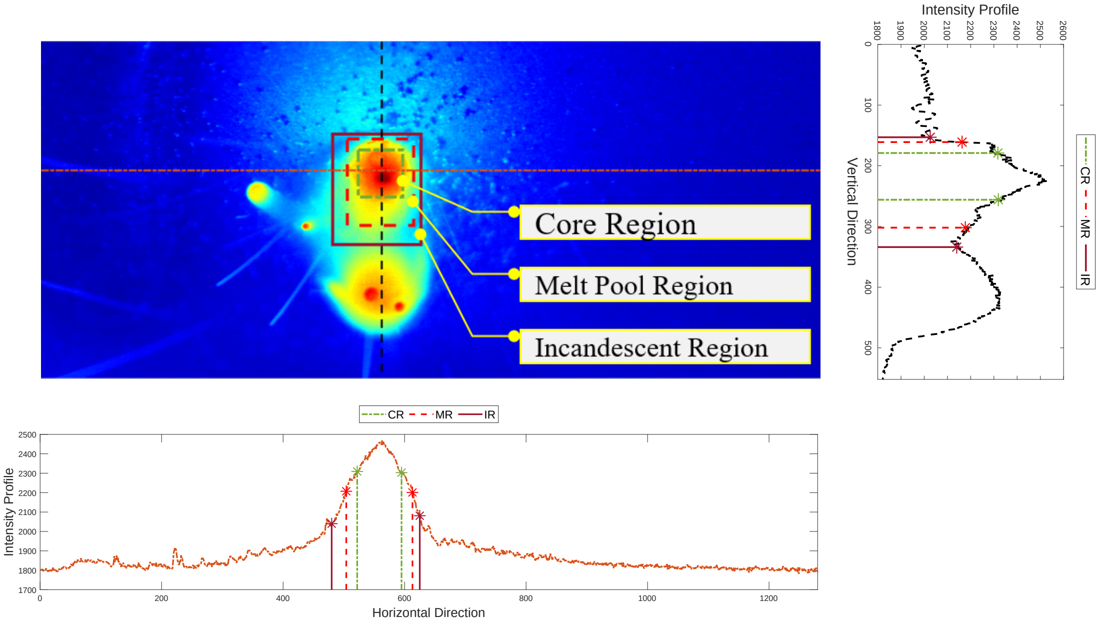

Figure 4.1: Illustration of the three target regions, namely Core, Melt pool and Incandescent, captured from the laser-material interaction zone using an HDR camera, where the bounding boxes annotations are constructed using the toolbox in [92]. The vertical and horizontal intensity profiles through the regions of interest along with there boundaries are provided. Note that applying intensity thresholding only will not be able to identify the three target regions without being affected by the intensities of nearby ejected particles.

4.3 Methodology for adaptive feature detection

4.3.1 Proposed spatially-resolved thermography and feature definitions

Our study focuses on low-cost thermography data acquisition paired with advanced visual feature extraction that can help in better understanding laser-material interaction. The goal is to develop a robust feature detection algorithm against intensity variations caused by spatial and temporal fluctuations in the laser-material process zone, intensity gradients in background illumination, and random inclusions in the field of view due to material ejecta. To achieve this goal, a monochrome high dynamic range (HDR) vision camera (XVC-1000 Weld Camera, Xiris Automation, Burlington, ON) is used to capture melt pool images off-axis during the DED process. The analytics framework introduced in this work can accommodate both on- and off-axis datasets.

Given an HDR frame, a color-coded map is constructed, an example of which is illustrated in Figure 4.1, to enable the user to select regions of interest while training and annotating datasets. For demonstration purposes, three regions were selected to develop and demonstrate the performance capability of our proposed approach.

The first geometric feature is the *Core* region, which falls immediately under the laser beam intersection with the substrate. The Core region has the highest intensity, as shown in Figure 4.1, and it is stable in position and size during the process. A second feature is the *Melt pool* region, larger in size than the Core, where melting takes place over a region which may change in size depending on the energy input and distribution. Both Core and Melt pool will generally be elliptical in shape. A third feature is the *Incandescent* region, the boundary between the heat-affected zone and the background. Qualitatively, the shape and size of the Incandescent region fluctuates the most between frames; as such, the Incandescent region is assumed to contain some contribution from the plasma plume, the recently solidified hot material, as well as from the Core and Melt pool regions.

This study does not involve temperature measurements of the laser-material interaction zone. As such, the three regions were user-defined and annotated, based on the intensity map shown in Figure 4.1. The mathematical scheme for developing, training and testing the feature detection is described in the following section.

4.3.2 Proposed scheme for region initialization and stabilization

As shown in Figure 4.1, the three regions of interest (Core, Melt pool and Incandescent) are centered around the brightest spot, which is stable in its location from one frame to another. Further, it can be noticed from the same figure that the brightness level varies when we move from one region to another. However, utilizing a single intensity threshold per region will not be able to meaningfully separate the target regions from each other or from nearby ejected particles, as can be seen in the example in Figure 4.1. Thus, in order to detect the three regions of interest, an adaptive image thresholding technique is first employed on every input image for detecting an initial region of interest, $\tilde{M}_t$, which acts as a seed for subsequently detecting the target regions; Figure 4.2 shows the block diagram of the proposed detection scheme.

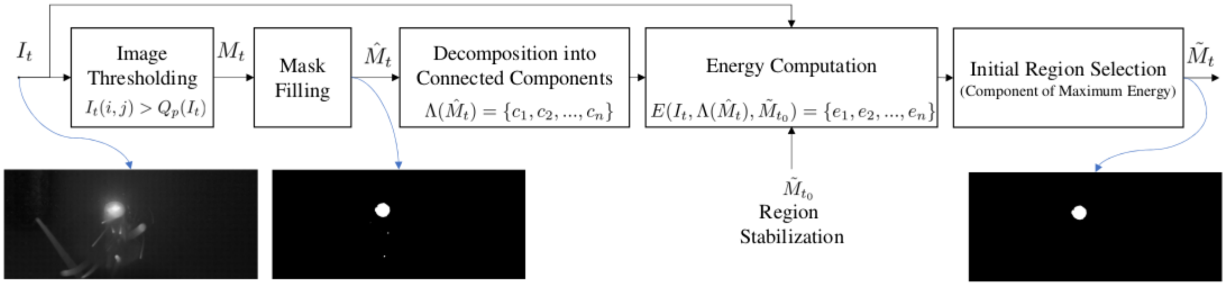

Figure 4.2: Block diagram of the proposed region initialization and stabilization technique. A given input image I_t at time t is transformed to region selection $\tilde{M}_t$.

Let $I_t \in \mathbb{R}^{m_1 \times m_2}$ denote the input image or video frame of size $m_1 \times m_2$ at time t, and let $Q_p(I)$ be the pth-percentile value that is greater than $p\%$ of the elements of I. Parameter p is found based on training data, as will be explained in Section 4.3.4.

Given an input image $I_t \in \mathbb{R}^{m_1 \times m_2}$, a percentile-based image thresholding is employed to obtain a mask M_t:

$$M_t(i,j) = \begin{cases} 1, & \text{if } I_t(i,j) > Q_p(I_t) \\ 0, & \text{otherwise} \end{cases} \tag{4.1}$$

where $1 \leq i \leq m_1$ and $1 \leq j \leq m_2$ denote pixel indices. Since the connected regions in M_t may contain small holes or imperfections, a morphological mask filling operator[1] is performed on M_t to obtain the filled mask $\hat{M}_t$, which is then decomposed into its connected components, its candidate region of interests, as

$$\Lambda(\hat{M}_t) = \{c_1, c_2, ..., c_n\} \tag{4.2}$$

where $\Lambda(\cdot)$ is a labeling function that decomposes an image into its connected components, each of same size as $\hat{M}_t$. Let $\tilde{M}_{t_0}$ denote a mask of size $m_1 \times m_2$ that highlights the region of interest obtained at some initial time t_0 and which can be used for region stabilization. To optimize the regions, we propose to associate an energy corresponding to each connected component:

$$E(I, \Lambda(\hat{M}_t), \tilde{M}_{t_0}) = \{e_1, e_2, ..., e_n\} \tag{4.3}$$

where

$$e_\ell = \sum_{i,j} I_t(i,j) c_\ell(i,j) \tilde{M}_{t_0}(i,j), \qquad \ell = 1, 2, ..., n \tag{4.4}$$

---

[1] The MATLAB function `imfill` is used, https://www.mathworks.com/help/images/ref/imfill.html

The chosen mask $\tilde{M}_t$ of the region of interest is selected as that mask corresponding to the connected component having the largest energy:

$$\tilde{M}_t = c_{\hat{\ell}}, \qquad \text{where} \qquad \hat{\ell} = \underset{\ell \in \{1,2,\ldots,n\}}{\text{argmax}} \; e_\ell \tag{4.5}$$

The use of the mask $\tilde{M}_{t_0}$ in (4.4) asserts a prior model, offering the proposed detector some robustness in computing $\tilde{M}_t$ for $t > t_0$, by reducing the effect of ejected particles of high intensity that may interfere with selecting the target region in (4.5). This region stabilization takes advantage of the constraint that the camera is moving with the same speed and direction of the laser scan path, as will be explained in Section 4.4.1. It is important to note that the only parameter needs to be specified for this method is p, which can be obtained empirically from the user-annotated regions of interest. However the actual pixel threshold $Q_p(I_t)$ is adaptive, since the pth percentile varies as a function of the input image I_t. Such adaptivity is important in DED, as the imaging detector continuously adjusts the dynamic range.

4.3.3 Proposed scheme for region growing

To accommodate the varying brightness levels of the regions, as shown in Figure 4.1, a region growing technique is employed to detect the Core, Melt pool and Incandescent regions, starting from $\tilde{M}_t$, as explained in Section 4.3.2. The proposed region growing technique is based on an iterative approach, in which the region $\tilde{M}_{t,k}$ is gradually expanded based on an energy criterion at each iteration k. Figure 4.3 shows the block diagram of the proposed scheme, showcasing an example for illustration purposes.

Our mask is initialized from $\tilde{M}_t$ in (4.5),

$$\tilde{M}_{t,0} = \tilde{M}_t \tag{4.6}$$

At iteration k, given $\tilde{M}_{t,k}$, binary mask $B_{t,k}$ represents the external boundaries of the selected region, obtained by applying the following operations on $\tilde{M}_{t,k}$:

$$B_{t,k} = (\tilde{M}_{t,k} \ominus S) \oplus \tilde{M}_{t,k}. \tag{4.7}$$

S is a circular structure element of radius $r_S \ll \min(m_1, m_2)$, and $\ominus$ and $\oplus$ denote dilation and pixel-wise logical XOR operations, respectively. We further refine $B_{t,k}$ to $\hat{B}_{t,k} \subset B_{t,k}$, those image pixels of significance within $B_{t,k}$:

$$\hat{B}_{t,k}(i,j) = \begin{cases} 1, & \text{if } I_t(i,j) B_{t,k}(i,j) \geq \tau_k \\ 0, & \text{otherwise} \end{cases} \tag{4.8}$$

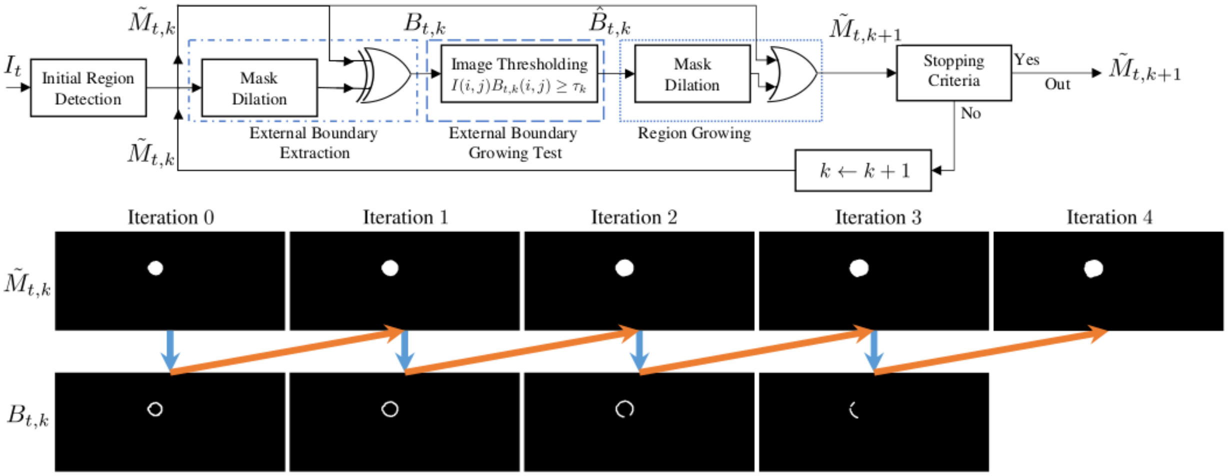

Figure 4.3: Block diagram of the proposed region growing-based detection technique, where τ_k is defined in Equation (4.9).

for threshold τ_k, defined as

$$\tau_k = \max\left(I_t^{min}, \text{avg}[I_t \odot \tilde{M}_{t,k}] - \beta\sqrt{\text{var}[I_t \odot \tilde{M}_{t,k}]}\right). \tag{4.9}$$

That is, the threshold is set to be the larger of the minimum pixel value and the average intensity (within mask $\tilde{M}_{t,k}$) minus β standard deviations, where β may be set empirically for each target region (Core, Melt pool, Incandescent), and where $\odot$ is element-wise multiplication.

At every iteration $\tilde{M}_{t,k}$ will grow based on the image pixels of significance, as

$$\tilde{M}_{t,k+1} = (\hat{B}_{t,k} \ominus S) \ \cup \tilde{M}_{t,k} \tag{4.10}$$

where $\cup$ is the pixel-wise logical OR operator. The algorithm stopping criterion is based on the average energy for pixels within $\hat{B}_{t,k}$,

$$\hat{E}_t(k) = \frac{\sum_{i,j} I_t(i,j)\hat{B}_{t,k}(i,j)}{\sum_{i,j} \hat{B}_{t,k}(i,j)} \tag{4.11}$$

such that the algorithm stops if any of the following criteria is met:

$$\frac{\hat{E}_t(k)}{\max(\hat{E}_t)} < \alpha \qquad \sum_{i,j} \hat{B}_{t,k}(i,j) = 0 \qquad k \geq K, \tag{4.12}$$

that is, based on energy, having no further pixels to add, or having exceeded the maximum number of iterations K. In the energy dropping ratio (4.12), the denominator $\max(\hat{E}_t)$ represents the maximum energy of all region growing iterations, and $0 < \alpha < 1$ is a region dependent parameter that must be set empirically, such that high, medium and low α will tend to stop the algorithm at the boundaries of the Core, Melt pool, and Incandescent regions, respectively.

The remaining task is the learning of system parameters based on annotated training image data, discussed in the following section.

4.3.4 Estimating p, r_S, β, and α

In order to learn the best parameter settings for the three target regions of Core, Melt pool, and Incandescent, the ground truth annotations of a number of training frames are used. Let $\Omega(I_t, p, r_S, \beta, \alpha)$ denote the process of applying the region initialization and stabilization (Section 4.3.2) followed by the region growing (Section 4.3.3) on an input image I_t, based on the parameters of percentile $p \in (0, 1]$, a structure element radius r_S, energy dropping factor β (4.9), and boundary energy dropping ratio α (4.12). In order to determine the optimum parameters for each target region, a fitness function can be formulated as

$$\underset{p, r_S, \beta, \alpha}{arg\,min} \; \frac{1}{N_f} \sum_t \mathrm{MSE}(\Phi_{gt}(I_t), \Phi_d(\Omega(I_t, p, r_S, \beta, \alpha))) \tag{4.13}$$

the mean-square-error between the ground truth Φ_{gt} and detected Φ_d region bounding boxes, based on annotations over N_f frames. By solving the optimization problem in Equation (4.13) using a genetic algorithm solver[2], the best parameter settings for p, r_S, β and α are obtained, which we will demonstrate in Section 4.5.2. [3]

4.4 Methodology for adaptive feature validation

4.4.1 Experimental setup and manufacturing plan

The same DED and material systems are used for this study as in Chapter 3. The process parameters for the experiments remain the same as in previous chapter. As mentioned

---

[2] The MATLAB function `ga` [140, 74, 75] is used, https://www.mathworks.com/help/gads/ga.html

[3] This section is reflective of written contributions from Dr. Mohamed Naiel

in Section 4.3.1, to capture melt pool images a monochrome HDR vision camera is used, having a resolution of 1280 × 552 pixels and a frame rate of 7 frames per second. In the context of this work, for off-axis measurements a bracket was designed to mount the camera on a robotic end-effector as seen in Figure 4.4. The bracket allows adjustments in order to view the melt pool at different perspectives, angles and working distances. For the present work, the camera is mounted in the lead view of the scan path, with the melt pool centered in the field of view.

In this work, a 75 mm lens is used with a 40 mm spacer. A green filter is used to preserve wavelengths of 470 to 600 nm, and a UV filter is employed for avoiding reflections in the field of view. A dimmable illumination source is also used to prevent dynamic range saturation and to decrease the contrast between the very bright melt pool area and the surroundings. The brightness of the illumination source was set by trial and error, and remained fixed for the entire set of experimental work. The melt pool images are taken at 5 ms of exposure time subject to automatic gain control.

For the purpose of this work, the bright areas captured by the monochrome detector are considered to be a general representation of the melt pool signature in terms of thermal gradient. As such, the algorithms developed in this work are intended to be generalized for such melt pool datasets. The idea behind using this low-cost camera was to correlate the dimensions of the regions extracted from the HDR images across a wide range of melting mode operating conditions.

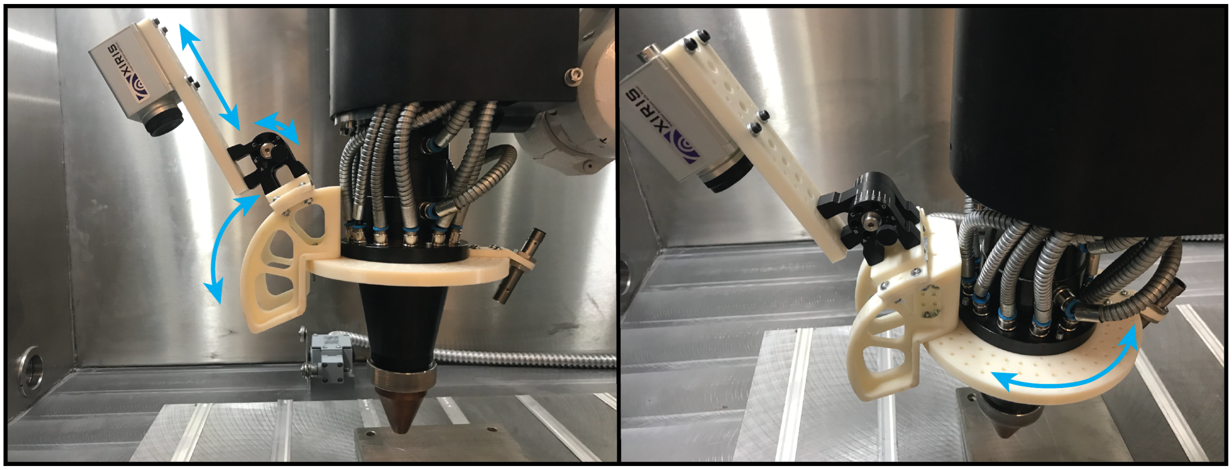

Figure 4.4: The vision system mounted on the DED robotic system. The mounting bracket can be adapted to different focal distances, viewing angles with respect to the vertical plane and with respect to the deposition path.

The keyhole melting mode transition is calculated by using the normalized enthalpy model [153]; based on existing literature for SS316L, the normalized enthalpy threshold is approximately 6 or higher in keyhole welding mode [194], whereas a laser power of 1000 W corresponds to a normalized enthalpy of 6.13 [391, 175], implying an expectation of keyhole melting.

4.4.2 Deposition geometry estimation

Confocal laser profilometry (VK-X250K, Keyence) scans at 2.5X magnification are performed ex-situ to measure the geometric features of the depositions (width and height) and to infer relationships with the trends in the vision datasets. The spatial resolution in the x and y directions is 17.05 μm and the resolution in the z direction is 0.1 μm. Scans are taken over the entire length of the depositions.

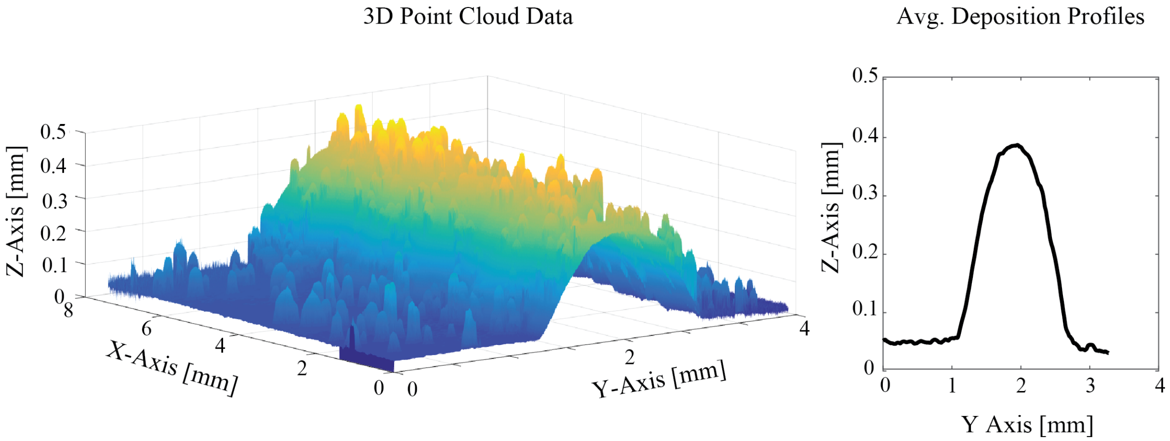

Figure 4.5: Point cloud (height) data of the deposition scanned with the laser profilometer.

The output of the laser profilometer is a height map of the deposition, such as the example shown in Figure 4.5. An algorithm is developed to extract the geometric features, the width and height, at each deposition cross-section. In order to dampen the noise caused by adhered particles, each deposition cross-section at discrete locations along the y-axis is filtered first with a moving-average filter with a window size of 10. In Figure 4.6, the black solid line and orange dashed line show the raw and filtered data, respectively. The global maxima and minima in the deposition profile derivative indicate the sharp slope at the deposition border; these are linearly interpolated, shown as green dashed lines. The intersection of the substrate and the interpolated lines determines the width boundaries of the deposited material. The height of the deposition profile is taken as the height value at the mid-point between the deposition width boundaries.

A direct comparison between the vision feature dimensions defined in the feature extraction framework (Core, Melt pool, and Incandescent regions) and the laser profilometer geometry features is not possible, for multiple reasons. The deposition zone detected by the vision system is in the plane of A_1 (Figure 4.7), a function of the actual melt pool width and length at each point in time, whereas the detectable geometric features from profilometry are in the plane of A_2 (Figure 4.7), describing the deposition width and height. An overview of the detectable features is shown in Table 4.1. The common features between the two datasets are the material deposition width and the melt pool region width; as a result these features were selected for comparison to illustrate the correlations between vision and profilometry data.

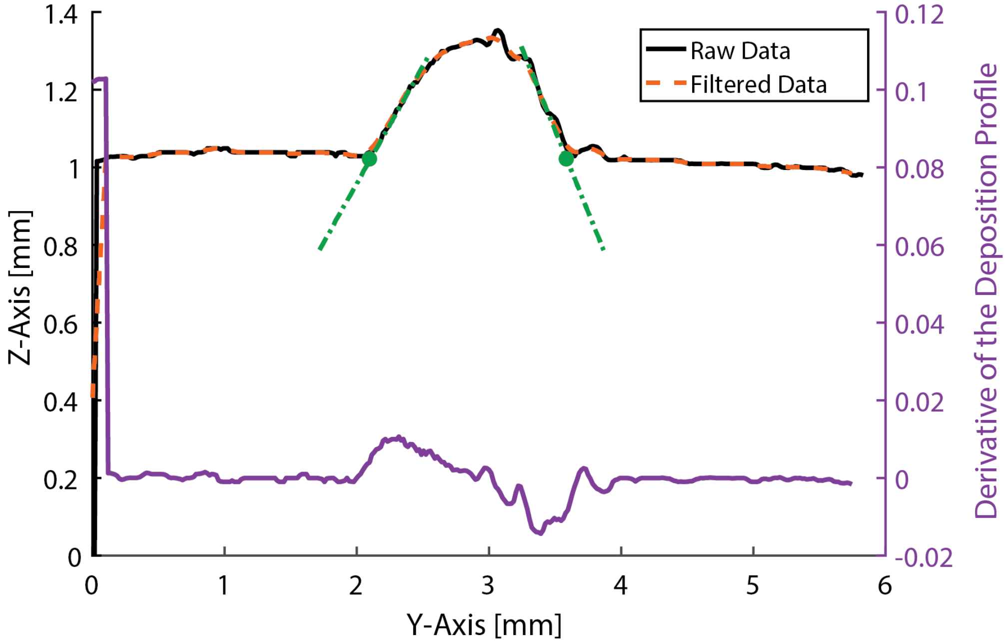

Figure 4.6: Feature extraction from the raw laser profilometer data. Green lines indicate straight-line fits to the profile edges.

Table 4.1: A comparison of detectable melt pool geometry features with the laser profilometer and HDR vision systems.

	Laser profilometry of clad deposition geometry	HDR vision detection of core, melt pool, or incandescent region
Length (l)		✓
Width (w)	✓	✓
Height (h)	✓	
Area A_1		✓
Area A_2	✓	

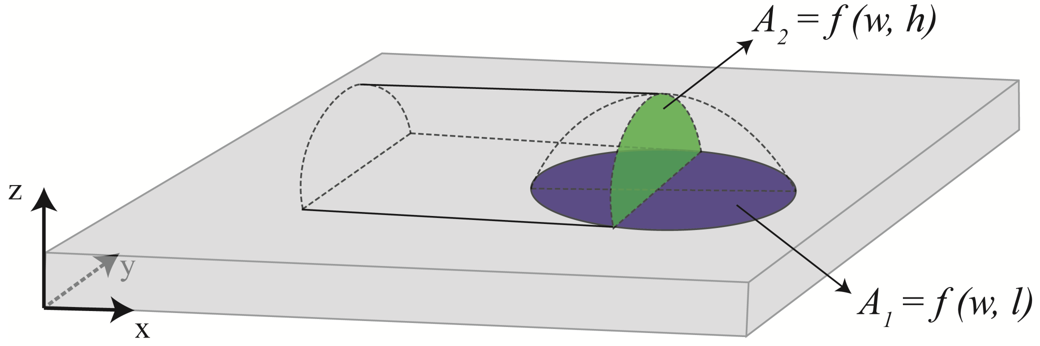

Figure 4.7: Different melt pool areas captured with laser profilometer and HDR vision system.

4.4.3 Measurements verification scheme

The region detection scheme of Section 4.3 is given by $\Omega(I_t, p, r_S, \beta, \alpha)$. Let Υ_W denote a function that extracts the width from a detected region, and let

$$W_{\mathcal{V}} = \left[\Upsilon_W(\Omega(I_t, p, r_S, \beta, \alpha)), \quad t = t_0, t_1, ..., t_{N_{\mathcal{V}}^t - 1}\right] \tag{4.14}$$

represent the measured width over the $N_{\mathcal{V}}^t$ frames. We will be seeking to register the melt pool region width $W_{\mathcal{V}}$ with the deposition width $W_{\mathcal{P}}$ from laser profilometry, as explained in Section 4.4.2. The number of elements in vectors $W_{\mathcal{V}}$ and $W_{\mathcal{P}}$ are denoted by $N_{\mathcal{V}}^t$ and $N_{\mathcal{P}}^x$, respectively, where the vectors are of unequal dimension because of differences between the higher profilometry resolution and much lower vision frame rate, implying a downsampling factor

$$1 < s_{\mathcal{P}} \leq \left\lfloor \frac{\hat{N}_{\mathcal{P}}^x}{\hat{N}_{\mathcal{V}}^t} \right\rfloor + 1. \tag{4.15}$$

Furthermore, the data collection processes of the profilometry and vision scans have variable start times, which causes an offset between the two signals, to be represented by $a_{\mathcal{P}}$.

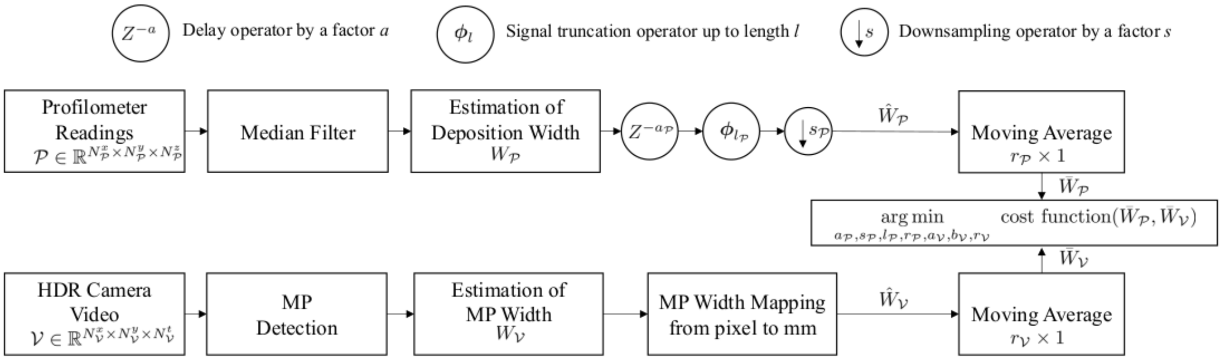

Figure 4.8: Block diagram of the proposed signal registration technique.

We develop a technique to register deposition and melt pool widths while addressing the challenging problems mentioned above. Figure 4.8 illustrates an overview of the proposed signal registration scheme. Let $\mathcal{P} \in \mathbb{R}^{N_{\mathcal{P}}^x \times N_{\mathcal{P}}^y \times N_{\mathcal{P}}^z}$ and $\mathcal{V} \in \mathbb{R}^{N_{\mathcal{V}}^x \times N_{\mathcal{V}}^y \times N_{\mathcal{V}}^t}$ denote the raw measurements and videos obtained by the profilometry and HDR camera, respectively. The two signals $W_{\mathcal{P}}$, of size $N_{\mathcal{P}}^x \times 1$, and $W_{\mathcal{V}}$, of size $N_{\mathcal{V}}^t \times 1$, will be first obtained from their corresponding raw data as presented in Sections 4.4.2 and 4.3, respectively. Next, since the two signals are of different units, resolutions, start and end times, the signals $W_{\mathcal{P}}$ and $W_{\mathcal{V}}$ are mapped as

$$\begin{aligned} \hat{W}_{\mathcal{P}}[n^t_{\mathcal{P}}] &= W_{\mathcal{P}}[s_{\mathcal{P}} n^t_{\mathcal{P}} - a_{\mathcal{P}}], & n^t_{\mathcal{P}} = 0, 1, ..., \hat{N}^t_{\mathcal{P}} - 1 \quad (4.16) \\ \hat{W}_{\mathcal{V}}[n^t_{\mathcal{V}}] &= a_{\mathcal{V}} W_{\mathcal{V}}[n^t_{\mathcal{V}}] + b_{\mathcal{V}}, & n^t_{\mathcal{V}} = 0, 1, ..., \hat{N}^t_{\mathcal{V}} - 1 \quad (4.17) \end{aligned}$$

where

$$\begin{aligned} s_{\mathcal{P}} &\in [1, 2, ..., \left\lfloor \frac{N^x_{\mathcal{P}}}{N^t_{\mathcal{V}}} \right\rfloor + 1), & (4.18) \\ \hat{N}^t_{\mathcal{P}} &= \frac{N^x_{\mathcal{P}} - a_{\mathcal{P}} - l_{\mathcal{P}}}{s_{\mathcal{P}}}, \qquad 0 \leq a_{\mathcal{P}}, l_{\mathcal{P}} << N^x_{\mathcal{P}} & (4.19) \end{aligned}$$

and $\lfloor \cdot \rfloor$ is the floor function. It is clear from (4.16) and (4.17) that $\hat{W}_{\mathcal{P}}$ is a downsampled, shifted and truncated version of $W_{\mathcal{P}}$, and that $\hat{W}_{\mathcal{V}}$ is linearly dependent on $W_{\mathcal{V}}$. In order to reduce the noisy transitions in $\hat{W}_{\mathcal{P}}$ and $\hat{W}_{\mathcal{V}}$ signals, a moving average is employed

$$\bar{W}_{\mathcal{P}} = \mathcal{M}(\hat{W}_{\mathcal{P}}, r_{\mathcal{P}}), \qquad \bar{W}_{\mathcal{V}} = \mathcal{M}(\hat{W}_{\mathcal{V}}, r_{\mathcal{V}}), \tag{4.20}$$

where $\mathcal{M}(W, r)$ denotes a 1D moving average filter with a window of size r applied to signal W. In order to quantify the similarity between $\bar{W}_{\mathcal{P}}$ and $\bar{W}_{\mathcal{V}}$, the cross-correlation, ρ, is used. Finally, the best parameters for registering these two signals are determined by using a genetic algorithm to solve the following optimization problem:

$$\begin{aligned} \underset{\hat{x}}{arg\,min} \; \{ & w_0 b_0^{-\rho(\bar{W}_{\mathcal{P}}, \bar{W}_{\mathcal{V}})} + w_1 |E[\bar{W}_{\mathcal{P}}] - E[\bar{W}_{\mathcal{V}}]| + \\ & w_2 |\max[\bar{W}_{\mathcal{P}}] - \max[\bar{W}_{\mathcal{V}}]| + \\ & w_3 |\min[\bar{W}_{\mathcal{P}}] - \min[\bar{W}_{\mathcal{V}}]| \} \end{aligned} \tag{4.21}$$

where $\hat{x} = [a_{\mathcal{P}}, s_{\mathcal{P}}, l_{\mathcal{P}}, r_{\mathcal{P}}, a_{\mathcal{V}}, b_{\mathcal{V}}, r_{\mathcal{V}}]^{\top}$, b_0 being the base of the exponential term, and the weights satisfy $\sum_i w_i = 1$. The cost function defined in (4.21) allows the estimated parameters in $\hat{x}$ to not only depend on maximizing the cross-correlation between the two aligned signals but also it allows selecting a solution that maps the signals to the same range. [4]

4.5 Experimental results and discussion

4.5.1 Vision and profilometry datasets

The HDR vision system and the experimental plan presented in Section 4.4.1 are used to extract the vision and profilometry datasets. In these datasets, three deposition replicates

---

[4] This section is reflective of written contributions from Dr. Mohamed Naiel

were conducted at each of the five power levels with three replicates presented in Table 3.4, resulting in 15 videos and their corresponding laser profilometry measurements, where the ground truth bounding boxes of three target regions that exist in the collected video dataset, namely, core region (CR), melt pool region (MR) and incandescent region (IR), are constructed using the toolbox in [92] and sample annotations are shown in Figure 4.1. The video dataset is partitioned into a *training dataset*, that consists of one video at each of the five power levels, and a *testing dataset*, that includes the remaining 10 videos.

4.5.2 Parameter estimation and analysis for vision-based feature detection

In order to study the effect of changing the main parameters of the proposed scheme (p, r_S, β, α, and number of iterations) on the performance of detecting each target region, the optimum parameter settings are first obtained by solving the optimization problem in (4.13), where only $N_f = 21$ frames from the training dataset (Section 4.5.1) are used. In this section, a set of experiments is conducted on the training dataset to quantify the detectors' performance when varying only one parameter at a time. To quantify the performance of the detectors, the overlap ratio, O, between a given ground truth bounding box, ϕ_{gt} and a detection bounding box, ϕ_d, is used as in [107]:

$$O = \frac{\text{Area}(\phi_{gt} \cap \phi_d)}{\text{Area}(\phi_{gt} \cup \phi_d)} \tag{4.22}$$

where a higher O value corresponds to a more accurate prediction. In this study, a detection bounding box that offers $O > 0.7$ is considered as a true positive detection, otherwise it is a false positive. The best parameter settings for detecting each of the target regions will be used in obtaining the feature extraction results in subsequent sections.

Effect of changing p

Figure 4.9(a) illustrates the effect of varying the value of p, the percentile for operator $Q_p(\cdot)$ in (4.1), varied as $p = 0.970, 0.972, ..., 0.998$. Changing p has a significant impact on the performance of detection in all regions. When $p < 0.986$ or $p > 0.996$, the TPRs of the three detectors deteriorate significantly, due to the corresponding regions being either over-estimated or under-estimated, respectively. Figure 4.9(a) also highlights the best p value for each of the regions based on solving the optimization problem in (4.13).

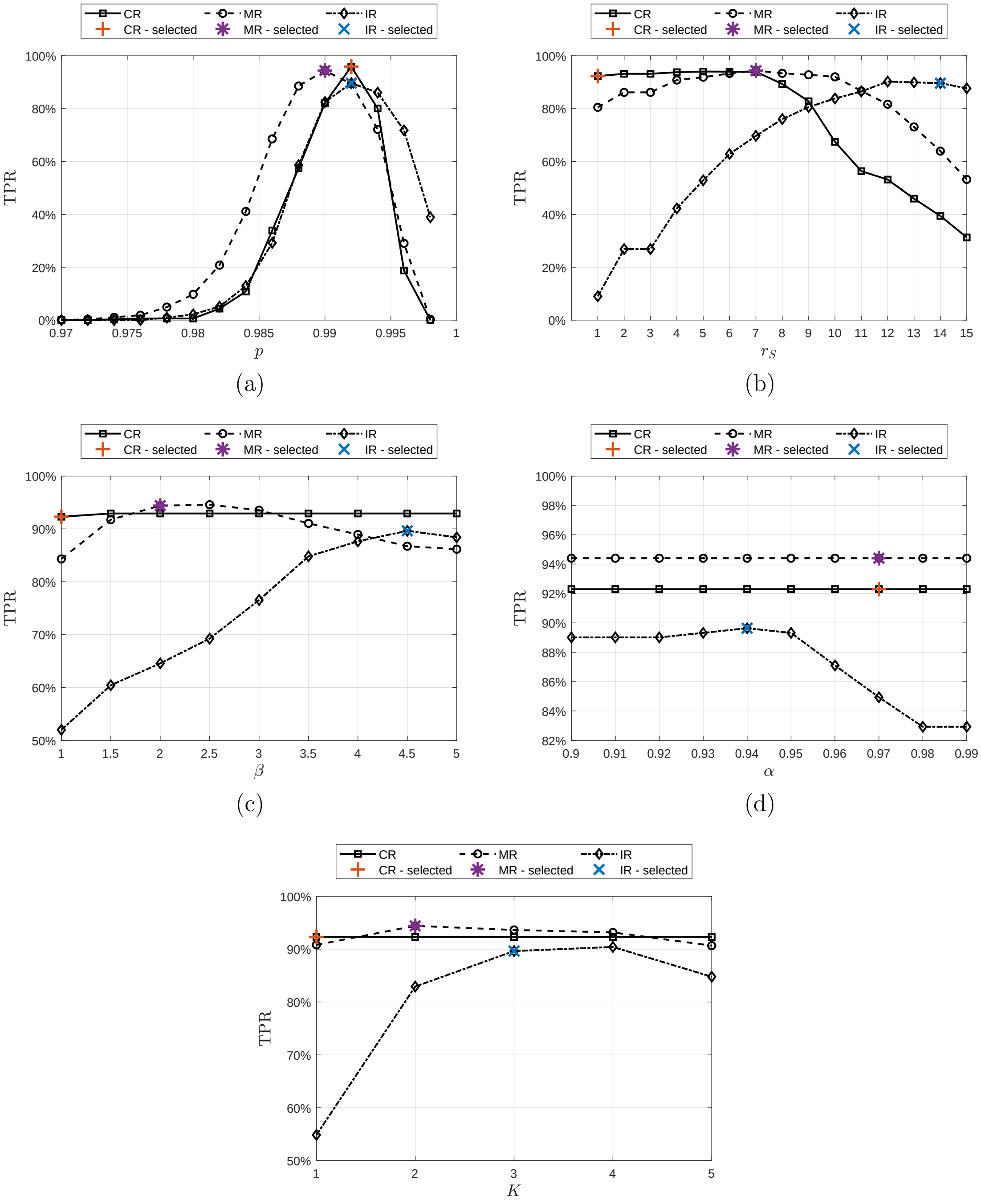

(a) (b) (c) (d) (e)

Figure 4.9: The effects of changing p, r_S, β, α and number of iterations on the TPR of the proposed region growing scheme are shown in (a) - (e), respectively. Note the highlighted best parameter settings for the core region (CR), melt pool region (MR) and incandescent region (IR), obtained by solving (4.13).

Effect of changing r_S and β

The external boundary thickness $r_S = 1, 2, ..., 15$, from (4.7) and (4.10), and factor $\beta = 1, 1.5, ..., 5$ were varied. As shown in Figure 4.9(b), the Core and Melt pool region detectors offer better TPRs values for $r_S \leq 7$ than for $r_S > 7$. On the other hand, the Incandescent region detector offered better TPRs values for $r_S \geq 12$.

Similarly, Figure 4.9(c) illustrates the effect of changing β from (4.9). Having a lower β value allows for fewer boundary pixels to grow a region. For the Core region, changing β was insignificant, most likely due to the initial estimate of the detector being close to the target value. In contrast, the Melt pool and Incandescent regions benefited from $\beta = 2$ and 4.6, respectively, offering an adequate increase in the sizes of the predicted regions.

Thus, r_S controlled the number of candidate boundary pixels to be evaluated, whereas β controlling the adding of boundary pixels.

Effect of changing α and the maximum number of iterations K

Parameters $0.9 \leq \alpha \leq 0.99$ and K both influence the stopping criterion of (4.12). Figures 4.9(d) and (e) demonstrate the TPRs when varying α and K, respectively. From (4.12), a lower value of α allows boundary pixels of lower energy to be added to the existing region over iterations. As shown in Figure 4.9(d), a lower value of α is selected for the Incandescent region than for Core or Melt pool. From Figure 4.9(e), it is clear that the performance of the Core region is fixed across all iterations, thus $K = 1$ iteration is selected to limit computational cost, whereas for Melt pool and Incandescent regions, using two and three iterations, respectively, was sufficient to balance between computational cost and detector performance. [5]

4.5.3 Qualitative results for vision-based feature detection

Figure 4.10 shows sample qualitative results for the proposed region detection scheme on test sequences recorded at five different power levels; additional qualitative results are available at [4].

In general, we note that at higher power levels there is a greater number of ejecta that may interfere with target regions, so the task of detecting the regions of interest becomes more challenging. Our proposed scheme is able to detect the three target regions very well

---

[5] This section is reflective of written contributions from Dr. Mohamed Naiel

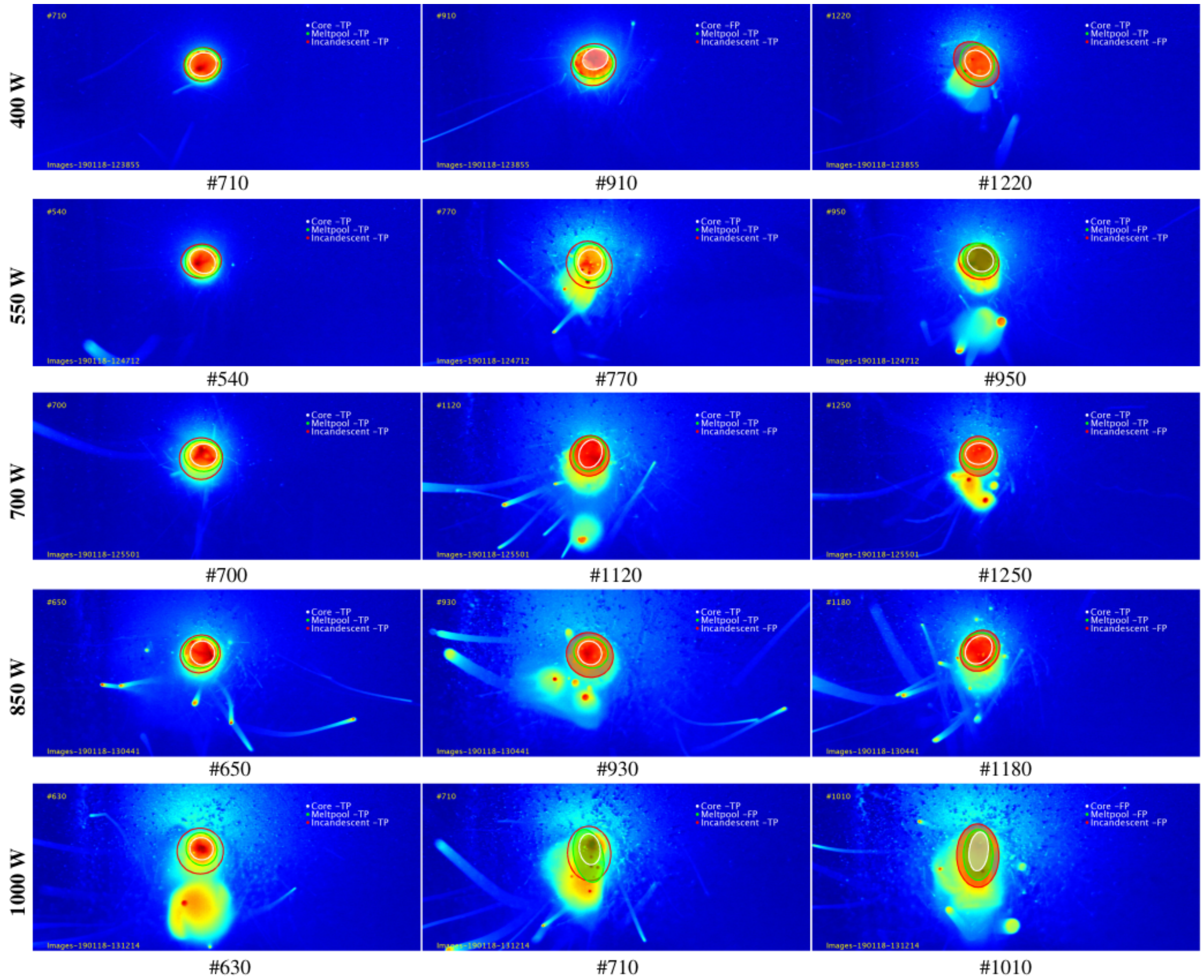

Figure 4.10: Sample qualitative results for the proposed scheme on the test dataset, where white, green and red ellipses denote core, melt pool and incandescent regions, respectively, TP and FP represent true positive and false positive detections, respectively. The camera is positioned in the lead view along the deposition track shown in Figure 4.4. It can be observed that the proposed scheme is able to reduce the effect of nearby bright regions in detecting the target regions at higher power levels.

at lower power levels, and despite the occlusion and brighter illumination conditions at higher power levels, the proposed scheme remains stable. For example, although frames number #770, #1250, #930, #710 at 550 W, 700 W, 850 W and 1000 W, respectively, include false positive detections, the proposed scheme performs well in following the target regions. Further, the proposed region growing scheme reduces the effect of nearby anomalous regions, as may be seen in frame #630 at 1000 W.

4.5.4 Quantitative results for vision-based feature detection

In order to evaluate the performance of the proposed detection scheme, ten annotated test sequences were captured at five different power levels. To study the effect of using the proposed region growing scheme on the detection performance, the detection scheme is evaluated *with* and *without* region growing, such that without region growing means that only the region initialization and stabilization techniques (Section 4.3.2) are used. Similar to the experiments in Section 4.5.2, a minimum overlap ratio [107] of 0.70 is used to test whether a detection result is a true or false positive.

Table 4.2 shows the true positive rate (TPR) and false detection rate (FDR) of detecting the core, melt pool and incandescent regions using the proposed detection scheme with and without region growing. The overall conclusions from the table are quite clear: there is a substantial improvement in performance associated with the region-growing method for all three regions, that all three regions are detected similarly well, and that performance is improved at reduced power levels.

The superiority of the proposed method is based on its robustness in the context of two challenging conditions. First, the robustness against illumination variations in the environment. The camera constantly adapts to the broad range of luminance in the FOV, which can result in spatial and temporal inhomogeneities of illumination, even with constant process parameters and melt pool temperature. Second, the robustness against saturation in the FOV as a function of variable exposure time settings [378, 325]. The robustness of the algorithm with region growing can be observed in Table 4.2, where the TPR is kept above 90% in all parameter settings. On the other hand, a simple thresholding algorithm (without region growing) cannot maintain its performance in detecting the incandescent region and the TPR drops to 55.78%. Since the incandescent region plays an important role, as it is directly related to the deposition cooling rate as well as to the microstructure of the final part [111]. Thus, correctly detecting this region is crucial for the process, a challenge which the proposed method is able to tackle successfully.

Similarly, Figure 4.11 shows the evaluation of the proposed detection scheme *with* and *without* region growing, in terms of the average TPR and the average speed[6] in frames per second. For the core region (CR) the region growing is of limited additional value, otherwise for the other regions the proposed region growing scheme offers higher TPR values but at the expense of twice the computing time, compared to *without* region growing. Thus, for detecting medium and large regions of interest further away from the center of the laser beam, the recommended detection scheme would be having detection *with* region growing, as it offers much higher detection accuracy, while for smaller regions, detection *without* region growing is expected to provide adequate results. [7]

Table 4.2: TPR and FDR at five different power levels for the core region (CR), melt pool region (MR) and incandescent region (IR) based on the test datasets, where RG refers to the proposed region growing technique.

Region	Power (W)	*Without* RG		*With* RG	
		TPR	FDR	TPR	FDR
CR	400	96.65%	3.35%	**97.29%**	**2.71%**
	550	96.85%	3.15%	**97.63%**	**2.37%**
	700	93.75%	6.25%	**94.53%**	**5.47%**
	850	**98.44%**	**1.56%**	**98.44%**	**1.56%**
	1000	93.05%	6.95%	**94.59%**	**5.41%**
MR	400	**100.00%**	**0.00%**	98.64%	1.36%
	550	96.85%	3.15%	**97.63%**	**2.37%**
	700	89.84%	10.16%	**93.75%**	**6.25%**
	850	92.19%	7.81%	**92.97%**	**7.03%**
	1000	70.61%	29.39%	**90.72%**	**9.28%**
IR	400	70.33%	29.67%	**98.57%**	**1.43%**
	550	86.63%	13.37%	**96.06%**	**3.94%**
	700	82.81%	17.19%	**93.75%**	**6.25%**
	850	83.59%	16.41%	**92.97%**	**7.03%**
	1000	55.78%	44.22%	**90.71%**	**9.29%**

Note: boldface denotes the best method for each region and power level.

---

[6] Using a modern computer of 2.8GHz CPU and 15.9G RAM.

[7] This section is mainly written by Dr. Mohamed Naiel

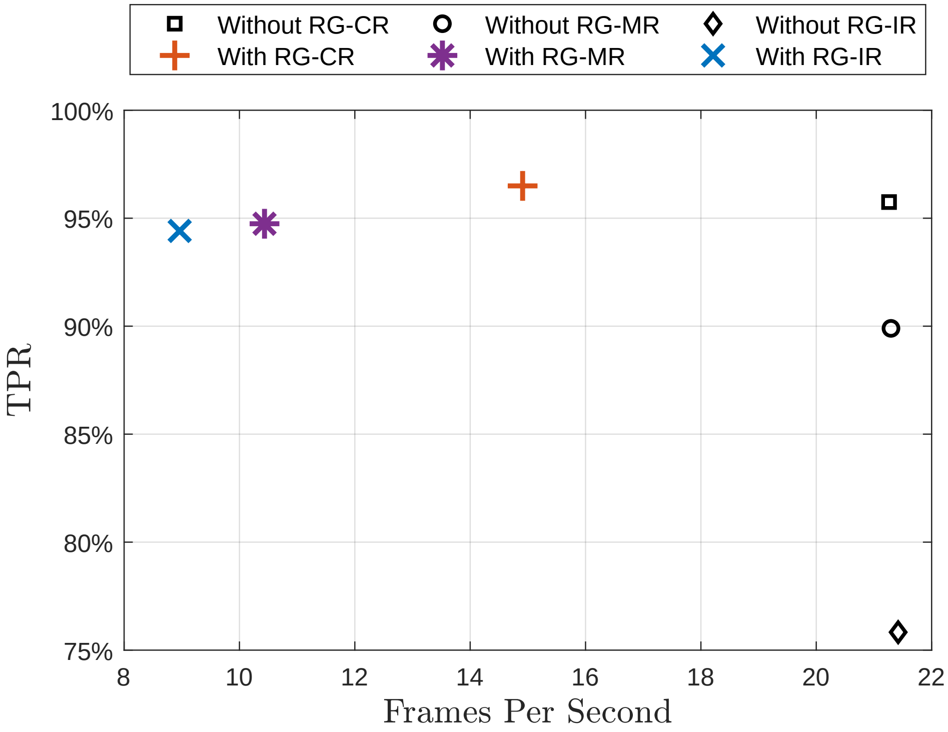

Figure 4.11: True positive rate (TPR) versus detection speed (frames per second) for detectors *with* and *without* region growing. The detectors *with* region growing are slower, but clearly offer higher TPRs than detection *without* region growing.

4.5.5 Process quality assessment using vision and profilometry datasets

Process quality assessment is performed by comparing the extracted region from the vision data against the deposition dimensions measured with the laser profilometer. For this comparison, the melt pool region and deposition width are chosen from the vision data and laser profilometer data, respectively, with results shown in Figure 4.12(a). The deposition width is in the range of 1.464 mm ± 0.204 mm at 400 W, and 2.152 mm ± 0.256 mm at 1000 W. The minimum standard deviation in deposition width occurred in the range of 550-850 W, which is attributed to the process stability in conduction melting mode. At low power (400 W) and high power (1000 W) deposition discontinuities occurred due to under-melting and keyhole melting, resulting in high variability of the width profile. The maximum divergence between vision and profilometry datasets can also be observed at 400 W and 1000 W. The width of the melt pool region extracted from the detection algorithm ranged from 113.0 ± 2.4 pixels at 400 W to 110.8 ± 3.7 pixels at 1000 W.

The absolute calibration from pixels to mm was not performed in this study. As such, the deposition width and melt pool width were normalized by their average over each laser power range. The normalized comparison can be seen in Figure 4.12(b). There are similar increasing trends from 550 W to 850 W. At 400 W, the normalized deposition width is lower when compared to melt pool width, and the HDR camera can still detect the bright region under the laser; however, the power level is not high enough to have a continuous material deposition. At 1000 W, the normalized deposition width is higher than the normalized melt pool width. In keyhole melting mode, the width of the melt pool decreases as the melt pool becomes deeper [192]. In this mode, the width of the deposition continues to increase, as the overall melt pool length is higher, thus capturing more powder material per unit area; this phenomenon was not analyzed in depth using the vision data.

The width of the melt pool region and the deposition width are also compared along the whole deposition line. The conversion from pixels to mm is done based on the averages of both datasets. The objective is to observe the similarities in the trends of both datasets, one of which is shown in Figure 4.13 at each power level. Periodic cyclic pattern was not found in this data set; however, the average x-correlation between the profilometry and vision results is found as $\rho_{avg} = 0.391 \pm 0.069$, with a highest x-correlation at laser power 850 W of value $\rho = 0.546$. Similar trends and discrepancies can also be seen in the literature [339], where optical profilometry results are compared against the data collected by an off-axis vision detector. The authors relate the discrepancies between the two datasets with black body or plasma-plume emissions, which can be potentially overcome using an improved illumination source on the melt pool.

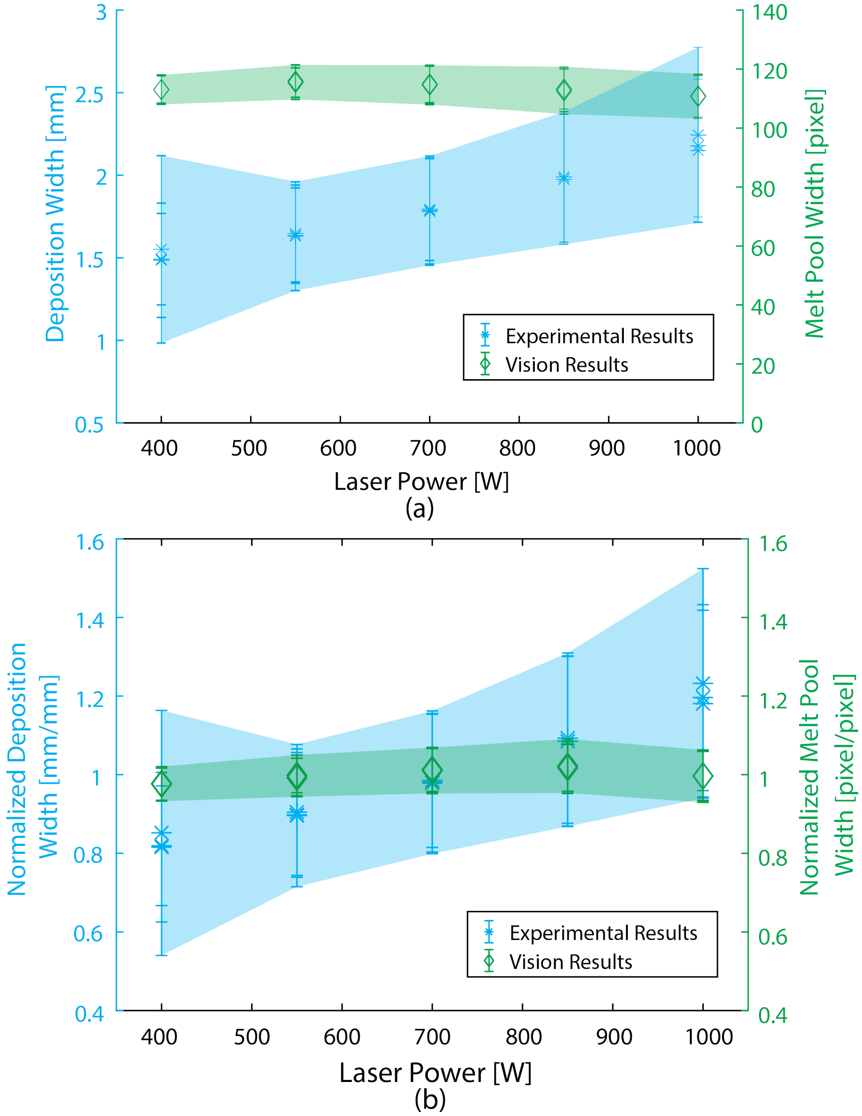

Figure 4.12: Comparison of (a) the melt pool width extracted from the vision data and deposition width measured with the laser profilometer, (b) the normalized melt pool width and the normalized deposition width.

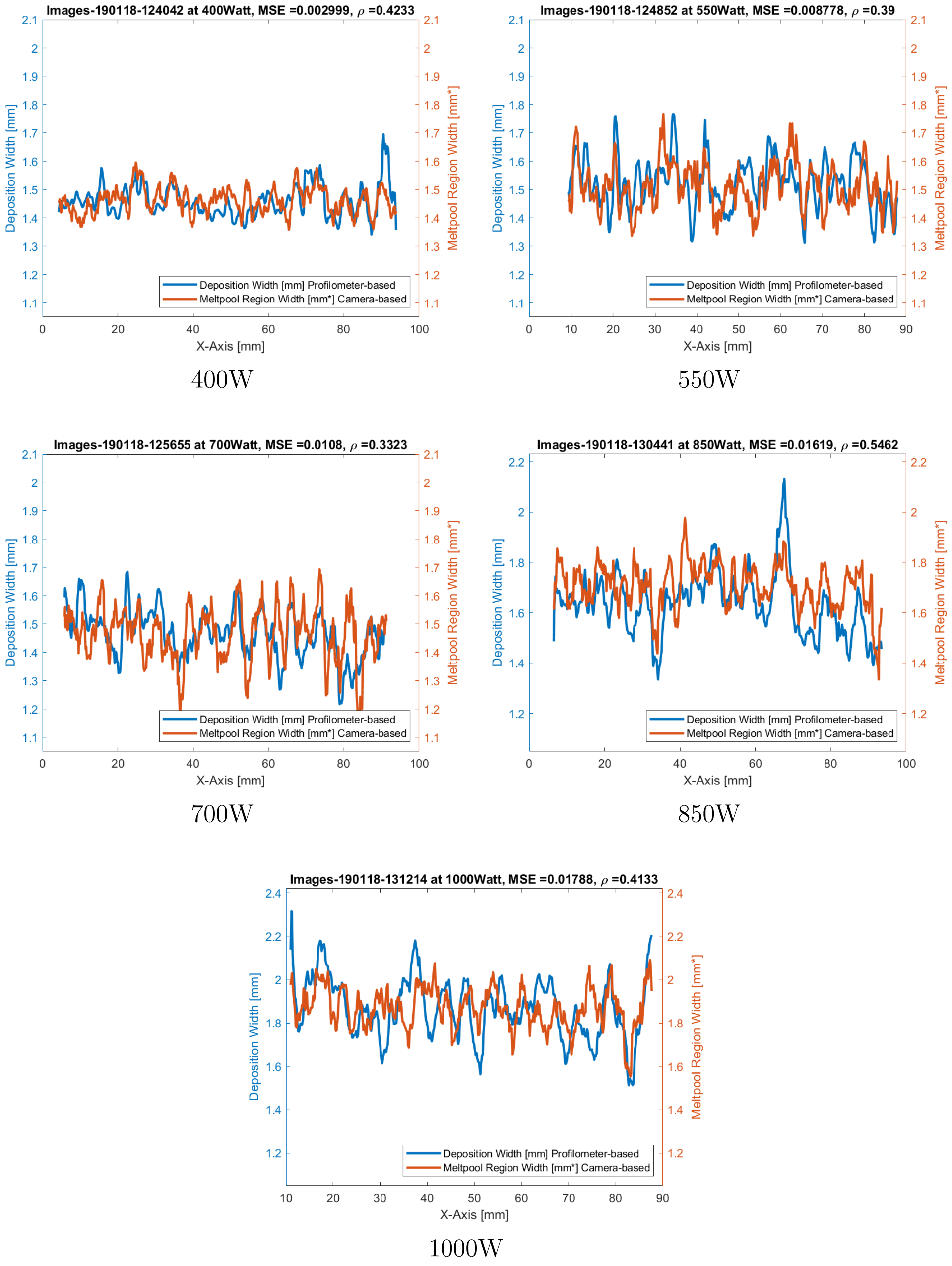

400W

550W

700W

850W

1000W

Figure 4.13: Sample results of registering the predicted deposition width with the melt pool width at five different power levels, where mm* denotes the unit length after scaling the melt pool width obtained from the camera, as explained in Section 4.4.3.

Although there are many challenges to tackle by registering two different datasets (vision and profilometry) due to sampling rates, uncertainties in data alignment, the observed correlations are promising. This study focuses on adaptive feature identification from image-based data, and Figure 4.13 does not aim to show full alignment between the laser profilometry data and the extracted melt pool features. This work illustrates one application of feature exaction, showcasing the potential of using vision-based data in process control as a feedback. As future work, the calibration from pixels to mm is proposed to fully leverage the potential of these algorithms for in-line feature detection.

4.6 Conclusions

In this study, a method is presented for detecting predefined target regions in the laser-material interaction zone by using a low-cost HDR vision detector.

1. The proposed framework is based on applying an adaptive image thresholding and a region growing technique with the use of an energy convergence criterion. The parameters used in this framework can be automatically obtained by solving an optimization problem using only a limited number of annotated frames.

2. In order to quantify the reliability of the proposed region detection technique, a registration scheme to align the measurements obtained from the vision sensor with that obtained by a high sampling rate laser profilometer is introduced.

3. Extensive experiments on sequences captured under five different power levels have shown that the proposed scheme has the ability to robustly detect the target regions. In this work, the True Positive Detection rate was significantly above 90%, while the False Detection Rate was less than 10%.

4. The proposed framework represents a significant improvement over basic thresholding without region growing. It was observed that the proposed method maintains its robustness with a true positive rate of higher than 90% for detecting all regions at all laser power levels. On the other hand, basic thresholding shows poor performance, especially in detecting instability-prone cases such as incandescent regions and melt pool regions at high laser power levels, with a significant drop in the true positive detection rate to 55.78%.

5. The aligned vision and profilometer data follow similar global and local trends, which is promising, however a more careful future investigation is needed using a precalibrated experimental setup in order to achieve real-time process monitoring as a way of controlling deposition geometry.

Chapter 5

Process performance evaluation and classification via in-situ melt pool monitoring in directed energy deposition

5.1 Preface

Metal additive manufacturing (AM) processes have transitioned from rapid prototyping applications to industrial adoption owing to their flexibility in product design, tooling, and process planning. Directed energy deposition (DED) is one of the most commonly used metal AM processes capable of producing large, high density parts, with a controlled microstructure. However, there are still ongoing challenges in maintaining a high level of reliability and repeatability when compared to conventional manufacturing processes. There is a need to define, identify and maintain regions of process stability in DED. In this study, a high-dynamic range camera and a physics-based model are used to monitor the melt pool, obtain process signatures, and predict deposition stability characteristics. The research efforts are focused on generating process maps to identify unstable process zones, with a reference to process physics, process signatures, and process outcomes using analytical modeling, in-situ melt pool monitoring, and ex-situ characterization, respectively. The goal is to classify the process signatures in pre-defined process zones (under-melt, conduction, keyhole, balling) to avoid instabilities, defects and anomalies using a low-cost high-dynamic range camera and kNN classifier, which has achieved 13% error rate. With this approach, decisions can be made to perform corrective actions (e.g. machining, re-manufacturing) or to scrap the manufactured part without ex-situ characterization.

5.2 Introduction

Laser directed energy deposition (DED) is a metal additive manufacturing (AM) process, where metal powder is guided through a nozzle by gas flow onto a substrate and fused by exposure to a laser beam. The relative motion between the substrate and the nozzle under such laser exposure results in deposition geometries [119, 356]. Parts can be manufactured in a layer-by-layer manner based on such complex toolpath depositions. The industrial adoption of the DED process has accelerated in the past decade, as it enables new product design potentials when compared to conventional manufacturing processes [332]; however, DED is still not as reliable and repeatable as conventional manufacturing processes. The complex physics behind the laser-material interaction and the cyclic thermal loading due to layer-by-layer manufacturing may cause quality issues such as pore defects, residual stresses, poor dimensional fidelity, and poor mechanical properties [142, 185, 63]. The goal of this study is to propose a method to define and detect process instabilities in DED based on in-situ vision data by generating process performance maps. Such process performance maps can be used to infer when the process is drifting towards instability and thus help to achieve higher accuracy, repeatability and reliability in DED processes.

In-situ monitoring is commonly used for detecting process signatures such as the melt pool morphology, temperature, spatter, and plasma plume characteristics [414, 214]. The purpose of deploying in-situ monitoring ranges from visualizing the process, to closed-loop process control [132]. Researchers have used in-situ radiometric sensors ranging from x-ray to infrared including visible light, depending on the process signature that needs to be captured [25, 282, 117], where each process signature could be an indicator for different process anomalies [236]. This present study focuses on vision sensors detecting visible light and the near infrared spectrum (Vis-NIR); examples of detectable process signatures via Vis-NIR include incandescence, indicative of melt pool morphology and size, and ejected particles, indicative of spatter phenomena [349]. Depending on the experimental setup configuration and sensor orientation, the melt pool height, width and length can be extracted from the Vis-NIR images [209]. The inferred melt pool morphology and ejected particles can help in determining the melting mode of the process and in identifying deposition anomalies [368]. For instance, the lack of fusion melting mode can result in deviation in deposition geometry, insufficient fusion between deposition layers and between deposition tracks within a layer, and irregular shaped porosity [189]. On the other hand, the keyhole melting mode can introduce inconsistencies in deposition geometry and spherical porosity [109, 197]. Although the conduction mode is a more stable melting mode for DED, stochastic defects can still occur due to the nature of the process.

Detection of deposition quality and discernment of process instability remain an important topic to address for DED, in order to increase process reliability, repeatability, productivity, and cost efficiency [306]. Error detection can help to guide error prevention by enabling the selection of appropriate process parameters to avoid unstable process zones, specifically in critical portions of the part such as sharp corners, thin cross-sections, and overhangs. Such error prevention strategies rely on process maps describing the relationship between process parameters and the likely outcome in product qualities, where the process maps can be developed using analytical or empirical modeling approaches, or a combination.

Physics-based modeling is used to predict the process signatures, such as the melt pool temperature profile [157], the melt pool geometry, and the material-specific cooling and solidification rates [255], in order to estimate the deposition geometry [139], density [20], microstructure [138, 34], and mechanical properties of the final part [20]. Physics-based modeling can also be used to infer regions of expected performance towards error prediction. For instance, existing models can theoretically predict the melting mode, where thresholds between melting modes are defined experimentally for most commonly used materials [371, 93]. Predicted thermal signatures, such as the melt pool temperature and the cooling rates, can also be an indicator of process anomalies [337], where process errors can be detected if the predicted melt pool dimensions deviate too much from the linear trend in the conduction mode [185]. Such physics-based models can provide an insight into the laser-material interaction phenomena [118] and can help in defining process instabilities such as keyhole, balling and lack of fusion [66, 109]. Process outcomes indicative of defects can be correlated to process instabilities to establish a cause-and-effect relationship [412], described as a process map.

A process map is a representation of the process outcome, either qualitative or quantitative, based on a range of input process parameters. Process maps are typically used in laser-material interaction AM processes, such as laser powder bed fusion (LPBF) and DED, to identify process windows with specific process quality outcomes or performance behaviours [380, 379, 44, 436]. They are usually visualized as laser power vs. scan speed and a third metric can be placed on the process maps to identify a trend or relationship between the third metric and the process parameters [172]. The third metric can be a process anomaly, defect or a mechanical property [16]. Process maps can be used to visualize anomalies experimentally based on in-situ process signatures or ex-situ testing [43]. Experimental data is used for mapping process zones based on melt pool geometric dimensions (length, height, width and depth), with geometric relationships between these dimensions indicating a sign of the laser-material interaction transitioning between two melting modes [69]. For instance, if the ratio of width over depth is below a certain ratio (identified empirically) the process falls into the keyhole melting mode in LPBF [336]. Such thresholds are now emerging in the literature for DED, and are empirically-established based on a large set of experiments [406, 226]. The defects as well as the mechanical properties are also investigated and captured in process maps based on a given process parameter range [186, 144]. For instance, for LPBF it is observed that a better performance in terms of density is achievable in conduction melting mode [117]. However, increasing the laser power and scan speed linearly in order to increase the productivity can cause balling [147, 213], from which fluctuations in the deposition profile [203] and poor bonding between the first layer and substrate or between consecutive layers can occur [376]. There are few studies using modeling predictions [436] to construct process maps which is considered to be a white-box approach; however the grey box approach of modeling and experimentally-informed datasets can better capture those process phenomena which are difficult to model analytically [119]. For instance, the melting modes can be estimated using physics-based modeling to define the transition between melting modes, with experimental data used to calibrate uncertainties in either model parameters or transition boundaries [153, 194]. Overall, generating process maps can help in process parameter development and optimization by bringing many approaches together such as process modeling and monitoring. There is a scarcity of process map studies in the literature that are focused on relating sensor data with process quality metrics for the DED process. Thus, there is an ongoing need to generate process performance maps for DED processes to help with process parameter optimization and process diagnostics [222].

The focus of this work is to leverage modeling, in-process sensing, and characterization of data towards constructing process maps for DED. This will be accomplished by pursuing three objectives. Our first objective is to map process outcomes (simulated and experimentally informed) and process signatures (Vis-NIR in-situ data) against ranges of process parameter inputs, such as deposition velocity and laser power. In this context, to simulate process outcomes, a previously developed physics-based model is used, which is based on energy, mass and momentum equations for the DED process and can predict the melt pool temperature and morphology [106], as well as deposition geometry. To experimentally measure process outcomes, the surface confocal microscopy datasets are utilized to quantify the geometric quality of the depositions. For in-situ process signature detection, a high dynamic range (HDR) camera is used to monitor the melt pool, to detect the material ejecta, and to extract pre-defined regions within the incandescent zone using image processing algorithms [264]. The second objective is to identify trends in the process maps and define so-called out-of-bounds behaviour, which are labeled as instability regions, based on the vision data with reference to geometric deposition quality and modeling predictors. The third objective is to demonstrate that a classifier can be constructed to detect different types of process instabilities based on the bulk statistics of the vision data alone. The performance of such an in-situ vision detection method, in conjunction with a pre-trained basic classifier derived from a process performance map, will be demonstrated, illustrating the potential for a simple yet powerful quality assurance method for DED processes.

5.3 Methodology and experiments

5.3.1 Methods overview

Figure 5.1 details the proposed process map workflow. The experimental plan spans a combination of laser power and scan speeds covering lack of fusion to keyhole melting mode phenomena in DED. In this study, three data sources are considered to be representative for process mapping:

1. Theoretical process physics inferred through modeling,
2. Process signatures detected via imaging, and
3. Process outcomes quantified via surface confocal microscopy.

White-box modeling [106] is used to predict process outcomes such as melt pool temperature and deposition dimensions (width and height), and to predict normalized enthalpy contours (Section 5.3.3.3) [153]. In order to detect process signatures, the laser-material interaction zone is monitored by an in-situ vision detector and then a feature detection algorithm is used to extract pre-selected regions of interests (ROIs) representative of the melt pool region and of the particle ejections captured in the images [264] (Section 5.3.3.2). After the process, the process outcomes are evaluated by scanning the depositions via confocal microscopy and the resulting height maps are used to extract deposition dimensions (Section 5.3.3.1).

These three data sources are used to create the process maps and to observe which data source is sensitive to expected out-of-bounds zones in Figure 5.1, corresponding to (I) lack of fusion, (II) balling, and (III) keyhole effects. Correlations between the theoretical laser-material interaction physics (i), process signatures (ii), and process outcomes (iii) are

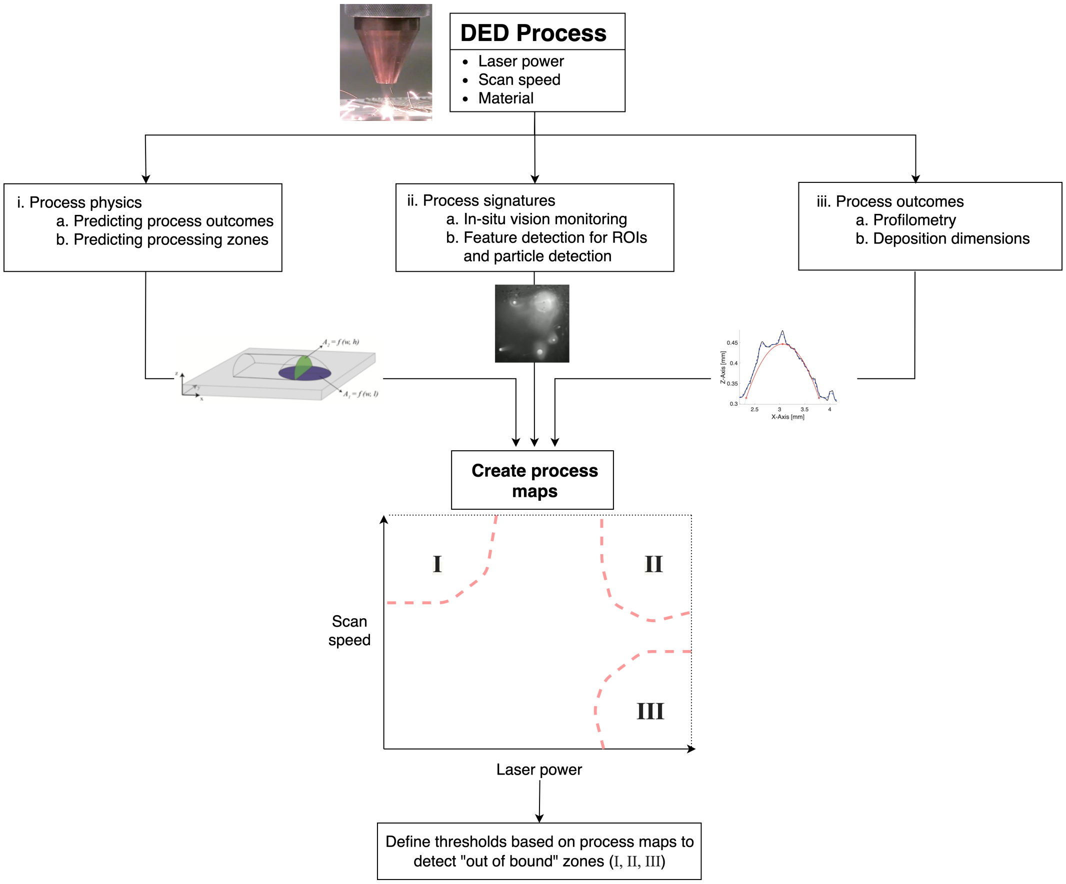

Figure 5.1: Workflow of this study starting with the selection of process parameters and material, and creating data sources to represent (i) process physics, (ii) process signatures, and (iii) process outcomes, which are used to create the process maps. In the sample map (I), (II) and (III) refer to out-of bounds zones: *lack of fusion*, *balling*, and *keyhole* effects, respectively.

explored (Section 5.3.4.1 and 5.3.4.2). Such correlations can be used to infer process map thresholds for process outcomes (confocal microscopy data) and process signatures (vision data), respectively. Quantitative thresholds are defined based on the process maps using a classification method and validated using experimental data. Such thresholds can be deployed in two important aspects of industrialization of DED: in the forward-approach, the thresholds can be used to avoid combinations of process parameters which could result in out-of-bound zones; in the inverse-approach, the thresholds can be used in conjunction with in-situ process signatures and modeling to identify whether the process has become unstable by reaching out-of-bounds performance.

Out-of-bounds performance or process anomalies can be defined in many ways, depending on the physical reason behind the observed phenomena. In DED, the most common anomalies are pores, cracks and dimensional inconsistencies. These anomalies can be caused by three physics phenomena occurring during laser-material interaction. One class of phenomena is observed when there is insufficient energy input, resulting in *lack of fusion* (shown as region I in Figure 5.1). This phenomenon is typically observed when the scan speed is too high and the laser power is too low and can result in dimensional discontinuities in the deposition profile, poor bonding between consecutive layers and irregular shaped pores. Lack of fusion can occur due to poor process path planning and process parameter selection. The other physics phenomenon is caused by excessive energy input, where the scan speed is low but the laser power is high. This is referred as *keyhole melting mode* (shown as region III in Figure 5.1). Due to the high energy input, the material can reach the boiling temperature where an instability occurs due to the recoil pressure controlling the depth of the melt pool and thermo-capillary convection becoming the ascendant heat transfer mode in the melt pool [394, 83, 287]. Avoiding keyhole melting mode is more challenging compared to lack of fusion, as it can occur while the scan speed is decelerating due to a sharp corner or high curvature, or can be caused by thermal accumulation due to adjacent depositions or previously deposited layers. The last physical phenomenon occurs at high scan speed and high laser power resulting in Rayleigh plateau instability (shown as region II in Figure 5.1) [385, 407] . As an anomaly in the deposition, *balling* or *humping* defects can be observed, which result in dimensional inconsistency and porosity within the deposition; these outcomes can occur if manufacturers try to increase the material deposition rate and the overall process speed to improve the economics of the process.

The process qualities (confocal microscopy data) and process signatures (Vis-NIR data) are mapped against process parameter inputs to observe whether any out-of-bounds outcomes (anomalies) are observed in the three regions identified above. Correlations between the process qualities and process signatures will be inferred to see whether process signa-

Table 5.1: Process parameters; check marks show the process parameter combinations for which experiments were performed.

	Laser Power [W]								
Scan Speed [mm/s]	400	475	550	625	700	775	850	925	1000
5	✓		✓		✓		✓		✓
8		✓		✓		✓		✓	
11	✓		✓		✓		✓		✓
14		✓		✓		✓		✓	
17	✓		✓		✓		✓		✓
20		✓		✓		✓		✓	

tures alone could be used to detect anomalies. A basic classifier is developed to be deployed in conjunction with process signature data for in-situ process quality monitoring.

5.3.2 Experimental setup

A robotic DED system (DM3D - DMD IC106, Auburn Hills, MI, US) is used, where the laser beam and the powder delivery are located co-axially. In this study, single line depositions are performed at different laser power and scan speed levels using stainless steel (SS316L). The powder particles are spherical with a size distribution of D10 at 73.06 μm, D50 at 106.26 μm, and D90 at 141.52 μm.

The powder delivery rate is kept constant at 7.5 g/min guided with Ar and He gasses. The laser source is a fiber laser (Trumpf - TruDisk2000, Ditzingen, Germany) with a wavelength of 1030 nm and a beam spot diameter of 1.2 mm. In this study, the laser power is varied from 400 to 1000 W in increments of 75 W and the scan speed is varied from 5 to 20 mm/s in increments of 3 mm/s. Every other laser power and scan speed are used together as a process parameter set in each experiment resulting in 27 different experiments at different laser power and scan speed levels. The experimented process parameter sets are shown in Table 5.1 and each parameter set has 3 replicates such that there are 81 experiments performed in total.

Melt pool monitoring is performed using a mono-chrome XVC-1000 high-dynamic range (HDR) weld camera (Xiris Automation, Burlington, ON) with a dimmable illumination source to minimize the contrast between the very bright laser-material interaction region and the surroundings. Camera and illumination are mounted on a bracket attached to the end effector monitoring off-axis, with visual details on the detection setup described elsewhere [264]. The camera is located in the leading view, capturing the width and the length of the melt pool for all experiments. A 75 mm lens is used with a 40 mm spacer in order to view the melt pool as close as possible. A green filter is used to detect the wavelengths between approximately 470 and 600 nm. Additionally, a UV filter is used to eliminate the reflections in the region of interest. The experiments are performed at 5 ms of exposure time at 7 frames per second frame rate and the automatic gain control is enabled.

5.3.3 Feature extraction and simulation

5.3.3.1 Deposition geometry measurements extracted from confocal microscopy data

The depositions are scanned using confocal laser microscope (VK-X250K, Keyence) to investigate the deposition profiles along the whole length using a 2.5X magnification lens. The spatial resolution in the x-y direction is 11.4 μm and the resolution in the z direction is 0.1 μm. The 3D deposition surface topography obtained by the confocal microscope are used to extract the 2D profile of the deposition. The 3D deposition surface is represented as a height map in a matrix, where every row is a 2D deposition profile. The width and the height of the depositions are calculated for each row. The 2D profile is filtered using a moving-average filter with a window size of 10. The raw and filtered data can be seen as black solid lines and blue dashed lines, respectively, in Figure 5.2. The first derivative of the 2D profile is calculated in the discrete domain to locate the inclination by obtaining the global maximum and minimum in the first derivative of the 2D profile. The locations of global maximum and minimum are interpolated using the inclination at these points. The deposition width boundaries are found by locating the intersection between the interpolated line and the base, and are shown as red markers in Figure 5.2. Once the points at width boundaries are determined, the height of the deposition is defined as the height value at the mid-point between the border points. The mid-point is then aligned with the point on the deposition profile, where the first derivative of the deposition changes sign (positive to negative). More details regarding this methodology are given in the authors' previous study [264]. The green parabola (simulated profile) will be used to evaluate the deviation between the simulation and the experimental profile, as explained in the caption of Figure 5.2a. The red parabola (experimental idealized profile) will be used to evaluate the occurrence of satellites along the deposition path, as explained in the caption of Figure 5.2b.

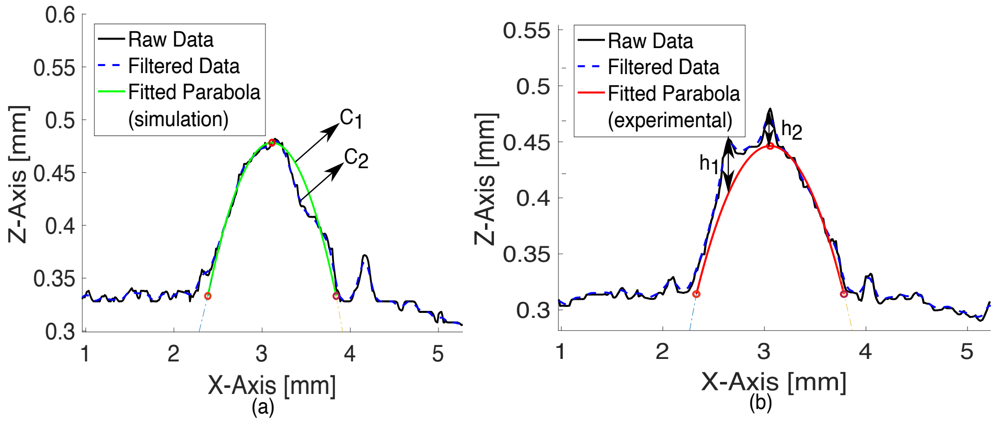

Figure 5.2: The plots show one cross-section of the raw, filtered data from the confocal microscope. The green and red curves are fitted parabolas based on predicted deposition geometry (simulation) and extracted deposition geometry via confocal microscopy (experimental) respectively. Plot (a) shows the area overlap between curve C_1 and C_2, which is used to define the anomaly-based on area overlap estimation; Plot (b) shows how the satellites are extracted using confocal microscopy data as local peaks larger than the D50 of the powder with respect to the fitted parabola (experimental) in the experimental plot.

5.3.3.2 Melt pool region and material ejecta detection extracted from vision sensor data

Each of the acquired HDR images (setup described in Section 5.3.2) is processed as shown in Figure 5.3 in order to detect the melt pool and incandescent regions, as well as to estimate the number of particle ejecta; the methodology for melt pool and incandescent regions feature extraction is described in detail elsewhere [264]. The process of detection is summarized as follows:

1. Given the input image I_t at time t, an adaptive thresholding technique [264] that suppresses pixels with values less than the pth-percentile of the input HDR image is applied to identify candidate target pixel mask M_t, which is filled[1] to obtain mask $\hat{M}_t$. From $\hat{M}_t$ the connected components $c_1, \ldots, c_n$ are found, representing the candidate

---

[1] The `imfill` function of MATLAB is used https://www.mathworks.com/help/images/ref/imfill.html.

target regions. We associate a fitness f_ℓ with each component c_ℓ,

$$f_\ell = \sum_{i,j} I_t(i,j) c_\ell(i,j) \tilde{M}_{t_0}(i,j), \ell = 1, 2, ..., n \tag{5.1}$$

where $\tilde{M}_{t_0}$ is a prior mask used to stabilize the region of interest by suppressing ejected particles. We then select the component with the highest fitness as the seed mask $\tilde{M}_t^0$ for the melt pool and incandescent regions:

$$\tilde{M}_t^0 = c_{\hat{\ell}} \qquad \text{where} \qquad \hat{\ell} = \underset{\ell}{\text{argmax}} \ f_\ell \tag{5.2}$$

2. In order to detect the melt pool and incandescent regions, an iterative region growing technique [264] is used as

   $$\tilde{M}_t^k = \Phi(\tilde{M}_t^{k-1}, r_S, \beta, \alpha) \tag{5.3}$$

   after k iterations of region growing operator $\Phi(\cdot)$. The region growing [264] is a function of structure element radius r_S, maximum change β in fitness associated with changes in boundary pixels, and iteration stopping parameter α.

   The region growing stops if any of the three following conditions are met:

   $$\frac{\hat{F}_t(k)}{\max(\hat{F}_t)} < \alpha \qquad \sum_{i,j} \hat{B}_t^k(i,j) = 0 \qquad k \geq K, \tag{5.4}$$

   where $\hat{F}_t$ is the average boundary fitness, $\hat{B}_t^k$ is a mask of boundary pixels at the kth iteration, and K is the maximum permitted number of iterations.

   Our chosen parameters are a pth percentile of 99.20%, radius $r_S = 14$ pixels, and factors $\beta = 4.6$, $\alpha = 0.94$, and maximum iteration count $K = 3$. Figure 5.3 demonstrates sample output from the region growing process that results in the final mask of the incandescent region $\tilde{M}_t \equiv \tilde{M}_t^K$.

3. Unlike [264], here the fitness of each connected component is also used to detect material ejecta:

   $$c_\ell \quad \text{such that} \quad \bar{f}_\ell > f_{\min} \quad \text{and} \quad a_\ell > a_{\min} \tag{5.5}$$

   where $\bar{f}_\ell = \sum_{i,j} I(i,j) c_\ell(i,j)$ and $a_\ell = \sum_{i,j} c_\ell(i,j)$ are the fitness and area of the ℓth connected component. Thresholds $f_{\min}$ and $a_{\min}$ are selected empirically to identify the ejected particles from noisy background elements. The count of ejected particles n_p is therefore equal to the number of connected components that satisfy (5.5), illustrated in Figure 5.3. [2]

---

[2] This section is reflective of written contributions from Dr. Mohamed Naiel

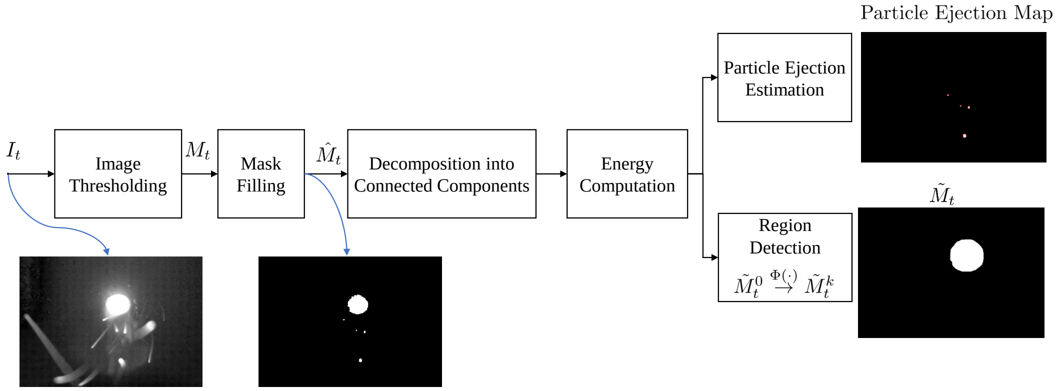

Figure 5.3: Illustration of melt pool and incandescent region detection, as well as particle ejection estimation. The connected components c_ℓ of the n_p detected particles lead to a final mask $\tilde{M}_t$. Further details are listed in Section 5.3.3.2.

5.3.3.3 Brief overview of physics-based modeling

Physics-based white-box models are developed to predict the thermal history, the melt pool temperature, the melt pool morphology, and the deposition geometry based on given process parameters and material system. The thermal history and melt pool temperature models are coupled with the geometry model. The thermal history model employs a voxel-based approach as described in prior work [106], where the deposition sequence is discretized. Voxels are indexed by following the sequence of the toolpath trajectory. The thermal model is solved recursively in discrete time by adding one voxel at a time step. The heat transfer equation is rewritten at each time step for each voxel as neighboring voxels dynamically change.

In this model, the heat transfer equations take into account the losses through conduction and convection, and neglect the radiation heat loss. Rosenthal's moving point heat source equation is used to determine the voxel size and to predict the instantaneous temperature of the voxel immediately after the laser exposure. Once the heat transfer equations are written for the current voxel configuration, they are solved in state space form in discrete time:

$$\frac{d}{dt}[T] = (A)_{n\times n}[T]_{n\times 1} + (B)_{n\times p}[u]_{p\times 1} \tag{5.6}$$

T is the state vector indicating the current temperature value of each voxel, u is the input vector containing the laser power, ambient and substrate temperature, and A and B matrices are state transition and input matrices respectively, which represents the voxel configuration. Detailed explanations of the thermomechanical model can be found elsewhere [106].

The geometric features of the material deposition are predicted using mass and momentum balance equations assuming that the melt pool has an ellipsoid shape. The mass balance equation

$$\frac{d(\rho V(t))}{dt} = -\rho A(t)v(t) + \mu f \tag{5.7}$$

calculates the cross-section area A of the melt pool, which is a function of width and height. V is the melt pool volume, which is a function of width, height and length of the melt pool assuming that the melt pool length is constant in the model. The scan speed and material density are shown as v and ρ, respectively, and f is the material deposition rate, which is parametrized as a function of laser power and scan speed. Detailed explanations can be found in the authors' previous study [106].

The momentum balance equation

$$\frac{d(\rho V(t)v(t))}{dt} = \rho A(t)v^2 + \sum F_v \tag{5.8}$$

is used to decouple the melt pool area into width and height as the momentum balance equation defines how the material holds on to the deposition surface. F_v represents the total momentum loss due to surface tension forces. Equation (5.8) can be simplified further as a constant speed is assumed throughout the process.

Additionally, a physics-based model is used in this study to estimate the melting mode of the process by calculating the normalized enthalpy [153]

$$h^* = \frac{\Delta H}{h_s} \tag{5.9}$$

where ΔH is the specific enthalpy, which is normalized by the enthalpy at melting h_s. When the expressions for h_s and ΔH are substituted, (5.9) becomes

$$h^* = \frac{A \cdot P}{\frac{k \cdot T_m}{\alpha}\sqrt{\pi \alpha v D^3}} \tag{5.10}$$

In this equation the material properties A, α, k and T_m represent the absorptivity, thermal diffusivity, thermal conductivity and melting point, respectively. P and v are the process parameters of laser power and scan speed, and D is the laser beam diameter. The threshold for the keyhole melting mode's normalized enthalpy is empirically found to be around the value of 6 for SS316L [194].

5.3.4 Anomaly detection

5.3.4.1 Process maps with confocal microscopy and reference modeling data

The physics-based modeling and confocal microscopy datasets can be used to explore deviations between the predicted versus actual material deposition dimensions. These deviations are explored for their potential in labeling depositions as out-of-bounds anomalies. To detect the deviations, a parabola is fitted to the actual 2D deposition profile using the predicted width and height of the deposition, shown in Figure 5.2(a) as C_1, and the alignment is performed based on the mid-points of the parabola and the 2D deposition profile, at each location along the deposition track. The curve obtained by filtering the raw data is shown in dashed blue line and is labeled as C_2. The filtered confocal microscopy and fitted curve areas (a_1 and a_2, respectively) are calculated by taking the numerical integration and the overlap between the two areas:

$$a_o = \frac{|a_1 - a_2|}{a_2} \tag{5.11}$$

If the area overlap a_o is more than 0.5, then the 2D profile is tagged as an anomaly. Furthermore, the root mean square of the error in predicting the width and height is taken and presented in a process map to highlight the critical process parameter set.

From a previous study [106], it is known that the model performs best in conduction melting mode and it loses accuracy in lack of fusion and keyhole melting modes. Thus, it is expected to have more anomalies in lack of fusion and keyhole process zones. The material satellites on depositions, which are the adhered powder particles, or molten material ejecta, can be indicative of process instability; for this reason material satellites are also investigated by detecting spikes in the 2D deposition profile obtained by confocal microscopy. If the height difference between the maximum point of the detected spike and the curve fitted based on the 2D deposition profile is more than the D50 size of the powder particle, it is counted as an adhered powder particle on the deposition.

5.3.4.2 Process maps based on vision data

The in-situ Vis-NIR detector is used to monitor the melt pool in the lead view. The approximate width and length of the laser-material interaction zone can be extracted based on the incandescence in the scenery. A previously proposed algorithm [264] was deployed for extracting the width and length of pre-defined regions in the area of interest, namely the core, the melt pool and the incandescent regions. The incandescent region (IR) contains the effects of the melt pool and the plasma plume, and has been proven to be susceptible to fluctuations [106], depending on the melting mode. The area ratio between the melt pool (MP) and the incandescent (IR) regions is investigated as a signature of instability. The melt pool and incandescent regions grow with increasing energy input to the material following a linear trend; however, when the energy input enters in instability zones, the incandescent region is observed to be growing much more than the melt pool region [129, 369]. Furthermore, the particle ejections visible in the scenery are also detected and counted per frame as a process signature (Section 5.3.3.2). The area of the particle ejections is also calculated to discover whether it could be used as an indication of a process anomaly.

The deposition geometry qualities and vision-based process signature metrics are presented on process maps in Section 5.4. The goal is to observe which metric is more statistically significant in which process zone, to infer correlations between process signatures and product qualities, and to decide whether the process signatures alone can be used in detecting anomalies.

5.3.4.3 Preliminary study of classification of process zones based on in-situ vision detection

K-Nearest neighbor (kNN) classification is used to classify the process zones using the in-situ Vis-NIR data set. Eight features are used to train and test the model, including detected melt pool features by the HDR camera and the process parameters. The process parameters are laser power p, scan speed v and the corresponding normalized enthalpy h^*. The detected melt pool features are normalized average melt pool width w^{mp} and area a^{mp}, the normalized standard deviation of melt pool width Δw^{mp} and area Δa^{mp}, and the number of particle ejections at time t n_p^t. The averages and standard deviations are performed across all images obtained from three repetitions of each experimental point. The number of frames varies from 550 to 800 for each experiment, depending on the scan speed. The minimum-maximum feature scaling method is used to normalize the melt pool features. Process signatures are included in the feature vector, rather than only process parameters, to achieve a better classification performance when a different DED or material system is used. The kNN implementation from MATLAB's statistics and machine learning toolbox is used, with k is set to 3 and using Euclidean distance. The labels are predefined as *conduction*, *keyhole*, *lack of fusion* and *balling* based on the process maps using observations from process modeling and process outcomes.

Let x_i and y_i denote the ith feature vector and its corresponding class label,

$$x_i = \left[p_i, v_i, h_i^*, w_i^{mp}, a_i^{mp}, \Delta w_i^{mp}, \Delta a_i^{mp}, n_p^t\right] \tag{5.12}$$

The classification algorithm is trained and tested using the whole experimental dataset $\{x_i, y_i \mid i = 1, 2, ..., N_t\}$. The t-distributed stochastic neighbor embedding function is used to visualize this dataset, as shown in Figure 5.4. It can be seen that the *lack of fusion* and *conduction* labels could be classified very easily, with a possibility of error at the boundary of labels. The distinction between *keyhole* and *balling* labels is the most challenging as they can result in similar features. In order to train a better classifier, the experimental range could be extended in a future study, especially in the *keyhole* and *balling* process zones.

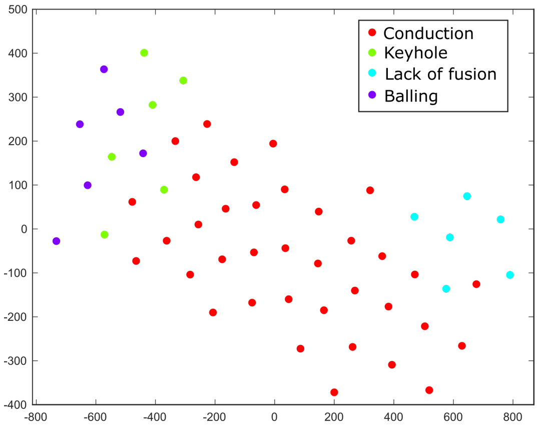

Figure 5.4: The labels conduction, keyhole, lack of fusion and balling are represented in red, green, blue and purple markers. The boundary between a lack of fusion and other labels can be observed quite distinctly. The separation between keyhole and balling process zones is the most challenging.

5.4 Results and discussions

In this section, the results obtained from the confocal microscopy, physics-based model, vision detection and the correlation between them are represented using process maps to identify the out-of-bounds behavior of the process. Every process map represented in this section has two color bars, one for normalized enthalpy on the left and one for the metric visualized on the right of each plot. The x-axis is the laser power in W and the y-axis is the scan speed in mm/s. The black dots in each plot represent the experimental data points. Linear interpolation is used for the points outside of the experimental data points to create the 2D process map surface.

5.4.1 Process maps and process anomalies based on simulation and confocal microscopy results

The depositions are scanned via a confocal microscope to measure the width and the height for each experiment. The confocal microscopy data are used in conjunction with the physics-based model predictions to develop new metrics to detect out-of-bounds process behavior. The confocal microscopy results are shown in Figure 5.5, where columns (I) and (II) show the results for deposition width and height, respectively, and rows (A), (B) and (C) represent the average, root mean square of error, and coefficient of variance (CoV) of the corresponding deposition geometric feature, respectively. These three metrics are calculated to observe not only the average behavior of the deposition width and height dimensions, but also the dynamic change within an experiment in terms of RMS and CoV. For RMS, the average of deposition height and width at each experimental point is taken as reference. However, for CoV, the standard deviation is calculated within the data of each experimental point.

The average deposition width and height show an increasing trend towards the keyhole region. A small dip is observed in both deposition width and height at a scan speed of 5 mm/s and laser power of 1000 W. This experimental point has the highest normalized enthalpy and the process is expected to be in a fully-developed keyhole mode, where the laser absorptivity is maximized due to multiple reflections in the keyhole, resulting in a narrower and deeper melt pool [81, 384], and fluctuations of the melt pool width and height.

The RMS error illustrates the difference between the average deposition dimensions and each deposition profile measured. The lack of fusion and the keyhole regions are highlighted as high values in RMS error in the process map for both deposition height and width. The height map visualizations of the depositions samples from the experiments in the lack of fusion and keyhole processing zones show the inconsistency of the deposition. Some gaps within the deposition line can be seen in the height map taken from the lack of fusion process zone. The high values of RMS in lack of fusion are attributed to the insufficient energy input required to create a stable melt pool, where discontinuities can be observed in the height map images above Figure 5.5 (B-I). The high values of the RMS in the keyhole region are representative of the excessive vaporization of the metal resulting in increased recoil pressure and melt pool instability [185], which can result in high deviations in deposition height and width shown in the height map images above Figure 5.5 (B-II).

The CoV is the ratio of standard deviation over the mean of the data. The process maps show that the highest variation in deposition height and width occurs in high scan speed and laser power regions; such extreme combinations of process parameters have been shown to result in balling [166, 434]. Due to the high speed in balling, poor bonding between layers and discontinuities can be observed. The associated examples of deposition profile height maps obtained by confocal microscopy show the variation both in width and height for the representative lack of fusion, keyhole, and balling regions.

The simulation results predicting the width and height of the deposition are compared against the average experimental results in Figure 5.6(a) and (b) as a function of the normalized enthalpy. The slight dip in both geometric features can be observed here as well and can be explained by the onset of keyhole phenomena. The previously developed physics-based model performs better in conduction melting mode compared to keyhole and lack of fusion, respectively, as the conduction mode assumptions were used to construct the model [106] and the powder catchment efficiency in lack of fusion zone drops significantly [351]. Thus, in predicting height and width compared to the experimental data, the RMS error increases in lack of fusion and keyhole melting zones, which can be seen in Figure 5.6(c) and (d). Figure 5.6(c) also illustrates that the predicted melt pool width is much more sensitive to deviations from the conduction mode region than the predicted melt pool height.

An out-of-bounds performance (or anomaly) can be defined based on the area overlap between the predicted and experimental profile, shown in Figure 5.2(a). For each scanned profile on a deposition, the area overlap in Equation (5.11) is calculated and the profile is flagged if the overlap is more than 0.5. The average number of anomalies due to this metric is plotted in Figure 5.7, which shows similar trends to Figure 5.6(c) and (d) in terms of the RMS error in predicting deposition width and height. This similarity highlights the lack of fusion and keyhole zones as the model predictions deviate from the actual values in those zones.

The definition of material satellites is provided in Section 5.3.4.2 and a representative scanned profile with satellites is shown in Figure 5.2(b). Material satellites contribute to poor surface quality and high surface roughness of depositions. The number of satellites is counted and the average is reported in Figure 5.8. The process map shows that more satellites are detected in the conduction zone, which aligns with the surface roughness literature in AM [286]. Although conduction melting mode can provide continuous stable depositions, the surface roughness can be high. The adhered particles can be seen in the height map in a form of red dots on the deposition line, taken from the conduction processing zone.

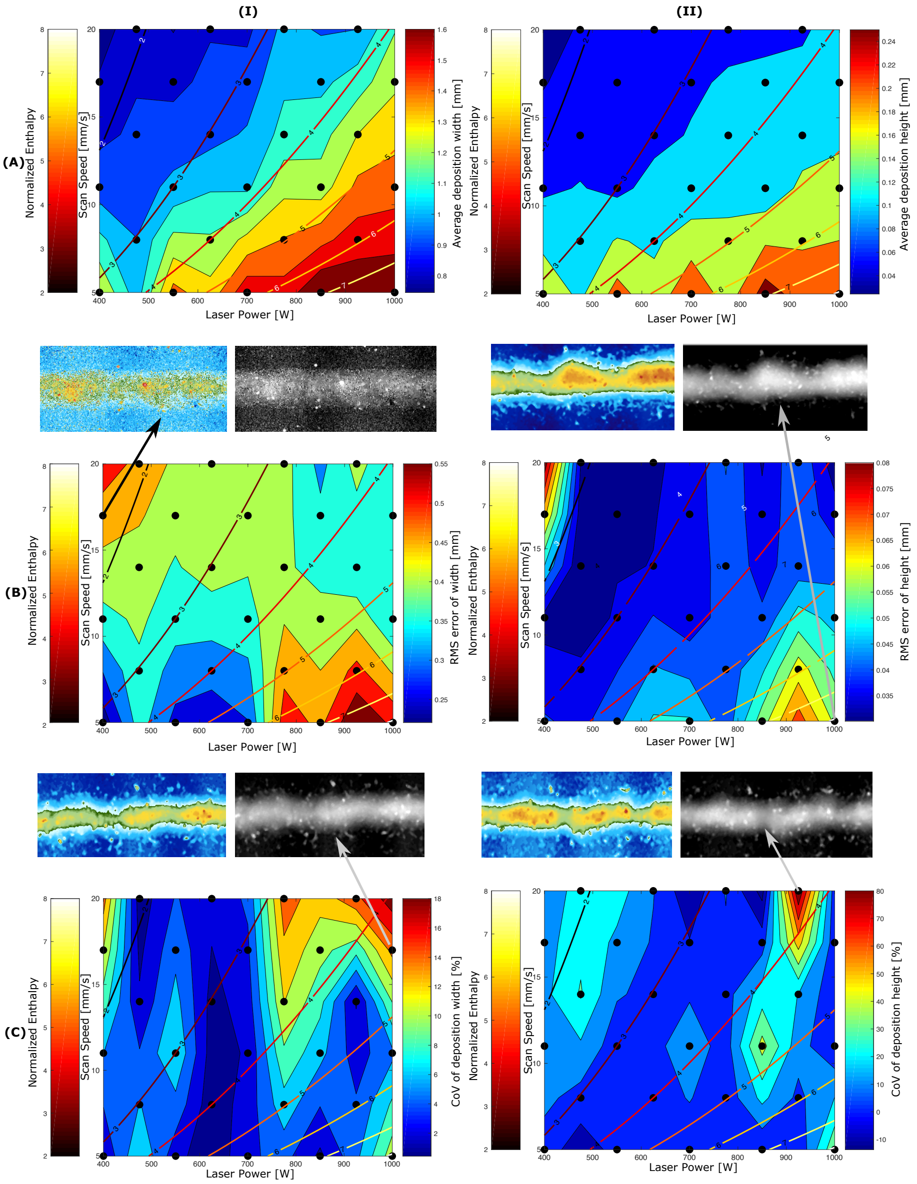

Figure 5.5: The process maps showing the confocal microscopy results of the average, root mean square of error and coefficient of variance (CoV — the ratio of standard deviation over the mean of the data) in rows (A), (B) and (C), respectively, for deposition width and height in columns (I) and (II), respectively. Sample confocal microscopy height-maps are shown in color and grayscale, representing deposition characteristics in lack of fusion, keyhole and balling regions.

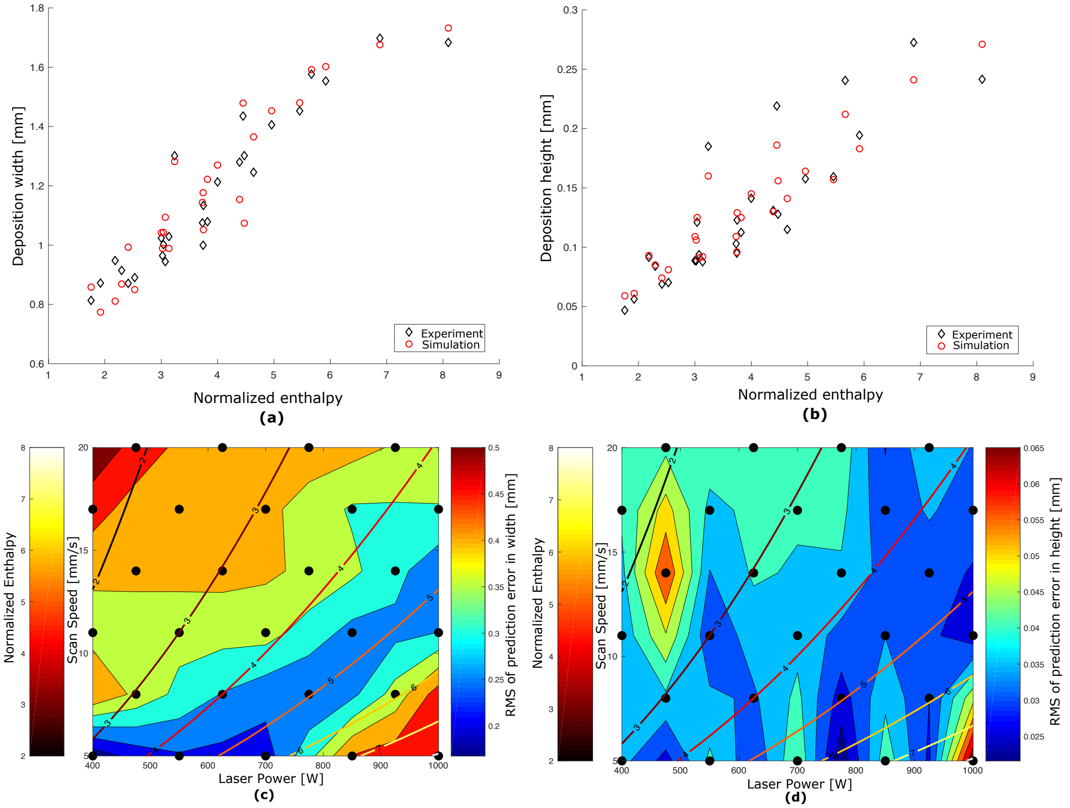

Figure 5.6: Comparison of simulation and experimental results in deposition (a) width and (b) height, where black diamonds and red circles show experimental and simulation results, respectively. (c) and (d) show the root mean square of the prediction error in width and height, respectively, on a process map, which demonstrates the higher error regimes in lack of fusion and keyhole.

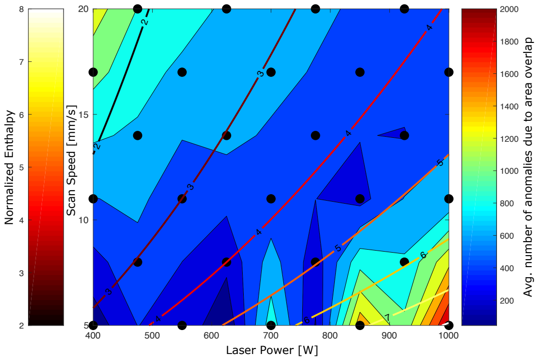

Figure 5.7: The average number of anomalies due to area overlap between the predicted and experimental deposition area, as defined in Figure 5.2(a), resulting in more anomalies in lack of fusion and keyhole melting modes.

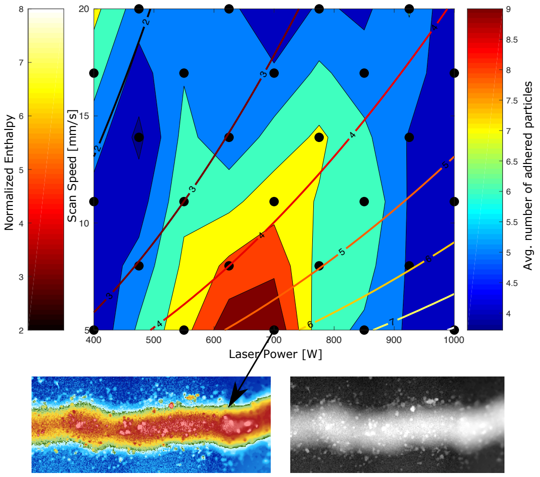

Figure 5.8: Average number of satellites detected on the deposition profiles obtained by the confocal microscope, as explained in Figure 5.2(b). The process map shows a higher number of satellites observed in conduction melting mode. The height map (in color and grayscale) obtained by the confocal microscopy shows a representative example with a high number of satellites.

5.4.2 Process maps and process anomalies based on vision results

The vision results represented in this section are focused on the the melt pool and the incandescent region features defined in [264]. The detected particle ejecta is also investigated in terms of their frequency and size. The aim is to explore out-of-bounds process zones using these process signatures detected by the vision sensor.

The width of the melt pool region is extracted as the minor axis of the detected ellipse. Figure 5.9 column (I) shows the average, standard deviation and CoV of melt pool region width. An increasing trend can be seen towards the keyhole melting mode, which overlaps with the behavior in deposition confocal microscopy as a process outcome. The process maps of Figure 5.9(B-I) and (C-I) highlight the high speed and high laser power region as having a high degree of variability in the melt pool width. The variation in melt pool region width is higher in this process zone, which results in balling and is expected due to the process physics of this zone. Similar trends can be also observed in Figure 5.9 (II) for melt pool region length. Sample video frames corresponding to the keyhole and balling process zones showcase the unstable plasma plume in keyhole melting mode and the variation in melt pool region length and width in balling zone.

The incandescent region includes the contributions from the melt pool and the plasma plume. The incandescent region area is calculated as it is most affected by the process instabilities [192, 264]. The average incandescent region area is shown in Figure 5.10(a). It can be seen that the incandescent region increases towards the keyhole melting mode, which is a similar trend observed in the average melt pool width in Figure 5.9, with similar behavior captured in Figure 5.10(b) and (c). Higher variations in the incandescent region is observed in high speed and high laser power process zone as a result of balling, which is expected knowing the process physics. Growth in plasma plume is generally observed with an increasing laser power and a decreasing scanning speed [198]. Through high-speed imaging, Caballero et al. [52] showed that higher intensity plasma plume is associated with keyhole melting with deeper penetration in the melt pool profile. The plasma plume can be more accurately monitored by spectroscopy for keyholing by capturing the chemical composition of the plasma plume [269] and its effects on absorption of laser radiation can be observed [362].

The ejected particles are detected and used as a metric to find out-of-bounds behavior of the process. Figure 5.11(a) and (b) show the average and standard deviation of the particle ejecta detected per frame, respectively. Both of the process maps show that the maximum average and the maximum deviation in number of particle ejecta occur in high scan speed and high laser power region, likely corresponding to the balling phenomena. Two representative frames from conduction and balling process zones are shown as in

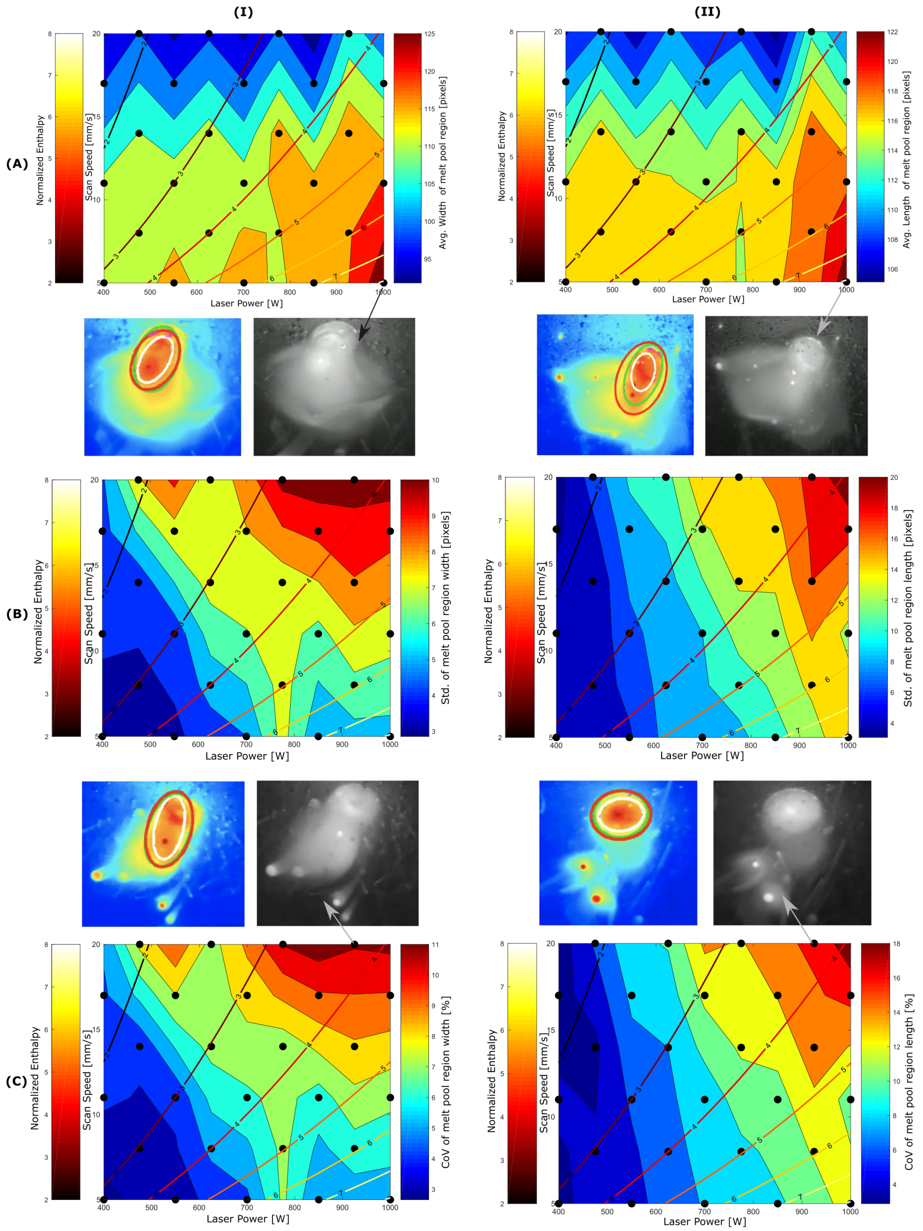

Figure 5.9: The process maps showing the vision-based results of the average, standard deviation and coefficient of variance in rows (A), (B) and (C), respectively, for melt pool region width and length in columns (I) and (II), respectively. Sample frames from the collected videos are shown in false-color and grayscale, illustrating fluctuations in melt pool morphology in the balling zone and plasma plumes in the keyhole process zone.

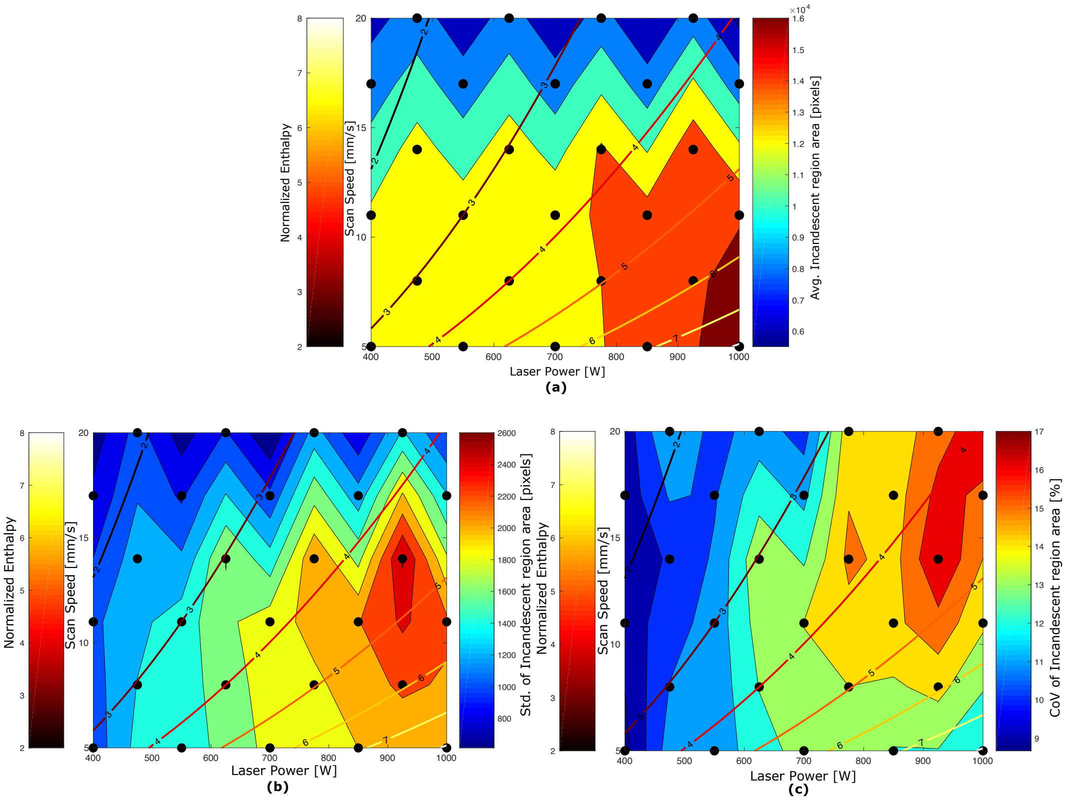

(a)

(b)

(c)

Figure 5.10: Average (a), standard deviation (b) and coefficient of variation (c) of the incandescent region area detected by the vision sensor monitoring the process zone in lead view. The detected area is a function of the length and width of the region.

color and gray-scale images. The frames show a typical case for material ejecta in these process zones. It is observed that some of the detected particle ejecta in this process zone appear within the detected incandescent region, which could be an indication of a different powder catchment phenomenon associated with this process zone. These particles are mainly detected at the melting front or top boundary of the melt pool.

The area of material ejecta is investigated and its average and standard deviation are presented in Figure 5.11(c) and (d). The maximum average material ejecta area is observed in the lack of fusion process zone and the maximum deviation is observed towards the high scan speed and high laser power process zone. The distance between the material ejecta and the vision detector, which would affect the appearance of the material ejecta size, is not known, however the number of frames is high enough to show the statistical trend in this metric.

5.4.3 Process map comparisons

In this section, process outcomes (confocal microscopy data) and process signatures (vision data) are correlated by comparing the process map outcomes for equivalent features. The aim is to find similar trends such that simulations and in-situ process signatures can be used real-time as an indicator of a process anomaly without any ex-situ part characterization. The results comparing melt pool and deposition dimensions between process outcomes and process signatures are normalized using Min-Max feature scaling, as direct translation between pixels and mm is not available.

The only equivalent geometric feature that can be directly comparable between process outcomes and process signatures are the deposition and melt pool region widths. In Figure 5.12(a) and (b), it can be seen that the deposition width and the melt pool region width show similar behaviors, with an increasing trend towards the keyhole process zone. The normalized standard deviation of deposition width and melt pool region width are shown in Figure 5.12(c) and (d), showing that the highest variation occurs in high speed and high laser power, which can be attributed to balling. These qualitative comparisons illustrate that the vision data has analogous behaviour in terms of deposition dimensions and quality, and may be ultimately be correlated to actual deposition width, given a future pixel to mm calibration.

The trends in deposition cross-sectional area and melt pool area are also compared to investigate the feasibility of detecting out-of-bounds behavior using the process signatures. The process maps in Figure 5.13 show the normalized average, standard deviation and coefficient of variance in row (A) to (C) for deposition area and melt pool region area

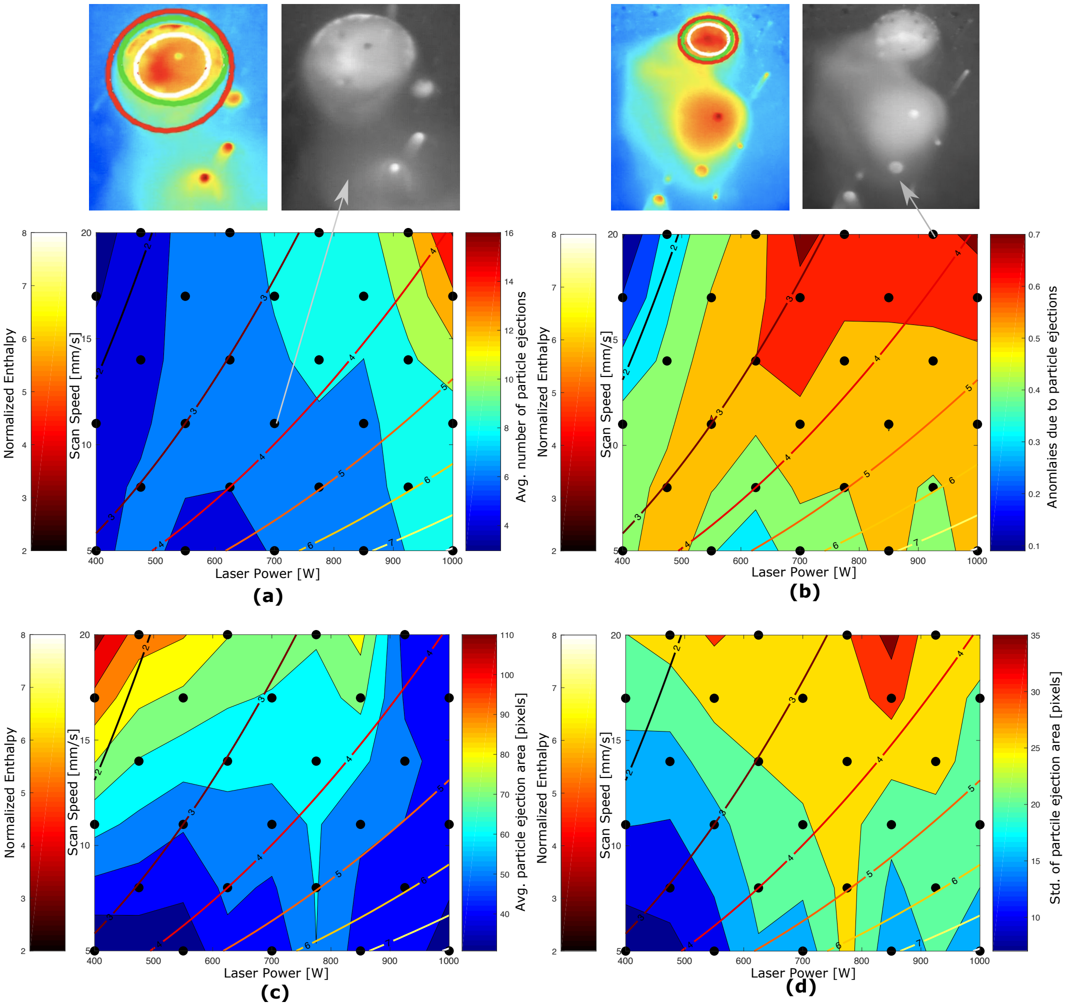

(a)

(b)

(c)

(d)

Figure 5.11: Process maps (a) and (b) show the average and standard deviation of the material ejecta count per frame, respectively, where the balling zone is highlighted in both process maps for higher volume and variance in material ejecta count. Process maps (c) and (d) show the average and standard deviation of the detected area of material ejecta.

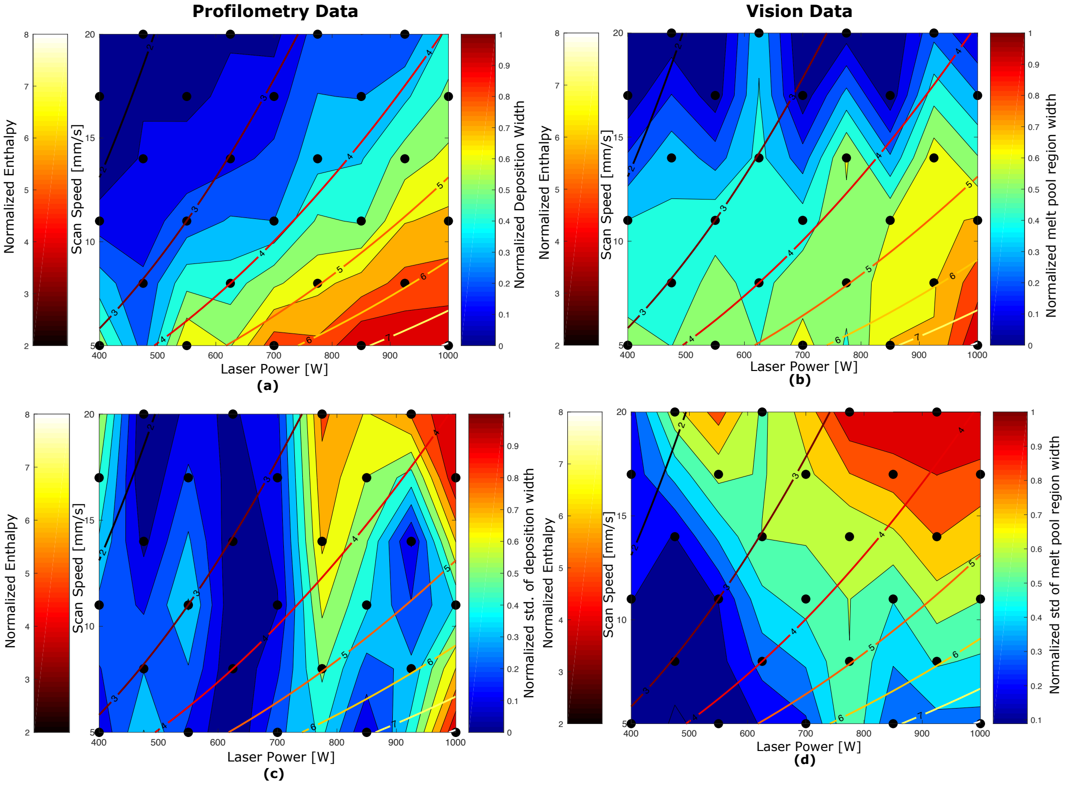

Figure 5.12: Process maps for average normalized deposition width extracted from the confocal microscopy data (a) and average normalized melt pool region width detected based on the vision sensor (b). Process maps (c) and (d) show the normalized standard deviation of the deposition width and the melt pool width, respectively.

in columns (I) and (II), respectively. It can be seen that the deposition and melt pool region area show similar behavior as they grow towards the keyhole melting zone. Furthermore, the maximum deviation in this metric is observed in high speed and high laser power process zone for both deposition and melt pool region area corresponding to the balling region. Although it may not be possible to draw a quantitative conclusion from the direct comparison between deposition area and melt pool area with respect to different dimensional axes, as they may be affected by different physics phenomena, the trends in similarities between these two metrics is apparent and are presented here for the purpose of drawing quality performance inferences.

Figure 5.14 compares (a) the anomalies due to area overlap using process physics and confocal microscopy deposition outcomes and (b) the anomalies due to area ratio of the incandescent over melt pool region. As these areas are different, they highlight different process zones. The anomalies due to area overlap between the simulation and confocal microscopy data show that the highest deviations occur in the zones of lack of fusion and keyhole, related to the poor performance of the physics model in these process zones. The number of anomalies as a function of area ratio is higher in high laser speed and high laser power zone as the growth of the incandescent region is not proportional to the growth of the melt pool region.

5.4.4 Preliminary classification results

The training and testing are performed using cross-validation with all of the Vis-NIR experimental data points, which consists of 81 experiments. The k-fold method is used in cross-validation, where k is set to ten, with random training and testing datasets. The kNN method can classify the process signatures based on the in-situ detected features and process parameters with an average classification error rate of 13%, where the standard deviation of the error rate is 4%. Although this is a preliminary study for classifying the process zones based on process signatures, the classifier shows promising results in terms of prediction accuracy and robustness. More experiments at different combinations of process parameters can be added to further improve the reliability of the classifier. Figure 5.15 shows the confusion matrix of the performed experiments, however more experimental data are needed to reach concrete conclusions on the performance of the classifier as the experimental range was mostly focused on the *conduction* melting mode. The dominance of conduction melting in the experimental data can also be observed in the confusion matrix, as most of the false predictions are predicted as conduction mode. Overall, this basic classifier shows that the Vis-NIR data has the potential to be used to infer a classifier to detect process behaviour.

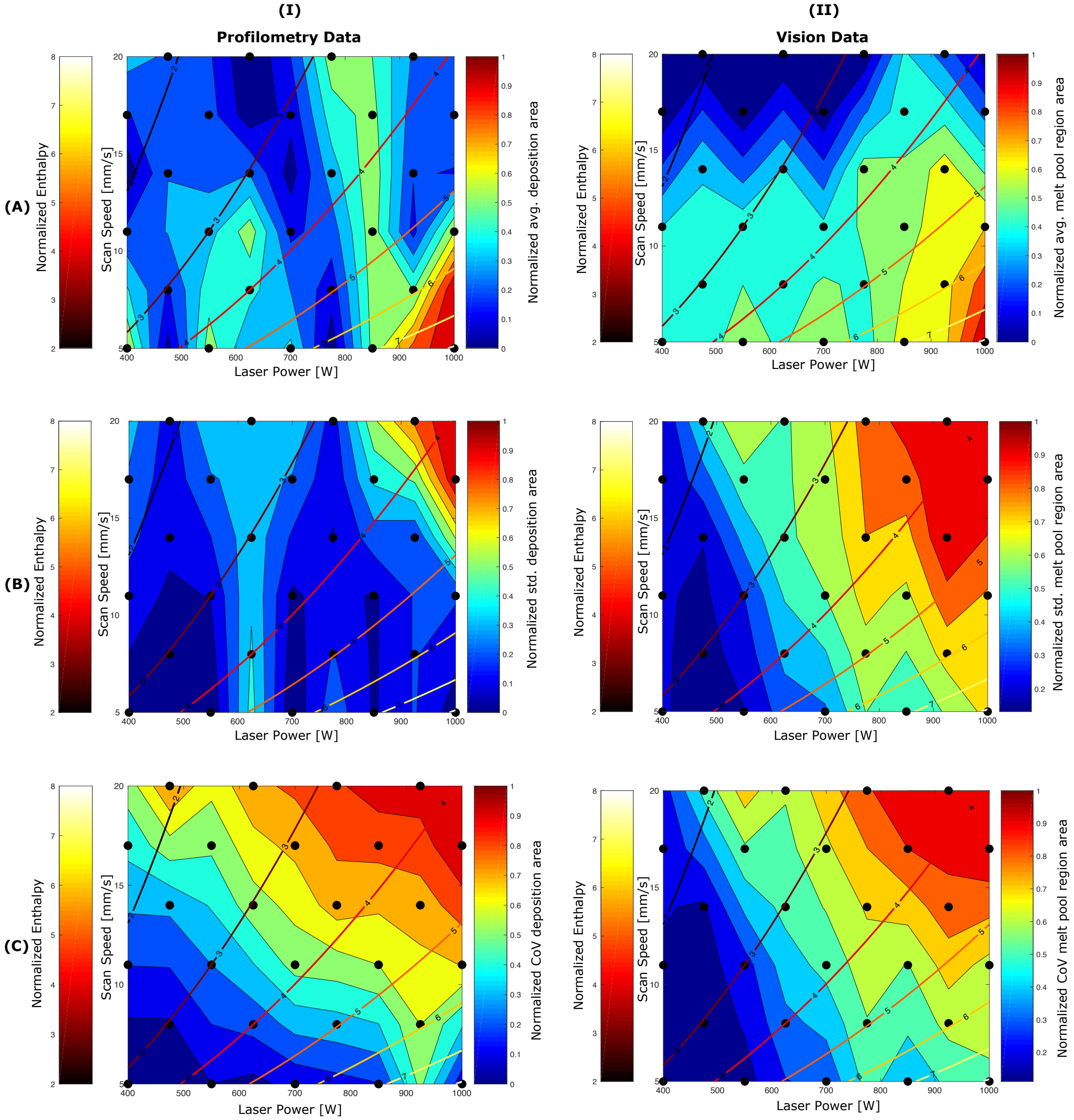

Figure 5.13: Process maps for normalized average, standard deviation and coefficient of variance shown in rows (A)-(C), for deposition area and melt pool region area in columns (I) and (II), respectively.

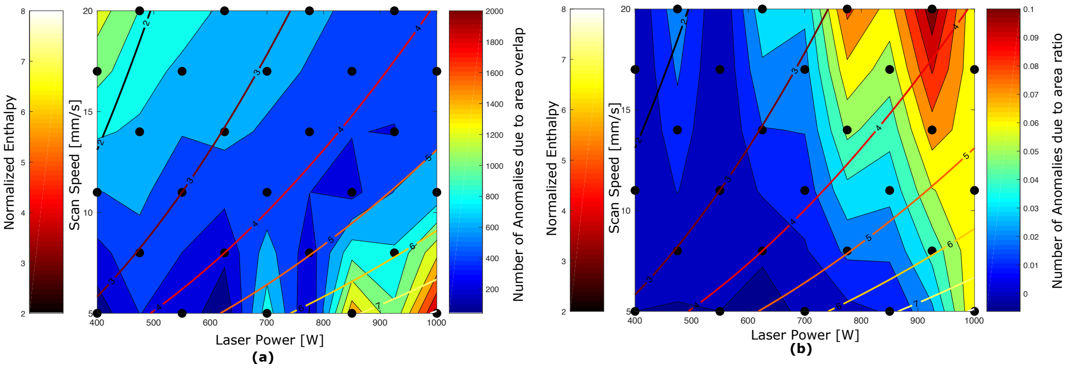

Figure 5.14: Average number of anomalies due to area overlap using process outcomes and physics (a) and the average number of anomalies due to area ratio using process signatures (b).

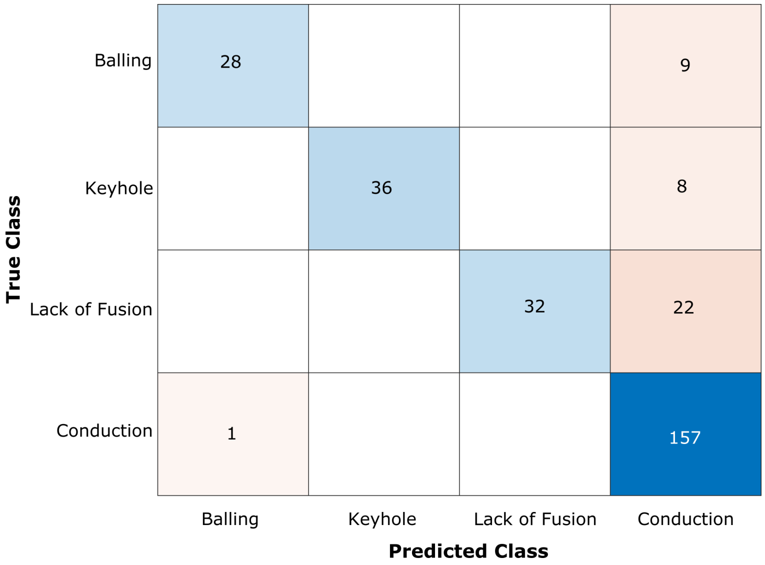

True Class \ Predicted Class	Balling	Keyhole	Lack of Fusion	Conduction
Balling	28			9
Keyhole		36		8
Lack of Fusion			32	22
Conduction	1			157

Figure 5.15: Confusion matrix showing the number of true and false predictions for the classes of 'Balling', 'Keyhole', 'Lack of Fusion' and 'Conduction'.

5.4.5 Reflections

In the present work, process maps have been represented based on process physics (captured via modeling), process signatures (captured via Vis-NIR data), and deposition quality outcomes (captured via confocal microscopy data). It has been shown that the comparison of physics-based process modeling and the process outcomes can successfully detect three regions in the process map, namely lack of fusion, keyhole and balling process zones. However, creating this type of process map needs ex-situ confocal microscopy measurements, which could be inconvenient in manufacturing complex geometries with multi-tracks and multi-layers, where ex-situ confocal microscopy is not possible at each layer. On the other hand, using the in-situ vision detection to create the process maps does not require any additional steps after the process. Vision-based data detected balling and keyhole process zones successfully by observing the melt pool region and incandescent region (Figures 5.9, 5.10, and 5.12), while the estimate of particle ejecta size was successfully used to detect the lack of fusion mode (Figure 5.11(c)), although it is more challenging to detect the lack of fusion process zone only with in-situ vision data.

Figure 5.12, 5.13 and 5.14 show that the Vis-NIR data and physics-based modeling can be used to determine if the process has reached instability zones namely lack of fusion, keyhole and balling. It has been represented that the instability thresholds detected by Vis-NIR data and physics-based modeling overlap with the ones established via experimental datasets (process outcomes-confocal microscopy) shown in process maps (Figure 5.5). In this study, the deposition geometry control and stability were targeted specifically. Other type of process maps can be generated using microstructure, pore defects and mechanical properties of the depositions to define the out-of-bounds thresholds.

The preliminary classification results demonstrate the performance in detecting *conduction* mode and *keyhole* melting mode (Figure 5.15). The number of experiments should be increased, especially for *keyhole* and *balling* process zones, which should be a richer and more common pool of data, since the lack of fusion process zone is relatively easy to avoid, as long as the material system and the minimum energy required to melt are well known. That is, providing sufficient energy makes it unlikely to have a *lack of fusion*, whereas *balling* and *keyhole* zones are frequently encountered due to acceleration and deceleration in the scan path trajectory or due to thermal cycling and accumulation. The transition between these melting mode domains can be detected, as demonstrated in this work, by virtue of Vis-NIR detection alone, and has been shown to correlate directly to deposition geometry, as shown in Figure 5.13: a powerful result, since it illustrates that low-cost Vis-NIR detectors can be used as an efficient tool to detect and respond to process instability. Furthermore, this methodology can be used in real-time by collecting data for each layer and give a label for each layer based on the kNN features, where corrective actions can be taken in a hybrid (additive/subtractive) system with layer-intermittent machining.

5.5 Conclusion

In this study it is shown that process outcomes, signatures and physics can be used to create process maps to detect process instabilities. Process modeling can predict the deposition width and height and normalized enthalpy, to define theoretical feature geometry and process zones respectively. Process signatures are captured by in-situ vision monitoring and a feature detection algorithm is used to detect pre-defined ROIs and particle ejections. Process outcomes are identified by scanning the samples with a confocal microscope and extracting the width and height of the deposition to quantify the quality of the features. Process maps are created based on the statistical representation (average, standard deviation, root mean square, coefficient of variance) of different data sources to investigate the correlations in performance and to identify different process performance zones. Although the combination of confocal microscopy and process modeling can detect all three process zones, the detection needs ex-situ metrology and instantaneous decisions cannot be made during manufacturing. It is shown that the balling and keyhole process zones can be detected just using the melt pool process signatures, captured by the in-situ vision sensors. Detecting lack of fusion is difficult with in-situ vision sensors, and can be inferred only based on the area of the material ejecta; however this instability is the easiest to avoid by ensuring a minimum input energy input. As a preliminary study, a kNN classifier is trained using statistical features detected by the vision sensor, normalized enthalpy, and process parameters. In future research, the reliability of the classification algorithm should be improved by performing more experiments to extend the range of the testing data, and the classifier should be further developed to allow it to reach conclusions in real time.

Chapter 6

Hybrid directed energy deposition and machining strategies informed by process modeling and process signatures

6.1 Preface

In this chapter, a dual wavelength pyrometer is used to validate the physics-based thermal model proposed in Chapter 3 in a multi-layer, multi-track 3D part manufactured via directed energy deposition (DED). The pyrometry data is further analyzed to find a correlation between the melt pool signatures and the process outcomes and to detect geometric defects, which can be corrected with post-process machining. Two correction strategies are proposed using machining. In the first approach, machining is used as a post-processing operation, where the geometric fidelity of the overall part is not met and/or surface quality requires improvement. The second strategy is a layer-intermittent approach, where the deposition quality of each layer is assessed based on the melt pool signatures. Layer-intermittent corrections are proposed based on a decision-making algorithm for quality assessment. The layer-intermittent approach can only be utilized in a hybrid manufacturing system, where DED and machining processes are combined in one manufacturing system. The machinability of additively manufactured parts is investigated experimentally by measuring the cutting forces and by observing the tool wear. A cutting force model is implemented to predict the cutting forces for additively manufactured parts.

6.2 Introduction

Directed energy deposition (DED) is known for manufacturing of large components in low-volume, with a high density and controllable microstructure [83]. In DED, there are limitations in maintaining a high level of process reliability and repeatability when compared to conventional manufacturing processes due to process instabilities [376]. For the purpose of this dissertation, process instabilities for DED are defined as contributions from stochastic events, systematic machine biases, improper selection of process parameters, and/or deviations from expected process parameter stability margins due to heat build-up and/or deposition substrate conditions. Examples of process instabilities which can occur due to random events or due to the complex physics behind the laser-material interaction can be found in literature [361]. In addition, cyclic thermal loading and temperature build-up throughout the process contribute to quality issues such as pore defects, residual stresses, poor dimensional fidelity, and poor mechanical properties [142, 185, 63]. In order to enhance the process reliability, research efforts have focused on process modeling to predict process outcomes [284], process monitoring to detect process signatures [72] and process control to avoid process instabilities as much as possible [45].

In this study, in-situ process monitoring is used to validate the previously-proposed physics-based model [106] as described in Chapter 3, with a focus on such validation for a complex 3D part. Process signatures obtained from pyrometry sensor data are used for this purpose and are furthermore analyzed to detect out-of-bound behavior of the process and to investigate the relationship between the process signatures and process quality outcomes such as the deposition geometry and hardness. Machining is then proposed as a corrective action to address the defects in the process geometry outcomes. Two different corrective action strategies are proposed: layer-intermittent and post-processing. The layer-intermittent strategy requires a hybrid manufacturing system to address the issues in a layer-based manner, where post-process machining can be done in both separate and hybrid manufacturing systems.

Detection of process instabilities is crucial in achieving a high level of process reliability, repeatability and cost efficiency with metal AM processes [193]. This plays a critically-important role to encourage the industrial adoption of metal AM. Research efforts have been focused on finding a relation between process signatures, outcomes and physics [257]. Identifying when a process is close to (or already experiencing) instabilities can enable the selection of appropriate process parameters (in-situ or ex-situ) to avoid defective parts [189]. Instabilities can occur specifically in parts with complicated geometric features such as parts with a large cross-sectional area, parts with thin cross-sections, and parts with overhangs [360]. In-situ monitoring is one of the main tools to detect process instabilities through inferring a relationship between the detected process signatures and part quality outcomes [369]. Process signatures such as melt pool temperature and morphology, as well as plasma plume characteristics are a few examples of signatures which can be captured with different in-situ monitoring sensors. In-situ process monitoring can be used for variety of reasons such as observing the process zone, better understanding the process physics, quality assurance and process control. As such, efficient feature extraction and analysis tools can be developed to process the data in real-time [269], where the results can be used to drive intelligent decisions on the part quality outcomes [360], as well as to generate feedback signals for a real-time process control [388].

Photodiode, pyrometer and infrared (IR) detectors are commonly-used devices which can capture infrared (IR) and near infrared (NIR) wavelengths from the melt pool region [65]. Thermal signatures can be detected using these methods, either in a point based (spatially-integrated) or an image-based (spatially resolved) manner. In point-based thermometry measurements (using a pyrometer or a photodiode), the thermal signatures are detected as a representative value over a surface area, where the value describes the radiation intensity at that location and is typically reported as voltage or an arbitrary unit of measurement [215] which may used to correlate to temperature values. Precise temperature values are difficult to infer, as the emissivity of the material system is required to convert IR/NIR detector intensity values to temperature. The emissivity value for the material system in DED is particularly challenging to determine because it is a highly temperature-dependent material property; furthermore, emissivity is different at the melt pool, un-melted powder and solidified surface [240], which may all be captured in the field of view of the detector. Nevertheless, IR/NIR detectors can still be useful in quantifying relative changes in the signal values such that over- and under-heated zones, cooling or heating rates within the printed part can be detected. Such signals can then be used as a feedback to the manufacturing process [299].

There are notable examples of research works focused on leveraging data from thermal signatures. Alberts et al. [11] integrated a photodiode to obtain thermal signatures from the process and made a correlation between the thermal signature and the density of the part. In thermography image-based measurements, IR/NIR cameras can provide the intensity across the field of view in a spatially-resolved dataset [64, 67, 55]. If the calibration is done carefully for emissivity and reflectivity of the material, it is possible to obtain accurate and repeatable data from such camera systems [310]. Rodriguez et al. [309] implemented a thermography system and detected process signatures such as over-melted regions and temperature gradients with an IR camera. It has been shown that leveraging online measurements and process planning have made a significant improvement in achieving a homogeneous temperature across the part and high quality parts [354]. Furthermore, closed loop control of the process provides the opportunity to keep the process within predefined stability limits based on the feedback signal obtained from process signatures [35]. An IR camera and a pyrometer can be used together to complement each other. Such an example is when an IR camera is used for observing the temperature distribution and for keeping the temperature history through the process, whereas the pyrometer is focused on the melt pool specifically [345]. Deposition defects such as pores and geometric deviations can be linked to in-situ sensor phenomena to create correlative models and infer when defects have occurred [189]. In DED, it is typical that such defects can result in scrapping the part or in addressing such via machining.

Some detected defects can be corrected to improve the part quality and avoid part scrap [321]. Machining is a post-processing technology commonly used to improve the dimensional accuracy and surface quality of components [324]. Furthermore, in a hybrid system, layer-intermittent machining can be performed to re-surface defective layers or regions within a layer, and to furthermore machine the locations within the part that will become inaccessible by the cutting tool due to changes in geometry during the deposition process [314]. Machinability of additively manufactured parts is traditionally more challenging compared to wrought materials due to high hardness values caused by fast solidification and cooling [160]. Similarly, cast metals could be relatively challenging compared to wrought metals and hardness can vary within the casted metals due to different solidification and cooling rates at critical geometric features of the part [350]. In addition, there are more aspects influencing the machinability of additively manufactured parts compared to wrought materials. For instance, changing the process parameters of the metal AM process can result in different microstructures and mechanical properties, which can affect the machinability directly, requiring different machining parameters for different combinations of process parameters [23]. Furthermore, anisotropy is commonly observed in additively manufactured parts due to cyclic thermal loading and temperature build up, which can result in different machining characteristics at different locations of the part [227].

Machinability of additively manufactured materials has been studied by measuring tool wear, cutting forces, and surface finish roughness [160]. Researchers found that cutting forces are generally higher, tool life is shorter and progress in tool wear is faster in machining of additively manufactured parts [170, 149, 161]. Furthermore, research indicates that the surface finish of AM parts could be improved by locally optimizing the machining process parameters [276]. In literature, there is a gap in integrating the additive and subtractive processes, where interruptions occur between two processes to define regions to machine and plan the cutting operation accordingly. Without addressing this gap, the transition between the two processes, DED and machining, remains inefficient in terms of part surface quality outcomes, geometric fidelity, production time, labor, and cost.

In this study, in-situ pyrometry measurements are used for two purposes. First, the physics-based model proposed in Chapter 3 is validated experimentally by comparing the instantaneous temperature detected during the deposition process with the predicted temperatures. Second, the collected data is further analyzed to distinguish out-of-bound signals and find a relationship between part quality outcomes (geometric fidelity) and process signatures (pyrometry data). Based on this correlation, two machining strategies are proposed, a post-processing and a layer-intermittent machining strategy. Finally, the machinability of the additively manufactured parts is studied to investigate the mechanisms which impact the cutting forces and discuss how such findings influence the two machinig strategies.

6.3 Methodology and experiments

6.3.1 Multi-layer, multi-track DED modeling

The voxel-based thermomechanical model and cascaded geometry-prediction model proposed in Chapter 3 is extended to a 3D model to simulate complex multi-track, multi-layer structures. The main structure of the model is kept the same, where the deposition is discretized into voxels following the sequence of the scan path. The neighboring voxels are defined for each voxel in a neighbourhood matrix, which is $N \times 6$. N is the total number of voxels and 6 columns represent the faces of the voxel. The instantaneous melt pool temperature is predicted using Equation 3.1 as described in Chapter 3 by the Rosenthal's moving point heat source equation for each voxel at the time of the deposition [106]. The voxel network thermal history is calculated based on the conduction and convection heat transfer through the voxels, recursively. It is assumed that one voxel is deposited at each time step and, based on the neighborhood matrix, the heat transfer between other pre-deposited voxels is modeled. Once all the set of heat transfer equations are generated, the equations are solved for each voxel's temperature using a state space model in discrete time.

In this voxel-based model structure, there are additional challenges when the scan path has multiple adjacent tracks and layers. Although the way that the heat transfer equations generated remains the same, discretization of the scan path and defining the neighboring voxels may become more difficult due to curvatures and sharp-corner scan paths. Thus, misalignments can occur between the neighbouring voxels such that a voxel can have two neighboring voxels on one side. In this study, a prismatic geometry is printed, where the scan path does not vary from one layer to another. Thus, misalignment is not an issue on the top and bottom faces of the voxels. However, there are misalignment between voxels within the x-y plane due to existence of curvatures in a multi-track scan path, which is illustrated in Figure 6.1

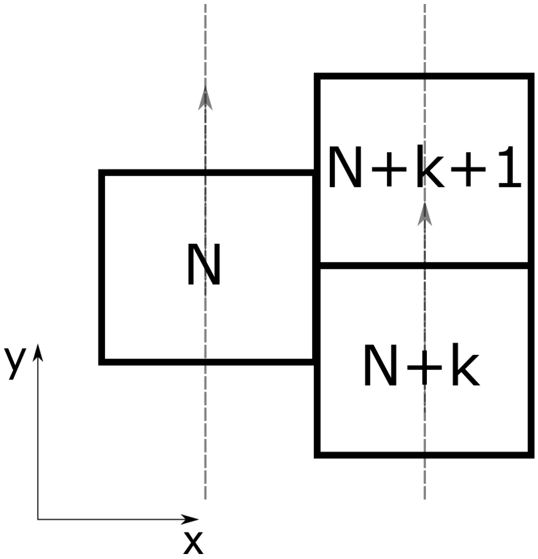

Figure 6.1: The misalignment of voxels in the x-y plane, which is one of the challenges when there are curvatures involved in the scan path.

The misalignment between the voxels in the x-y plane is addressed by taking the average of the temperatures of two neighboring voxels. For instance voxel N has two neighboring voxels on its right side, which are voxels $N + k$ and $N + k + 1$ shown in Figure 6.1. The model defines two neighboring voxels on the right side and takes the average of temperature values of voxels $N + k$ and $N + k + 1$. Further refinements to this approach are proposed as future work.

6.3.2 DED experimental setup

The experiments were performed in a CNC based DED system, also referred to as a laser engineered net shaping (LENS) system (Optomec, NM). The laser beam and powder delivery system are coaxially located and the metal powder is delivered through four nozzles, which are equally radially distributed around the laser beam central path. The laser beam diameter is set to 700 μm and the powder deposition rate is set to 7.5 g/min; these values are kept constant throughout the experiments. The material is SS316L. The process chamber has a fully gas sealed Argon atmosphere to prevent oxidation and provide a safer environment for the laser-material interaction.

The geometry is inspired by a radial heat exchanger design shown in Figure 6.2(a). Only one tear drop-shaped fin is printed for the experimental study and it was assumed to be a representative feature due to the repetitive geometry of the heat exchanger. The tear drop geometry was modified, as shown in Figure 6.2(b), to accommodate multi-tracks in the layer-wise scan path. The scan path involves five contours per layer and multiple layers, where the number of layers depends on the resulting layer thickness, dependent on the process parameters deployed. The deposition sequence of the five contours varies from starting at the outer-most contour to starting at inner-most from one layer to the next one, where the direction of the deposition remains the same for each contour at each layer. The process parameters used in this study are listed in Table 6.1, as so-called process parameter recipes. Recipe 2 provides a more aggressive melting mode compared to Recipe 1 based on the normalized enthalpy given in Equation 3.28 and 3.29. For each recipe, two replicates are manufactured.

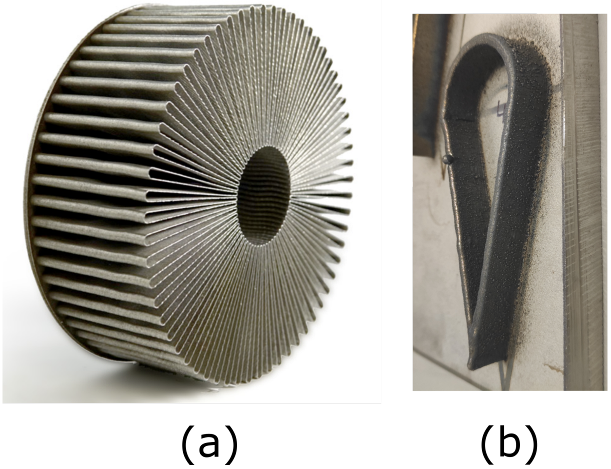

Figure 6.2: (a) The geometry of the printed object for the experiments is inspired by a radial heat exchanger [3] (b) The modified tear drop-shaped geometry for the DED experiments

A dual-wavelength pyrometer (ThermaViz, Stratonics, CA) is used to detect thermal signatures from the melt pool, where the pyrometer is integrated coaxially with the laser

Table 6.1: Process parameters used in the experiments

	Recipe 1	Recipe 2
Laser power [W]	450	550
Scan speed [mm/s]	8.5	6.4
Layer thickness [mm]	0.254	0.457
Total # of layers	39	25
Hatch spacing [mm]	0.457	0.610
Workpiece #	6, 8	4, 5

beam, as illustrated in Figure 6.3. The exposure time is 1.2 ms and the sampling rate is 400 ms. Dual-wavelength pyrometers measure the radiation energy at two different wavelengths; the sensor deployed in this study used wavelengths of 700 nm and 950 nm. Dual-wavelength pyrometers are more commonly preferred due to the effective way in which the contribution of emissivity in temperature correlatios is addressed. The sensor raw data values are intensity values detected at the two wavelengths, which are representative of the radiation energy of the melt pool. The calibration of the sensor is done using a near black body object. The ratio of the emissivity values at these wavelengths is calibrated such that the calculated temperature value matches with the actual temperature of the near black body object.

Temperature calibration procedure is performed over the range of 1100^{o}C - 2500^{o}C over 15 calibration points. The current and temperature chart is provided by the manufacturer to calibrate the ratio of the measured intensity values to a certain temperature for the given current value. Once the intensity measurements are performed at each calibration point, the calibration values are defined based on the linearity between the inverse of temperature values and the natural logarithm of intensity ratios [392, 158].

During the experiments, the melt pool is detected within the predefined field of view and the raw data is converted to a data sheet based on the calibration, which includes the average and the peak temperature of the melt pool. Furthermore, the long and short peak data are reported, which given as a unitless values to represent the peak intensity value measured by the long and short wavelengths respectively. At each measurement point, the time stamp and the positions in x, y and z in the CNC coordinate system are also reported. Furthermore, the temperature values across the field of view in x' and y' axis originated at the melt pool center are given. The melt pool length and width can be calculated from the x' and x' profile data, where the melting temperature of the material is assumed to be the melt pool boundaries.

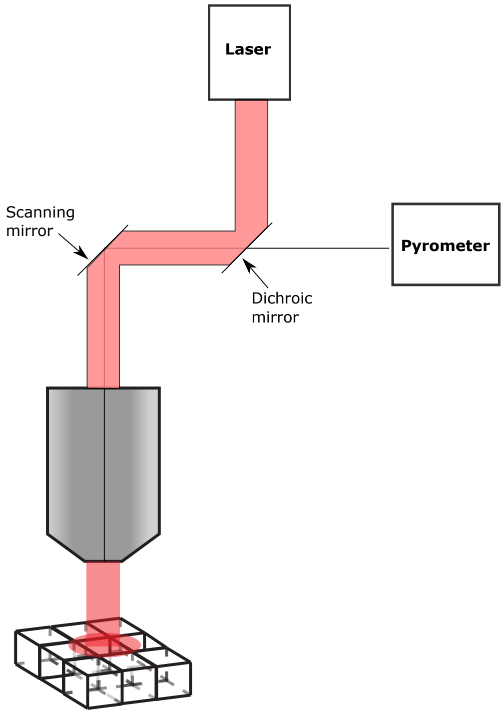

Figure 6.3: The configuration of the dual-wavelength pyrometer as an in-situ monitoring device integrated coaxially with the laser beam

6.3.3 Cutting force model

A common cutting force model is the oblique cutting force model [14], illustrated in Figure 6.4. In this model, there are three orthogonal cutting force components. The first is the tangential force, F_t, which is parallel to the cutting velocity, V_c. The second is the feed force, F_f, which is normal to the workpiece surface and is directed into the workpiece surface. The third is the radial force, F_r, which is normal to the other two forces and is directed out of the cutting edge inclination. The radial force is zero if the inclination angle, i, is zero. The normal rake angle, α_n, is defined as the angle between the direction normal to the workpiece surface and the rake face.

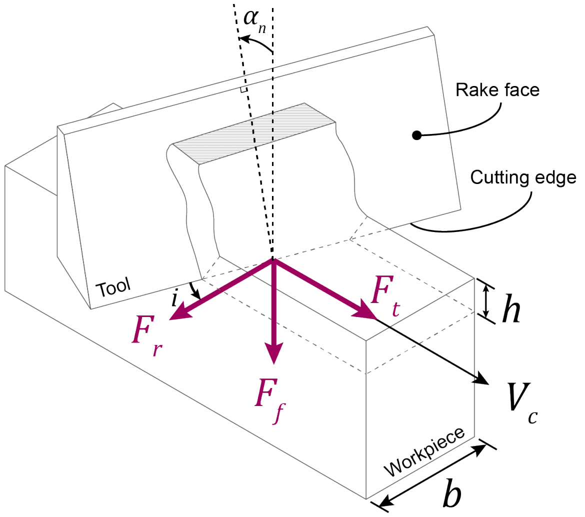

Figure 6.4: Oblique cutting force model

The three cutting force components can be expressed as linear equations, as a function of the chip thickness, h, chip width, b, cutting coefficients, K_{tc}, K_{fc}, K_{rc}, and edge coefficients, K_{te}, K_{fe}, K_{re}. The cutting and edge coefficients are influenced by many factors, including workpiece material, tool coating, tool edge preparation, tool wear, cutting coolant/lubricant, and temperature. Therefore, they must be determined from experimental cutting force data.

$$\begin{aligned} F_t &= K_{tc}hb + K_{te}b \\ F_f &= K_{fc}hb + K_{fe}b \\ F_r &= K_{rc}hb + K_{re}b \end{aligned} \tag{6.1}$$

In order to simulate cutting forces or to calibrate cutting force coefficients from experimental cutting force data, the cutter-workpiece engagement (CWE), i.e., chip thickness and width, must be known. Unless the workpiece is a simple block (for milling) or tube (for turning), it is advantageous to use a geometric engine to accurately simulate the chip geometry at each instance of the cutting process. For the teardrop workpiece shapes used in this study, the ModuleWorks cutting simulation engine was used to calculate the CWE during machining trials. In this engine, the workpiece can be defined using a CAD file representing the blank geometry, while the milling tool can be defined parametrically. The workpiece CAD file was generated by, first, scanning the actual workpiece using a coordinate-measuring machine (CMM) at multiple heights. Then, a simplified model of the workpiece was generated by tracing the CMM scans, as shown in Figure 6.5.

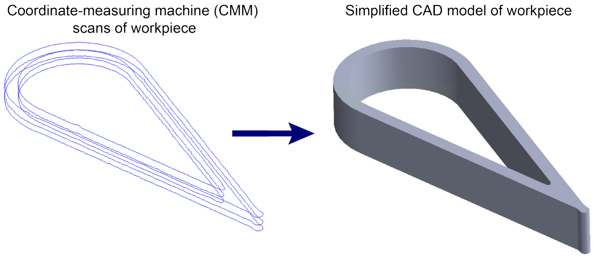

Figure 6.5: CMM scans and simplified CAD model of workpiece

A milling tool was chosen with a diameter slightly larger than the nominal wall thickness of the teardrop workpiece – a two-fluted carbide end mill coated with TiAlN with diameter of 3.175mm ($\frac{1}{8}$"), height of 12.7mm ($\frac{1}{2}$"), helix angle of 30^o, and rake angle of 10^o. With the workpiece and tool defined within the engine, machining cuts can be performed in the virtual environment, as illustrated in Figure 6.6, where the green areas show the machined surfaces.

From the simulation engine, the entry and exit engagement angles (ϕ_{en}, ϕ_{ex}) of the cutter can be obtained and used to estimate the cutting force. At each instant of the cutting process, if a cutting edge is engaged, then it contributes incremental cutting forces (dF_t, dF_f, dF_r). To account for the varying engagement angle of the cutting edge along

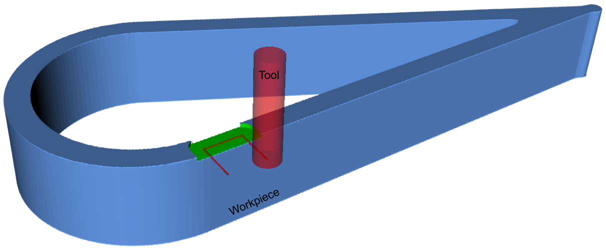

Figure 6.6: Workpiece and tool in cutting simulation engine

the height of the cutter due to the helix angle of the cutter (β), the tool is discretized into axial slices, each with a height of dz, as shown in Figure 6.7. The axial slices are denoted by z=1,2,. . .,N_Z, where N_Z is the number of axial slices. The total depth of cut is denoted by a. Finally, the flute number is denoted by the subscript j=1,2,. . .,N_J, where N_J is the number of flutes on the tool. Considering this and equation 6.1, the three incremental force components for a particular flute on a particular axial slice is given by:

$$\begin{aligned} dF_{t,j,z} &= K_{tc}h_{j,z}dz + K_{te}dz \\ dF_{f,j,z} &= K_{fc}h_{j,z}dz + K_{fe}dz \\ dF_{r,j,z} &= K_{rc}h_{j,z}dz + K_{re}dz \end{aligned} \tag{6.2}$$

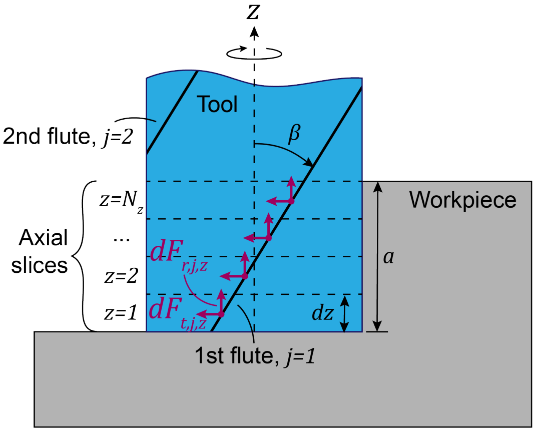

Figure 6.7: Cutting discretization

To summate the incremental forces and calculate a total cutting force vector, the incremental forces must be transformed into a common coordinate system. Using the machine coordinate system (MCS) also allows for easy comparison to measured cutting forces on an actual machine. Hence, the incremental cutting forces are transformed from the tool coordinate system (TCS) into the MCS, and then summated to calculate the total cutting force vector. These coordinate systems are illustrated in Figure 6.8. The components of the total cutting force vector in the MCS are given by:

$$\begin{aligned} F_x &= \sum_{z=1}^{N_Z}\sum_{j=1}^{N_J}\begin{cases} dF_{t,j,z}\sin\phi_{j,z} + dF_{f,j,z}\cos\phi_{j,z} & , \quad \phi_{ex} \leq \phi_{j,z} \leq \phi_{en} \\ 0 & , \quad \text{otherwise} \end{cases} \\ F_y &= \sum_{z=1}^{N_Z}\sum_{j=1}^{N_J}\begin{cases} -dF_{t,j,z}\cos\phi_{j,z} + dF_{f,j,z}\sin\phi_{j,z} & , \quad \phi_{ex} \leq \phi_{j,z} \leq \phi_{en} \\ 0 & , \quad \text{otherwise} \end{cases} \\ F_z &= \sum_{z=1}^{N_Z}\sum_{j=1}^{N_J}\begin{cases} dF_{r,j,z} & , \quad \phi_{ex} \leq \phi_{j,z} \leq \phi_{en} \\ 0 & , \quad \text{otherwise} \end{cases} \end{aligned} \tag{6.3}$$

Above, $\phi_{j,z}$ is the angle of a particular flute on a particular axial slice relative to the x axis of the MCS, and can be calculated by:

$$\phi_{j,z} = \phi_{j=1,z=1} + \frac{(j-1)\,2\pi}{N_J} + \frac{(z-1)\,dz\tan\beta}{r_{\text{cutter}}} \tag{6.4}$$

Above, $\phi_{j=1,z=1}$ is the current rotation angle of the first flute at the bottom of the cutter, which is a function of time and the spindle rotation speed.

r_{cutter} is the radius of the cutter. The chip thickness $(h_{j,z})$ for a particular incremental cutting force, can be approximated by the following formula:

$$h_{j,z} = \text{FPT}\cos\phi_{j,z} - \phi_f \tag{6.5}$$

Above, FPT is the feed rate per tooth in units of millimeters, and ϕ_f is the feed direction angle.

With the ability to calculate cutting forces virtually, the cutting coefficients can also be calibrated using the simulated cutter-workpiece engagement and measured cutting forces. Combining and rearranging equations 6.1, 6.2, and 6.3, the following equation can be formed for the x axis force:

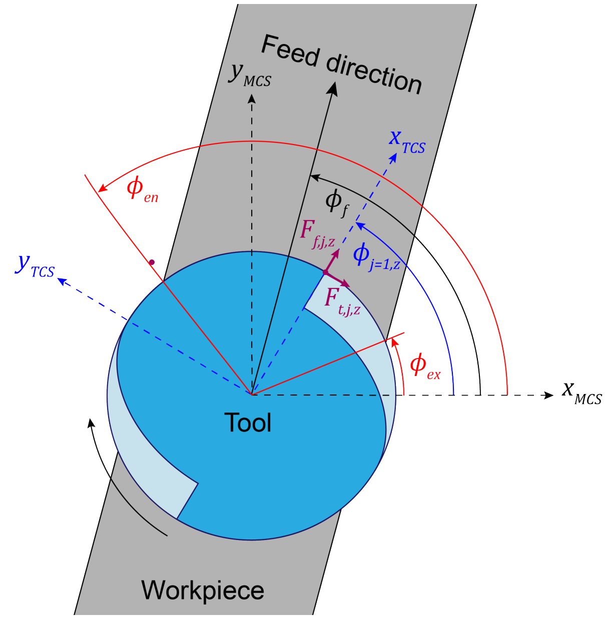

Figure 6.8: Cutting force simulation coordinate systems

$$
\begin{aligned}
F_x = & \underbrace{\sum_{z=1}^{N_Z}\sum_{j=1}^{N_J}\begin{cases}\underbrace{h_{j,z} dz \sin\phi_{j,z}}_{} & , \quad \phi_{ex} \leq \phi_{j,z} \leq \phi_{en} \\ 0 & , \quad \text{otherwise}\end{cases}}_{R_{tc_x}} K_{tc} \\
& + \underbrace{\sum_{z=1}^{N_Z}\sum_{j=1}^{N_J}\begin{cases}\underbrace{dz \sin\phi_{j,z}}_{} & , \quad \phi_{ex} \leq \phi_{j,z} \leq \phi_{en} \\ 0 & , \quad \text{otherwise}\end{cases}}_{R_{te_x}} K_{te} \\
& + \underbrace{\sum_{z=1}^{N_Z}\sum_{j=1}^{N_J}\begin{cases}\underbrace{h_{j,z} dz \cos\phi_{j,z}}_{} & , \quad \phi_{ex} \leq \phi_{j,z} \leq \phi_{en} \\ 0 & , \quad \text{otherwise}\end{cases}}_{R_{fc_x}} K_{fc} \\
& + \underbrace{\sum_{z=1}^{N_Z}\sum_{j=1}^{N_J}\begin{cases}\underbrace{dz \cos\phi_{j,z}}_{} & , \quad \phi_{ex} \leq \phi_{j,z} \leq \phi_{en} \\ 0 & , \quad \text{otherwise}\end{cases}}_{R_{fe_x}} K_{fe}
\end{aligned}
\tag{6.6}
$$

Above, R_{tc_x}, R_{te_x}, R_{fc_x}, and R_{fe_x} are regressors which will be used in a linear least squares regression formulation. Expanding to all three axes and expressed in matrix form:

$$\begin{bmatrix}F_x\\F_y\\F_z\end{bmatrix} = \begin{bmatrix}R_{tc_x} & R_{te_x} & R_{fc_x} & R_{fe_x} & 0 & 0\\ R_{tc_y} & R_{te_y} & R_{fc_y} & R_{fe_y} & 0 & 0\\ 0 & 0 & 0 & 0 & R_{rc_z} & R_{re_z}\end{bmatrix} \begin{bmatrix}K_{tc}\\K_{te}\\K_{fc}\\K_{fe}\\K_{rc}\\K_{re}\end{bmatrix} \tag{6.7}$$

Considering all time steps of the simulation, $t = 1, 2, \ldots, N_T$, where N_T is the total number of time steps:

$$\underbrace{\begin{bmatrix} \begin{bmatrix}F_x\\F_y\\F_z\end{bmatrix}_{t=1} \\ \begin{bmatrix}F_x\\F_y\\F_z\end{bmatrix}_{t=2} \\ \vdots \\ \begin{bmatrix}F_x\\F_y\\F_z\end{bmatrix}_{t=N_T} \end{bmatrix}}_{F} = \underbrace{\begin{bmatrix} \begin{bmatrix}R_{tc_x} & R_{te_x} & R_{fc_x} & R_{fe_x} & 0 & 0\\ R_{tc_y} & R_{te_y} & R_{fc_y} & R_{fe_y} & 0 & 0\\ 0 & 0 & 0 & 0 & R_{rc_z} & R_{re_z}\end{bmatrix}_{t=1} \\ \begin{bmatrix}R_{tc_x} & R_{te_x} & R_{fc_x} & R_{fe_x} & 0 & 0\\ R_{tc_y} & R_{te_y} & R_{fc_y} & R_{fe_y} & 0 & 0\\ 0 & 0 & 0 & 0 & R_{rc_z} & R_{re_z}\end{bmatrix}_{t=2} \\ \vdots \\ \begin{bmatrix}R_{tc_x} & R_{te_x} & R_{fc_x} & R_{fe_x} & 0 & 0\\ R_{tc_y} & R_{te_y} & R_{fc_y} & R_{fe_y} & 0 & 0\\ 0 & 0 & 0 & 0 & R_{rc_z} & R_{re_z}\end{bmatrix}_{t=N_T} \end{bmatrix}}_{R} \underbrace{\begin{bmatrix}K_{tc}\\K_{te}\\K_{fc}\\K_{fe}\\K_{rc}\\K_{re}\end{bmatrix}}_{K} \tag{6.8}$$

Finally, using linear least squares regression, the cutting coefficients can be estimated from the measured forces (F_{meas}):

$$K = pinv(R)F_{meas} \tag{6.9}$$

Above, *pinv* is the Moore-Penrose pseudoinverse function. [1]

6.3.4 Machining experimental setup

The workpiece geometry was segmented into rows and columns in order to characterize the cutting coefficients at different depths into the workpiece. As illustrated in Figure

---

[1] This section is reflective of written contributions from Andrew Katz

6.9, the height of the workpiece was sectioned into 10 rows, each being 1 mm in depth. Similarly, along the direction of the workpiece wall, 10 equally spaced columns are defined, each about 5 mm in length. A staircase pattern is generated to allow for hardness testing at different depths.

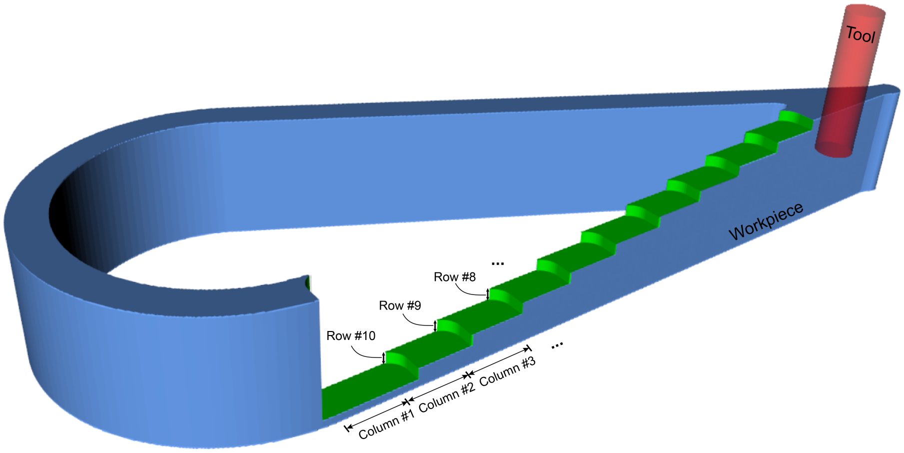

Figure 6.9: The workpiece is divided into rows and columns for the machining experiments

Using a Kistler 9255A dynamometer, cutting forces were collected on a Haas VF-2YT 3-axis CNC vertical mill. The staircase pattern (pictured in Figure 6.9) was machined into four workpieces (#4, #5, #6, and #8). The rows and columns were machined in segments, each at a specific row and column and being 0.5 mm in depth, as shown in Figure 6.10. The staircase in workpiece #5 was machined in row-major order two segments at a time, while workpieces #4, #6, #8 (shown in Table 6.1) were machined in column-major order one segment at a time. Figure 6.11 shows the experimental setup and an example of a finished workpiece. The spindle speed in all cases was 4500 rpm. The feed rate per tooth while machining workpiece #5 varied between 0.0152 and 0.0356 mm. It was found that a feed rate per tooth of 0.0254 mm gave the most consistent (stable) cut, and was thus used for all segments in workpieces #4, #6, and #8. [2]

6.3.5 Characterization tests

The DED-manufactured parts are scanned by a 3D optical structured light scanner (HEXAGON MI, UK) to obtain the 3D topography data. The white light scanner digitizes objects at

---

[2] This section is reflective of written contributions from Andrew Katz

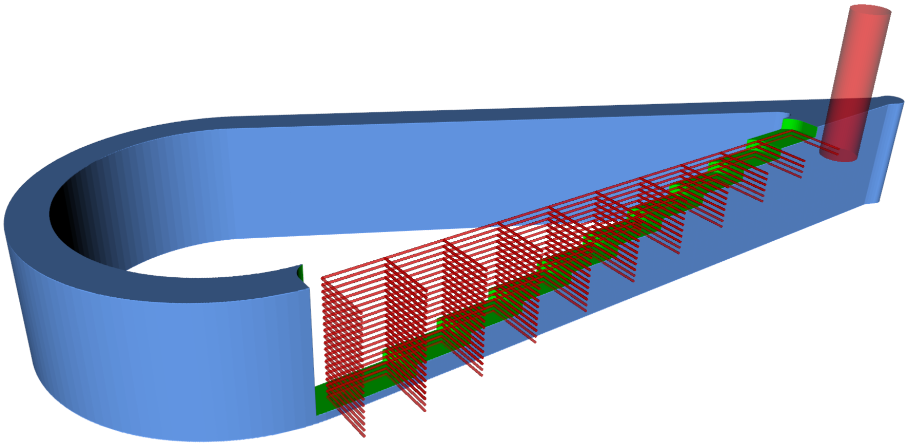

Figure 6.10: Workpiece segments showing the cutting test pattern for the columns and rows

Figure 6.11: Experimental setup and finished workpiece

a high speed irrespective of their size in a time efficient way. The data collected is then converted to an stl file. The stl file is then corrected to ensure that the resulting alignment of the scanned build plate is parallel to x-y plane and that the build direction is along the z axis in a positive direction. In order to detect the geometric inconsistencies in a height map representation, the stl file is converted to a point cloud data.

The machinability of the parts is directly related to the hardness of the material. Thus, two cross-sections are obtained from each sample to perform hardness tests along the height of the deposition. Vickers microhardness testing was performed on the polished samples using a Clemex CMT Automated microhardness machine with an indentation force of 500 gf. The approximate location of the cross-sections is shown in Figure 6.12. The cross-section plane is selected to perform the hardness tests because the cutting tool engages with this surface during machining. Furthermore, multiple points are measured throughout the height of the sample to investigate the changes in hardness and the effect of cyclic thermal loading on the hardness of the material. The measurement locations of the points are shown in Figure 6.13. There are in total of 8 measurement points for each cross-section, distributed in 4 rows and 2 columns. The distance between columns is approximately 1 mm and the distance between the rows is approximately 3 mm.

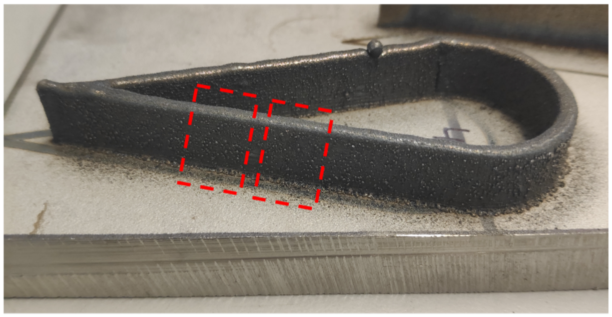

Figure 6.12: Two cross-sections taken from each sample from one of the straight walls of the sample shown in red dashed boxes

6.3.6 Hybrid approach strategies

Machining is one of the commonly used post-processing technologies deployed after the AM step to improve the dimensional accuracy, surface quality and to remove defective regions of the part. In this study, two machining strategies are proposed for additively manufactured parts. Both of strategies aim to deploy intelligent decision schemas based

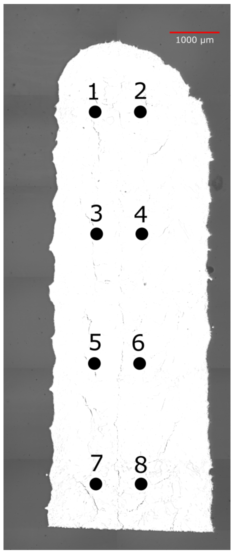

Figure 6.13: Cross-section taken from one of the samples, showing the measurement points for the micro hardness testing

on the pyrometry data based on correlations with geometric fidelity data. The out-of-bound melt pool signatures are detected to flag possible defective regions or layers to machine and potentially remanufacture, or to identify regions in the part where defects commonly occur such that post-process inspection and machining may prioritize and address those sites. The first strategy described focuses on this latter strategy of post-process machining and does not necessarily require a hybrid system for implementation. The second strategy is a layer-intermittent machining operation. The machining process can be performed in between layers of the DED process and AM process continues after layer-intermittent machining, where a hybrid (additive and subtractive) manufacturing system is essential for maximizing efficiency during operation.

6.3.6.1 Post-processing machining schema

Post-process machining is performed on the final geometry of the part, which can be done in a separate manufacturing system or in a hybrid system. Post-process machining is commonly used after the AM processes, if the required dimensional tolerances are tight and the surface quality requirements are high. However, post-process machining may not be needed in certain regions of the part, depending on the AM process performance. Thus, an inspection is traditionally needed to decide where and how much to machine the part.

This inspection could be as simple as measuring geometric features (CMM, structure light scanning, touch probe), or as complicated as CT scanning and high resolution microscopy, which require more time and effort to perform. In this study, the in-situ monitoring data is investigated to determine a correlation between the process signatures and final part geometric feature outcomes. With this correlation, the lengthy post-process inspection of the whole part could be simplified and post-process machining planning could be done in a more intelligent and effective way by prioritizing on regions of interest.

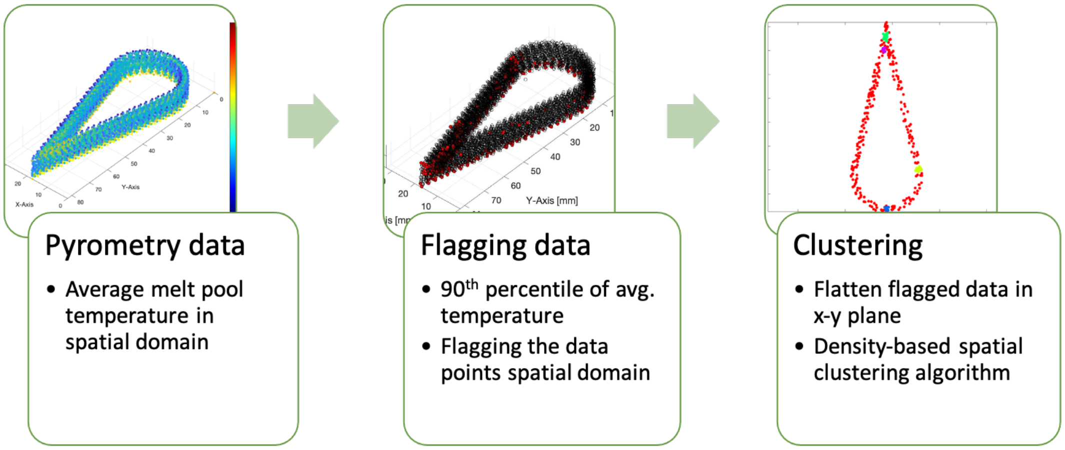

Figure 6.14: Workflow of the proposed post-processing machining schema

The workflow of the proposed strategy is illustrated in Figure 6.14. The proposed strategy finds the out-of-bound pyrometry signals by taking the 90^{th} percentile of the detected average temperature data and by flagging these data points. It is hypothesized that the flagged data points accumulate in specific regions, which can result in a geometric defects. Although the geometric defects can be small for one layer and can be within the dimensional toleracnes of the final part, the geometric defects can propagate to upper layers and can grow if they are not addressed early on due to misalignment between the focal distance of the nozzle and the substrate. Some of these regions could be predicted and expected due to critical geometric features such as sharp corners and curvatures, where acceleration and deceleration occur. However, some of the flagged data points could occur in unexpected regions due to random events occurring during the AM process and their propagation on the upcoming layers can contribute to out-of-bound pyrometry signals. The accumulation of the flagged data points is calculated on the x-y plane by performing a density-based spatial clustering algorithm. Density-based spatial clustering is a non-parametric algorithm that is commonly used in data mining and machine learning. Given a set of points in spatial domain, the algorithm groups together points that are closely packed based on a distance measurement and a minimum number of points. In this study Euclidean distance is used and the size of the group for one cluster is 10, which is defined based on a sensitivity analysis. The clustered regions are then compared with the optical 3D scan data qualitatively to match the clustered data points with the geometry deviations in the final part. Such clusters are proposed to be used to identify regions that may require machining intervention in the final part.

6.3.6.2 Layer-intermittent machining schema

Layer-intermittent machining can be performed in case there are significant defects on the current layer or in case there is a need to machine features which are going to be inaccessible by the cutting tool due to the changes in the geometry during the AM process. This study focuses on the first case and proposes a classifier to make intelligent decisions to qualify the deposition process in a layer-by-layer manner. The workflow of the proposed schema is shown in Figure 6.15. A hyrbid manufacturing system is needed to be able to perform layer-intermittent machining and remanufacturing in a time efficient way.

A kNN classifier is trained based on four features: (i) the standard deviation of the average (measured) temperature, (ii) the standard deviation of the normalized enthalpy, (iii) the standard deviation of melt pool width, and (iv) the standard deviation of the melt pool length. Two labels are created as out-of-bound and normal, based on the average normalized enthalpy per layer. The layer is tagged as out-of-bound if normalized enthalpy is larger than 6, which is known as the keyhole threshold for SS316L [185]. In the kNN algorithm, k is set to 5 and the distances are calculated based on Euclidean method. The k-fold method is used in cross-validation, where k is set to ten, with random training and testing datasets.

Once the decision is made based on the kNN classifier, the machining process can be partially planned based on the predictions from the thermomechanical and geometry models. By simulating the cooling of the part, it can be decided when to start the machining operation and how to prioritize the sequence of regions for machining (out of scope for the present study; part of future work). This could be highly critical because the freshly-deposited material can be more difficult to cut depending on the material temperature and may generate higher forces and friction between the cutting tool and the material specifically in dry cutting, where coolant cannot be used in a hybrid system. The geometry model can be used for simulating the layer thickness of the last year based on the temperature measurements. This can help in defining the depth of cut for the machining operation, although other parameters such as cutting tool, feedrate and spindle speed should be considered in conjunction with the depth of cut.

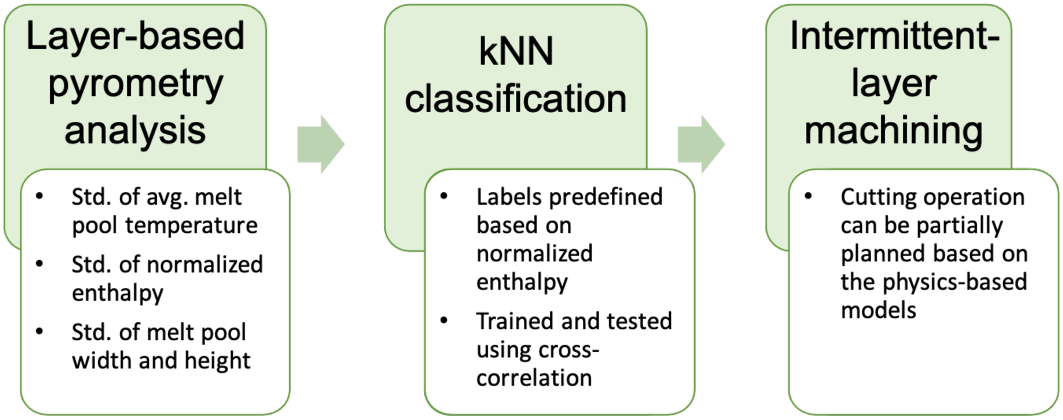

Figure 6.15: Workflow of the proposed intermittent-layer machining schema

6.4 Results and discussion

6.4.1 Pyrometer and simulated temperature results

The physics-based thermomechanical model is simulated for the manufactured geometry by discretizing the toolpath, defining the neighboring voxels, and computing the heat transfer equations between the voxels recursively, at each time step. A dual-wavelength pyrometer is integrated coaxially with the laser beam to estimate the instantaneous melt pool temperature. The simulation results and the average melt pool data collected experimentally are compared to validate the performance of the physics-based model. Figure 6.16 shows the comparison of the simulation and experimental results. Row (A) and (B) represent the results for recipe 1 and 2, respectively, as described in Table 6.1; the figure compares the simulation and experimental results as a function of the travelling distance for each recipe, where the red and blue lines show the experimental results for replicate 1 and replicate 2 for wach recipe, respectively, and the black dashed line shows the simulation results. Figure 6.17 (A) and (B) is another representation of the recipe 1 and 2, respectively, showing the root mean square of the prediction error as a point cloud throughout the 3D object for replicate 1. There were outlier data points observed in pyrometry signals for recipe 2, which have been removed because it represents saturated data. The simulation points in the spatial domain (in x-y plane) are down-sampled to match the data points from the pyrometry measurements.

The experimental results illustrate two different trends, as captured in Figure 6.16 in rows (A) and (B). Row (B) shows the results for recipe 2, which is in keyhole mode based

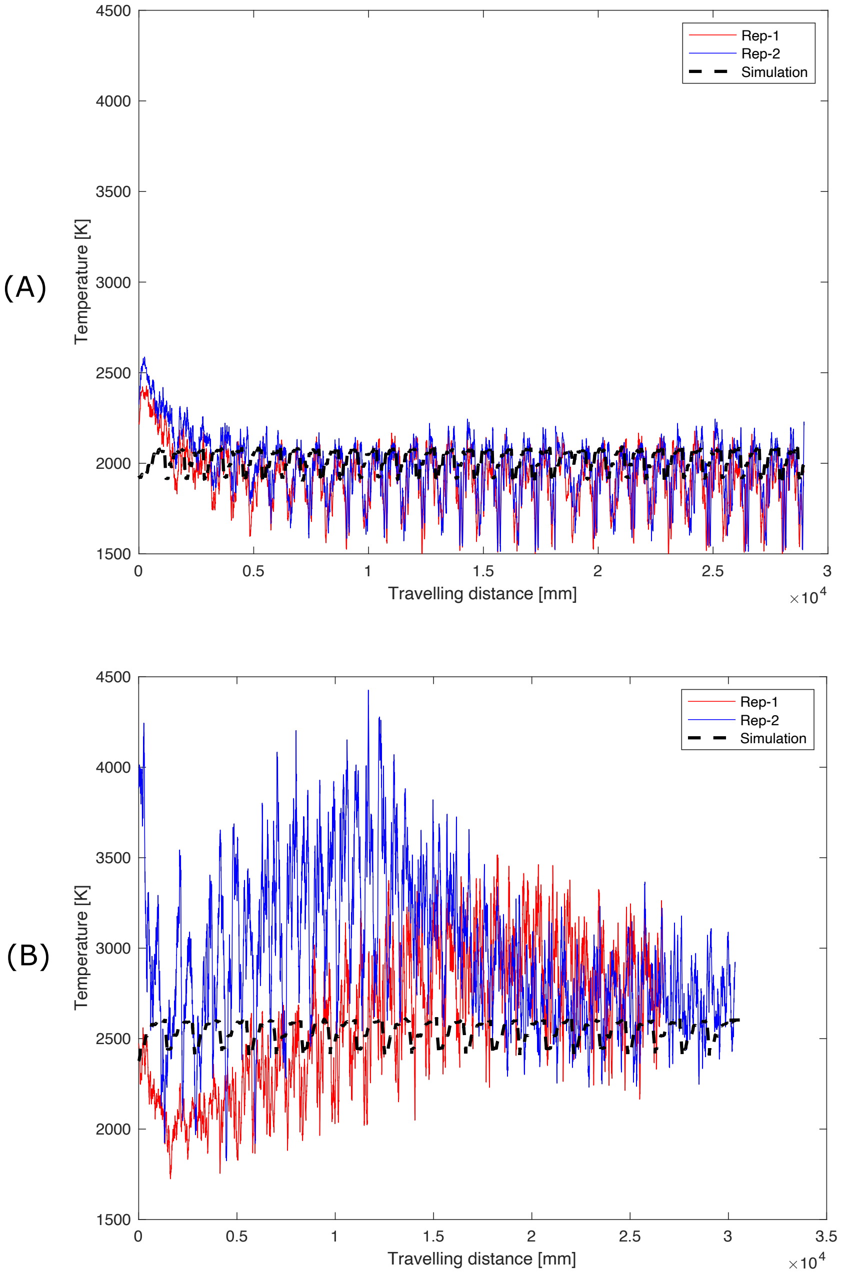

Figure 6.16: Comparison of the simulation and experimental results as a functional of travelling distance, where row (A) and (B) show the comparison for Recipe 1 and 2, respectively.

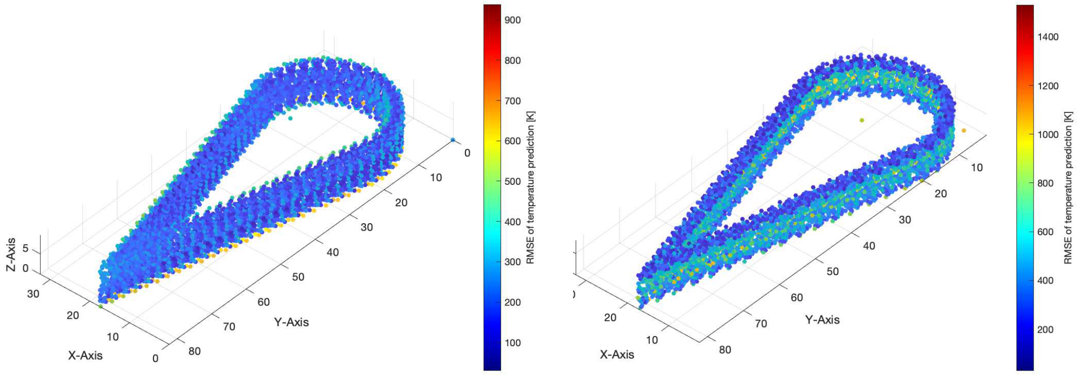

(A)

(B)

Figure 6.17: Comparison of the simulation and experimental results, where column (A) and (B) show the comparison for Recipe 1 and 2, respectively. The comparison is represented as the root mean square of the prediction error, where the average of the temperature signal from two replicates for each recipe is taken and the error is calculated.

on the normalized enthalpy calculation [152] and experienced higher plasma plume formation and smoke during the experiments; these factors contribute to severe uncertainties in pyrometer signal data, as seen by a noise pattern overlayed with the signal and increased low frequency drift and fluctuations in the data. In addition, the sensor calibration spans 1100^{o}C - 2500^{o}C, therefore the temperature readings outside of this range can be considered as unreliable. In looking at trends only, for recipe 2, the pyrometry-inferred melt pool temperature data shows an increasing trend at the beginning and it drops for replicate 2; however, after the increase it settles down for replicate 1, as shown in Figure 6.16(B). The temperature results for recipe 1 show more consistent results between replicate 1 and 2, where higher temperatures are seen at the first few layers, with reaching steady state after. An increasing trend in instantaneous melt pool temperature is not observed while printing upper layers. The reason for this could be that the contours are printed unidirectional such that enough time passes between two consecutive contours. Recipe 1 observes a better match between the trends in the simulation and experimental results, as shown in Figure 6.16(A). The reason for different trends between two recipes could be that they are chosen from different melting modes, with recipe 2 operating outside of the sensor calibration range, as well as the order of the printing process. Recipe 2 samples are printed first and then recipe 1, where the built plate reaches a steady state temperature after manufacturing the first batch of samples; this hypothesis is plausible, however it is difficult to demonstrate after the fact. A higher variation is observed for recipe 2, where unstable thermal signatures can be seen in Figure 6.16(B), owing to the sensor operating outside of the calibration range during keyhole melting mode, in addition to the data compounding contributions from increased process temperatures, plasma plume effects, smoke, spatter, and meltpool instability. This affects the prediction error, where a maximum of 1400 K is observed as RMSE of the predicted melt pool temperature value.

Similar findings were achieved by Jelinek et al., where they developed a 2D thermal heat transfer model using an open source finite element suite for a DED process and validated their results with a dual-wavelength pyrometer [169]. They state that alternating deposition directions causes an increase in melt pool temperature, where unidirectional depositions lead to more uniform melt pool temperatures [169]. Furthermore, Nair et al. developed a method to monitor the cooling rate of deposited tracks using two pyrometers in tandem and concluded that the instantaneous melt pool temperature does not vary throughout a multi-layer object [265]; however, the cooling rate is affected significantly with the temperature build-up throughout the part [265]. Although an increase in melt pool temperature is observed towards upper layers in recipe 2 results with a high variation, the recipe 1 results show a more stable signal with a better agreement with the proposed model in Chapter 3 and in [106] and with literature.

It is valuable to simulate the DED process using physics-based process model before the deposition experiment to infer a prior knowledge of the expected melting mode studied in Chapters 3 and 5 and to infer reliability of sensor data as the process pivots into instability zones such as lack of fusion, keyhole and balling regions, also shown in Chapter 5. Deployment of secondary vision-based detectors as described in Chapter 5 plays an important role to detect spatially-resolved process phenomena and confirm the process drift into such instability zones. Furthermore, the geometric deviations can be modeled and observed, which can be further indicative of unstable process zones where the process can result in geometric, porous, or microstructural defects. To conclude, neither pyrometry data alone, nor modeling data alone are sufficient to rely upon due to the complex nature of the DED process. Ideally they should be used in combination to be able to asses the confidence level in sensor data, infer process condition and part quality [90]; furthermore, data fusion from multiple sensors should be deployed for this purpose.

6.4.2 Machining test results

Using the measured cutting forces and the cutting force simulation model (presented in Section 6.3.3), the cutting coefficients were calibrated. In 3-axis milling, especially with small feed rates and small chip thicknesses, the z axis force provides a poor signal-to-noise ratio. It is generated by the radial force (F_r), which is the smallest force component in most milling cases. Additionally, it was found that calibration of the edge coefficients (K_{te}, K_{fe}, K_{re}) was unstable and gave invalid (e.g., negative) values. This is likely due to rapid deterioration of the cutting edge and the very thin chips produced (0.5 mm wide by 0.0254 thick). These thin chips would thus make the calculated cutting force very sensitive to the edge coefficient. Thus, it was decided to use a simplified model, only considering the tangential and feed cutting coefficients (K_{tc} and K_{fc}), and performing comparison with only the tangential cutting coefficient (K_{tc}), which is also known as the specific cutting pressure.

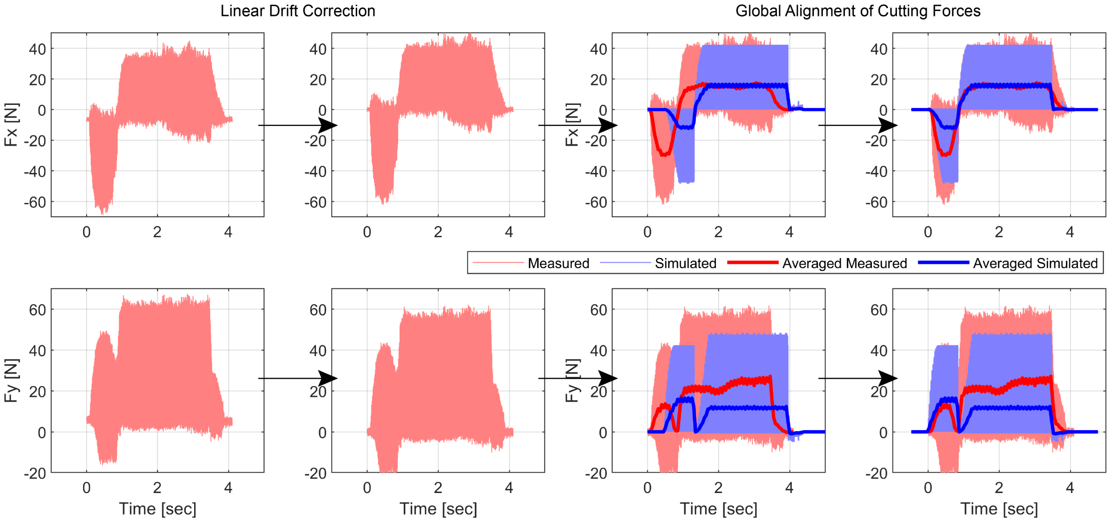

Figure 6.18: Linear drift correction and global alignment of measured cutting force

To calibrate the cutting coefficients, the measured cutting forces must be aligned precisely to the simulated signal. For each segment, the measured cutting force is corrected for linear drift as shown in the left side of Figure 6.18. Then, the moving average of both the measured and simulated signals are calculated and aligned globally using an automated trial-and-error algorithm, as shown in the right side of Figure 6.18. Then, a main calibration window is defined, manually, during a steady-state portion of the cutting (Figure 6.19). The entire cutting profile cannot be used because the exact kinematics of the tool path are unknown — only the coordinates of the path are known. The kinematics between the coordinates are machine-dependent, and the Haas machine does not allow for collection of the position CNC signals. Within the main calibration window, small subwindows are defined, and the simulated and measured signals are aligned again, locally within each subwindow. This is necessary, since the spindle speed of the actual machine is not exact, thus the simulated and measured profiles go out of synchronicity eventually.

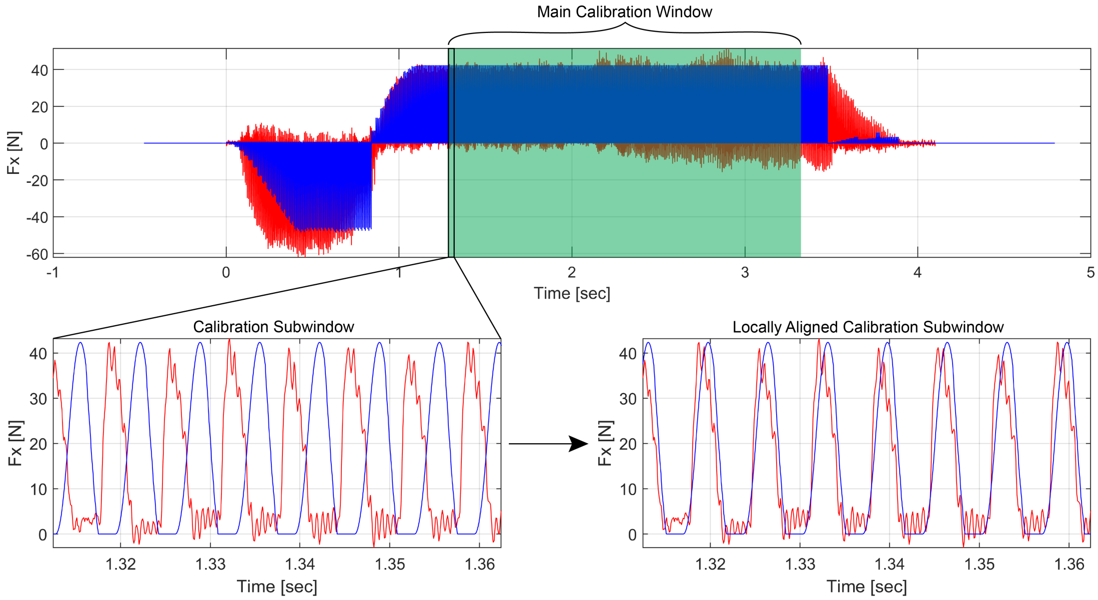

Figure 6.19: Main calibration window, calibration subwindows, and local alignment of subwindow

Figure 6.20 through Figure 6.23 below show the resulting specific cutting pressure, as a function of depth below the workpiece surface. For each workpiece, two to three tools were budgeted, and the asterisks indicate where the tool changes occurred. Note that the top two segments of each column were ignored in the cutting coefficient calibration since the top surface of the workpieces were rough and rounded and thus needed to be faced for the cutter to be fully engaged, hence the plots start at 1.5 mm depth below surface (except for workpiece #6, which starts at 2 mm since it was particularly rough). Figure 6.24 shows the specific cutting pressure for each new tool as a function of number of segments cut. From this data, two major trends can be seen. First, the specific cutting pressure increases as depth below surface increases. Second, the specific cutting pressure increases as number of segments cut increases. However, it is unclear if the first trend with respect to depth below surface is due to differing workpiece material properties or due to tool wear. Tool wear images were collected intermittently throughout the cutting trials using a Dino-Lite Pro USB microscope. Figure 6.25 shows an example of the tool wear progression for workpiece #8 tool #1. It can be seen that the cutting edge deteriorates quickly and substantially, thus it is hypothesized that the trend with respect to depth below surface is due to tool wear and not workpiece material properties.

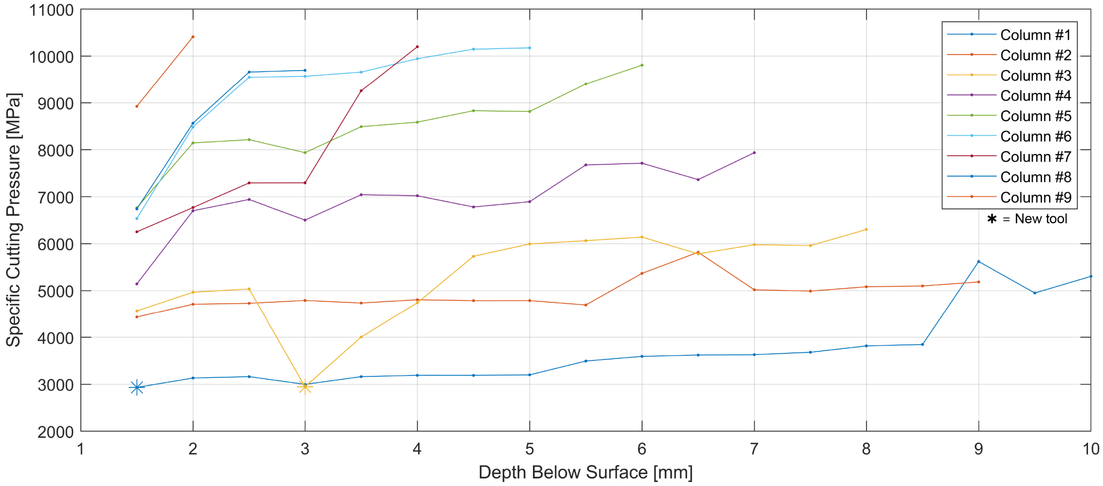

Figure 6.20: Trial #1 workpiece #4 specific cutting pressure vs. depth below surface

To gain clarity on how the depth below surface affects the specific cutting pressure, a second set of cutting trials were performed. In these trials, only a single column of segments was machined in each workpiece. However, the tool was changed after every second segment, thus using a total of 10 tools per workpiece. The tool wear would then have very little impact on the specific cutting pressure as it does not have adequate cutting length to develop a deteriorated cutting edge. Figure 6.26 shows the results from these trials. It can be seen that the specific cutting pressure does not show any major trend as a function of the depth below surface. From these trials, it can be concluded that the factor which most significantly impacts the specific cutting pressure is the tool wear. To come up with economical strategies for hybrid machining, further trials should be performed investigating the best tool coatings, feeds, and speeds to use in order to minimize the tool wear and maximize productivity, specific to the deposited material type. This is, however, an area for future research.

Similar findings can be seen in literature, where tool wear and tool life are highlighted as important issues in machinability of additively manufactured parts [82, 61, 160]; however, there are no studies to date pointing that tool wear is the main mechanism that causes increase in cutting forces. Although it is difficult to make comparisons with literature due to high variability in the material, microstructure, tool design, coating and additive/subtractive process conditions [227], tool wear and tool life were found to be

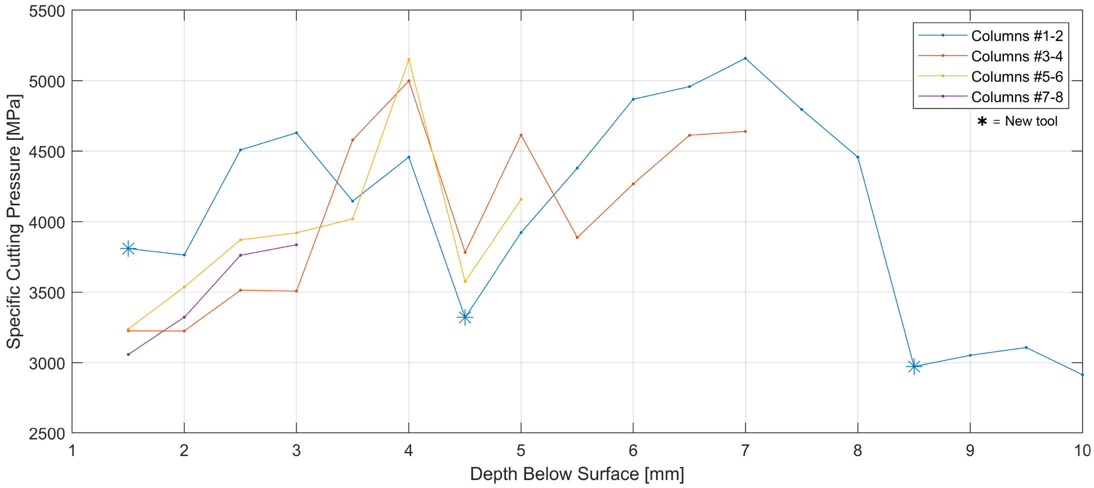

Figure 6.21: Trial #1 workpiece #5 specific cutting pressure vs. depth below surface

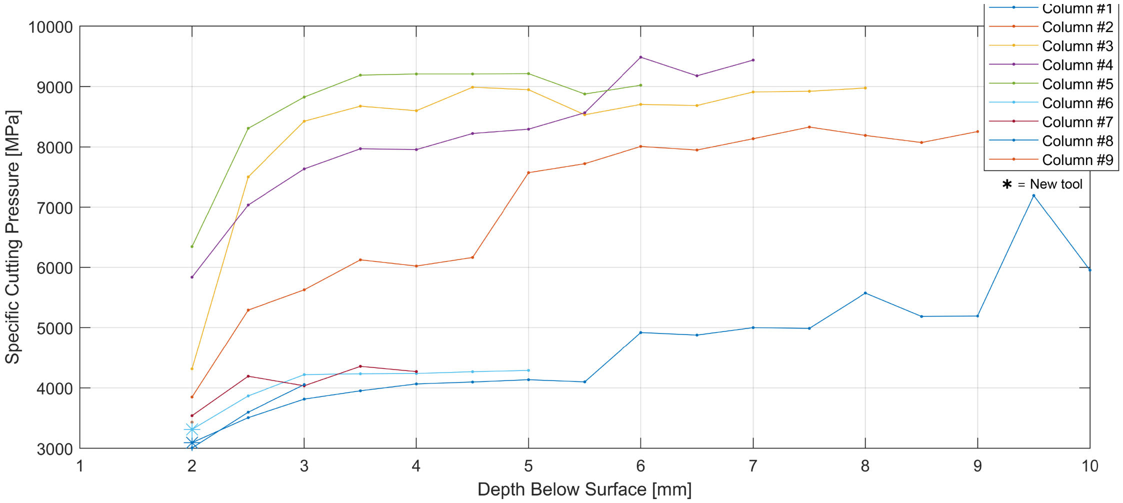

Figure 6.22: Trial #1 workpiece #6 specific cutting pressure vs. depth below surface

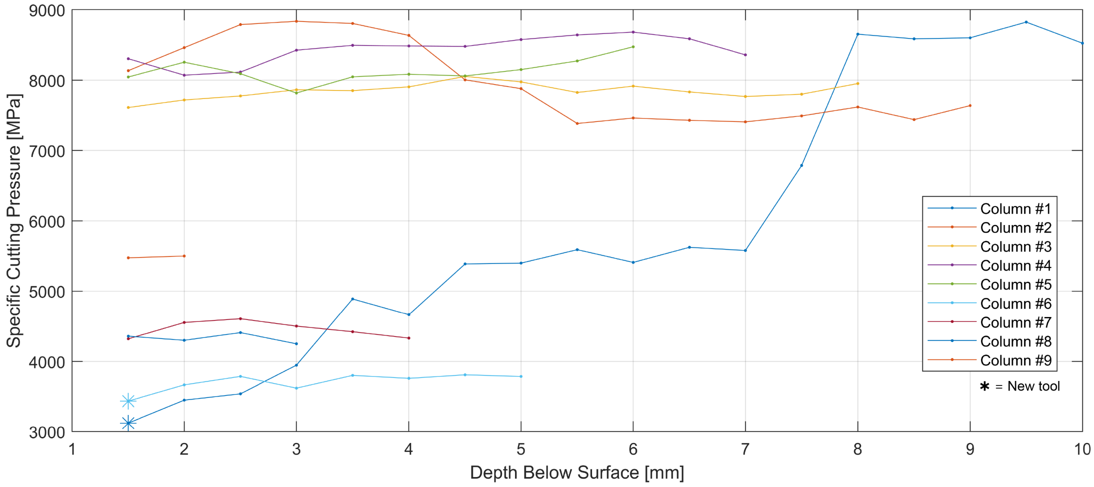

Figure 6.23: Trial #1 workpiece #8 specific cutting pressure vs. depth below surface

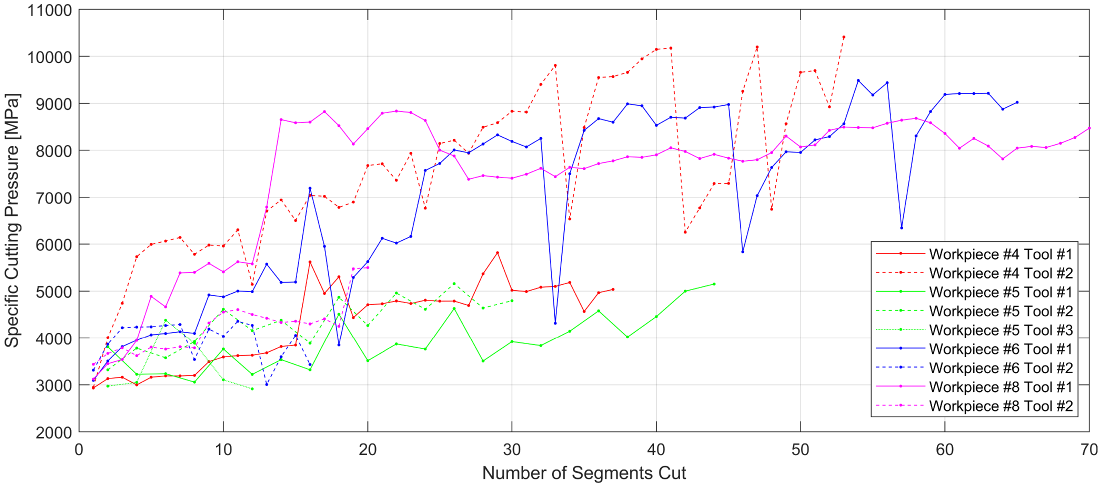

Figure 6.24: Trial #1 specific cutting pressure vs. number of segments cut

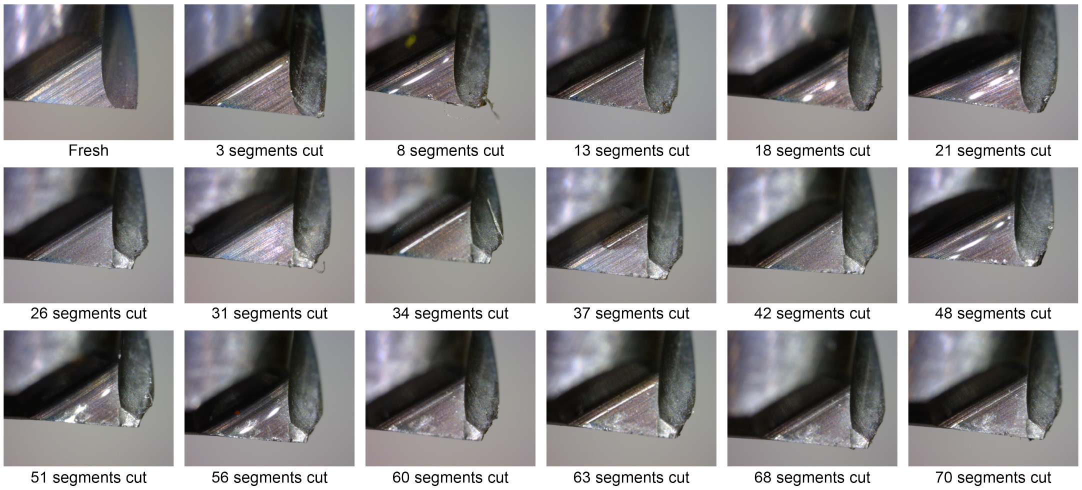

Fresh

3 segments cut

8 segments cut

13 segments cut

18 segments cut

21 segments cut

26 segments cut

31 segments cut

34 segments cut

37 segments cut

42 segments cut

48 segments cut

51 segments cut

56 segments cut

60 segments cut

63 segments cut

68 segments cut

70 segments cut

Figure 6.25: Tool wear progression for workpiece #8 tool #1

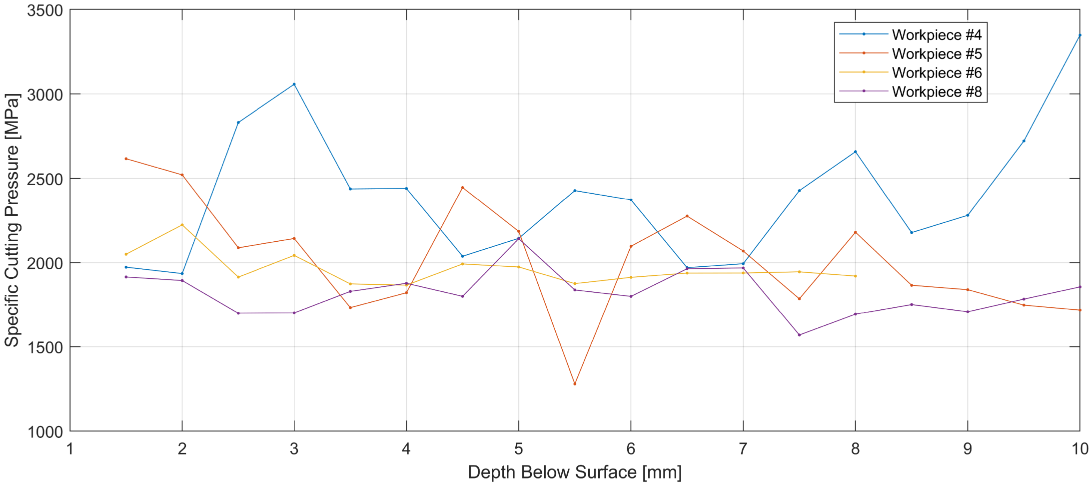

Figure 6.26: Trial #2 specific cutting pressure vs. depth below surface

a common concern by the researchers [423]. Thus, better process control is required to minimize machining interventions, and better strategies for efficient identification of areas where machining are required, rather than machining of large areas. In addition, a prior knowledge of expected thermal cycling experienced by the material system (inferred from modeling and/or pyrometry) can help in the selection of machining parameters. Furthermore, cutting force models can predict forces and manage expectations on tool life, where machining process parameters can be adjusted based on the predictions.

6.4.3 Part characterization - surface topography and hardness results

The samples were scanned by a 3D optical structured light scanner to obtain the final shape of the samples in stl format. An example of one of the raw scanned stl files can be seen in Figure 6.27, which is a sample deposited with recipe 2. After some processing on the stl files such as eliminating the unnecessary data points and making the substrate surface parallel to the x-y plane, the data is converted to a point cloud data. The height maps are generated using the point cloud shown in Figure 6.28, where row (A) and (B) show the scans of the samples manufactured by recipe 1 and 2, respectively. Columns (I) and (II) represent the first and second replicate. The point cloud data shown in the height maps involve only 3 mm in depth starting from the top point of the point cloud data for each sample to be able to visualize the dimensional fluctuations on the top surface in a better way.

Figure 6.28 illustrates the processed data, as converted to height maps for each of the samples analyzed in this study. It can be seen that recipe 1 samples were more consistent in terms of having a similar height profile for the final part deposition when the replicates are compared. The average height is 9.62 and 9.37 mm for replicate 1 and 2 in recipe 1 samples, respectively, shown in Figure 6.28(A)-(I)&(II). The maximum height is 10.48 and 10.02 mm for replicate 1 and 2 in recipe 1 samples, respectively, as shown. In contrast, the average height is 9.93 and 12.12 mm for replicate 1 and 2 in recipe 2 samples, respectively, shown in Figure 6.28(B)-(I)&(II). The maximum height is 11.58 and 12.54 mm for replicate 1 and 2 in recipe 2 samples, respectively, as shown. Recipe 2 showed a significant deviation between the two replicates in terms of total height of the deposition. The max point of recipe 2 replicate 1 is at 11.58 mm mainly due to the bump on the straight wall on the right side, which can be seen in Figure 6.28(B)-(I). The rest of the top surface profile fluctuates from 10 to 10.5 mm. However, the second replicate top surface profile shows a smooth profile with minimal fluctuations ranging from 12 to 12.5 mm, shown in Figure 6.28(B)-(II). The significant differences in the replicates for recipe 2 are indicative of the types of

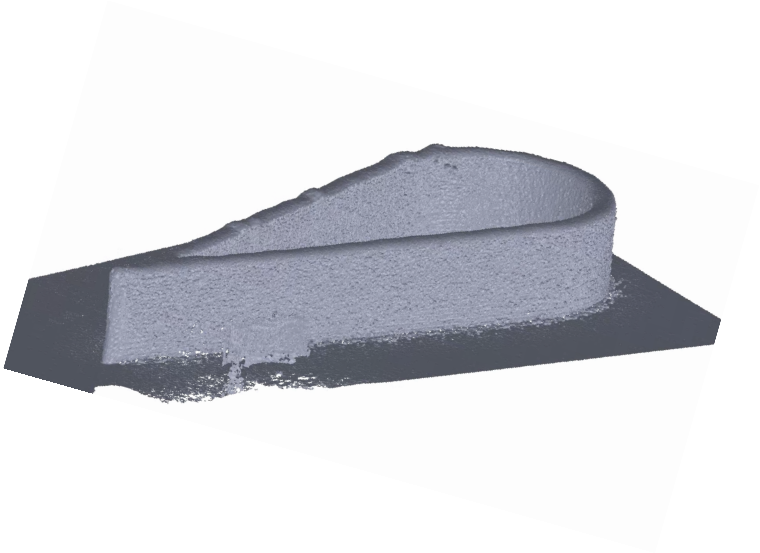

Figure 6.27: The scanned sample in its final shape after the deposition process in stl format obtained by a 3D optical scanner

uncertain quality outcomes when process parameters are selected in a keyhole domain; such deviations may be caused by the fact that the process is less stable in keyhole, resulting in unpredictable changes in powder catchment efficiency due to higher meltpool dimensions [199], changes in focal distance due to irregular surface topography [322, 151], and material spatter caused by meltpool instability phenomena [360].

Geometric deviations occur on the top surface of DED tracks, when the process is tuned, by virtue of DED process itself where weld tracks are stitched together layer-by-layer. Depending on severity, instead of scrapping the part, the dimensional accuracy can be further improved by post-process machining; however, as explained in Section 6.4.2, it is important to specify the regions and address the issue where it is needed to improve process efficiency and tool life. Although optical 3D scanning could be a fast approach compared to confocal microscopy, it is an ex-situ characterization method and the data needs post-processing to identify the regions. In-process sensor data can be leveraged to identify areas of interest for machining.

The micro hardness measurements are preformed on the vertical cross sections taken from the samples. The measurement points are shown in Figure 6.13, where there are 4 points across the height of the sample and 2 points across the width of the sample resulting in a total of 8 measurement points for each sample. The average of the 2 points across

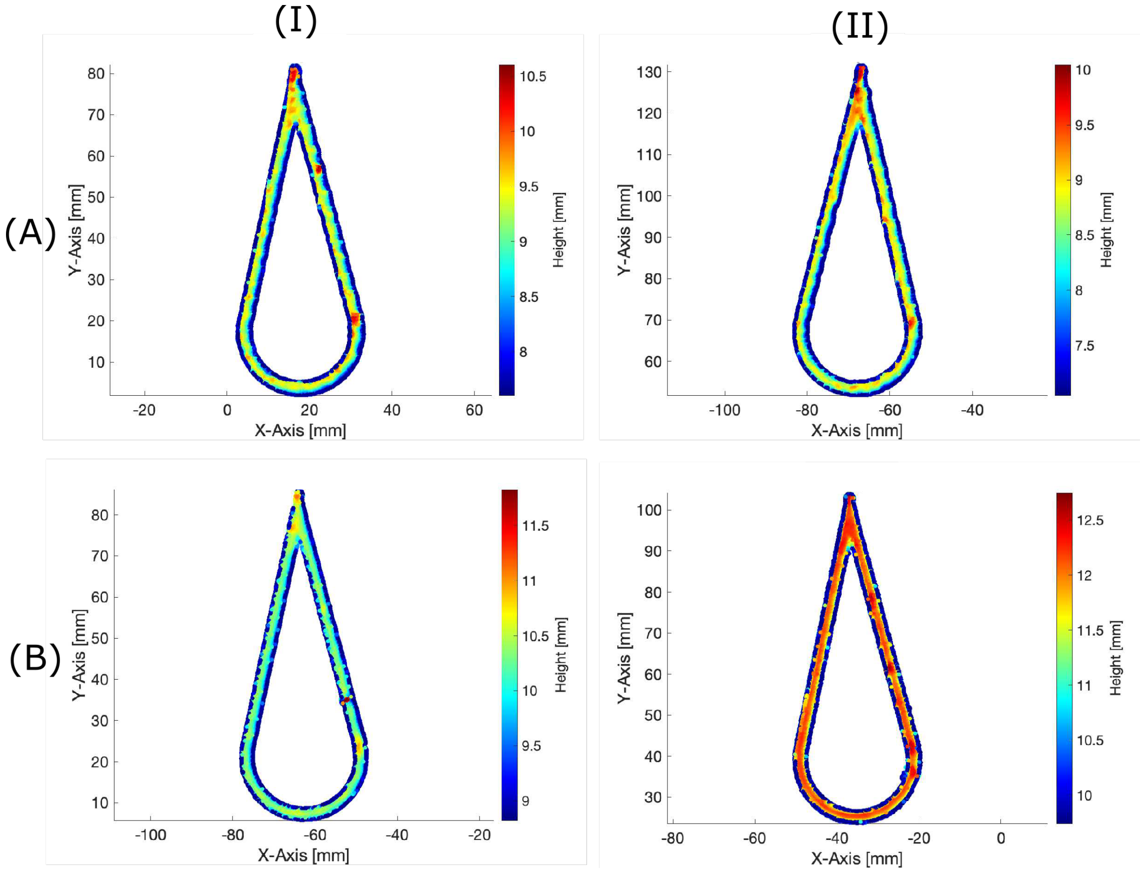

Figure 6.28: Height maps generated using the stl files obtained by 3D optical scanner. Row (A) and (B) show the samples manufactured with recipe 1 and 2, respectively. Column (I) and (II) represent the first and second replicate.

the width is taken, then each such value is plotted to show the average hardness change across the height of the samples. The results are shown in Figure 6.29, where the axes show the hardness value in HV vs. the sample height in mm, respectively. Although a consistent trend cannot be observed throughout all of the the samples, the lowest hardness is mostly on the bottom level of the samples. Some of the samples such as 6-1, 6-2, 5-2, 8-2, and 4-2 show an increasing trend when the hardness is observed from the bottom to the top, which is expected due to the cyclic thermal loading on the lower layers, as they are tempered and, as a result, soften when compared to the upper layers. A similar trend is also observed in literature [276]. In contrast, other samples such as 8-1, 4-1, and 5-1 do not show a consistently increasing or decreasing trend, although they are replicates of the samples which originally show an increasing trend when increasing the sample height. Due to the scarcity of data points, it is not possible to draw a concrete correlation between the hardness results and the cutting forces presented in Section 6.4.2. Although the hardness is directly related to the machinability of the materials, it is observed that the tool wear was the major contributing factor on the observed cutting forces. This is proven in the second trial of the machining tests, where cutting tools are changed frequently.

6.4.4 Hybrid machining decision results

Two machining strategies are explored in this study, as explained in Section 6.3.6. Both strategies explore the use of the pyrometry dataset and physics-based modeling to make decisions on the machining process, with a reference to the geometric defects measured ex-situ. Although the limitations on relying solely on the pyrometry data are highlighted in Section 6.4.1, the approaches presented herein represent a starting point for exploring hybrid machining strategies, as informed by in-situ measurement data. The first strategy is for post-processing, where the pyrometry data is collected and analyzed after the deposition process to decide where to prioritize the machining post-processing step. The second strategy is for a hybrid process, where layer-intermittent machining is proposed, where the specific layer requiring machining intervention is identified.

Post-process machining strategy

For the post-process machining strategy, the average melt pool temperature across the entire build is used based on the pyrometry dataset for each part and the outlier data is found by flagging the data points where the average temperature is in the 90th percentile of the dataset. This averaging and data flagging is performed for all the samples and replicates respectively. The flagged data is represented for each sample and each replicate in Figure 6.30. Rows (A) and (B) show the results for recipe 1 and 2, respectively, and column (I)

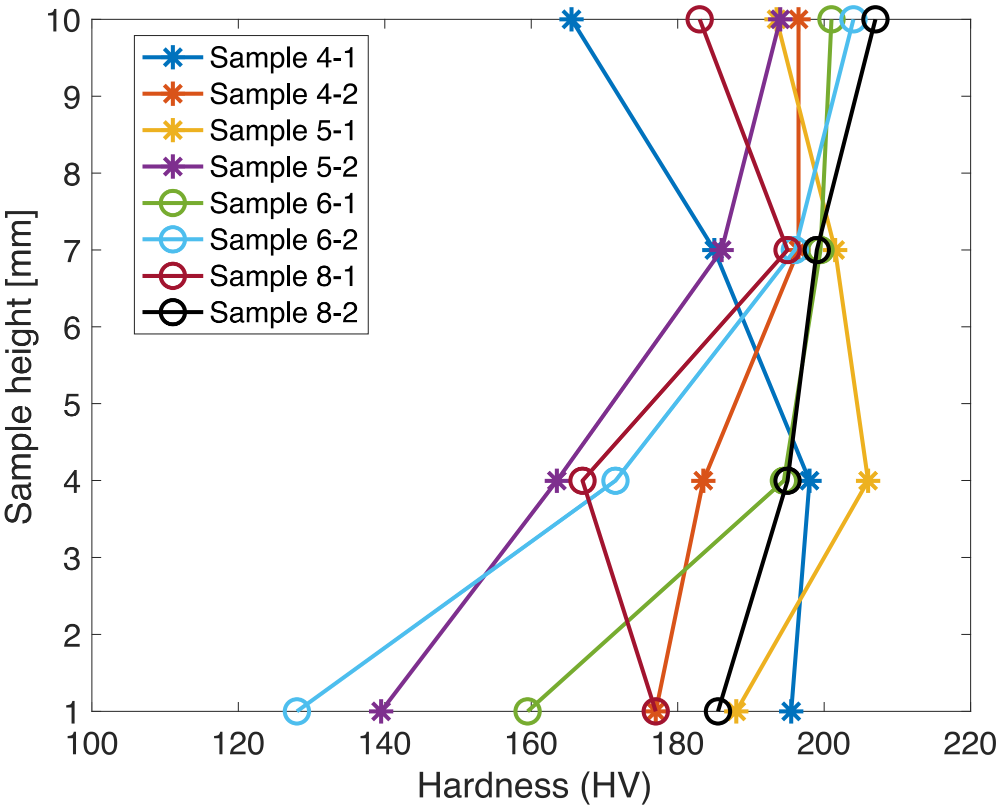

Figure 6.29: Micro hardness results shown throughout the height of each cross-section.

and (II) show the results for replicates 1 and 2. For recipe 1, in Figure 6.30(A)-(I)&(II) the flagged data is observed on the bottom layers, which was also observed in the pyrometry results shown in Figure 6.16(A). In addition, there are randomly distributed flagged data throughout the sample. On the recipe 2 replicates, more flagged data is observed in the middle layers of the sample.

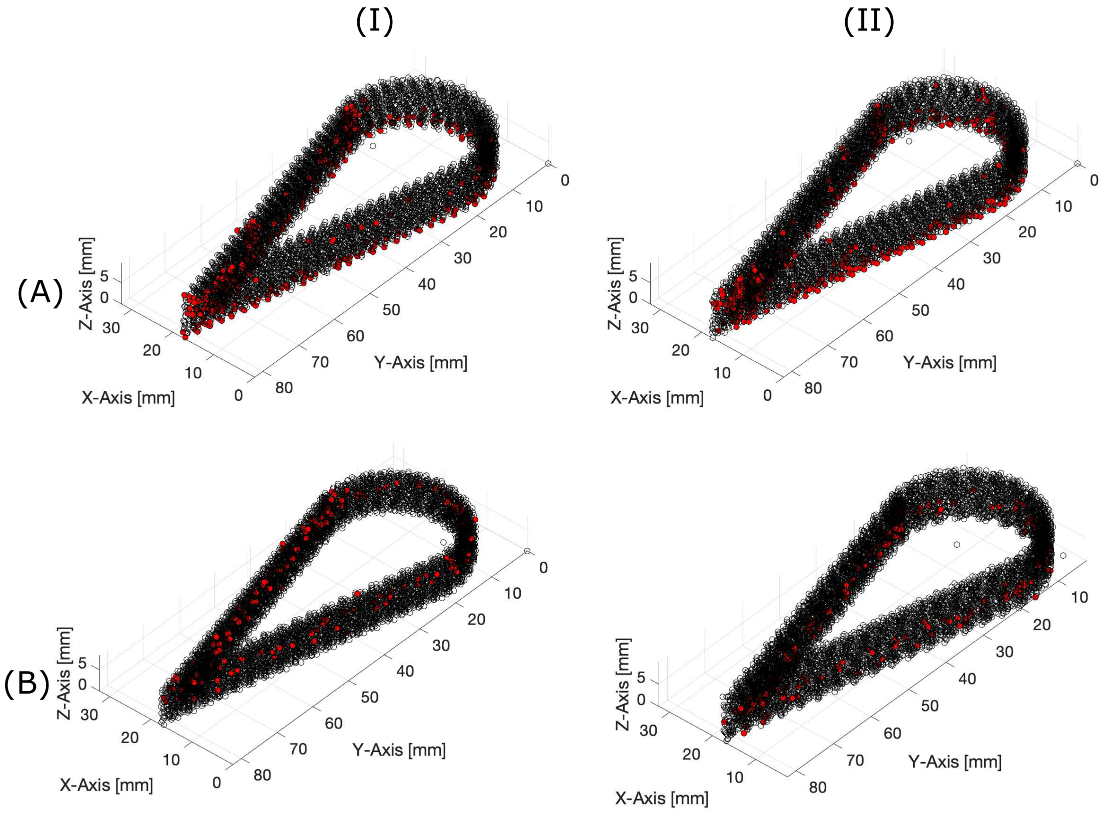

Figure 6.30: The flagged pyrometry data in 3D space, where it shows the 90th percentile of the average melt pool temperature. Row (A) and (B) show the flagged data for the samples manufactured with recipe 1 and 2, respectively. Column (I) and (II) represent the first and second replicate.

Select regions of the 3D plot in Figure 6.30 showcase an accumulation of the flagged data points. Some of these regions are located in areas where distinct DED deposition features occur, such as at sharp corners or at the beginning or end points of the contours, where the scan speed comes to a full stop. At these regions, an excessive energy input is expected due to the interplay between the constant laser power and deceleration of the deposition head. Due to the higher effective energy input, higher temperature values are expected, which can result in deviations in deposition geometry and other porous defects [117]. The accumulation of flagged data can also be observed in different regions due to instantaneous random events within the layer at the deposition site and also due to propagation of the geometric protrusions present on previous layers. Thus, a density-based spatial clustering algorithm is proposed and deployed on the 3D flagged dataset to find the regions on the x-y plane, where the flagged dataset has a higher density. The clustering results are shown in Figure 6.31, where rows (A) and (B) show the results for recipe 1 and 2, respectively. Columns (I) and (II) represent the replicates 1 and 2, respectively. The red data points show the flagged data, which are evenly distributed on the x-y plane for random events. The other data points clustered based on the proposed algorithm are shown in different colors; such points are where the algorithm detected a higher density of flagged data points projected onto the x-y plane.

In the clustering results for recipe 1, there are regions highlighted and labeled as 1, 2, and 3, which show clustering of flagged data points. The region labeled as 2 in Figure 6.31(A)-(I)&(II) contains two clusters highlighted in different colors; these two clusters may be assumed to belong to one cluster region, due to the close vicinity in location. The regions labeled as 1 and 2 have a higher density of flagged data points because the scan speed comes to a full stop at these regions, either at the start and end of a deposition (for region 1), or due to sharp changes in direction requiring acceleration and decceleration of the deposition head (for region 2). The regions labeled as 3 for both replicates in recipe 1 represent the accumulation of flagged data, where process anomalies were not expected, but where something occurred in the process. This site could be a result of random events propagated to the upper layers. At the regions labeled as 1, 2 and 3 in Figure 6.31(A)-(I)&(II), bumps at the top surface are observed in the scanned topography shown in Figure 6.28(A)-(I)&(II).

In the clustering results for recipe 2, there are no accumulated clusters of flagged data observed throughout the two sample replicates samples. Although this recipe is in keyhole melting mode and there are flagged data observed in the pyrometry dataset, there is no accumulation of flagged points that can detail cluster regions. Analogously, the surface 3D scan also observed a smoother topography at the top surface for these samples, as shown in Figure 6.28(B)-(I)&(II); however, the replicate sample variability is significant. In recipe 2, the process parameters push the boundary of the pyrometer significantly outside of the calibration margins. It is therefore not recommended to rely solely on the pyrometer data to draw decisions on the machining strategy.

Figure 6.32 shows the surface topography data overlayed on the clustering results as a sample comparison for recipe 1 and replicate 1. The highest surface topography points are shown in red dots and the background is shown in gray dots from the surface topography data. The diamond shaped markers are based on the clustering data. The blue markers show the clustered data and the black ones show the outliers. It can be seen that there is a good match on x-y plane for the blue diamond and red dot markers. This methodology can be used for identifying the regions for post-process machining, which leads to a more efficient post-processing operation in terms of time, tool life and productivity.

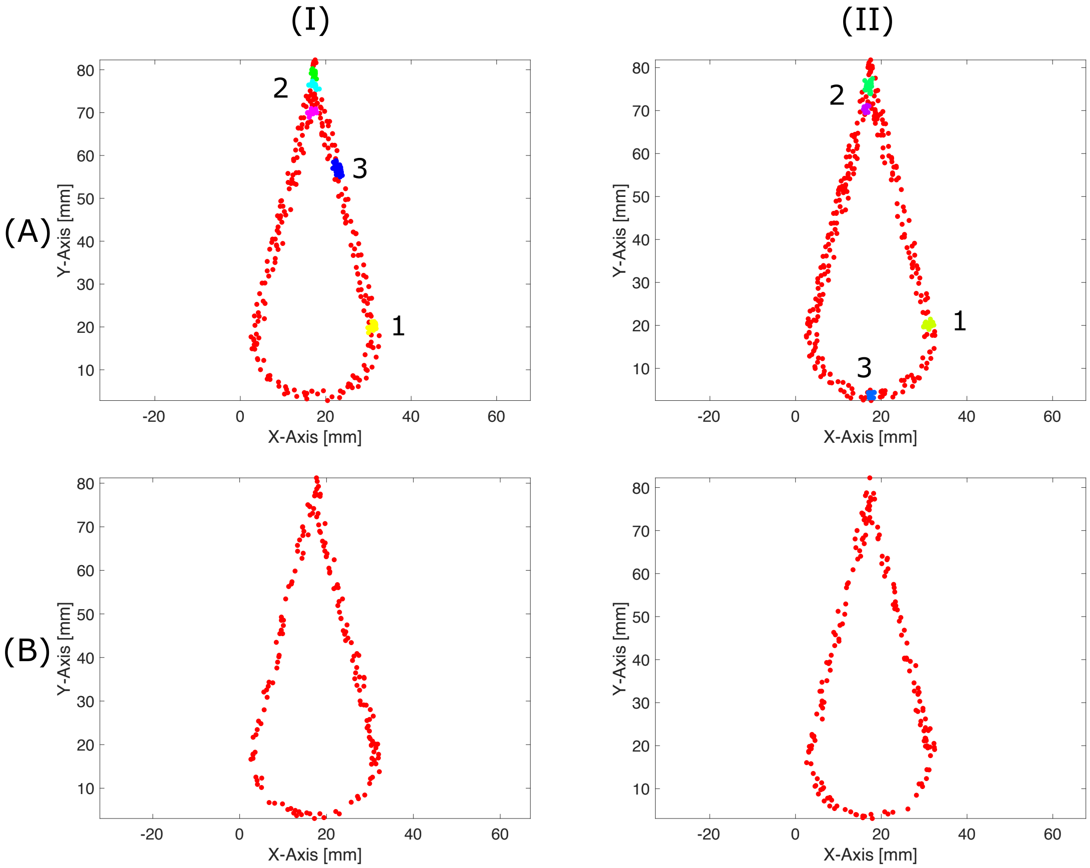

Figure 6.31: The results of density-based spatial clustering on the flagged average temperature data shown in Figure 6.30 flattened on the x-y plane

This present work shows that the clustering algorithm proposed can be used to identify the areas where geometric inconsistencies are expected to occur for conduction mode recipes; data fusion from multiple sensors and/or further experiments are required for drawing conclusions on the performance of the clustering algorithm for the keyhole melting mode. Geometric inconsistencies can be prioritized and addressed by post-process machining to obtain a smoother top surface. Furthermore, modeling can be deployed to estimate the expected geometric deviations in order estimate the anticipated height of the material at the tool engagement site and to furthermore optimize machining parameters; this aspect is out of scope for the present work. This proposed sensor-informed clustering to identify sites for post-processing machining can help to improve tool life, which was proven to be one of the most important factors in the machining process, and increase time efficiency by addressing only areas of interest on the surface.

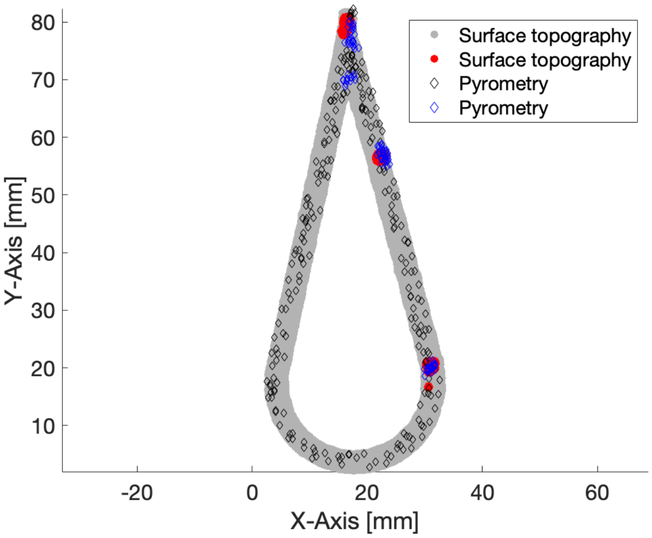

Figure 6.32: The clustering results are overlayed on surface topography results for recipe 1 replicate 1. The highest surface topography points are shown in red dots and the background is shown in gray dots from the surface topography data. The diamond shaped markers are based on the clustering data. The blue markers show the clustered data and the black ones show the outliers.

Layer intermittent machining strategy

The second machining strategy proposed in this study is layer-intermittent machining, which can only be performed in a hybrid system. To execute this methodology, a kNN classifier is trained and tested on the pyrometry dataset. Two labels are defined, namely ”out-of-bound” and ”normal”, based on the standard deviation of the normalized enthalpy of each layer, with the formulae explained in Section 3. The labels are defined based on the process physics and the features used in this classifier are only informed based on the pyrometry data. The aim is to find out if the sensor data can be used to correctly label the layers as out-of-bound or normal, where the labels are pre-defined based on the process physics as described by the normalized enthalpy criterion. It is important to note that this is a preliminary study to explore if such layer-wise quality classifiers show promise. Cross-correlation is performed using the k-fold method to test and train the classifier. The confusion matrix is shown in Figure 6.33. The average error rate obtained is 9.3% and the true positive rate is 92.2%; these results show that there is a correlation between the process signatures captured by the sensor data and the process physics what could inform a classification model. Extensive experimental work is recommended to strengthen this conclusion and to enhance the training pool of the data for such a model.

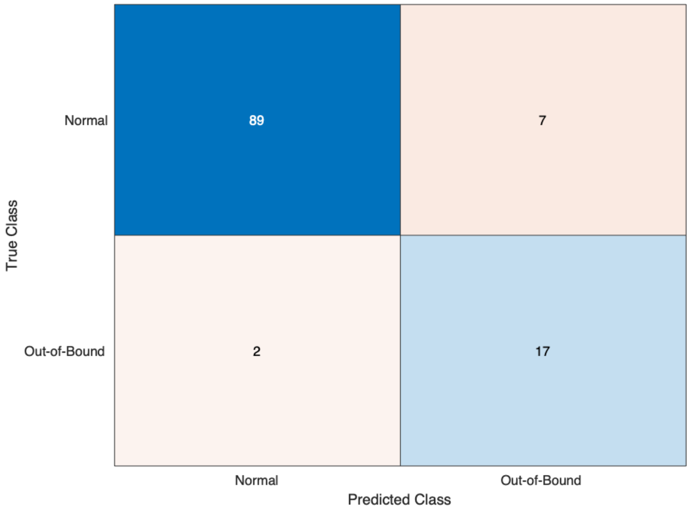

Figure 6.33: The confusion matrix of the kNN classification results of the layer-by-layer analysis

Figure 6.34 shows the pyrometry results as a function of the travelling distance extracted from two layers, where one layer was predicted as ”normal” and is shown in Figure 6.34(A) and the other layer shown in Figure 6.34(B) was predicted as ”out-of-bounds”; both example layers are taken from recipe 2 replicate 1. It can be seen that Figure 6.34(A) shows a more uniform average melt pool temperature across the whole layer, where Figure 6.34(B) shows a high temperature profile overall compared to (A) as well as a high variation across the layer. This layer-based classification method can be deployed for recipe 1 and recipe 2 samples to extract layers which can be indicative of thermal instability and severe fluctuations, since the labels are predefined based on the standard deviation of the predicted normalized enthalpy. This is in contrast to the clustering method, which showed a poor performance in recipe 2 samples, where the method did not show any sensitivity to anomalies in recipe 2 samples shown in Figure 6.31 due to the high variation in the pyrometry signal rendering the clustering technique as ineffective.

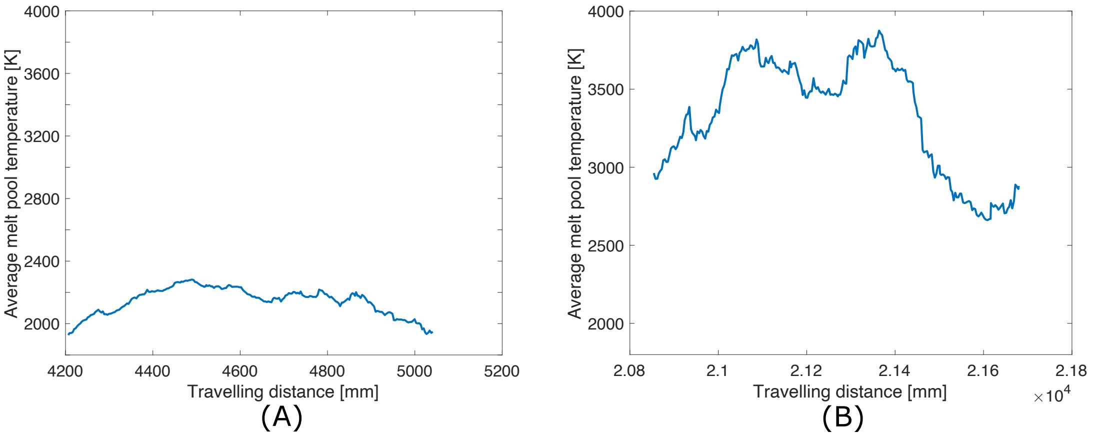

Figure 6.34: Comparison of pyrometry in two layers, where one of them (A) is predicted as "normal" and the other one (B) is predicted "out-of-bound".

In literature, pyrometry is commonly used not only for monitoring the DED process but also for validating predictive models [398], training statistical predictive models [431] and for detecting pore defects [360]. The correlation between pyrometry signals and geometric features of the deposition has not been studied in literature. This study shows that pyrometry signals can offer opportunities to detect geometric defects to assess the part quality as well as to assist the post-process machining operation. In addition, pyrometry data was used to classify layers and assist towards flagging layers for layer-intermittent machining. The proposed post-process and layer-intermittent decision-making approaches require further experimental datasets to refine and demonstrate efficacy.

6.5 Conclusions

In this study, thermal signatures from the melt pool were collected using a dual-wavelength pyrometer while manufacturing 3D parts. The thermal signatures were used for 2 primary purposes. First, to validate the physics-based model proposed in Chapter 3 and second, to find a correlation between the process signatures and geometric outcomes and propose machining strategies for post-processing or layer-intermittent machining. The machinability of the additively manufactured parts are investigated by performing cutting tests and by measuring the cutting forces. In summary:

1. The thermal model shows a good prediction fidelity when compared to in-situ pyrometry measurements for conduction melting mode; however, the pyrometry signals show an unstable behaviour when the process enters into keyhole melting mode, which affects the prediction error of the physics-based model. The thermal model can be further improved by accounting the physics phenomena in different melting modes and the work can be extended to different material systems.

2. The dual wavelength pyrometry sensor feedback can be analyzed to train algorithms which enable intelligent decisions for post-process machining. Such algorithms can be used to predict where the geometric inconsistencies occur, which can be addressed by post-process machining. Similarly, such algorithms performed better in conduction mode recipes.

3. A layer-intermittent machining approach can be performed in a hybrid system, where the in-situ sensor data is analyzed layer-by-layer. The physics-based predefined labels can be predicted by a kNN classifier using in-situ sensor data within an average error rate of 9.3%.

4. The machinability of the additively manufactured parts is mostly influenced by the tool wear and a rapid progression in tool wear is observed. Within the constraints of this study, there was no strong correlation between the hardness of the material and the cutting forces.

5. The cutting forces can be predicted accurately using the oblique cutting force model. This can help in predicting cutting load on the tool when machining inconsistent surfaces due to geometry variation, which can occur during additive manufacturing.

Chapter 7

Conclusions and future work

7.1 Conclusions

In this dissertation, a combination of process modeling, in-situ monitoring approaches, and part quality outcomes are utilized to define and detect process instabilities, provide a schema for intelligent decisions on process quality, and propose corrective actions such as machining. The theoretical and experimental methodologies described in this dissertation can directly contribute towards accelerating industrial adoption of metal AM processes. Specifically, the outcomes from implementing the methodologies described herein can directly enhance part quality assessment by detecting and predicting the most common defects in DED, such as geometric and meltpool instability. This can be achieved by performing in-situ process monitoring via imaging and pyrometry, extracting features of interest from the feedback signal, and classifying such features using statistical or machine learning methods proposed in this dissertation. Furthermore, process quality outcomes can be predicted by using process maps based on process modeling before manufacturing the part. Lastly, the methods proposed in this dissertation can offer insights into corrective machining strategies to avoid scrapping the part, which makes the process more cost- and time-efficient. The methodologies described in this dissertation have the potential to improve process reliability and efficiency.

The main dissertation conclusions are outlined as follows:

1. In Chapter 3, the proposed physics-based thermal and geometry models predict the melt pool temperature (compared against experimental data in Chapter 6) and deposition geometry (compared against experimental data in Chapters 3 and 5), with

a high fidelity in conduction melting mode. Deviations between the predicted and experimental values are observed in other melting modes due to change in process physics phenomena. The thermal history model was compared against an existing model in literature for comparing performance; the model from prior art has the limitation of only simulating thermal history for a straight path deposition, in one direction. The proposed model in the dissertation shows a good agreement compared to the predictions in [218], and the maximum prediction error is less than 15% depending on the layer of deposition. The proposed thermomechanical model is structured to be able to predict the melt pool temperature, keep thermal history and simulate the deposition geometry.

Upon further reflections of Chapter 3, the proposed method offers the opportunity to simulate deposition tracks not only in 1D scan paths but also more complicated scan path involving curvatures and sharp corners, which was demonstrated in Chapter 6. The limitation of the proposed methods is that it performs optimal in conduction melting mode since it is derived according to conduction melting mode physics and other melting modes may involve different process physics phenomena.

2. In Chapter 4, the proposed vision-based feature detection algorithm deploys an adaptive image thresholding and a region growing technique with the use of an energy convergence criterion to detect features of interest in the laser-material interaction zone (core, meltpool, incandescent plasma plume region). The adaptive nature of the algorithm allows for a robust detection of the regions of interest against manually anotated data, despite changes in environment lighting and system perturbations. In order to quantify the reliability of the proposed region detection technique, a registration scheme to align the measurements obtained from the vision sensor with that obtained by a high sampling rate laser confocal microscopy is introduced. In this work, the True Positive Detection rate was significantly above 90%, while the False Detection Rate was less than 10%. It was observed that the proposed method maintains its robustness with a true positive rate of higher than 90% for detecting all regions at all laser power levels. The aligned vision and profilometer data follow similar global and local trends, which is promising, however a more careful future investigation is needed using a precalibrated experimental setup in order to achieve real-time process monitoring as a way of controlling deposition geometry.

   The proposed vision-based feature detection algorithm has the ability of detecting regions in the laser-material interaction zone in a wide range of process conditions, which was also demonstrated in Chapter 5. This robust algorithm provides a low-cost process monitoring solution with the flexibility of targeting different regions in the melt pool. Further datasets, beyond the preliminary experiments, may be needed to increase the robustness of the algorithms if the material and DED system change for calibration and training of the algorithm.

3. In Chapter 5, part quality outcomes (geometric features), process signatures (near-infrared high dynamic range vision) and process physics (modeling outcomes) are used to create process maps to define, detect and classify process instabilities. Process modeling can predict the deposition width and height, and the normalized enthalpy, to define theoretical feature geometry and process zones (lack of fusion, conduction, keyhole, balling) respectively. Process signatures are captured by in-situ vision monitoring and a feature detection algorithm is used to detect pre-defined regions of interest and material ejections. Part quality outcomes are identified by scanning the resulting samples with a confocal microscope and extracting the width and height of the deposition to quantify the quality of the features. Process maps are created based on the statistical representation (average, standard deviation, root mean square, coefficient of variance) of different data sources to investigate the correlations in performance and to identify different process performance zones. Although the combination of confocal microscopy and process modeling can classify all three instability regions in process zones (undermelt, keyhole, balling), instantaneous decisions cannot be made during manufacturing; in-situ monitoring is required. It is shown that the balling and keyhole process zones can be detected just using the melt pool process signatures, captured by the in-situ vision sensors. Detecting lack of fusion is difficult with in-situ vision sensors, and can be inferred only based on the area of the material ejecta; however this instability is the easiest to avoid by ensuring a minimum input energy input. As a preliminary study, a kNN classifier is trained using statistical features detected by the vision sensor, the normalized enthalpy, and the input process parameters.

   The proposed method has the benefit of using multiple data sources to detect not only one process instability, but multiple classes of such, to be able to make a comprehensive assessment of the deposition quality. The limitation of the proposed algorithm could be that the trained kNN algorithm may not be able to predict the process labels accurately when the material and DED systems are changed. Thus, further experiments and testing are needed to train a robust kNN algorithm and grow this research path into an industrially-robust tool.

4. In Chapter 6, the pyrometry signals can be analyzed to train algorithms that enable intelligent decisions for post-process machining. Furthermore, such algorithms can be used to predict where the geometric inconsistencies occur, which can be addressed

by post-process machining. The machinability of the additively manufactured parts is mostly influenced by the tool wear, with a rapid progression in tool wear being observed despite using coolant during the cutting operation. For the material system and process parameter windows studied, there is no strong correlation between the hardness of the material and the cutting forces. The cutting forces can be predicted accurately using the oblique cutting force model. This can help in predicting cutting load on the tool when machining inconsistent surfaces due to geometry variation, which can occur during additive manufacturing.

Upon further reflections of outcomes from Chapter 6, dual-wavelength pyrometry can be used to experimentally validate thermal models with some potential errors due to plasma emission, which may lead to incorrect measurements. The proposed method offers the opportunity to provide intelligent decisions on post-processing or layer-intermittent machining using multiple data sources. This helps in improving the process integration of two processes additive and subtractive in a hybrid system. Furthermore, this is a step forward towards automated process planning for the machining process.

7.2 Future work

The correlative analytics between process physics and product quality outcomes is also used laser powder bed fusion (LPBF) process as described in [104]. A sub-surface pore predictor is developed using process modeling and machine learning. In future work, such methods can be to expanded this work to predict the defects in the whole part such that the algorithm can also predict the defects in the part core. Such methodologies could be applied to the new class of hybrid LPBF and machining technologies.

In future research, the scientific methodologies proposed in this dissertation can be further improved to increase their applicability for industry. For instance, The reliability and robustness of the proposed machine learning and statistical algorithms can be further improved by substantially increasing the experimental data in a wider range of process conditions, by increasing the amount of annotated datasets, and by exploring new or more advanced algorithms.

In future research, the proposed methods can be utilized in real-time applications such that defect detection can be done to qualify the parts, and to provide intelligent decisions about the quality assessment and post-processing during the process. This can minimize the need of ex-situ characterization and non-destructive testing (NDT) to qualify the parts in industrial applications. Thus, in-situ part qualification can have a direct impact on the process efficiency. Furthermore, real-time applications can offer the opportunity for implementing closed-loop process control, where the DED process repeatability can be further improved. A controller scheme can be developed or adopted from the literature to complement the data extracted from the sensor feedback presented in this dissertation in order to maintain the DED process outcomes, such as melt pool morphology, temperature, and/or deposition geometry, within a desired range or process zone. In addition, surrogate modeling can be deployed, where the process outcomes can be simulated prior to fabrication to anticipate control signal outcomes and correct regions, which are indicative of process instabilities. Such offline control schemes can be a lo-cost solution to explore.

The real-time measurements and feedback can be also used to better integrate the additive and subtractive manufacturing processes in a hybrid system. Multiple sensors can be used, not only for the feedback signal in controlling the DED process, but also for inferring geometric properties. As such, other sensors such as a touch probe or a in-line scanner can be deployed as future work. Exploring data fusion from multiple sensors (vision, pyrometry, line scanning and/or touch probe) could be beneficial, as the geometry is dynamically changing during the deposition process. In addition, a robust correlation between the thermal history of the part (as simulated) with the resulting material properties such as microstructure and hardness can inform the planning of machining parameters.

Machinability of the additively manufactured parts needs further research because there are many parameters affecting it, such as the processing conditions of metal AM process, the direction of the machining process relative to the deposition direction and the cutting process conditions. The processing conditions of metal AM can affect the mechanical properties and microstructure of the material. In addition to this, anisotropy is commonly observed in additively manufactured parts due to changes in geometry at each layer, cyclic thermal loading at different frequencies at different regions and critical geometric features such as thin walls and overhangs. Anisotropy is likely to be observed in machinability of the parts too, as it is directly influenced by the mechanical properties of the substrate material. In such cases, the process planning for the cutting operation can become more challenging, as the chosen cutting parameters may cause unstable cutting conditions and excessive loading on the tool, which can result in tool breakage or low surface quality. Thus, adaptive control in machining of AM parts would be very beneficial to avoid such cases.

References

[1] Adding and taking away. `https://www.economist.com/babbage/2013/12/31/adding-and-taking-away`. Last accessed on June 20th, 2021.

[2] Alsi10mg-0403 powder for additive manufacturing. `https://www.renishaw.com/en/data-sheets-additive-manufacturing--17862`. Accessed: 2019-08-30.

[3] Printing geometry. `https://manufactur3dmag.com/velo3d-launches-sapphire-system-metal-additive-manufacturing-solution/velo3d-radial-heat-exchanger/`. Last accessed on June 6th, 2021.

[4] Sample qualitative results. `https://youtu.be/m2_Jx4tahmE`. Last accessed on July 26th, 2020.

[5] Mostafa Abdelrahman, Edward W Reutzel, Abdalla R Nassar, and Thomas L Starr. Flaw detection in powder bed fusion using optical imaging. *Additive Manufacturing*, 15:1–11, 2017.

[6] Eberhard Abele, Hanns A Stoffregen, Michael Kniepkamp, Sebastian Lang, and Manfred Hampe. Selective laser melting for manufacturing of thin-walled porous elements. *Journal of Materials Processing Technology*, 215:114–122, 2015.

[7] Nesma T Aboulkhair, Nicola M Everitt, Ian Ashcroft, and Chris Tuck. Reducing porosity in alsi10mg parts processed by selective laser melting. *Additive Manufacturing*, 1:77–86, 2014.

[8] E Ahmadi, Z Azimifar, P Fieguth, and S Ayatollahi. Discriminative graphical model for porous media image synthesis. *Iranian Journal of Science and Technology. Transactions of Electrical Engineering*, 38(E2):177, 2014.

[9] Horacio Ahuett-Garza and T Kurfess. A brief discussion on the trends of habilitating technologies for industry 4.0 and smart manufacturing. *Manufacturing Letters*, 15:60–63, 2018.

[10] Kassim S Al-Rubaie, Saulo Melotti, Alexsandro Rabelo, José M Paiva, Mohamed A Elbestawi, and Stephen C Veldhuis. Machinability of slm-produced ti6al4v titanium alloy parts. *Journal of Manufacturing Processes*, 57:768–786, 2020.

[11] D Alberts, D Schwarze, and G Witt. In situ melt pool monitoring and the correlation to part density of inconel® 718 for quality assurance in selective laser melting. In *Proceedings of the 28th Annual International Solid Freeform Fabrication Symposium, Austin, TX, USA*, pages 7–9, 2017.

[12] Y Altintaş and Erhan Budak. Analytical prediction of stability lobes in milling. *CIRP annals*, 44(1):357–362, 1995.

[13] Y Altintas, M Eynian, and H Onozuka. Identification of dynamic cutting force coefficients and chatter stability with process damping. *CIRP annals*, 57(1):371–374, 2008.

[14] Yusuf Altintas and AA Ber. Manufacturing automation: metal cutting mechanics, machine tool vibrations, and cnc design. *Appl. Mech. Rev.*, 54(5):B84–B84, 2001.

[15] Giuseppina Ambrogio, Francesco Gagliardi, Maurizio Muzzupappa, and Luigino Filice. Additive-incremental forming hybrid manufacturing technique to improve customised part performance. *Journal of Manufacturing Processes*, 37:386–391, 2019.

[16] Kenta Aoyagi, Hao Wang, Hideki Sudo, and Akihiko Chiba. Simple method to construct process maps for additive manufacturing using a support vector machine. *Additive Manufacturing*, 27:353–362, 2019.

[17] Necati Aras, Vedat Verter, and Tamer Boyaci. Coordination and priority decisions in hybrid manufacturing/remanufacturing systems. *Production and Operations Management*, 15(4):528–543, 2006.

[18] Maite Aretxabaleta, Alexander B Xepapadeas, Christian F Poets, Bernd Koos, and Sebastian Spintzyk. Comparison of additive and subtractive cad/cam materials for their potential use as tübingen palatal plate: An in-vitro study on flexural strength. *Additive Manufacturing*, 37:101693, 2021.

[19] F Arias-González, O Barro, J del Val, F Lusquiños, M Fernández-Arias, R Comesaña, A Riveiro, and J Pou. Laser-directed energy deposition: principles and applications. In *Additive Manufacturing*, pages 121–157. Elsevier, 2021.

[20] Jon Iñaki Arrizubieta, Aitzol Lamikiz, Fritz Klocke, Silvia Martínez, Kristian Arntz, and Eneko Ukar. Evaluation of the relevance of melt pool dynamics in laser material deposition process modeling. *International Journal of Heat and Mass Transfer*, 115:80–91, 2017.

[21] M Assid, Ali Gharbi, and Adnène Hajji. Production planning of an unreliable hybrid manufacturing–remanufacturing system under uncertainties and supply constraints. *Computers & Industrial Engineering*, 136:31–45, 2019.

[22] Qian Bai, Bingzhe Wu, Xiaoling Qiu, Bi Zhang, and Juanjuan Chen. Experimental study on additive/subtractive hybrid manufacturing of 6511 steel: process optimization and machining characteristics. *The International Journal of Advanced Manufacturing Technology*, 108:1389–1398, 2020.

[23] Yuchao Bai, Cuiling Zhao, Yu Zhang, Jie Chen, and Hao Wang. Additively manufactured cucrzr alloy: Microstructure, mechanical properties and machinability. *Materials Science and Engineering: A*, page 141528, 2021.

[24] A. Bandyopadhyay and K.D. Traxel. Invited review article: Metal-additive manufacturing—modeling strategies for application-optimized designs. *Additive Manufacturing*, 22:758–774, 2018. cited By 68.

[25] Stefano Baraldo, Ambra Vandone, Anna Valente, and Emanuele Carpanzano. Closed-loop control by laser power modulation in direct energy deposition additive manufacturing. In *Proceedings of 5th International Conference on the Industry 4.0 Model for Advanced Manufacturing*, pages 129–143. Springer, 2020.

[26] Fabrice Bardin, Stephen Morgan, Stewart Williams, Roy McBride, Andrew J Moore, Julian DC Jones, and Duncan P Hand. Process control of laser conduction welding by thermal imaging measurement with a color camera. *Appl. Opt.*, 44(32):6841–6848, 2005.

[27] Paulo Jorge Bártolo. *Stereolithography: materials, processes and applications.* Springer Science & Business Media, 2011.

[28] Shyam Barua, Frank Liou, Joseph Newkirk, and Todd Sparks. Vision-based defect detection in laser metal deposition Process. *Rapid Prototyp. J.*, 20(1):77–85, 2014.

[29] Katie Basinger, Caroline Webster, Carter Keough, Richard Wysk, and Ola Harrysson. Advanced manufacturing using linked processes: Hybrid manufacturing. In *Mass Production Processes*. IntechOpen, 2019.

[30] Katie L Basinger, Carter B Keough, Caroline E Webster, Richard A Wysk, Thomas M Martin, and Ola L Harrysson. Development of a modular computer-aided process planning (capp) system for additive-subtractive hybrid manufacturing of pockets, holes, and flat surfaces. *The International Journal of Advanced Manufacturing Technology*, 96(5):2407–2420, 2018.

[31] Martin Baumers, Phill Dickens, Chris Tuck, and Richard Hague. The cost of additive manufacturing: machine productivity, economies of scale and technology-push. *Technological forecasting and social change*, 102:193–201, 2016.

[32] H Baumgartl, J Tomas, R Buettner, and M Merkel. A novel deep-learning approach for automated non-destructive testing in quality assurance based on convolutional neural networks. *ACEX-2019 Proceedings*, 2019.

[33] C. Baykasoglu, O. Akyildiz, D. Candemir, Q. Yang, and A.C. To. Predicting microstructure evolution during directed energy deposition additive manufacturing of ti-6al-4v. *Journal of Manufacturing Science and Engineering, Transactions of the ASME*, 140(5), 2018. cited By 31.

[34] Cengiz Baykasoglu, Oncu Akyildiz, Duygu Candemir, Qingcheng Yang, and Albert C To. Predicting microstructure evolution during directed energy deposition additive manufacturing of ti-6al-4v. *Journal of Manufacturing Science and Engineering*, 140(5), 2018.

[35] F Bayle and M Doubenskaia. Selective laser melting process monitoring with high speed infra-red camera and pyrometer. In *Fundamentals of laser assisted micro-and nanotechnologies*, volume 6985, page 698505. International Society for Optics and Photonics, 2008.

[36] VE Beal, Poonjolai Erasenthiran, Neil Hopkinson, P Dickens, and Carlos Henrique Ahrens. Scanning strategies and spacing effect on laser fusion of h13 tool steel powder using high power nd: Yag pulsed laser. *International journal of production research*, 46(1):217–232, 2008.

[37] Morad Behandish, Saigopal Nelaturi, and Johan de Kleer. Automated process planning for hybrid manufacturing. *Computer-Aided Design*, 102:115–127, 2018.

[38] Roland Bejjani, Erik Bamford, Stefan Cedergren, Andreas Archenti, and Amir Rashid. Variations in the surface integrity of ti-6al-4v by combinations of additive and subtractive manufacturing processes. *Materials*, 13(8):1825, 2020.

[39] Mirjam Beltrami, Guido Orzes, Joseph Sarkis, and Marco Sartor. Industry 4.0 and sustainability: Towards conceptualization and theory. *Journal of Cleaner Production*, page 127733, 2021.

[40] Vincent Benoist, Lionel Arnaud, and Maher Baili. A new method of design for additive manufacturing including machining constraints. *The International Journal of Advanced Manufacturing Technology*, 111(1):25–36, 2020.

[41] Roland Berger. Additive manufacturing: a game changer for the manufacturing industry. *Roland Berger Strategy Consultants GmbH, Munich*, 1(5.1), 2013.

[42] Sebastian Berumen, Florian Bechmann, Stefan Lindner, Jean-Pierre Kruth, and Tom Craeghs. Quality control of laser- and powder bed-based additive manufacturing (AM) technologies. *Phys. Procedia*, 5:617 – 622, 2010. Proc. of Laser Assisted Net Shape Engineering (LANE).

[43] Jack Beuth, Jason Fox, Joy Gockel, Colt Montgomery, Rui Yang, Haipeng Qiao, Emrecan Soylemez, Pete Reeseewatt, Amin Anvari, Sneha Narra, et al. Process mapping for qualification across multiple direct metal additive manufacturing processes. In *Solid freeform fabrication proceedings*, pages 655–665. Univ. Tex. Austin, 2013.

[44] Jack Beuth and Nathan Klingbeil. The role of process variables in laser-based direct metal solid freeform fabrication. *Jom*, 53(9):36–39, 2001.

[45] G Bi, CN Sun, and A Gasser. Study on influential factors for process monitoring and control in laser aided additive manufacturing. *Journal of Materials Processing Technology*, 213(3):463–468, 2013.

[46] Harry Bikas, Sotiris Koutsoukos, and Panagiotis Stavropoulos. A decision support method for evaluation and process selection of additive manufacturing. *Procedia CIRP*, 81:1107–1112, 2019.

[47] Harry Bikas, Panagiotis Stavropoulos, and George Chryssolouris. Additive manufacturing methods and modelling approaches: a critical review. *The International Journal of Advanced Manufacturing Technology*, 83(1-4):389–405, 2016.

[48] K.A. Bourne, P. Farahmand, and D. Roberson. Simulation of cross-sectional geometry during laser powder deposition of tall thin-walled and thick-walled features. volume 3, 2016. cited By 2.

[49] Lisa Brock. Laser powder bed fusion of alsi10mg for fabrication of fluid power components. Master's thesis, University of Waterloo, 2020.

[50] E Budak and Y Altintas. Analytical prediction of chatter stability in milling—part i: general formulation. *ASME. J. Manuf. Sci. Eng.*, 120(1):22–30, 1998.

[51] E Budak, Y Altintas, and EJA Armarego. Prediction of milling force coefficients from orthogonal cutting data. *ASME. J. Manuf. Sci. Eng.*, 118(2):216–224, 1996.

[52] Armando Caballero, Wojciech Suder, Xin Chen, Goncalo Pardal, and Stewart Williams. Effect of shielding conditions on bead profile and melting behaviour in laser powder bed fusion additive manufacturing. *Additive Manufacturing*, page 101342, 2020.

[53] Alessandra Caggiano, Jianjing Zhang, Vittorio Alfieri, Fabrizia Caiazzo, Robert Gao, and Roberto Teti. Machine learning-based image processing for on-line defect recognition in additive manufacturing. *CIRP Annals*, 68(1):451–454, 2019.

[54] Flaviana Calignano, Diego Manfredi, Elisa Paola Ambrosio, Sara Biamino, Mariangela Lombardi, Eleonora Atzeni, Alessandro Salmi, Paolo Minetola, Luca Iuliano, and Paolo Fino. Overview on additive manufacturing technologies. *Proceedings of the IEEE*, 105(4):593–612, 2017.

[55] Nicholas P Calta, Gabe Guss, Sheldon Wu, Sonny Ly, Dave Deane, Michael F Crumb, and Manyalibo J Matthews. High speed hyperspectral thermal imaging of the melt pool dynamics during metal additive manufacturing. In *2017 Conference on Lasers and Electro-Optics (CLEO)*, pages 1–2. IEEE, 2017.

[56] Daniel Delgado Camacho, Patricia Clayton, William J O'Brien, Carolyn Seepersad, Maria Juenger, Raissa Ferron, and Salvatore Salamone. Applications of additive manufacturing in the construction industry–a forward-looking review. *Automation in construction*, 89:110–119, 2018.

[57] J. Cao. Linking thermal history to mechanical behavior in directed energy deposited materials. pages 97–98, 2019. cited By 1.

[58] X. Cao and B. Ayalew. Control-oriented mimo modeling of laser-aided powder deposition processes. volume 2015-July, pages 3637–3642, 2015. cited By 26.

[59] Francesco Careri, Domenico Umbrello, Khamis Essa, Moataz M Attallah, and Stano Imbrogno. The effect of the heat treatments on the tool wear of hybrid additive manufacturing of in718. *Wear*, page 203617, 2021.

[60] Amir Charmi, Rainer Falkenberg, Luis Ávila, Gunther Mohr, Konstantin Sommer, Alexander Ulbricht, Maximilian Sprengel, R Saliwan Neumann, B Skrotzki, and A Evans. Mechanical anisotropy of additively manufactured stainless steel 316l: An experimental and numerical study. *Materials Science and Engineering: A*, 799:140154, 2020.

[61] Liyong Chen, Qingzhong Xu, Yan Liu, Gangjun Cai, and Jichen Liu. Machinability of the laser additively manufactured inconel 718 superalloy in turning. *The International Journal of Advanced Manufacturing Technology*, 114(3):871–882, 2021.

[62] Niechen Chen and Matthew Frank. Process planning for hybrid additive and subtractive manufacturing to integrate machining and directed energy deposition. *Procedia Manufacturing*, 34:205–213, 2019.

[63] Y Chen, S Clark, ACL Leung, L Sinclair, S Marussi, R Atwood, T Connoley, M Jones, G Baxter, and PD Lee. Melt pool morphology in directed energy deposition additive manufacturing process. In *IOP Conference Series: Materials Science and Engineering*, volume 861, page 012012. IOP Publishing, 2020.

[64] B Cheng, J Lydon, K Cooper, V Cole, P Northrop, and K Chou. Melt pool dimension measurement in selective laser melting using thermal imaging. *Solid Freeform Fabrication*, pages 1252–1263, 2017.

[65] Bo Cheng, James Lydon, Kenneth Cooper, Vernon Cole, Paul Northrop, and Kevin Chou. Melt pool sensing and size analysis in laser powder-bed metal additive manufacturing. *J. Manuf. Processes*, 32:744–753, 2018.

[66] THC Childs, C Hauser, and M Badrossamay. Mapping and modelling single scan track formation in direct metal selective laser melting. *CIRP Annals*, 53(1):191–194, 2004.

[67] Yu Chivel and I Smurov. On-line temperature monitoring in selective laser sintering/melting. *Physics Procedia*, 5:515–521, 2010.

[68] Li Chong, Seeram Ramakrishna, and Sunpreet Singh. A review of digital manufacturing-based hybrid additive manufacturing processes. *The International Journal of Advanced Manufacturing Technology*, 95(5):2281–2300, 2018.

[69] Sohini Chowdhury, Yadaiah Nirsanametla, M Muralidhar, Swarup Bag, CP Paul, and KS Bindra. Identification of modes of welding using parametric studies during ytterbium fiber laser welding. *Journal of Manufacturing Processes*, 57:748–761, 2020.

[70] N. Christensen, V.D.L. Davies, and K. Gjermundsen. Distribution of temperatures in arc welding. *British Welding Journal*, 12(2):54–75, 1965. cited By 262.

[71] Won-Shik Chu, Min-Soo Kim, Ki-Hwan Jang, Ji-Hyeon Song, Hugo Rodrigue, Doo-Man Chun, Young Tae Cho, Seung Hwan Ko, Kyu-Jin Cho, Suk Won Cha, et al. From design for manufacturing (dfm) to manufacturing for design (mfd) via hybrid manufacturing and smart factory: A review and perspective of paradigm shift. *International Journal of Precision Engineering and Manufacturing-Green Technology*, 3(2):209–222, 2016.

[72] Zhong Yang Chua, Il Hyuk Ahn, and Seung Ki Moon. Process monitoring and inspection systems in metal additive manufacturing: Status and applications. *International Journal of Precision Engineering and Manufacturing-Green Technology*, 4(2):235–245, 2017.

[73] Sam Coeck, Manisha Bisht, Jan Plas, and Frederik Verbist. Prediction of lack of fusion porosity in selective laser melting based on melt pool monitoring data. *Addit. Manuf.*, 25:347–356, 2019.

[74] Andrew R. Conn, Nicholas I. M. Gould, and Philippe Toint. A globally convergent augmented lagrangian algorithm for optimization with general constraints and simple bounds. *SIAM J. Numer. Anal.*, 28(2):545–572, 1991.

[75] Andrew R. Conn, Nicholas I. M. Gould, and Philippe Toint. A globally convergent augmented lagrangian barrier algorithm for optimization with general inequality constraints and simple bounds. *Math. Comput.*, 66(217):261–288, 1997.

[76] D.J. Corbin, A.R. Nassar, E.W. Reutzel, A.M. Beese, and N.A. Kistler. Effect of directed energy deposition processing parameters on laser deposited inconel® 718: External morphology. *Journal of Laser Applications*, 29(2), 2017. cited By 16.

[77] Tom Craeghs, Florian Bechmann, Sebastian Berumen, and Jean-Pierre Kruth. Feedback control of layerwise laser melting using optical sensors. *Phys. Procedia*, 5:505–514, 2010. Proc. of Laser Assisted Net Shape Engineering (LANE).

[78] Tom Craeghs, Stijn Clijsters, Jean-Pierre Kruth, Florian Bechmann, and Marie-Christin Ebert. Detection of process failures in layerwise laser melting with optical process monitoring. *Physics Procedia*, 39:753–759, 2012.

[79] Tom Craeghs, Stijn Clijsters, Evren Yasa, Florian Bechmann, Sebastian Berumen, and Jean-Pierre Kruth. Determination of geometrical factors in layerwise laser melting using optical process monitoring. *Optics and Lasers in Engineering*, 49(12):1440 – 1446, 2011.

[80] Ross Cunningham, Sneha P Narra, Colt Montgomery, Jack Beuth, and AD Rollett. Synchrotron-based x-ray microtomography characterization of the effect of processing variables on porosity formation in laser power-bed additive manufacturing of ti-6al-4v. *Jom*, 69(3):479–484, 2017.

[81] Ross Cunningham, Cang Zhao, Niranjan Parab, Christopher Kantzos, Joseph Pauza, Kamel Fezzaa, Tao Sun, and Anthony D Rollett. Keyhole threshold and morphology in laser melting revealed by ultrahigh-speed x-ray imaging. *Science*, 363(6429):849–852, 2019.

[82] Jiaqiang Dang, Xiaojiang Cai, Dedong Yu, Qinglong An, Weiwei Ming, and Ming Chen. Effect of material microstructure on tool wear behavior during machining additively manufactured ti6al4v. *Archives of Civil and Mechanical Engineering*, 20(1):1–15, 2020.

[83] Adrita Dass and Atieh Moridi. State of the art in directed energy deposition: from additive manufacturing to materials design. *Coatings*, 9(7):418, 2019.

[84] José Luis Dávila, Paulo Inforçatti Neto, Pedro Yoshito Noritomi, Reginaldo Teixeira Coelho, and Jorge Vicente Lopes da Silva. Algorithms-aided design applied to the tool-paths generation for hybrid manufacturing. *Manufacturing Letters*, 2020.

[85] Jesse Davis and Mark Goadrich. The relationship between precision-recall and roc curves. In *Proceedings of the 23rd international conference on Machine learning*, pages 233–240. ACM, 2006.

[86] T. DebRoy, H.L. Wei, J.S. Zuback, T. Mukherjee, J.W. Elmer, J.O. Milewski, A.M. Beese, A. Wilson-Heid, A. De, and W. Zhang. Additive manufacturing of metallic components – process, structure and properties. *Progress in Materials Science*, 92:112–224, 2018. cited By 1552.

[87] Ali Gökhan Demir, Luca Mazzoleni, Leonardo Caprio, Matteo Pacher, and Barbara Previtali. Complementary use of pulsed and continuous wave emission modes to stabilize melt pool geometry in laser powder bed fusion. *Opt. Laser Technol.*, 113:15–26, 2019.

[88] Andrew Dickins, S Lawes, P Stravroulakis, and R Leach. Design of a multi-sensor in-situ inspection system for additive manufacturing. *Proc. ASPE/euspen Advancing Precision in Additive Manufacturing*, pages 248–242, 2018.

[89] Ugur M Dilberoglu, Bahar Gharehpapagh, Ulas Yaman, and Melik Dolen. The role of additive manufacturing in the era of industry 4.0. *Procedia Manufacturing*, 11:545–554, 2017.

[90] David Dillkötter, Johann Stoppok, Magnus Thiele, Cemal Esen, and Martin Mönnigmann. Model-based temperature offset compensation for additive manufacturing by directed energy deposition. *IFAC-PapersOnLine*, 53(2):11812–11817, 2020.

[91] Carl Doersch. Tutorial on variational autoencoders. *arXiv preprint arXiv:1606.05908*, 2016.

[92] P. Dollár, C. Wojek, B. Schiele, and P. Perona. Pedestrian detection: An evaluation of the state of the art. *IEEE Trans. Pattern Anal. Mach. Intell.*, 34(4):743–761, 2012.

[93] Sean P Donegan, Edwin J Schwalbach, and Michael A Groeber. Zoning additive manufacturing process histories using unsupervised machine learning. *Materials Characterization*, 161:110123, 2020.

[94] C. Doumanidis and Y.-M. Kwak. Geometry modeling and control by infrared and laser sensing in thermal manufacturing with material deposition. *Journal of Manufacturing Science and Engineering, Transactions of the ASME*, 123(1):45–52, 2001. cited By 66.

[95] Wei Du, Qian Bai, and Bi Zhang. A novel method for additive/subtractive hybrid manufacturing of metallic parts. *Procedia Manufacturing*, 5:1018–1030, 2016.

[96] Anton du Plessis. Effects of process parameters on porosity in laser powder bed fusion revealed by x-ray tomography. *Additive Manufacturing*, page 100871, 2019.

[97] Bhaskar Dutta. Nozzle with laser scanning head for direct metal deposition, November 10 2020. US Patent 10,828,721.

[98] Bhaskar Dutta and FH Sam Froes. The additive manufacturing (am) of titanium alloys. *Metal powder report*, 72(2):96–106, 2017.

[99] T.W. Eagar and N.-S. Tsai. Temperature fields produced by traveling distributed heat sources. *Welding Journal (Miami, Fla)*, 62(12):346–355, 1983. cited By 287.

[100] H. El Cheikh, B. Courant, J.-Y. Hascoët, and R. Guillén. Prediction and analytical description of the single laser track geometry in direct laser fabrication from process parameters and energy balance reasoning. *Journal of Materials Processing Technology*, 212(9):1832–1839, 2012. cited By 34.

[101] Anja Elser, Michael Königs, Alexander Verl, and Michael Servos. On achieving accuracy and efficiency in additive manufacturing: Requirements on a hybrid cam system. *Procedia CIRP*, 72:1512–1517, 2018.

[102] Kaan Erkorkmaz and Yusuf Altintas. High speed cnc system design. part i: jerk limited trajectory generation and quintic spline interpolation. *International Journal of machine tools and manufacture*, 41(9):1323–1345, 2001.

[103] Kaan Erkorkmaz, Andrew Katz, Yasin Hosseinkhani, Denys Plakhotnik, Marc Stautner, and Fathy Ismail. Chip geometry and cutting forces in gear shaping. *CIRP Annals*, 65(1):133–136, 2016.

[104] Deniz Sera Ertay, Shima Kamyab, Mihaela Vlasea, Zohreh Azimifar, Thanh Ma, Allan D Rogalsky, and Paul Fieguth. Toward sub-surface pore prediction capabilities for laser powder bed fusion using data science. *Journal of Manufacturing Science and Engineering*, 143(7):071016, 2021.

[105] Deniz Sera Ertay, Henry Ma, and Mihaela Vlasea. Correlative beam path and pore defect space analysis for modulated powder bed laser fusion process. In *Proceedings of the 29th Annual International Solid Freeform Fabrication Symposium*, pages 274–284, 2018.

[106] Deniz Sera Ertay, Mihaela Vlasea, and Kaan Erkorkmaz. Thermomechanical and geometry model for directed energy deposition with 2d/3d toolpaths. *Additive Manufacturing*, page 101294, 2020.

[107] M. Everingham, L. Van Gool, C. K. Williams, J.Winn, and A. Zisserman. The Pascal visual object classes (VOC) challenge. *Int. J. of Comput. Vis.*, 88(2):303–338, 2010.

[108] Sarah K Everton, Matthias Hirsch, Petros Stravroulakis, Richard K Leach, and Adam T Clare. Review of in-situ process monitoring and in-situ metrology for metal additive manufacturing. *Materials & Design*, 95:431–445, 2016.

[109] Rémy Fabbro. Melt pool and keyhole behaviour analysis for deep penetration laser welding. *Journal of Physics D: Applied Physics*, 43(44):445501, 2010.

[110] Clement Farabet, Camille Couprie, Laurent Najman, and Yann LeCun. Learning hierarchical features for scene labeling. *IEEE transactions on pattern analysis and machine intelligence*, 35(8):1915–1929, 2012.

[111] Mohammad H Farshidianfar, Amir Khajepour, and Adrian P Gerlich. Effect of real-time cooling rate on microstructure in laser additive manufacturing. *J. Mater. Process. Technol.*, 231:468–478, 2016.

[112] A. Fathi, A. Khajepour, E. Toyserkani, and M. Durali. Clad height control in laser solid freeform fabrication using a feedforward pid controller. *International Journal of Advanced Manufacturing Technology*, 35(3-4):280–292, 2007. cited By 97.

[113] Jixiong Fei, Guoliang Liu, Kaushalendra Patel, and Tuğrul Özel. Effects of machining parameters on finishing additively manufactured nickel-based alloy inconel 625. *Journal of Manufacturing and Materials Processing*, 4(2):32, 2020.

[114] Brian A Fisher, Brandon Lane, Ho Yeung, and Jack Beuth. Toward determining melt pool quality metrics via coaxial monitoring in laser powder bed fusion. *Manuf. Lett.*, 15:119–121, 2018.

[115] Joseph M Flynn, Alborz Shokrani, Stephen T Newman, and Vimal Dhokia. Hybrid additive and subtractive machine tools–research and industrial developments. *International Journal of Machine Tools and Manufacture*, 101:79–101, 2016.

[116] Simon Ford and Mélanie Despeisse. Additive manufacturing and sustainability: an exploratory study of the advantages and challenges. *Journal of cleaner Production*, 137:1573–1587, 2016.

[117] Jean-Baptiste Forien, Nicholas P Calta, Philip J DePond, Gabe M Guss, Tien T Roehling, and Manyalibo J Matthews. Detecting keyhole pore defects and monitoring process signatures during laser powder bed fusion: a correlation between in situ

pyrometry and ex situ x-ray radiography. *Additive Manufacturing*, page 101336, 2020.

[118] Panagis Foteinopoulos, Alexios Papacharalampopoulos, and Panagiotis Stavropoulos. On thermal modeling of additive manufacturing processes. *CIRP Journal of Manufacturing Science and Technology*, 20:66–83, 2018.

[119] Behzad Fotovvati, Steven F Wayne, Gladius Lewis, and Ebrahim Asadi. A review on melt-pool characteristics in laser welding of metals. *Advances in Materials Science and Engineering*, 2018, 2018.

[120] Jason C Fox, Felix Kim, Zachary Reese, and Christopher Evans. Complementary use of optical metrology and x-ray computed tomography for surface finish and defect detection in laser powder bed fusion additive manufacturing. In *2018 ASPE and euspen Summer Topical Meeting-Advancing Precision in Additive Manufacturing*, volume 69, 2018.

[121] Jason C Fox, Shawn P Moylan, and Brandon M Lane. Effect of process parameters on the surface roughness of overhanging structures in laser powder bed fusion additive manufacturing. *Procedia Cirp*, 45:131–134, 2016.

[122] Jack Francis and Linkan Bian. Deep learning for distortion prediction in laser-based additive manufacturing using big data. *Manufacturing Letters*, 20:10–14, 2019.

[123] M.M. Francois, A. Sun, W.E. King, N.J. Henson, D. Tourret, C.A. Bronkhorst, N.N. Carlson, C.K. Newman, T. Haut, J. Bakosi, J.W. Gibbs, V. Livescu, S.A. Vander Wiel, A.J. Clarke, M.W. Schraad, T. Blacker, H. Lim, T. Rodgers, S. Owen, F. Abdeljawad, J. Madison, A.T. Anderson, J.-L. Fattebert, R.M. Ferencz, N.E. Hodge, S.A. Khairallah, and O. Walton. Modeling of additive manufacturing processes for metals: Challenges and opportunities. *Current Opinion in Solid State and Materials Science*, 21(4):198–206, 2017. cited By 156.

[124] Matthew C Frank, Jakob Croghan, Samantha Larson, and Logan Beguhn. Integration challenges with additive/subtractive in-envelope hybrid manufacturing. In *Proceedings of the 30th Annual International Solid Freeform Fabrication Symposium*, pages 294–300, 2019.

[125] William E Frazier. Metal additive manufacturing: a review. *Journal of Materials Engineering and Performance*, 23(6):1917–1928, 2014.

[126] FH Froes and B Dutta. The additive manufacturing (am) of titanium alloys. In *Advanced Materials Research*, volume 1019, pages 19–25. Trans Tech Publ, 2014.

[127] Tatsuaki Furumoto, Mohd Rizal Alkahari, Takashi Ueda, Mohd Sanusi Abdul Aziz, and Akira Hosokawa. Monitoring of laser consolidation process of metal powder with high speed video camera. *Phys. Procedia*, 39:760–766, 2012.

[128] Basavraj Gadagi and Ramesh Lekurwale. A review on advances in 3d metal printing. *Materials Today: Proceedings*, 2020.

[129] Aniruddha Gaikwad, Reza Yavari, Mohammad Montazeri, Kevin Cole, Linkan Bian, and Prahalada Rao. Toward the digital twin of additive manufacturing: Integrating thermal simulations, sensing, and analytics to detect process faults. *IISE Transactions*, pages 1–14, 2020.

[130] Haythem Gaja and Frank Liou. Automatic detection of depth of cut during end milling operation using acoustic emission sensor. *The International Journal of Advanced Manufacturing Technology*, 86(9):2913–2925, 2016.

[131] Iker Garmendia, Jon Flores, Mikel Madarieta, Aitzol Lamikiz, Luis Gerardo Uriarte, and Carlos Soriana. Geometrical control of ded processes based on 3d scanning applied to the manufacture of complex parts. *Procedia CIRP*, 94:425–429, 2020.

[132] BT Gibson, Yashwanth Kumar Bandari, BS Richardson, William C Henry, Emma J Vetland, TW Sundermann, and LJ Love. Melt pool size control through multiple closed-loop modalities in laser-wire directed energy deposition of ti-6al-4v. *Additive Manufacturing*, 32:100993, 2020.

[133] I. Gibson, D. Rosen, and B. Stucker. *Additive manufacturing technologies: 3D printing, rapid prototyping, and direct digital manufacturing, second edition.* 2015. cited By 1060.

[134] I. Gibson, D.W. Rosen, and B. Stucker. *Additive manufacturing technologies: Rapid prototyping to direct digital manufacturing.* 2010. cited By 2137.

[135] Ian Gibson, David Rosen, Brent Stucker, and Mahyar Khorasani. *Additive manufacturing technologies*, volume 17. Springer, 2014.

[136] Gennady G Gladush and Igor Smurov. *Physics of laser materials processing: theory and experiment*, volume 146. Springer Science & Business Media, 2011.

[137] Christian Gobert, Edward W Reutzel, Jan Petrich, Abdalla R Nassar, and Shashi Phoha. Application of supervised machine learning for defect detection during metallic powder bed fusion additive manufacturing using high resolution imaging. *Additive Manufacturing*, 21:517–528, 2018.

[138] J Gockel, J Fox, J Beuth, and R Hafley. Integrated melt pool and microstructure control for ti–6al–4v thin wall additive manufacturing. *Materials Science and Technology*, 31(8):912–916, 2015.

[139] Joy Gockel, Jack Beuth, and Karen Taminger. Integrated control of solidification microstructure and melt pool dimensions in electron beam wire feed additive manufacturing of ti-6al-4v. *Additive Manufacturing*, 1:119–126, 2014.

[140] David E. Goldberg. *Genetic Algorithms in Search, Optimization and Machine Learning*. Addison-Wesley Longman Publishing Co., Inc., 1st edition, 1989.

[141] Haijun Gong, Venkata Karthik Nadimpalli, Khalid Rafi, Thomas Starr, and Brent Stucker. Micro-ct evaluation of defects in ti-6al-4v parts fabricated by metal additive manufacturing. *Technologies*, 7(2):44, 2019.

[142] Haijun Gong, Khalid Rafi, Hengfeng Gu, Thomas Starr, and Brent Stucker. Analysis of defect generation in ti–6al–4v parts made using powder bed fusion additive manufacturing processes. *Additive Manufacturing*, 1:87–98, 2014.

[143] Ian Goodfellow, Yoshua Bengio, Aaron Courville, and Yoshua Bengio. *Deep learning*, volume 1. MIT press Cambridge, 2016.

[144] Jerard V Gordon, Sneha P Narra, Ross W Cunningham, He Liu, Hangman Chen, Robert M Suter, Jack L Beuth, and Anthony D Rollett. Defect structure process maps for laser powder bed fusion additive manufacturing. *Additive Manufacturing*, page 101552, 2020.

[145] M Grasso and BM Colosimo. A statistical learning method for image-based monitoring of the plume signature in laser powder bed fusion. *Rob. Comput. Integr. Manuf.*, 57:103–115, 2019.

[146] Marco Grasso and Bianca Maria Colosimo. Process defects and *in situ* monitoring methods in metal powder bed fusion: A review. *Meas. Sci. Technol.*, 28(4):044005–044005–25, 2017.

[147] U Gratzke, PD Kapadia, J Dowden, J Kroos, and G Simon. Theoretical approach to the humping phenomenon in welding processes. *Journal of Physics D: Applied Physics*, 25(11):1640, 1992.

[148] Thilo Grove, Berend Denkena, Oliver Maiß, Alexander Krödel, Holger Schwab, and Uta Kühn. Cutting mechanism and surface integrity in milling of ti-5553 processed by selective laser melting. *Journal of Mechanical Science and Technology*, 32(10):4883–4892, 2018.

[149] Jae-Hyeon Ha and Choon-Man Lee. A study on the thermal effect by multi heat sources and machining characteristics of laser and induction assisted milling. *Materials*, 12(7):1032, 2019.

[150] Abid Haleem and Mohd Javaid. Additive manufacturing applications in industry 4.0: a review. *Journal of Industrial Integration and Management*, 4(04):1930001, 2019.

[151] James C Haley, Baolong Zheng, Umberto Scipioni Bertoli, Alexander D Dupuy, Julie M Schoenung, and Enrique J Lavernia. Working distance passive stability in laser directed energy deposition additive manufacturing. *Materials & Design*, 161:86–94, 2019.

[152] D.B. Hann, J. Iammi, and J. Folkes. A simple methodology for predicting laser-weld properties from material and laser parameters. *Journal of Physics D: Applied Physics*, 44(44), 2011. cited By 92.

[153] DB Hann, J Iammi, and J Folkes. A simple methodology for predicting laser-weld properties from material and laser parameters. *J. Phys. D: Appl. Phys.*, 44(44):445401, 2011.

[154] Haibo He and Yunqian Ma. *Imbalanced learning: foundations, algorithms, and applications.* John Wiley & Sons, 2013.

[155] Jarred C Heigel and Brandon M Lane. Measurement of the melt pool length during single scan tracks in a commercial laser powder bed fusion process. *J. Manuf. Sci. Eng.*, 140(5):051012, 2018.

[156] Jarred C Heigel, Thien Q Phan, Jason C Fox, and Thomas H Gnaupel-Herold. Experimental investigation of residual stress and its impact on machining in hybrid additive/subtractive manufacturing. *Procedia Manufacturing*, 26:929–940, 2018.

[157] Hamidreza Hekmatjou, Zhi Zeng, Jiajia Shen, João Pedro Oliveira, and Homam Naffakh-Moosavy. A comparative study of analytical rosenthal, finite element, and experimental approaches in laser welding of aa5456 alloy. *Metals*, 10(4):436, 2020.

[158] A Hijazi, S Sachidanandan, R Singh, and V Madhavan. A calibrated dual-wavelength infrared thermometry approach with non-greybody compensation for machining temperature measurements. *Measurement Science and Technology*, 22(2):025106, 2011.

[159] Marika Hirvimäki, Matti Manninen, Antti Lehti, Ari Happonen, Antti Salminen, and Olli Nyrhilä. Evaluation of different monitoring methods of laser additive manufacturing of stainless steel. In *Engineering Materials and Application*, volume 651 of *Advanced Materials Research*, pages 812–819. Trans Tech Publications Ltd, 3 2013.

[160] Faramarz Hojati, Amir Daneshi, Babak Soltani, Bahman Azarhoushang, and Dirk Biermann. Study on machinability of additively manufactured and conventional titanium alloys in micro-milling process. *Precision Engineering*, 62:1–9, 2020.

[161] MI Hossain, AKM Nurul Amin, AU Patwari, and A Karim. Enhancement of machinability by workpiece preheating in end milling of ti-6al-4v. *Journal of Achievements in Materials and Manufacturing Engineering*, 31(2):320–326, 2008.

[162] T. Hua, C. Jing, L. Xin, Z. Fengying, and H. Weidong. Research on molten pool temperature in the process of laser rapid forming. *Journal of Materials Processing Technology*, 198(1-3):454–462, 2008. cited By 73.

[163] Y. Huang, M.B. Khamesee, and E. Toyserkani. A comprehensive analytical model for laser powder-fed additive manufacturing. *Additive Manufacturing*, 12:90–99, 2016. cited By 37.

[164] Y. Huang, M.B. Khamesee, and E. Toyserkani. A new physics-based model for laser directed energy deposition (powder-fed additive manufacturing): From single-track to multi-track and multi-layer. *Optics and Laser Technology*, 109:584–599, 2019. cited By 18.

[165] Farhad Imani, Ruimin Chen, Evan P Diewald, EW Reutzel, and Hui Yang. Deep learning of variant geometry in layerwise imaging profiles for additive manufacturing quality control. *Journal of Manufacturing Science and Engineering*, pages 1–16, 2019.

[166] M Islam, T Purtonen, H Piili, A Salminen, and O Nyrhilä. Temperature profile and imaging analysis of laser additive manufacturing of stainless steel. *Physics Procedia*, 41:835–842, 2013.

[167] M. Izadi, A. Farzaneh, I. Gibson, and B. Rolfe. The effect of process parameters and mechanical properties of direct energy deposited stainless steel 316. pages 1058–1067, 2020. cited By 4.

[168] M. Javidani, J. Arreguin-Zavala, J. Danovitch, Y. Tian, and M. Brochu. Additive manufacturing of alsi10mg alloy using direct energy deposition: Microstructure and hardness characterization. *Journal of Thermal Spray Technology*, 26(4):587–597, 2017. cited By 42.

[169] Bohumir Jelinek, William J Young, Matthew Dantin, William Furr, Haley Doude, and Matthew W Priddy. Two-dimensional thermal finite element model of directed energy deposition: matching melt pool temperature profile with pyrometer measurement. *Journal of Manufacturing Processes*, 57:187–195, 2020.

[170] Yongho Jeon and Frank Pfefferkorn. Effect of laser preheating the workpiece on micro end milling of metals. *Journal of manufacturing science and engineering*, 130(1), 2008.

[171] A.N. Jinoop, C.P. Paul, and K.S. Bindra. Laser assisted direct energy deposition of hastelloy-x. *Optics and Laser Technology*, 109:14–19, 2019. cited By 24.

[172] Luke Johnson, Mohamad Mahmoudi, Bing Zhang, Raiyan Seede, Xueqin Huang, Janine T Maier, Hans J Maier, Ibrahim Karaman, Alaa Elwany, and Raymundo Arróyave. Assessing printability maps in additive manufacturing of metal alloys. *Acta Materialia*, 176:199–210, 2019.

[173] Vishnuu Jothi Prakash, Malte Buhr, and Claus Emmelmann. Digitalization of directed energy deposition process through a multidirectional height monitoring sensor system. *Journal of Laser Applications*, 33(1):012044, 2021.

[174] C. Kamath, B. El-Dasher, G.F. Gallegos, W.E. King, and A. Sisto. Density of additively-manufactured, 316l ss parts using laser powder-bed fusion at powers up to 400 w. *International Journal of Advanced Manufacturing Technology*, 74(1-4):65–78, 2014. cited By 197.

[175] Chandrika Kamath, Bassem El-dasher, Gilbert F Gallegos, Wayne E King, and Aaron Sisto. Density of additively-manufactured, 316l SS parts using laser powder-bed fusion at powers up to 400 W. *Int. J. Adv. Manuf. Technol.*, 74(1-4):65–78, 2014.

[176] Shima Kamyab, Rasool Sabzi, and Zohreh Azimifar. Deep generative models: Deterministic prediction with an application in inverse rendering. In *2019 4th International Conference on Pattern Recognition and Image Analysis (IPRIA)*, pages 257–262. IEEE, 2019.

[177] A.F.H. Kaplan and G. Groboth. Process analysis of laser beam cladding. *Journal of Manufacturing Science and Engineering, Transactions of the ASME*, 123(4):609–614, 2001. cited By 68.

[178] S. Karnati, N. Matta, T. Sparks, and F. Liou. Vision-based process monitoring for laser metal deposition processes. In *Proc. 24th Solid Freeform Fabr. Symp.*, pages 88–94, 2013.

[179] Galina Kasperovich, Jan Haubrich, Joachim Gussone, and Guillermo Requena. Correlation between porosity and processing parameters in tial6v4 produced by selective laser melting. *Materials & Design*, 105:160–170, 2016.

[180] Yusuf Kaynak and Ozhan Kitay. The effect of post-processing operations on surface characteristics of 316l stainless steel produced by selective laser melting. *Additive Manufacturing*, 26:84–93, 2019.

[181] Yusuf Kaynak and Emre Tascioglu. Post-processing effects on the surface characteristics of inconel 718 alloy fabricated by selective laser melting additive manufacturing. *Progress in Additive Manufacturing*, pages 1–14, 2019.

[182] Jean-Pierre Kenné, Pierre Dejax, and Ali Gharbi. Production planning of a hybrid manufacturing–remanufacturing system under uncertainty within a closed-loop supply chain. *International Journal of Production Economics*, 135(1):81–93, 2012.

[183] Olivier Kerbrat, Pascal Mognol, and Jean-Yves Hascoët. A new dfm approach to combine machining and additive manufacturing. *Computers in Industry*, 62(7):684–692, 2011.

[184] S.A. Khairallah, A.T. Anderson, A. Rubenchik, and W.E. King. Laser powder-bed fusion additive manufacturing: Physics of complex melt flow and formation mechanisms of pores, spatter, and denudation zones. *Acta Materialia*, 108:36–45, 2016. cited By 898.

[185] Saad A Khairallah, Andrew T Anderson, Alexander Rubenchik, and Wayne E King. Laser powder-bed fusion additive manufacturing: Physics of complex melt flow and formation mechanisms of pores, spatter, and denudation zones. *Acta Materialia*, 108:36–45, 2016.

[186] Mojtaba Khanzadeh, Linkan Bian, Nima Shamsaei, and Scott M Thompson. Porosity detection of laser based additive manufacturing using melt pool morphology clustering. In *Annual International Solid Freeform Fabrication Symposium (SFF)*, pages 8–10, 2016.

[187] Mojtaba Khanzadeh, Sudipta Chowdhury, Mohammad Marufuzzaman, Mark A Tschopp, and Linkan Bian. Porosity prediction: Supervised-learning of thermal history for direct laser deposition. *Journal of manufacturing systems*, 47:69–82, 2018.

[188] Mojtaba Khanzadeh, Sudipta Chowdhury, Mark A Tschopp, Haley R Doude, Mohammad Marufuzzaman, and Linkan Bian. In-situ monitoring of melt pool images for porosity prediction in directed energy deposition processes. *IISE Transactions*, pages 1–19, 2018.

[189] Mojtaba Khanzadeh, Sudipta Chowdhury, Mark A Tschopp, Haley R Doude, Mohammad Marufuzzaman, and Linkan Bian. In-situ monitoring of melt pool images for porosity prediction in directed energy deposition processes. *IISE Transactions*, 51(5):437–455, 2019.

[190] Mojtaba Khanzadeh, Wenmeng Tian, Aref Yadollahi, Haley R Doude, Mark A Tschopp, and Linkan Bian. Dual process monitoring of metal-based additive manufacturing using tensor decomposition of thermal image streams. *Additive Manufacturing*, 23:443–456, 2018.

[191] A.M. Khorasani, I. Gibson, N. Godarzvand Chegini, M. Goldberg, A.H. Ghasemi, and G. Littlefair. An improved static model for tool deflection in machining of ti–6al–4v acetabular shell produced by selective laser melting. *Measurement: Journal of the International Measurement Confederation*, 92:534–544, 2016. cited By 14.

[192] Hyungson Ki, Jyoti Mazumder, and Pravansu S Mohanty. Modeling of laser keyhole welding: Part II. simulation of keyhole evolution, velocity, temperature profile, and experimental verification. *Metall. Mater. Trans. A*, 33(6):1831–1842, 2002.

[193] Fabian Kies, Markus B Wilms, Norbert Pirch, Konda G Pradeep, Johannes H Schleifenbaum, and Christian Haase. Defect formation and prevention in directed

energy deposition of high-manganese steels and the effect on mechanical properties. *Materials Science and Engineering: A*, 772:138688, 2020.

[194] Wayne E King, Holly D Barth, Victor M Castillo, Gilbert F Gallegos, John W Gibbs, Douglas E Hahn, Chandrika Kamath, and Alexander M Rubenchik. Observation of keyhole-mode laser melting in laser powder-bed fusion additive manufacturing. *J. Mater. Process. Technol.*, 214(12):2915–2925, 2014.

[195] W.E. King, H.D. Barth, V.M. Castillo, G.F. Gallegos, J.W. Gibbs, D.E. Hahn, C. Kamath, and A.M. Rubenchik. Observation of keyhole-mode laser melting in laser powder-bed fusion additive manufacturing. *Journal of Materials Processing Technology*, 214(12):2915–2925, 2014. cited By 480.

[196] Diederik P Kingma, Max Welling, et al. An introduction to variational autoencoders. *Foundations and Trends® in Machine Learning*, 12(4):307–392, 2019.

[197] Andrew M Kiss, Anthony Y Fong, Nicholas P Calta, Vivek Thampy, Aiden A Martin, Philip J Depond, Jenny Wang, Manyalibo J Matthews, Ryan T Ott, Christopher J Tassone, et al. Laser-induced keyhole defect dynamics during metal additive manufacturing. *Advanced Engineering Materials*, 21(10):1900455, 2019.

[198] Christian Kledwig, Holger Perfahl, Martin Reisacher, Frank Brückner, Jens Bliedtner, and Christoph Leyens. Analysis of melt pool characteristics and process parameters using a coaxial monitoring system during directed energy deposition in additive manufacturing. *Materials*, 12(2):308, 2019.

[199] Cameron Myron Knapp, Thomas J Lienert, Paul Burgardt, Patrick Wayne Hochanadel, and Desiderio Kovar. A model to predict deposition parameters for directed energy deposition: part i theory and modeling. *Rapid Prototyping Journal*, 2019.

[200] T Kolb, A Mahr, F Huber, J Tremel, and M Schmidt. Qualification of channels produced by laser powder bed fusion: Analysis of cleaning methods, flow rate and melt pool monitoring data. *Addit. Manuf.*, 25:430–436, 2019.

[201] Tobias Kolb, Philipp Gebhardt, Oliver Schmidt, Jan Tremel, and Michael Schmidt. Melt pool monitoring for laser beam melting of metals: Assistance for material qualification for the stainless steel 1.4057. *Procedia CIRP*, 74:116–121, 2018.

[202] Tobias Kolb, Lars Müller, Jan Tremel, and Michael Schmidt. Melt pool monitoring for laser beam melting of metals: inline-evaluation and remelting of surfaces. *Procedia CIRP*, 74:111–115, 2018.

[203] Daisuke Kono, Haruyuki Yamaguchi, Yohei Oda, and Toshimasa Sakai. Stabilization of standoff distance by efficient and adaptive updating of layer height command in directed energy deposition. *CIRP Journal of Manufacturing Science and Technology*, 31:244–250, 2020.

[204] Dennis A Kriczky, Jeff Irwin, Edward W Reutzel, Pan Michaleris, Abdalla R Nassar, and James Craig. 3D spatial reconstruction of thermal characteristics in directed energy deposition through optical thermal imaging. *J. Mater. Process. Technol.*, 221:172–186, 2015.

[205] Nikhil Nivrutti Kumbhar and AV Mulay. Post processing methods used to improve surface finish of products which are manufactured by additive manufacturing technologies: a review. *Journal of The Institution of Engineers (India): Series C*, 99(4):481–487, 2018.

[206] Ohyung Kwon, Hyung Giun Kim, Min Ji Ham, Wonrae Kim, Gun-Hee Kim, Jae-Hyung Cho, Nam Il Kim, and Kangil Kim. A deep neural network for classification of melt-pool images in metal additive manufacturing. *Journal of Intelligent Manufacturing*, pages 1–12, 2018.

[207] C. Lalas, K. Tsirbas, K. Salonitis, and G. Chryssolouris. An analytical model of the laser clad geometry. *International Journal of Advanced Manufacturing Technology*, 32(1-2):34–41, 2007. cited By 67.

[208] B Lane, S Grantham, Ho Yeung, C Zarobila, and J Fox. Performance characterization of process monitoring sensors on the NIST additive manufacturing metrology testbed. In *Proc. 28th Solid Freeform Fabr. Symp.*, pages 1279–1288, 2017.

[209] Brandon Lane, Ivan Zhirnov, Sergey Mekhontsev, Steven Grantham, Richard Ricker, Santosh Rauniyar, and Kevin Chou. Transient laser energy absorption, co-axial melt pool monitoring, and relationship to melt pool morphology. *Additive Manufacturing*, page 101504, 2020.

[210] NO Larrosa, W Wang, N Read, MH Loretto, C Evans, J Carr, U Tradowsky, MM Attallah, and PJ Withers. Linking microstructure and processing defects to mechanical properties of selectively laser melted alsi10mg alloy. *Theoretical and Applied Fracture Mechanics*, 98:123–133, 2018.

[211] RK Leach, David Bourell, Simone Carmignato, Alkan Donmez, Nicola Senin, and Wim Dewulf. Geometrical metrology for metal additive manufacturing. *CIRP annals*, 68(2):677–700, 2019.

[212] H.-K. Lee. Effects of the cladding parameters on the deposition efficiency in pulsed nd:yag laser cladding. *Journal of Materials Processing Technology*, 202(1-3):321–327, 2008. cited By 60.

[213] Jae Y Lee, Sung H Ko, Dave F Farson, and Choong D Yoo. Mechanism of keyhole formation and stability in stationary laser welding. *Journal of Physics D: Applied Physics*, 35(13):1570, 2002.

[214] Dirk Lehmhus, Claus Aumund-Kopp, Frank Petzoldt, Dirk Godlinski, Arne Haberkorn, Volker Zöllmer, and Matthias Busse. Customized smartness: a survey on links between additive manufacturing and sensor integration. *Procedia Technology*, 26:284–301, 2016.

[215] Antti Lehti, Lauri Taimisto, Heidi Piili, Antti Salminen, and Olli Nyrhilä. Evaluation of different monitoring methods of laser assisted additive manufacturing of stainless steel. In *Proc. 12th Conference of the European Ceramic Society*, 2011.

[216] Chu Lun Alex Leung, Sebastian Marussi, Robert C Atwood, Michael Towrie, Philip J Withers, and Peter D Lee. In situ x-ray imaging of defect and molten pool dynamics in laser additive manufacturing. *Nature communications*, 9(1):1355, 2018.

[217] J. Li, Q. Wang, P. Michaleris, and E.W. Reutzel. Model prediction for deposition height during a direct metal deposition process. pages 2188–2194, 2017. cited By 2.

[218] J. Li, Q. Wang, P. Michaleris, E.W. Reutzel, and A.R. Nassar. An extended lumped-parameter model of melt-pool geometry to predict part height for directed energy deposition. *Journal of Manufacturing Science and Engineering, Transactions of the ASME*, 139(9), 2017. cited By 15.

[219] Lin Li, Azadeh Haghighi, and Yiran Yang. A novel 6-axis hybrid additive-subtractive manufacturing process: Design and case studies. *Journal of Manufacturing Processes*, 33:150–160, 2018.

[220] Shuai Li, Bi Zhang, and Qian Bai. Effect of temperature buildup on milling forces in additive/subtractive hybrid manufacturing of ti-6al-4v. *The International Journal of Advanced Manufacturing Technology*, 107(9):4191–4200, 2020.

[221] Andreas K Lianos, Harry Bikas, and Panagiotis Stavropoulos. A shape optimization method for part design derived from the buildability restrictions of the directed energy deposition additive manufacturing process. *Designs*, 4(3):19, 2020.

[222] Pei-Yi Lin, Fang-Cheng Shen, Kuo-Tsai Wu, Sheng-Jye Hwang, and Huei-Huang Lee. Process optimization for directed energy deposition of ss316l components. *The International Journal of Advanced Manufacturing Technology*, 111(5):1387–1400, 2020.

[223] Frank Liou, Kevin Slattery, Mary Kinsella, Joseph Newkirk, Hsin-Nan Chou, and Robert Landers. Applications of a hybrid manufacturing process for fabrication of metallic structures. *Rapid Prototyping Journal*, 2007.

[224] Bing Liu, Hongyao Shen, Rongxin Deng, Shun Li, Sheng Tang, Jianzhong Fu, and Yu Wang. Research on a planning method for switching moments in hybrid manufacturing processes. *Journal of Manufacturing Processes*, 56:786–795, 2020.

[225] Changyong Liu, Deng Yan, Jianwei Tan, Zhuokeng Mai, Zhixiang Cai, Yuhong Dai, Mingguang Jiang, Pei Wang, Zhiyuan Liu, Chia-Chen Li, et al. Development and experimental validation of a hybrid selective laser melting and cnc milling system. *Additive Manufacturing*, 36:101550, 2020.

[226] Dong-Rong Liu, Shuhao Wang, and Wentao Yan. Grain structure evolution in transition-mode melting in direct energy deposition. *Materials & Design*, 194:108919, 2020.

[227] Lucia Lizzul, Marco Sorgato, Rachele Bertolini, Andrea Ghiotti, and Stefania Bruschi. Anisotropy effect of additively manufactured ti6al4v titanium alloy on surface quality after milling. *Precision Engineering*, 67:301–310, 2021.

[228] Jonathan Long, Evan Shelhamer, and Trevor Darrell. Fully convolutional networks for semantic segmentation. In *Proceedings of the IEEE conference on computer vision and pattern recognition*, pages 3431–3440, 2015.

[229] Ana Lopez, Ricardo Bacelar, Inês Pires, Telmo G Santos, José Pedro Sousa, and Luísa Quintino. Non-destructive testing application of radiography and ultrasound for wire and arc additive manufacturing. *Additive Manufacturing*, 21:298–306, 2018.

[230] Ana Beatriz Lopez, João Santos, José Pedro Sousa, Telmo G Santos, and Luísa Quintino. Phased array ultrasonic inspection of metal additive manufacturing parts. *Journal of Nondestructive Evaluation*, 38(3):62, 2019.

[231] KA Lorenz, JB Jones, DI Wimpenny, and MR Jackson. A review of hybrid manufacturing. In *Solid freeform fabrication conference proceedings*, volume 53, pages 96–108, 2015.

[232] Keith Lorenz. *Process monitoring for laser-directed energy deposition with respect to a retrofit hybrid manufacturing system.* PhD thesis, Loughborough University, 2019.

[233] Philipp Lott, Henrich Schleifenbaum, Wilhelm Meiners, Konrad Wissenbach, Christian Hinke, and Jan Bültmann. Design of an optical system for the in situ process monitoring of selective laser melting (SLM). *Phys. Procedia*, 12:683–690, 2011.

[234] Qing Yang Lu and Chee How Wong. Additive manufacturing process monitoring and control by non-destructive testing techniques: challenges and in-process monitoring. *Virtual and physical prototyping*, 13(2):39–48, 2018.

[235] QY Lu, NV Nguyen, AJW Hum, T Tran, and CH Wong. Optical in-situ monitoring and correlation of density and mechanical properties of stainless steel parts produced by selective laser melting process based on varied energy density. *J. Mater. Process. Technol.*, 271:520 – 531, 2019.

[236] Rundong Lu, Haiying Wei, Fazhi Li, Zhehao Zhang, Zhichao Liang, and Bin Li. In-situ monitoring of the penetration status of keyhole laser welding by using a support vector machine with interaction time conditioned keyhole behaviors. *Optics and Lasers in Engineering*, 130:106099, 2020.

[237] Mohamad Mahmoudi, Ahmed Aziz Ezzat, and Alaa Elwany. Layerwise anomaly detection in laser powder-bed fusion metal additive manufacturing. *Journal of Manufacturing Science and Engineering*, 141(3):031002, 2019.

[238] Jyotsna Dutta Majumdar and Indranil Manna. *Laser-assisted fabrication of materials*, volume 161. Springer Sci. Bus. Media, 2012.

[239] S Makris and P Aivaliotis. Framework for accurate simulation and model-based control of hybrid manufacturing processes. *Procedia CIRP*, 97:470–475, 2021.

[240] Mahesh Mani, Shaw Feng, Lane Brandon, Alkan Donmez, Shawn Moylan, and Ronnie Fesperman. *Measurement science needs for real-time control of additive manufacturing powder-bed fusion processes.* CRC Press, 2017.

[241] Guha Manogharan, Richard A Wysk, and Ola LA Harrysson. Additive manufacturing–integrated hybrid manufacturing and subtractive processes: economic

model and analysis. *International Journal of Computer Integrated Manufacturing*, 29(5):473–488, 2016.

[242] V.D. Manvatkar, A.A. Gokhale, G. Jagan Reddy, A. Venkataramana, and A. De. Estimation of melt pool dimensions, thermal cycle, and hardness distribution in the laser-engineered net shaping process of austenitic stainless steel. *Metallurgical and Materials Transactions A: Physical Metallurgy and Materials Science*, 42(13):4080–4087, 2011. cited By 53.

[243] Advaith Maragowdanahalli Somasundar and David Paul. Geometrical locating scheme for complex hybrid manufacturing: Multiple additive manufacturing and machining. 2019.

[244] Felipe Marin, Adriano Fagali de Souza, Carlos Henrique Ahrens, and Luis Norberto López de Lacalle. A new hybrid process combining machining and selective laser melting to manufacture an advanced concept of conformal cooling channels for plastic injection molds. *The International Journal of Advanced Manufacturing Technology*, pages 1–16, 2021.

[245] Daniele Marini, David Cunningham, and Jonathan R Corney. Near net shape manufacturing of metal: a review of approaches and their evolutions. *Proceedings of the institution of mechanical engineers, Part B: journal of engineering manufacture*, 232(4):650–669, 2018.

[246] Aiden A Martin, Nicholas P Calta, Joshua A Hammons, Saad A Khairallah, Michael H Nielsen, Richard M Shuttlesworth, Nicholas Sinclair, Manyalibo J Matthews, Jason R Jeffries, Trevor M Willey, et al. Ultrafast dynamics of laser-metal interactions in additive manufacturing alloys captured by in situ x-ray imaging. *Materials Today Advances*, 1:100002, 2019.

[247] Aiden A Martin, Nicholas P Calta, Saad A Khairallah, Jenny Wang, Phillip J Depond, Anthony Y Fong, Vivek Thampy, Gabe M Guss, Andrew M Kiss, Kevin H Stone, et al. Dynamics of pore formation during laser powder bed fusion additive manufacturing. *Nature communications*, 10(1):1987, 2019.

[248] Ville-Pekka Matilainen, Heidi Piili, Antti Salminen, and Olli Nyrhilä. Preliminary investigation of keyhole phenomena during single layer fabrication in laser additive manufacturing of stainless steel. *Phys. Procedia*, 78:377–387, 2015.

[249] Mustafa Megahed, Hans-Wilfried Mindt, Narcisse N'Dri, Hongzhi Duan, and Olivier Desmaison. Metal additive-manufacturing process and residual stress modeling. *Integrating Materials and Manufacturing Innovation*, 5(1):61–93, 2016.

[250] S Merkt, C Hinke, H Schleifenbaum, and H Voswinckel. Geometric complexity analysis in an integrative technology evaluation model (item) for selective laser melting (slm). *South African journal of industrial engineering*, 23(2):97–105, 2012.

[251] Maxwell K Micali and David Dornfeld. Fully three-dimensional toolpath generation for point-based additive manufacturing systems. In *Solid Freeform Fabrication Symposium*, volume 27, 2016.

[252] J.G. Michopoulos, A.P. Iliopoulos, J.C. Steuben, A.J. Birnbaum, and S.G. Lambrakos. On the multiphysics modeling challenges for metal additive manufacturing processes. *Additive Manufacturing*, 22:784–799, 2018. cited By 17.

[253] Weiwei Ming, Jie Chen, Qinglong An, and Ming Chen. Dynamic mechanical properties and machinability characteristics of selective laser melted and forged ti6al4v. *Journal of Materials Processing Technology*, 271:284–292, 2019.

[254] Jordi Minnema, Maureen van Eijnatten, Wouter Kouw, Faruk Diblen, Adriënne Mendrik, and Jan Wolff. Ct image segmentation of bone for medical additive manufacturing using a convolutional neural network. *Computers in biology and medicine*, 103:130–139, 2018.

[255] Elham Mirkoohi, Daniel E Sievers, Hamid Garmestani, and Steven Y Liang. Thermo-mechanical modeling of thermal stress in metal additive manufacturing considering elastoplastic hardening. *CIRP Journal of Manufacturing Science and Technology*, 28:52–67, 2020.

[256] M Montazeri and P Rao. Sensor-based build condition monitoring in laser powder bed fusion additive manufacturing process using a spectral graph theoretic approach. *ASME J. Manuf. Sci. Eng.*, 140(9):091002–091002–16, 2018.

[257] Mohammad Montazeri, Abdalla R Nassar, Christopher B Stutzman, and Prahalada Rao. Heterogeneous sensor-based condition monitoring in directed energy deposition. *Additive Manufacturing*, 30:100916, 2019.

[258] Juliane Moritz, André Seidel, Michael Kopper, Jörg Bretschneider, Johannes Gumpinger, Thomas Finaske, Mirko Riede, Michael Schneeweiß, Elena López, Frank Brückner, et al. Hybrid manufacturing of titanium ti-6al-4v combining laser metal

deposition and cryogenic milling. *The International Journal of Advanced Manufacturing Technology*, 107(7):2995–3009, 2020.

[259] Benjamin M Morrow, Thomas J Lienert, Cameron M Knapp, Jacob O Sutton, Michael J Brand, Robin M Pacheco, Veronica Livescu, John S Carpenter, and George T Gray. Impact of defects in powder feedstock materials on microstructure of 304l and 316l stainless steel produced by additive manufacturing. *Metallurgical and Materials Transactions A*, 49(8):3637–3650, 2018.

[260] M. Mozaffar, A. Paul, R. Al-Bahrani, S. Wolff, A. Choudhary, A. Agrawal, K. Ehmann, and J. Cao. Data-driven prediction of the high-dimensional thermal history in directed energy deposition processes via recurrent neural networks. *Manufacturing Letters*, 18:35–39, 2018. cited By 31.

[261] Bernhard Mueller. Additive manufacturing technologies–rapid prototyping to direct digital manufacturing. *Assembly Automation*, 2012.

[262] T. Mukherjee, W. Zhang, and T. DebRoy. An improved prediction of residual stresses and distortion in additive manufacturing. *Computational Materials Science*, 126:360–372, 2017. cited By 237.

[263] T. Mukherjee, J.S. Zuback, W. Zhang, and T. DebRoy. Residual stresses and distortion in additively manufactured compositionally graded and dissimilar joints. *Computational Materials Science*, 143:325–337, 2018. cited By 52.

[264] Mohamed A Naiel, Deniz Sera Ertay, Mihaela Vlasea, and Paul Fieguth. Adaptive vision-based detection of laser-material interaction for directed energy deposition. *Additive Manufacturing*, page 101468, 2020.

[265] Amal M Nair, Gopinath Muvvala, Sagar Sarkar, and Ashish Kumar Nath. Real-time detection of cooling rate using pyrometers in tandem in laser material processing and directed energy deposition. *Materials Letters*, 277:128330, 2020.

[266] Vinod Nair and Geoffrey E Hinton. Rectified linear units improve restricted boltzmann machines. In *ICML*, 2010.

[267] S. Nam, H. Cho, C. Kim, and Y.-M. Kim. Effect of process parameters on deposition properties of functionally graded sts 316/fe manufactured by laser direct metal deposition. *Metals*, 8(8), 2018. cited By 14.

[268] Abdalla R Nassar, Molly A Gundermann, Edward W Reutzel, Paul Guerrier, Michael H Krane, and Matthew J Weldon. Formation processes for large ejecta and interactions with melt pool formation in powder bed fusion additive manufacturing. *Scientific reports*, 9(1):5038, 2019.

[269] AR Nassar, TJ Spurgeon, and EW Reutzel. Sensing defects during directed-energy additive manufacturing of metal parts using optical emissions spectroscopy. In *Solid Freeform Fabrication Symposium Proceedings*, pages 278–287. University of Texas Austin, TX, 2014.

[270] O. Nenadl, W. Kuipers, N. Koelewijn, V. Ocelík, and J.T.M. De Hosson. A versatile model for the prediction of complex geometry in 3d direct laser deposition. *Surface and Coatings Technology*, 307:292–300, 2016. cited By 16.

[271] Stephen T Newman, Zicheng Zhu, Vimal Dhokia, and Alborz Shokrani. Process planning for additive and subtractive manufacturing technologies. *CIRP Annals*, 64(1):467–470, 2015.

[272] Zhenguo Nie, Sangjin Jung, Levent Burak Kara, and Kate S Whitefoot. Optimization of part consolidation for minimum production costs and time using additive manufacturing. *Journal of Mechanical Design*, 142(7), 2020.

[273] Jinqiang Ning, Daniel E Sievers, Hamid Garmestani, and Steven Y Liang. Analytical modeling of part porosity in metal additive manufacturing. *International Journal of Mechanical Sciences*, 172:105428, 2020.

[274] Niyanth Niyanth S, Justin S Baba, Brian H Jordan, Ralph Barton Dinwiddie, and Ryan R Dehoff. Understanding part to part variability during directed energy deposition processes using in-situ and ex-situ process characterization. Technical report, Oak Ridge National Lab.(ORNL), Oak Ridge, TN (United States), 2018.

[275] Chinedum E Okwudire and Jihyun Lee. Minimization of the residual vibrations of ultra-precision manufacturing machines via optimal placement of vibration isolators. *Precision engineering*, 37(2):425–432, 2013.

[276] Txomin Ostra, Unai Alonso, Fernando Veiga, Mikel Ortiz, Pedro Ramiro, and Amaia Alberdi. Analysis of the machining process of inconel 718 parts manufactured by laser metal deposition. *Materials*, 12(13):2159, 2019.

[277] Nobuyuki Otsu. A threshold selection method from gray-level histograms. *IEEE transactions on systems, man, and cybernetics*, 9(1):62–66, 1979.

[278] Olusola Oyelola, Pete Crawforth, Rachid M'Saoubi, and Adam T Clare. Machining of functionally graded ti6al4v/wc produced by directed energy deposition. *Additive Manufacturing*, 24:20–29, 2018.

[279] Olusola Oyelola, Pete Crawforth, Rachid M'Saoubi, and Adam T Clare. On the machinability of directed energy deposited ti6al4v. *Additive Manufacturing*, 19:39–50, 2018.

[280] Moses O Oyesola, Khumbulani Mpofu, Ntombi R Mathe, and Ilesanmi A Daniyan. Hybrid-additive manufacturing cost model: A sustainable through-life engineering support for maintenance repair overhaul in the aerospace. *Procedia Manufacturing*, 49:199–205, 2020.

[281] Tuğrul Özel, Ayça Altay, Bilgin Kaftanoğlu, Richard Leach, Nicola Senin, and Alkan Donmez. Focus variation measurement and prediction of surface texture parameters using machine learning in laser powder bed fusion. *Journal of Manufacturing Science and Engineering*, 142(1), 2020.

[282] Tuğrul Özel, Animek Shaurya, Ayça Altay, and Liang Yang. Process monitoring of meltpool and spatter for temporal-spatial modeling of laser powder bed fusion process. *Procedia CIRP*, 74:102–106, 2018.

[283] Matteo Pacher, Luca Mazzoleni, Leonardo Caprio, Ali Gökhan Demir, and Barbara Previtali. Estimation of melt pool size by complementary use of external illumination and process emission in coaxial monitoring of selective laser melting. *J. Laser Appl.*, 31(2):022305:1–9, 2019.

[284] Deepankar Pal, Nachiket Patil, Kai Zeng, and Brent Stucker. An integrated approach to additive manufacturing simulations using physics based, coupled multiscale process modeling. *Journal of Manufacturing Science and Engineering*, 136(6), 2014.

[285] Henri Paris, Hossein Mokhtarian, Eric Coatanéa, Matthieu Museau, and Inigo Flores Ituarte. Comparative environmental impacts of additive and subtractive manufacturing technologies. *CIRP Annals*, 65(1):29–32, 2016.

[286] Sagar Patel, Allan Rogalsky, and Mihaela Vlasea. Towards understanding side-skin surface characteristics in laser powder bed fusion. *Journal of Materials Research*, 35(15):2055–2064, 2020.

[287] Sagar Patel and Mihaela Vlasea. Melting modes in laser powder bed fusion. *Materialia*, 9:100591, 2020.

[288] A. Paul, M. Mozaffar, Z. Yang, W.-k. Liao, A. Choudhary, J. Cao, and A. Agrawal. A real-time iterative machine learning approach for temperature profile prediction in additive manufacturing processes. *A real-time iterative machine learning approach for temperature profile prediction in additive manufacturing processes*, 2019. cited By 2.

[289] Arindam Paul, Mojtaba Mozaffar, Zijiang Yang, Wei-keng Liao, Alok Choudhary, Jian Cao, and Ankit Agrawal. A real-time iterative machine learning approach for temperature profile prediction in additive manufacturing processes. In *2019 IEEE International Conference on Data Science and Advanced Analytics (DSAA)*, pages 541–550. IEEE, 2019.

[290] Xing Peng, Lingbao Kong, Jerry Ying Hsi Fuh, and Hao Wang. A review of post-processing technologies in additive manufacturing. *Journal of Manufacturing and Materials Processing*, 5(2):38, 2021.

[291] Tanisha Pereira, John V Kennedy, and Johan Potgieter. A comparison of traditional manufacturing vs additive manufacturing, the best method for the job. *Procedia Manufacturing*, 30:11–18, 2019.

[292] P. Peyre, P. Aubry, R. Fabbro, R. Neveu, and A. Longuet. Analytical and numerical modelling of the direct metal deposition laser process. *Journal of Physics D: Applied Physics*, 41(2), 2008. cited By 203.

[293] M. Picasso, C.F. Marsden, J.D. Wagniere, A. Frenk, and M. Rappaz. A simple but realistic model for laser cladding. *Metallurgical and Materials Transactions B*, 25(2):281–291, 1994. cited By 249.

[294] A.J. Pinkerton and L. Li. Modelling the geometry of a moving laser melt pool and deposition track via energy and mass balances. *Journal of Physics D: Applied Physics*, 37(14):1885–1895, 2004. cited By 141.

[295] A.J. Pinkerton, W. Wang, and L. Li. Component repair using laser direct metal deposition. *Proceedings of the Institution of Mechanical Engineers, Part B: Journal of Engineering Manufacture*, 222(7):827–836, 2008. cited By 114.

[296] JPM Pragana, RFV Sampaio, IMF Bragança, CMA Silva, and PAF Martins. Hybrid metal additive manufacturing: A state-of-the-art review. *Advances in Industrial and Manufacturing Engineering*, 2:100032, 2021.

[297] Maxwell Praniewicz, Thomas Kurfess, and Christopher Saldana. An adaptive geometry transformation and repair method for hybrid manufacturing. *Journal of Manufacturing Science and Engineering*, 141(1), 2019.

[298] Maxwell R Praniewicz. *Adaptive geometry transformation and repair methodology for hybrid manufacturing.* PhD thesis, Georgia Institute of Technology, 2018.

[299] Tuomas Purtonen, Anne Kalliosaari, and Antti Salminen. Monitoring and adaptive control of laser processes. *Phys. Procedia*, 56:1218–1231, 2014.

[300] M Qian, W Xu, M Brandt, and HP Tang. Additive manufacturing and postprocessing of ti-6al-4v for superior mechanical properties. *MRS Bulletin*, 41(10):775–784, 2016.

[301] N. Raghavan, B.H. Jordan, and R.R. Dehoff. Controlling microstructure in deposits fabricated using powder blown direct energy deposition technique. 2018. cited By 1.

[302] Baker Ralph. Method of making decorative articles, April 14 1925. US Patent 1,533,300.

[303] Arvind Shankar Raman, Karl R Haapala, Kamyar Raoufi, Barbara S Linke, William Z Bernstein, and Katherine C Morris. Defining near-term to long-term research opportunities to advance metrics, models, and methods for smart and sustainable manufacturing. *Smart and sustainable manufacturing systems*, 4(2), 2020.

[304] Nariman Razaviarab, Safura Sharifi, and Yaser M Banadaki. Smart additive manufacturing empowered by a closed-loop machine learning algorithm. In *Nano-, Bio-, Info-Tech Sensors and 3D Systems III*, volume 10969, page 109690H. International Society for Optics and Photonics, 2019.

[305] Lan Ren, Todd Sparks, Jianzhong Ruan, and Frank Liou. Integrated process planning for a multiaxis hybrid manufacturing system. *Journal of Manufacturing Science and Engineering*, 132(2), 2010.

[306] Volker Renken, Stephan Albinger, Gert Goch, Arne Neef, and Claus Emmelmann. Development of an adaptive, self-learning control concept for an additive manufacturing process. *CIRP Journal of Manufacturing Science and Technology*, 19:57–61, 2017.

[307] Danilo Jimenez Rezende, Shakir Mohamed, and Daan Wierstra. Stochastic backpropagation and approximate inference in deep generative models. *arXiv preprint arXiv:1401.4082*, 2014.

[308] Kandice SB Ribeiro, Fábio E Mariani, and Reginaldo T Coelho. A study of different deposition strategies in direct energy deposition (ded) processes. *Procedia Manufacturing*, 48:663–670, 2020.

[309] Emmanuel Rodriguez, Francisco Medina, David Espalin, Cesar Terrazas, Dan Muse, Chad Henry, Eric MacDonald, and Ryan B Wicker. Integration of a thermal imaging feedback control system in electron beam melting. *WM Keck Center for 3D Innovation, University of Texas at El Paso*, pages 945–961, 2012.

[310] Emmanuel Rodriguez, Jorge Mireles, Cesar A Terrazas, David Espalin, Mireya A Perez, and Ryan B Wicker. Approximation of absolute surface temperature measurements of powder bed fusion additive manufacturing technology using in situ infrared thermography. *Additive Manufacturing*, 5:31–39, 2015.

[311] S Romano, A Brückner-Foit, A Brandão, J Gumpinger, T Ghidini, and S Beretta. Fatigue properties of alsi10mg obtained by additive manufacturing: Defect-based modelling and prediction of fatigue strength. *Engineering Fracture Mechanics*, 187:165–189, 2018.

[312] Simone Romano, A Brandão, J Gumpinger, M Gschweitl, and S Beretta. Qualification of am parts: extreme value statistics applied to tomographic measurements. *Materials & Design*, 131:32–48, 2017.

[313] D. Rosenthal. The theory of moving sources of heat and its application to metal treatments. *Trans. ASME*, 68(11):849–866, 1946. cited By 1052.

[314] Andrea Rossi and Michele Lanzetta. Integration of hybrid additive/subtractive manufacturing planning and scheduling by metaheuristics. *Computers & Industrial Engineering*, 144:106428, 2020.

[315] Giovanna Rotella, Stano Imbrogno, Sebastiano Candamano, and Domenico Umbrello. Surface integrity of machined additively manufactured ti alloys. *Journal of Materials Processing Technology*, 259:180–185, 2018.

[316] Jochem C Roukema and Yusuf Altintas. Generalized modeling of drilling vibrations. part i: Time domain model of drilling kinematics, dynamics and hole formation. *International Journal of Machine Tools and Manufacture*, 47(9):1455–1473, 2007.

[317] Jianzhong Ruan, Kunnayut Eiamsa-ard, and Frank W Liou. Automatic process planning and toolpath generation of a multiaxis hybrid manufacturing system. *Journal of manufacturing processes*, 7(1):57–68, 2005.

[318] Jianzhong Ruan, Kunnayut Eiamsa-ard, Jun Zhang, and Frank W Liou. Automatic process planning of a multi-axis hybrid manufacturing system. In *International Design Engineering Technical Conferences and Computers and Information in Engineering Conference*, volume 36223, pages 965–971, 2002.

[319] Alexander M Rubenchik, Wayne E King, and Sheldon S Wu. Scaling laws for the additive manufacturing. *Journal of Materials Processing Technology*, 257:234–243, 2018.

[320] A. Saboori, D. Gallo, S. Biamino, P. Fino, and M. Lombardi. An overview of additive manufacturing of titanium components by directed energy deposition: Microstructure and mechanical properties. *Applied Sciences (Switzerland)*, 7(9), 2017. cited By 97.

[321] Abdollah Saboori, Alberta Aversa, Giulio Marchese, Sara Biamino, Mariangela Lombardi, and Paolo Fino. Application of directed energy deposition-based additive manufacturing in repair. *Applied Sciences*, 9(16):3316, 2019.

[322] Abdollah Saboori, Sara Biamino, Mariangela Lombardi, Simona Tusacciu, Mattia Busatto, Manuel Lai, and Paolo Fino. How the nozzle position affects the geometry of the melt pool in directed energy deposition process. *Powder Metallurgy*, 62(4):213–217, 2019.

[323] Mika Salmi, Iñigo Flores Ituarte, Sergei Chekurov, and Eero Huotilainen. Effect of build orientation in 3d printing production for material extrusion, material jetting, binder jetting, sheet object lamination, vat photopolymerisation, and powder bed fusion. *International Journal of Collaborative Enterprise*, 5(3-4):218–231, 2016.

[324] Konstantinos Salonitis, Laurent D'Alvise, Babis Schoinochoritis, and Dimitrios Chantzis. Additive manufacturing and post-processing simulation: laser cladding followed by high speed machining. *The International Journal of Advanced Manufacturing Technology*, 85(9):2401–2411, 2016.

[325] William J Sames, FA List, Sreekanth Pannala, Ryan R Dehoff, and Sudarsanam Suresh Babu. The metallurgy and processing science of metal additive manufacturing. *Int. Mater. Rev.*, 61(5):315–360, 2016.

[326] P.M. Sammons, D.A. Bristow, and R.G. Landers. Height dependent laser metal deposition process modeling. *Journal of Manufacturing Science and Engineering, Transactions of the ASME*, 135(5), 2013. cited By 60.

[327] P.M. Sammons, D.A. Bristow, and R.G. Landers. Control-oriented modeling of laser metal deposition as a repetitive process. pages 1817–1820, 2014. cited By 13.

[328] R. Sampson, R. Lancaster, and M. Weston. Melt pool image process acceleration using general purpose computing on graphics processing units. In *Proc. 28th Solid Freeform Fabr. Symp.*, pages 1557–1571, 2017.

[329] Robert Sampson, Robert Lancaster, Mark Sutcliffe, David Carswell, Carl Hauser, and Josh Barras. An improved methodology of melt pool monitoring of direct energy deposition processes. *Optics & Laser Technol.*, 127:106194, 2020.

[330] John Schmelzle, Eric V Kline, Corey J Dickman, Edward W Reutzel, Griffin Jones, and Timothy W Simpson. (re) designing for part consolidation: understanding the challenges of metal additive manufacturing. *Journal of Mechanical Design*, 137(11), 2015.

[331] M. Schmidt, M. Merklein, D. Bourell, D. Dimitrov, T. Hausotte, K. Wegener, L. Overmeyer, F. Vollertsen, and G.N. Levy. Laser based additive manufacturing in industry and academia. *CIRP Annals*, 66(2):561–583, 2017. cited By 228.

[332] Michael Schmidt, Marion Merklein, David Bourell, Dimitri Dimitrov, Tino Hausotte, Konrad Wegener, Ludger Overmeyer, Frank Vollertsen, and Gideon N Levy. Laser based additive manufacturing in industry and academia. *CIRP Annals*, 66(2):561–583, 2017.

[333] Edwin J Schwalbach, Sean P Donegan, Michael G Chapman, Kevin J Chaput, and Michael A Groeber. A discrete source model of powder bed fusion additive manufacturing thermal history. *Additive Manufacturing*, 25:485–498, 2019.

[334] Luke Scime and Jack Beuth. Anomaly detection and classification in a laser powder bed additive manufacturing process using a trained computer vision algorithm. *Addit. Manuf.*, 19:114–126, 2018.

[335] Luke Scime and Jack Beuth. A multi-scale convolutional neural network for autonomous anomaly detection and classification in a laser powder bed fusion additive manufacturing process. *Additive Manufacturing*, 24:273–286, 2018.

[336] Luke Scime and Jack Beuth. Melt pool geometry and morphology variability for the inconel 718 alloy in a laser powder bed fusion additive manufacturing process. *Additive Manufacturing*, 29:100830, 2019.

[337] Luke Scime and Jack Beuth. Using machine learning to identify in-situ melt pool signatures indicative of flaw formation in a laser powder bed fusion additive manufacturing process. *Addit. Manuf.*, 25:151–165, 2019.

[338] A Seidel, C Gollee, T Schnellhardt, M Hammer, J Dassing, R Vogt, T Wiese, U Teicher, A Hellmich, S Ihlenfeldt, et al. Cyber-physical approach toward semiautonomous postprocessing of additive manufactured parts and components. *Journal of Laser Applications*, 33(1):012033, 2021.

[339] D Seltzer, JL Schiano, AR Nassar, and EW Reutzel. Illumination and image processing for real-time control of directed energy deposition additive manufacturing. In *Proc. 28th Solid Freeform Fabr. Symp.*, pages 1479–1486, 2016.

[340] B Sencer, Y Altintas, and E Croft. Feed optimization for five-axis cnc machine tools with drive constraints. *International Journal of Machine Tools and Manufacture*, 48(7-8):733–745, 2008.

[341] Burak Sencer and Yusuf Altintas. Modeling and control of contouring errors for five-axis machine tools—part ii: Precision contour controller design. *Journal of manufacturing science and engineering*, 131(3), 2009.

[342] L. Sexton, S. Lavin, G. Byrne, and A. Kennedy. Laser cladding of aerospace materials. *Journal of Materials Processing Technology*, 122(1):63–68, 2002. cited By 276.

[343] L Sexton, S Lavin, G Byrne, and A Kennedy. Laser cladding of aerospace materials. *J. Mater. Process. Technol.*, 122(1):63–68, 2002.

[344] K. Shah, A.J. Pinkerton, A. Salman, and L. Li. Effects of melt pool variables and process parameters in laser direct metal deposition of aerospace alloys. *Materials and Manufacturing Processes*, 25(12):1372–1380, 2010. cited By 61.

[345] Nima Shamsaei, Aref Yadollahi, Linkan Bian, and Scott M Thompson. An overview of direct laser deposition for additive manufacturing; part ii: Mechanical behavior, process parameter optimization and control. *Additive Manufacturing*, 8:12–35, 2015.

[346] Sergey A Shevchik, Christoph Kenel, Christian Leinenbach, and Kilian Wasmer. Acoustic emission for in situ quality monitoring in additive manufacturing using spectral convolutional neural networks. *Additive Manufacturing*, 21:598–604, 2018.

[347] Sergey A Shevchik, Giulio Giulio Masinelli, Christoph Kenel, Christian Leinenbach, and Kilian Wasmer. Deep learning for in situ and real-time quality monitoring in additive manufacturing using acoustic emission. *IEEE Transactions on Industrial Informatics*, 2019.

[348] Manikandakumar Shunmugavel, Ashwin Polishetty, Junior Nomani, Moshe Goldberg, and Guy Littlefair. Metallurgical and machinability characteristics of wrought and selective laser melted ti-6al-4v. *Journal of Metallurgy*, 2016, 2016.

[349] T Sibillano, A Ancona, V Berardi, E Schingaro, G Basile, and PM Lugarà. Optical detection of conduction/keyhole mode transition in laser welding. *Journal of materials processing technology*, 191(1-3):364–367, 2007.

[350] SP Sundar Singh Sivam, A Rajasekaran, S RajendraKumar, K SathiyaMoorthy, and M Gopal. A study of cooling time, copper reduction and effects of alloying elements on the microstructure and mechanical properties of sg iron casting during machining. *Australian Journal of Mechanical Engineering*, 19(1):10–18, 2021.

[351] Himani Siva Prasad, Frank Brueckner, and Alexander FH Kaplan. Powder catchment in laser metal deposition. *Journal of Laser Applications*, 31(2):022308, 2019.

[352] Marina Sokolova and Guy Lapalme. A systematic analysis of performance measures for classification tasks. *Information processing & management*, 45(4):427–437, 2009.

[353] E. Soylemez, J.L. Beuth, and K. Taminger. Controlling melt pool dimensions over a wide range of material deposition rates in electron beam additive manufacturing. *Proceedings of 21St Solid Freeform Fabrication Symposium*, pages 9–11, 2010. cited By 9.

[354] Thomas G Spears and Scott A Gold. In-process sensing in selective laser melting (SLM) additive manufacturing. *Integr. Mater. Manuf. Innovation*, 5(1):2, 2016.

[355] Panagiotis Stavropoulos, Panagis Foteinopoulos, Alexios Papacharalampopoulos, and Harry Bikas. Addressing the challenges for the industrial application of additive manufacturing: Towards a hybrid solution. *International Journal of Lightweight Materials and Manufacture*, 1(3):157–168, 2018.

[356] William M Steen and Jyotirmoy Mazumder. *Laser material processing.* Springer Sci. Bus. Media, 2010.

[357] Jeremy Straub. Initial work on the characterization of additive manufacturing (3D printing) using software image analysis. *Machines*, 3(2):55–71, 2015.

[358] Danielle Strong, Michael Kay, Brett Conner, Thomas Wakefield, and Guha Manogharan. Hybrid manufacturing–integrating traditional manufacturers with additive manufacturing (am) supply chain. *Additive Manufacturing*, 21:159–173, 2018.

[359] Danielle Strong, Issariya Sirichakwal, Guha P Manogharan, and Thomas Wakefield. Current state and potential of additive–hybrid manufacturing for metal parts. *Rapid Prototyping Journal*, 2017.

[360] Christopher B Stutzman, Abdalla R Nassar, and Edward W Reutzel. Multi-sensor investigations of optical emissions and their relations to directed energy deposition processes and quality. *Additive Manufacturing*, 21:333–339, 2018.

[361] David Svetlizky, Mitun Das, Baolong Zheng, Alexandra L Vyatskikh, Susmita Bose, Amit Bandyopadhyay, Julie M Schoenung, Enrique J Lavernia, and Noam Eliaz. Directed energy deposition (ded) additive manufacturing: Physical characteristics, defects, challenges and applications. *Materials Today*, 2021.

[362] Z Szymanski, J Kurzyna, and W Kalita. The spectroscopy of the plasma plume induced during laser welding of stainless steel and titanium. *Journal of Physics D: Applied Physics*, 30(22):3153, 1997.

[363] S Tammas-Williams, H Zhao, Fabien Léonard, F Derguti, I Todd, and PB Prangnell. Xct analysis of the influence of melt strategies on defect population in ti–6al–4v components manufactured by selective electron beam melting. *Materials Characterization*, 102:47–61, 2015.

[364] H. Tan, J. Chen, F. Zhang, X. Lin, and W. Huang. Process analysis for laser solid forming of thin-wall structure. *International Journal of Machine Tools and Manufacture*, 50(1):1–8, 2010. cited By 45.

[365] Yingshui Tan, Baihong Jin, Alexander Nettekoven, Yuxin Chen, Yisong Yue, Ufuk Topcu, and Alberto Sangiovanni-Vincentelli. An encoder-decoder based approach for anomaly detection with application in additive manufacturing. In *2019 18th IEEE International Conference On Machine Learning And Applications (ICMLA)*, pages 1008–1015. IEEE, 2019.

[366] Ming Tang and P Chris Pistorius. Oxides, porosity and fatigue performance of alsi10mg parts produced by selective laser melting. *International Journal of Fatigue*, 94:192–201, 2017.

[367] Shangyong Tang, Guilan Wang, Haiou Zhang, and Rui Wang. An online surface defects detection system for awam based on deep learning. In *Solid Freeform Fabrication 2017: Proc. of the 28th Annual International Solid Freeform Fabrication Symposium–An Additive Manufacturing Conference*, volume 81, pages 1965–1981, 2017.

[368] Xin Tang, Ping Zhong, Lingling Zhang, Jun Gu, Zhaopeng Liu, Yinrui Gao, Haowei Hu, and Xutong Yang. A new method to assess fiber laser welding quality of stainless steel 304 based on machine vision and hidden markov models. *IEEE Access*, 8:130633–130646, 2020.

[369] Zi-jue Tang, Wei-wei Liu, Yi-wen Wang, Kaze Mojtaba Saleheen, Zhi-chao Liu, Shi-tong Peng, Zhao Zhang, and Hong-chao Zhang. A review on in situ monitoring technology for directed energy deposition of metals. *The International Journal of Advanced Manufacturing Technology*, pages 1–27, 2020.

[370] Xin Tao, Hongyun Gao, Xiaoyong Shen, Jue Wang, and Jiaya Jia. Scale-recurrent network for deep image deblurring. In *Proceedings of the IEEE Conference on Computer Vision and Pattern Recognition*, pages 8174–8182, 2018.

[371] Gustavo Tapia, Saad Khairallah, Manyalibo Matthews, Wayne E King, and Alaa Elwany. Gaussian process-based surrogate modeling framework for process planning in laser powder-bed fusion additive manufacturing of 316l stainless steel. *The International Journal of Advanced Manufacturing Technology*, 94(9-12):3591–3603, 2018.

[372] Nikolaos Tapoglou and Joseph Clulow. Investigation of hybrid manufacturing of stainless steel 316l components using direct energy deposition. *Proceedings of the Institution of Mechanical Engineers, Part B: Journal of Engineering Manufacture*, page 0954405420949360, 2020.

[373] Douglas S Thomas and Stanley W Gilbert. Costs and cost effectiveness of additive manufacturing. *NIST special publication*, 1176:12, 2014.

[374] Adam Thompson, Ian Maskery, and Richard K Leach. X-ray computed tomography for additive manufacturing: a review. *Measurement Science and Technology*, 27(7):072001, 2016.

[375] Syed AM Tofail, Elias P Koumoulos, Amit Bandyopadhyay, Susmita Bose, Lisa O'Donoghue, and Costas Charitidis. Additive manufacturing: scientific and technological challenges, market uptake and opportunities. *Materials today*, 21(1):22–37, 2018.

[376] Gleb Turichin, Evgeny Zemlyakov, Olga Klimova, and Konstantin Babkin. Hydrodynamic instability in high-speed direct laser deposition for additive manufacturing. *Physics Procedia*, 83:674–683, 2016.

[377] R.J. Urbanic, S.M. Saqib, and K. Aggarwal. Using predictive modeling and classification methods for single and overlapping bead laser cladding to understand bead geometry to process parameter relationships. *Journal of Manufacturing Science and Engineering, Transactions of the ASME*, 138(5), 2016. cited By 22.

[378] Ambra Vandone, Stefano Baraldo, Anna Valente, and Federico Mazzucato. Vision-based melt pool monitoring system setup for additive manufacturing. In *Proc. 52nd CIRP Conf. on Manuf. Systems (CMS)*, volume 81, pages 747–752. Elsevier, 2019.

[379] Aditad Vasinonta, Jack L Beuth, and Michelle L Griffith. A process map for consistent build conditions in the solid freeform fabrication of thin-walled structures. *J. Manuf. Sci. Eng.*, 123(4):615–622, 2001.

[380] Aditad Vasinonta, Jack L Beuth, and Raymond Ong. Melt pool size control in thin-walled and bulky parts via process maps. In *Solid Freeform Fabrication Proceedings*, pages 432–440. Citeseer, 2001.

[381] G Vastola, QX Pei, and Y-W Zhang. Predictive model for porosity in powder-bed fusion additive manufacturing at high beam energy regime. *Additive Manufacturing*, 22:817–822, 2018.

[382] Johannes Waldschmidt, Peter Lindecke, Marcel Wichmann, Berend Denkena, and Claus Emmelmann. Improved machining of additive manufactured workpieces using a systematic clamping concept and automated process planning.

[383] Min Wan, Zekai Murat Kilic, and Yusuf Altintas. Mechanics and dynamics of multifunctional tools. *Journal of Manufacturing Science and Engineering*, 137(1), 2015.

[384] Hongze Wang and Yu Zou. Microscale interaction between laser and metal powder in powder-bed additive manufacturing: Conduction mode versus keyhole mode. *International Journal of Heat and Mass Transfer*, 142:118473, 2019.

[385] Lu Wang, Yanming Zhang, and Wentao Yan. Evaporation model for keyhole dynamics during additive manufacturing of metal. *Physical Review Applied*, 14(6):064039, 2020.

[386] Q. Wang, J. Li, M. Gouge, A.R. Nassar, P. Michaleris, and E.W. Reutzel. Reduced-order multivariable modeling and nonlinear control of melt-pool geometry and temperature in directed energy deposition. volume 2016-July, pages 845–851, 2016. cited By 4.

[387] Q. Wang, J. Li, M. Gouge, A.R. Nassar, P. Michaleris, and E.W. Reutzel. Physics-based multivariable modeling and feedback linearization control of melt-pool geometry and temperature in directed energy deposition. *Journal of Manufacturing Science and Engineering, Transactions of the ASME*, 139(2), 2017. cited By 28.

[388] Qian Wang, Jianyi Li, Abdalla R Nassar, Edward W Reutzel, and Wesley F Mitchell. Model-based feedforward control of part height in directed energy deposition. *Materials*, 14(2):337, 2021.

[389] X. Wang, D. Deng, Y. Hu, Z. Liu, and H. Zhang. Analytical modeling and experimental investigation of laser clad geometry. *Optical Engineering*, 56(9), 2017. cited By 7.

[390] Y. Wang, C. Kamath, T. Voisin, and Z. Li. A processing diagram for high-density ti-6al-4v by selective laser melting. *Rapid Prototyping Journal*, 24(9):1469–1478, 2018. cited By 18.

[391] Yinmin Wang, Chandrika Kamath, Thomas Voisin, and Zan Li. A processing diagram for high-density Ti-6Al-4V by selective laser melting. *Rapid Prototyp. J.*, 24(9):1469–1478, 2018.

[392] Yong Wang, Minyan Yao, and Yanbiao Liao. Selection of optimal working wavelengths and bandwidths for dual-wavelength optical fiber pyrometer. In *Self-Calibrated Intelligent Optical Sensors and Systems*, volume 2594, pages 75–80. International Society for Optics and Photonics, 1996.

[393] Zhiyuan Wang, Renwei Liu, Todd Sparks, Heng Liu, and Frank Liou. Stereo vision based hybrid manufacturing process for precision metal parts. *Precision engineering*, 42:1–5, 2015.

[394] Zhuqing Wang, Todd A Palmer, and Allison M Beese. Effect of processing parameters on microstructure and tensile properties of austenitic stainless steel 304l made by

directed energy deposition additive manufacturing. *Acta Materialia*, 110:226–235, 2016.

[395] Nirupama Warrier and Kunal H Kate. Fused filament fabrication 3d printing with low-melt alloys. *Progress in Additive Manufacturing*, 3(1):51–63, 2018.

[396] K Wasmer, C Kenel, C Leinenbach, and SA Shevchik. In situ and real-time monitoring of powder-bed am by combining acoustic emission and artificial intelligence. In *International Conference on Additive Manufacturing in Products and Applications*, pages 200–209. Springer, 2017.

[397] L.C. Wei, L.E. Ehrlich, M.J. Powell-Palm, C. Montgomery, J. Beuth, and J.A. Malen. Thermal conductivity of metal powders for powder bed additive manufacturing. *Additive Manufacturing*, 21:201–208, 2018. cited By 67.

[398] Daniel Weisz-Patrault. Fast simulation of temperature and phase transitions in directed energy deposition additive manufacturing. *Additive Manufacturing*, 31:100990, 2020.

[399] Petra Wiederkehr and Jim A Bergmann. An integrated macroscopic model for simulating slm and milling processes. *Production Engineering*, 12(3):465–472, 2018.

[400] Jacob Williams, Paul Dryburgh, Adam Clare, Prahalada Rao, and Ashok Samal. Defect detection and monitoring in metal additive manufactured parts through deep learning of spatially resolved acoustic spectroscopy signals. *Smart and Sustainable Manufacturing Systems*, 2(1), 2018.

[401] J.M. Wilson, C. Piya, Y.C. Shin, F. Zhao, and K. Ramani. Remanufacturing of turbine blades by laser direct deposition with its energy and environmental impact analysis. *Journal of Cleaner Production*, 80:170–178, 2014. cited By 198.

[402] David Ian Wimpenny, Pulak M Pandey, L Jyothish Kumar, et al. *Advances in 3D printing & additive manufacturing technologies*. Springer, 2017.

[403] A Wippermann, TG Gutowski, B Denkena, M-A Dittrich, and Y Wessarges. Electrical energy and material efficiency analysis of machining, additive and hybrid manufacturing. *Journal of Cleaner Production*, 251:119731, 2020.

[404] F. Wirth and K. Wegener. A physical modeling and predictive simulation of the laser cladding process. *Additive Manufacturing*, 22:307–319, 2018. cited By 29.

[405] Terry Wohlers, Tim Caffrey, Robert Ian Campbell, Olaf Diegel, and Joseph Kowen. *Wohlers Report 2018: 3D Printing and Additive Manufacturing State of the Industry; Annual Worldwide Progress Report*. Wohlers Associates, 2018.

[406] Sarah J Wolff, Samantha Webster, Niranjan D Parab, Benjamin Aronson, Benjamin Gould, Aaron Greco, and Tao Sun. In-situ observations of directed energy deposition additive manufacturing using high-speed x-ray imaging. *JOM*, pages 1–12, 2020.

[407] Bin Xiao and Yuwen Zhang. Marangoni and buoyancy effects on direct metal laser sintering with a moving laser beam. *Numerical Heat Transfer, Part A: Applications*, 51(8):715–733, 2007.

[408] X. Xiao and S. Joshi. Automatic toolpath generation for heterogeneous objects manufactured by directed energy deposition additive manufacturing process. *Journal of Manufacturing Science and Engineering, Transactions of the ASME*, 140(7), 2018. cited By 5.

[409] Jun Xiong and Guangjun Zhang. Online measurement of bead geometry in GMAW-based additive manufacturing using passive vision. *Meas. Sci. Technol.*, 24(11):115103, 2013.

[410] Zifa Xu, Wentai Ouyang, Shaohui Jia, Junke Jiao, Mina Zhang, and Wenwu Zhang. Cracks repairing by using laser additive and subtractive hybrid manufacturing technology. *Journal of Manufacturing Science and Engineering*, 142(3), 2020.

[411] W. Ya, B. Pathiraj, and S. Liu. 2d modelling of clad geometry and resulting thermal cycles during laser cladding. *Journal of Materials Processing Technology*, 230:217–232, 2016. cited By 71.

[412] I Yadroitsev, A Gusarov, I Yadroitsava, and I Smurov. Single track formation in selective laser melting of metal powders. *Journal of Materials Processing Technology*, 210(12):1624–1631, 2010.

[413] Lei Yan, Wenyuan Cui, Joseph W Newkirk, Frank Liou, Eric E Thomas, Andrew H Baker, and James B Castle. Build strategy investigation of ti-6al-4v produced via a hybrid manufacturing process. *JOM*, 70(9):1706–1713, 2018.

[414] Lihang Yang, Lydia Lo, Sijie Ding, and Tuğrul Özel. Monitoring and detection of meltpool and spatter regions in laser powder bed fusion of super alloy inconel 625. *Progress in Additive Manufacturing*, pages 1–12, 2020.

[415] Lihang Yang, Kaushalendra V Patel, Krzysztof Jarosz, and Tuğrul Özel. Surface integrity induced in machining additively fabricated nickel alloy inconel 625. *Procedia CIRP*, 87:351–354, 2020.

[416] Yuying Yang, Yadong Gong, Shuoshuo Qu, Guoqiang Yin, Chunyou Liang, and Pengfei Li. Additive and subtractive hybrid manufacturing (ashm) of 316l stainless steel: Single-track specimens, microstructure, and mechanical properties. *JOM*, pages 1–11, 2020.

[417] Dongsen Ye, Geok Soon Hong, Yingjie Zhang, Kunpeng Zhu, and Jerry Ying Hsi Fuh. Defect detection in selective laser melting technology by acoustic signals with deep belief networks. *The International Journal of Advanced Manufacturing Technology*, 96(5-8):2791–2801, 2018.

[418] Bodi Yuan, Brian Giera, Gabe Guss, Ibo Matthews, and Sara Mcmains. Semi-supervised convolutional neural networks for in-situ video monitoring of selective laser melting. In *Proc. IEEE Winter Conf. on Appl. Comput. Vis.*, pages 744–753, 2019.

[419] Bodi Yuan, Gabriel M Guss, Aaron C Wilson, Stefan P Hau-Riege, Phillip J DePond, Sara McMains, Manyalibo J Matthews, and Brian Giera. Machine-learning-based monitoring of laser powder bed fusion. *Advanced Materials Technologies*, 3(12):1800136, 2018.

[420] Shahir Yusuf, Yifei Chen, Richard Boardman, Shoufeng Yang, and Nong Gao. Investigation on porosity and microhardness of 316l stainless steel fabricated by selective laser melting. *Metals*, 7(2):64, 2017.

[421] Kai Zeng, Deepankar Pal, and Brent Stucker. A review of thermal analysis methods in laser sintering and selective laser melting. In *Proceedings of Solid Freeform Fabrication Symposium Austin, TX*, volume 60, pages 796–814, 2012.

[422] Bin Zhang, Shunyu Liu, and Yung C Shin. In-process monitoring of porosity during laser additive manufacturing process. *Additive Manufacturing*, 2019.

[423] Peirong Zhang, Zhanqiang Liu, Jin Du, Guosheng Su, Jingjie Zhang, and Chonghai Xu. On machinability and surface integrity in subsequent machining of additively-manufactured thick coatings: A review. *Journal of Manufacturing Processes*, 53:123–143, 2020.

[424] Shuai Zhang, Yazhou Zhang, Ming Gao, Fude Wang, Quan Li, and Xiaoyan Zeng. Effects of milling thickness on wire deposition accuracy of hybrid additive/subtractive manufacturing. *Science and Technology of Welding and Joining*, 24(5):375–381, 2019.

[425] Song Zhang, JF Li, Jie Sun, and F Jiang. Tool wear and cutting forces variation in high-speed end-milling ti-6al-4v alloy. *The International Journal of Advanced Manufacturing Technology*, 46(1-4):69–78, 2010.

[426] Weijun Zhang, Masakazu Soshi, and Kazuo Yamazaki. Development of an additive and subtractive hybrid manufacturing process planning strategy of planar surface for productivity and geometric accuracy. *The International Journal of Advanced Manufacturing Technology*, 109(5):1479–1491, 2020.

[427] Xinchang Zhang, Wenyuan Cui, Wei Li, and Frank Liou. A hybrid process integrating reverse engineering, pre-repair processing, additive manufacturing, and material testing for component remanufacturing. *Materials*, 12(12):1961, 2019.

[428] Xinchang Zhang, Wenyuan Cui, and Frank Liou. Voxel-based geometry reconstruction for repairing and remanufacturing of metallic components via additive manufacturing. *International Journal of Precision Engineering and Manufacturing-Green Technology*, pages 1–24, 2021.

[429] Yingjie Zhang, Jerry YH Fuh, Dongsen Ye, and Geok Soon Hong. In-situ monitoring of laser-based PBF via off-axis vision and image processing approaches. *Addit. Manuf.*, 25:263–274, 2019.

[430] Yingjie Zhang, Geok Soon Hong, Dongsen Ye, Kunpeng Zhu, and Jerry YH Fuh. Extraction and evaluation of melt pool, plume and spatter information for powder-bed fusion am process monitoring. *Materials & Design*, 156:458–469, 2018.

[431] Ziyang Zhang, Zhichao Liu, and Dazhong Wu. Prediction of melt pool temperature in directed energy deposition using machine learning. *Additive Manufacturing*, 37:101692, 2021.

[432] G. Zhao, G. Ma, W. Xiao, and Y. Tian. Feature-based five-axis path planning method for robotic additive manufacturing. *Proceedings of the Institution of Mechanical Engineers, Part B: Journal of Engineering Manufacture*, 233(5):1412–1424, 2019. cited By 11.

[433] Yufan Zheng, Jikai Liu, and Rafiq Ahmad. A cost-driven process planning method for hybrid additive–subtractive remanufacturing. *Journal of Manufacturing Systems*, 55:248–263, 2020.

[434] Xin Zhou, Xihe Liu, Dandan Zhang, Zhijian Shen, and Wei Liu. Balling phenomena in selective laser melted tungsten. *Journal of Materials Processing Technology*, 222:33–42, 2015.

[435] Xin Zhou, Dianzheng Wang, Xihe Liu, DanDan Zhang, Shilian Qu, Jing Ma, Gary London, Zhijian Shen, and Wei Liu. 3d-imaging of selective laser melting defects in a co–cr–mo alloy by synchrotron radiation micro-ct. *Acta Materialia*, 98:1–16, 2015.

[436] Jia-Ning Zhu, Evgenii Borisov, Xiaohui Liang, Eduard Farber, MJM Hermans, and VA Popovich. Predictive analytical modelling and experimental validation of processing maps in additive manufacturing of nitinol alloys. *Additive Manufacturing*, 38:101802, 2021.

[437] Zicheng Zhu, Vimal G Dhokia, Aydin Nassehi, and Stephen T Newman. A review of hybrid manufacturing processes–state of the art and future perspectives. *International Journal of Computer Integrated Manufacturing*, 26(7):596–615, 2013.

[438] Zuowei Zhu, Nabil Anwer, Qiang Huang, and Luc Mathieu. Machine learning in tolerancing for additive manufacturing. *CIRP Annals*, 67(1):157–160, 2018.

[439] G Ziółkowski, E Chlebus, P Szymczyk, and J Kurzac. Application of x-ray ct method for discontinuity and porosity detection in 316l stainless steel parts produced with slm technology. *Archives of Civil and Mechanical Engineering*, 14(4):608–614, 2014.